NEUP-13-4908
Award Number: DE-NE0000710
Safeguards in Pyroprocessing: an Integrated Model Development and Measurement Data Analysis

Principal Investigator: Jinsuo Zhang
Graduate Student: Wentao Zhou (Ph.D), Yafei Wang (M.S.)

Nuclear Engineering Program, Department of Mechanical and Aerospace Engineering
The Ohio State University, Columbus, OH 43210

Co-principal Investigator: Supathorn Phongikaron (Virginia Commonwealth University)
Graduate Student : Dalsung Yoon (Ph.D)
Undergraduate student: Juan Ramonet, Jamie ParkHunter, Andrews
Postdoc: Seung H Kim
Mechanical and Nuclear Engineering, Virginia Commonwealth University
Richmond, Virginia 23284

Final Report
October 1st, 2017

Table of Contents

A. Publications, conference papers, and presentations

- Peer-reviewed journal publications

1. Yoon, Dalsung, and Supathorn Phongikaroon. "Measurement and Analysis of Exchange Current Density for U/U^{3+} Reaction in LiCl-KCl Eutectic Salt via Various Electrochemical Techniques." *Electrochimica Acta* **227** (2017): 170-179.
2. Yoon, Dalsung, Supathorn Phongikaroon, and Jinsuo Zhang. "Electrochemical and Thermodynamic Properties of $CeCl_3$ on Liquid Cadmium Cathode (LCC) in LiCl-KCl Eutectic Salt." *Journal of The Electrochemical Society* **163**.3 (2016): E97-E103.
3. Yoon, D., and S. Phongikaroon. "Electrochemical Properties and Analyses of $CeCl_3$ in LiCl-KCl Eutectic Salt." *Journal of The Electrochemical Society* **162**.10 (2015): E237-E243.
4. Zhou, Wentao, and Jinsuo Zhang. "Thermodynamic evaluation of LiCl-KCl-$PuCl_3$ system." *Journal of Alloys and Compounds* **695** (2017): 2306-2313.
5. Zhou, Wentao, and Jinsuo Zhang. "Chemical diffusion coefficient calculation of U^{3+} in LiCl-KCl molten salt." *Progress in Nuclear Energy* **91** (2016): 170-174.
6. Wang, Yafei, Wentao Zhou, and Jinsuo Zhang. "Investigation of concentration-dependence of thermodynamic properties of lanthanum, yttrium, scandium and terbium in eutectic LiCl-KCl molten salt." *Journal of Nuclear Materials* **478** (2016): 61-73.
7. Zhou, Wentao, and Jinsuo Zhang. "Direct calculation of concentration-dependent activity coefficient of UCl3 in molten LiCl-KCl." *Journal of The Electrochemical Society* **162**.10 (2015): E199-E204.
8. Zhang, Jinsuo, Erik A. Lahti, and Wentao Zhou. "Thermodynamic properties of actinides and rare earth fission products in liquid cadmium." *Journal of Radioanalytical and Nuclear Chemistry* **303**.3 (2015): 1637-1648.
9. Zhou, Wentao, Yafei Wang, and Jinsuo Zhang, “Integrated Model Development for Safeguarding Pyroprocessing Facility Part I-Model Development and Validation”, Annals of Nuclear Energy,112 (2017), 603-614.
10. Zhou, Wentao, Yafei Wang, and Jinsuo, Zhang, “Integrated Model Development for Safeguarding Pyroprocessing Facility Part II-Case Studies and Model Integration”, Annals of Nuclear Energy 112 (2017): 48-61.

- Conference papers

1. Yoon D, Phongikarron S, “Evaluation of thermodynamic properties of cerium in liquid cadmium cathode within LiCl-KCl salt system”, 24th International Conference on Nuclear Engineering, Charlotte, NC, June 26-30, 2016
2. Yoon D, Phongikaroon S, Shaltry M, “Analysis of electrochemical impedance spectra using constant phase element for $SmCl_3$ in LiCl-KCl eutectic”, ANS Transaction, 113.1 (2015): 1595:1597

3. Zhou W, Zhang J, “Thermodynamic assessment of LiCl-KCl-$PuCl_3$ ternary system”, ANS Transaction, 114.1 (2016): 181-182
4. Zhou W, Zhang J, “Direct Calculation of Concentration-Dependent Activity Coefficient of UCl_3 in Molten LiCl-KCl”, ANS Transaction, 112.1 (2015): 62-63

○ Presentations

1. Yoon D, Phongikarron S, “Effects of $GdCl_3$ on U Electrochemical Properties in LiCl-KCl-UCl_3-$GdCl_3$ Salt” ANS Annual meeting, San Francisco, CA, Jun. 11-15, 2017
2. Yoon D, Phongikarron S, “Electrochemical and Thermodynamic Properties of U in LiCl-KCl-UCl_3 Salt System”, San Francisco, CA, Jun. 11-15, 2017
3. Yoon D, Phongikarron S, “Measurement and Analysis of Exchange Current Density for U/U^{3+} Reaction in LiCl-KCl Eutectic via Various Electrochemical Techniques”, Jeju City, South Korea, Sep. 29, 2016
4. Yoon D, Phongikarron S, “Evaluation of Thermodynamic Properties of Cerium in Liquid Cadmium Cathode within LiCl-KCl Salt System”, 24th International Conference on Nuclear Engineering, Charlotte, NC, Jun. 10, 2016
5. Zhou W, Zhang J, “Integrated Model Development for Pyroprocesssing Safeguards”, MPACT/MRWFD Working Group Meeting, Albuquerque, NM, Mar. 28-31, 2017
6. Zhou W, Zhang J, “Thermodynamic assessment of LiCl-KCl-$PuCl_3$ ternary system”, 2016 ANS Annual Meeting, New Orleans, Jun 12-16, 2016
7. Wang Y, Zhou W, Zhang J, “Activity Coefficient of Rare Earth Elements in Eutectic LiCl-KCl, 2016 ANS Annual Meeting”, New Orleans, Jun 12-16, 2016
8. Zhou. W, Zhang J, “Direct Calculation of Concentration-Dependent Activity Coefficient of UCl_3 in Molten LiCl-KCl”, 2015 ANS Annual Meeting, San Antonio, TX, Jun. 7-11, 2015
9. Zhou W, Zhang J, “Multi-Component Deposition Model, 39^{th} Annual Actinide Separations Conference”, Salt Lake City, UT, May 18-21, 2015

B. Tasks and achievements

There are two main tasks of this NEUP project:

1) Develop the experimental and simulation methods to evaluate the electrochemical and thermodynamic properties of nuclear materials in the LiCl-KCl molten salt. Emphasis was placed on the U and Pu due to the safeguards concerns.

2) Develop an integrated model to predict the material flow and inventories during the electrorefining.

To achieve these goals, molecular dynamics simulation and phase assessment have been conducted at The Ohio State University (OSU) to calculate the properties of U, Pu, and other lanthanides in LiCl-KCl molten salt. These properties include apparent potential, activity coefficient, diffusion coefficient, and solubility. Simultaneously, extensive electrochemical experiments including cyclic voltammetry (CV), open circuit potential (OCP), Tafel plot, linear polarization (LP), and electrochemical impedance spectroscopy (EIS) techniques were performed in Virginia Commonwealth University (VCU) to determine the parameters of U. Specially, the exchange current density (i_0) of U/U^{3+} reaction was intensively explored in LiCl-KCl eutectic salt. Based on all the fundamental data obtained, the project developed an integrated model to predict the material separations in electrorefining, actinide drawdown and rare earth drawdown processes. The resulting database will provide an insight into fundamental understanding and signatures for material accountability for the electrorefining process in pyroprocessing for spent fuel treatment.

Part I: Technical Report from the Ohio State University

--Thermodynamic property calculation for U, La, Y, Sc, and Tb in LiCl-KCl molten salt and integrated model development to safeguard the pyroprocessing facility

Wentao Zhou[a], Yafei Wang[a,b], Jinsuo Zhang[a,b]

[a] Nuclear Engineering Program, Department of Mechanical and Aerospace Engineering The Ohio State University, Columbus, OH 43210

[b] Nuclear Engineering Program, Department of Mechanical Engineering, Virginia Polytechnic Institute and State University, Blacksburg, VA 24060

Nomenclature

A	surface area or constant
B	constant
C	concentration
D	diffusion coefficient
E	potential
F	Faraday constant or Helmholtz free energy
H	height of the solid anode
I	current
K	mass transfer coefficient
L	thickness
M	metal
N	total element number
N	interface normal
R	gas constant
S	solubility
T	temperature
U	flow velocity
V	volume
W	weight percent
a	activity
d	hydraulic diameter
e	electron
f	mass flux or constant
g	constant
j	exchange current
k	rate constant
k_d	constant
m	molar weight
n	number of electron
r	radius
x	molar fraction
z	atom number
δ	thickness of Nernst diffusion layer
v	kinematic viscosity
μ	dynamic viscosity
θ	constrictivity factor of porous structure
ϕ	effective transport-through porosity
τ	tortuosity factor
ρ	mass density
γ	activity coefficient
α	electron transfer coefficient
η	overpotential

Superscript and subscript

0	standard condition
ap	apparent potential
a	anode
alloy	undissolved alloy
AE	active elements
b	bulk concentration
Cd	cadmium
c	Cathode or crystal
dis	dissolution
EC	Einstein crystal
f	formal potential
fusion	property of fusion
i	element
id	ideal condition
j	element
l	liquid electrode
ms	molten salt
n	electron number
O	oxidant
porous	porous structure
open	open space solution
p_Zr	porous Zr layer
R	reductant
s	surface concentration or solid electrode
sc	supercooled
slb	solubility

EXECUTIVE SUMARRY

Pyroprocessing is an electrochemical method based on the molten salt electrolyte, mainly the LiCl-KCl eutectic molten salt, to recycle the used nuclear fuel. For a conceptual design of commercial pyroprocessing facility, tons of special nuclear materials, namely U and Pu, may be involved, which could be used for non-peaceful purposes if they are diverted. Effective safeguards approaches have to be developed prior to the development and construction of a pyroprocessing facility. Present research focused on two main objectives, namely calculating the properties of nuclear species in LiCl-KCl molten salt and developing integrated model to safeguard a pyroprocessing facility. Understanding the characteristics of special nuclear materials in LiCl-KCl eutectic salt is extremely important to understand their behaviors in an electrorefiner. The model development for the separation processes in the pyroprocessing, including electrorefining, actinide drawdown, and rare earth drawdown benefits the understanding of material transport and separation performance of these processes under various conditions. The output signals, such as potential, current, and species concentration contribute to the material balance closure and provide safeguards signatures to detect the scenarios of diversion. U and Pu are the two main elements concerned in this study due to our interest in safeguards.

By molecular dynamics simulation, fundamental data of UCl_3, $LaCl_3$, YCl_3, $ScCl_3$, and $TbCl_3$ in LiCl-KCl molten salt, namely activity coefficient, apparent potential, and diffusion coefficient, were calculated by molecular dynamics simulation method up to a high concentration of around 3 mol%. Emphasis was placed on their concentration dependence since almost all the literature data were obtained in dilute solutions, which may not be applicable to the practical facilities with high concentration nuclear materials. Our results indicate that the activity coefficient and apparent potential increase with the concentration. The diffusion coefficient keeps nearly constant at low concentration but it proceeds to increase followed by a decrease at high concentration even though the variation range of diffusivity is small.

The phase diagram of LiCl-KCl-$PuCl_3$ was assessed by the CALculation of PHAse Diagram (CALPHAD) method. It was found that the apparent potential also increases with the concentration. The solubility of $PuCl_3$ in LiCl-KCl was determined to be 41.5 mol% at 773 K.

Integrating these fundamental data with electrochemical theory, a kinetic model was eventually developed to predict the material transport in the electrorefiner. After being validated by literature data, a transport case with seven species, including Zr, U, Pu, Am, La, Gd, and Ce was studied to investigate the separation between noble metals, actinides, and lanthanides, The electrorefining, actinide drawdown, and rare earth drawdown were run under different conditions, such as different electrodes and current patterns. The potential, current, and species concentration obtained from the model were used to analyze the material transport behaviors and separation degrees under different cases. Extensive data was determined and collected to provide the signatures of safeguards for the pyroprocessing.

1 Introduction

Pyroprocessing is an electrochemical method to recycle the actinides contained in used nuclear fuel (UNF) based on the molten salt electrolyte. It was originally developed by ANL [1][2] and used to process the metallic fuel discharged from EBR-II as a part of the Integral Fast Reactor (IFR) program initiated in 1984 to demonstrate the fast reactor on-site fuel cycle closure [3]. The conceptual flowsheet of the method is illustrated in Figure 1.1.

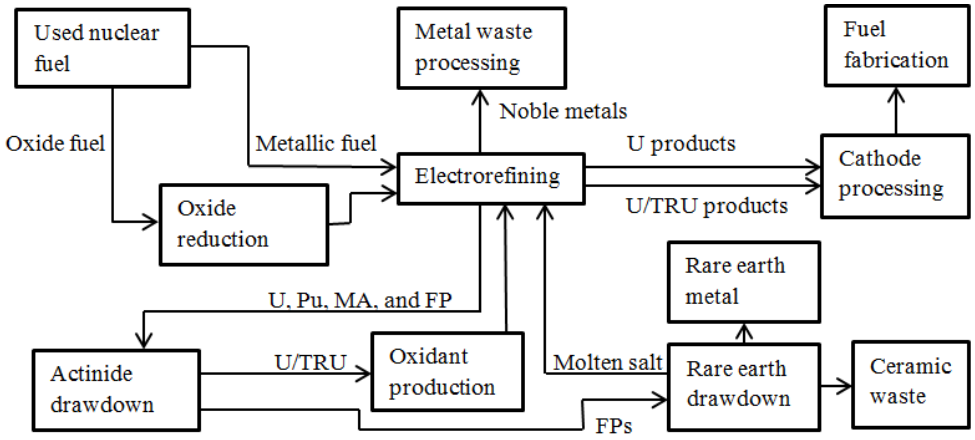

Figure 1.1. Conceptual flowsheet of pyroprocessing to process oxide and metallic fuels

Even though it was initially designed for the treatment of metallic used fuels from fast reactors, pyroprocessing can also be extended to process oxide fuel from light water reactors (LWRs) with an additional step of oxide reduction based on a molten Li_2O-LiCl salt, which has been well reviewed by Choi et al. [4]. The key element of the pyroprocessing is the electrorefining process, where U and transuranium (TRU) elements are electrochemically separated with noble metals (NMs) and fission products (FPs), as is shown in Figure 1.2 [5]. Metallic UNF or reduced oxide fuel are charged in a perforated basket as the anode, inside which active elements, such as actinides and active fission products are oxidized into the LiCl-KCl electrolyte. The elements whose potentials are lower than that of U are dissolved into the LiCl-KCl electrolyte with U and others are left in the anode basket. At the cathode side, uranium is deposited on the solid cathode selectively by controlling the applied current. Residual uranium, plutonium, and minor actinides are then deposited into liquid cadmium cathode (LCC) or on a solid electrode based on electrorefiner design. Both products go through the cathode processing to clean the salt or cadmium by distillation before injection casting and fuel fabrication [6,7]. More active FPs such as lanthanide metals and alkaline earth metals remain in the electrolyte, with some actinides. Actinide drawdown is applied to clean the actinides, which are oxidized and returned to the electrorefiner for current support [8]. The remaining rare earth FPs are cleaned by rare earth drawdown. Other waste, for example, Cs and Sr, is prepared in ceramic form for the final disposal [8]. Cladding materials and other NMs residing in anode basket or at the bottom of electrorefiner are consolidated into metallic ingots in a metal waste furnace for the disposal [9].

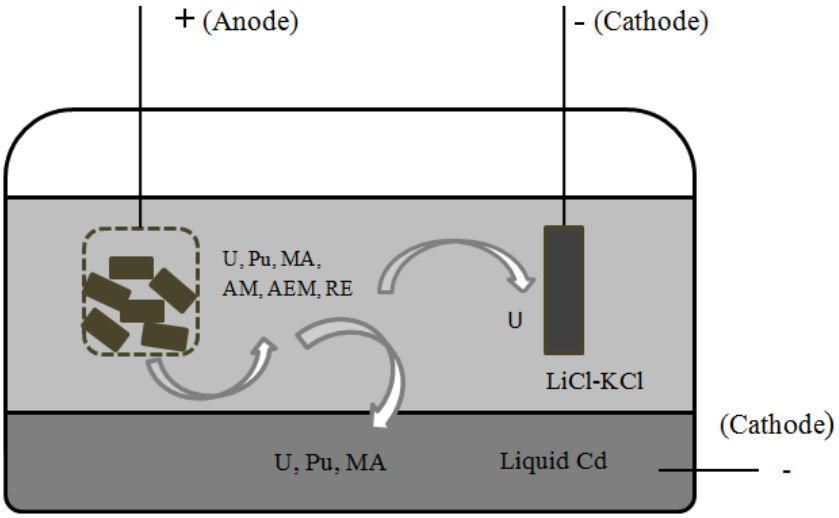

AM: Alkali metal FPs AEM: Alkaline earth metal FPs
RE: Rare earth FPs MA: Minor actinides

Figure 1.2. Schematic figure of typical design of electrorefiner

The reactions in electrorefiner can be expressed as

Anode: $M \rightarrow M^{n+} + ne^{-}$

Cathode: $M^{n+} + ne^{-} \rightarrow M$

Net: $M\,(anode) \rightarrow M\,(cathode)$

Pyroprocessing is a dry process without the involvement of water. The LiCl-KCl molten salt has high radiation resistance. Therefore it has the potential capability to process a large amount of hot fissile materials, even when only cooling for several months through remote control with little worry about criticality risks and material degradation [10,11]. An economic advantage is also expected considering a more compact site with fewer steps, less equipment, and footprint [12,13]. Additionally, plutonium is co-deposited with uranium and other minor actinides as U/TRU products, which provides a barrier to the proliferation. Therefore, pyroprocessing is being considered as a promising alternative to the traditional PUREX process to recycle the UNF. Obviously, quantities of special nuclear materials (SNMs) are involved in the pyroprocessing. Approaches to secure and safeguard the pyroprocessing facility are essential before it can be commercialized.

1.1 Safeguards of Special Nuclear Materials

According to the International Atomic Energy Agency (IAEA), the objective of safeguards is the timely detection of the diversion of SNMs, in significant quantities, from peaceful to non-peaceful or unknown purposes [14], which is imperative for the civil use of nuclear energy. Timely detection indicates that the time from diversion to detection should be less than the time needed to

convert the nuclear materials to the component of a nuclear explosive device (conversion time). Significant quantities are the quantities minimally required to manufacture a nuclear explosive device for different kinds of special nuclear materials [14]. Significant quantities declared by IAEA are listed in Table 1.1 [15]. The main species needing safeguard are Pu and U considering their amount in UNF. The IAEA basically needs to verify the inventories of Pu and U and be aware of their distributions at various positions of the process flow to ensure that the operation is the same as declared and to detect any possible diversion scenarios [16]. Once the materials unaccounted for exceed their significant quantities in a conversion time, an alert should be given to stop the nuclear facility and close the material balances.

Table 1.1. Significant quantities of different kinds of materials [15]

Material	Significant quantities
Direct use nuclear material	
Pu (^{238}Pu<80%)	8 kg Pu
^{233}U	8 kg ^{233}U
High enriched U (^{235}U≥ 20%)	25 kg ^{235}U
Indirect use nuclear material	
Low enriched U (^{235}U< 20%)	75 kg ^{235}U
Natural U	10 t natural U
Depleted U	20 t depleted U
Th	20 t Th

1.1.1 Safeguards issues in pyroprocessing

Considering a commercial facility with the reprocessing capacity of 100 tHM per year, Pu involved in the process could be up to 1 tHM, which is hundreds of times of its significant quantity. Because all the reprocessing plants nowadays are PUREX based process, unique safeguards methods for it have been well developed. However, key differences between PUREX process and pyroprocessing [17] challenges the application of these developed safeguards approaches to the pyroprocessing facilities. These key differences include:

1.1.1.1 No accountability tank

The most traditional method for safeguards is the material control and accountability by destructive (DA) or nondestructive assay (NDA). However, this is only suitable for the PUREX process. In the PUREX process, all the UNF is dissolved into the accountability tank to generate a homogenous solution. Samples taken from it can represent the overall concentrations of Pu and U. Therefore their inventories can be determined easily by DA or NDA methods. Additionally, due to the continuity of the process, Pu and U can be readily tracked by analyzing the flow and separation conditions [18]. However, the method is hard to apply in the pyroprocessing, where the UNF is dissolved into LiCl-KCl electrolyte electrochemically instead of chemically. The anode

dissolution happens at the same time as the cathode deposition. It is a dynamic process and at no time during the process will all the UNF be distributed only in the electrolyte. It is thus not possible to determine inventories of Pu and U by sampling the electrolyte. Other NDA methods to directly measure the Pu composition in UNF assembly, such as neutron counting, could have an uncertainty of several percent since it needs to be based on the DA to determine the Cm/Pu ratio first, which introduces uncertainty because of the heterogeneity of the fuel [19]. A significant quantity of Pu will be accumulated quickly even for a throughput of 100 tHM/year.

1.1.1.2 Inability to flush out

In the aqueous process, a flushout can be conducted to close the material balance with low uncertainty to determine whether the diversion of SNM occurs. In pyroprocessing, however, it may not be feasible to apply this. With the main purpose to separate the U from TRU and FPs by the electrochemical method, U should be kept above a certain concentration to support the applied current and guarantee the purity of the deposition [20]. Removing all the salt and actinides would interrupt the process and affect its efficiency [21].

1.1.1.3 Electrorefiner

The electrorefiner is where all the separations happen. With the deposition of U, Pu is accumulated gradually inside with to a high concentration. A measurement with low uncertainty could result in a discrepancy of 1 SQ Pu. Also, the large processing volume with multiple cathodes makes the measurement more complicated [17]. The dendritic solid deposition also requires new approaches for composition assay considering it is impossible to obtain a homogeneous sample as in aqueous process with an accountability tank. All these features of pyroprocessing set barriers for the application of existing safeguard approaches and require more effective and proper material tracking and assay technologies

1.1.1.4 Harsh environment

The electrorefining is generally running at the elevated temperature ranging from 450 ^{0}C to 550 ^{0}C. The molten salt and metal solutions are highly corrosive [22]. Such an environment will be a very challenging for the safeguards equipment and instruments.

1.1.1.5 Little experience

Not like the aqueous process that has been commercialized for more than a half century. The pyroprocessing now is still in earlier design stage and this is no facility beyond the laboratory or pilot-scale. The design of such facilities are not well defined yet. Not much experience or literature thus has been accumulated to refer to.

1.2 Goals/Outcome

All these features discussed above set barriers for the application of existing safeguards approaches to pyroprocessing facility and motivate us to develop more effective and proper material tracking and assay technologies. The primary goal of OSU is to develop an integrated model to help safeguarding pyroprocessing facility. The premise is apparently to collect all the necessary electrochemical and thermodynamic data of nuclear materials in LiCl-KCl molten salt. Two steps therefore performed in OSU: fundamental data calculation and model develop. Fundamental data of UCl_3 in LiCl-KCl molten salt, namely activity coefficient, apparent potential, and diffusion coefficient, were calculated by molecular dynamics simulation method up to a high concentration of around 3 mol%. Emphasis was placed on their concentration dependence since almost all the literature data were obtained in dilute solutions, which may not be applicable to the practical facilities with high concentration actinides. Our results indicate that the activity coefficient and apparent potential increase with the concentration. The diffusion coefficient keeps nearly constant at low concentration but it proceeds to increase followed by a decrease at high concentration even though the variation range of diffusivity is small. The phase diagram of LiCl-KCl-$PuCl_3$ was assessed by the CALPHAD method. It was found that the apparent potential also increases with the concentration. The solubility of $PuCl_3$ in LiCl-KCl was determined to be 41.5 mol% at 773 K. Integrating all these fundamental data with electrochemical theory, a kinetic model was developed to predict the material transport in the electrorefiner. After being validated by studies in literature, cases about electrorefining, actinide drawdown, and rare earth drawdown were run under different conditions, such as different electrodes and current patterns. Potential, current, and species concentration obtained from the model were used to analyze the material transport properties and separation efficiency under different cases. Extensive data was determined to provide the signatures of safeguards for the pyroprocessing.

1.3 Literature review

For the safeguards of the pyroprocessing, the main materials considered are the U and Pu due to their properties of being manufactured to be nuclear explosive devices. Therefore, their fundamental data in LiCl-KCl molten salt are essential to any model development and to understand the design, control, efficiency, and safeguards of the pyroprocessing facilities. Previous studies were reviewed and reanalyzed to identify what has been done and what needs to be further researched. Additionally, various safeguards methods that have been widely investigated were reviewed to understand the state-of-the-art safeguard techniques. These reviews provide the basis of the present work about the model development.

1.3.1 Thermodynamic properties of UCl_3 and $PuCl_3$

As the major actinides, extensive studies have been carried out to investigate the electrochemical behaviors, including the apparent potentials, activity coefficients, and diffusion coefficients of UCl_3 and $PuCl_3$, in LiCl-KCl eutectic salt with various electrodes, temperatures, and concentrations by different electrochemical techniques [23-46].

1.3.1.1 Apparent potential

As discussed above, the potential is the deciding factor for separating one element from another. When the applied potential is more negative than the redox potential of an element, the element can be reduced and deposited out. For a reduction reaction shown as

$$M^{n+} + ne^- = M \qquad \text{Eq. 1.1}$$

the equilibrium potential can be expressed by the Nernst equation

$$E_{eq} = E^0_{MCl_n} + \frac{RT}{nF}\ln(\frac{a_{MCl_n}}{a_M}) \qquad \text{Eq. 1.2}$$

where E^0 is the standard potential, R is the universal gas constant, T is the temperature in Kelvin, n is the number of electrons involved, F is the Faraday constant, and a is the activity coefficient. It can be written as

$$a = \gamma x \qquad \text{Eq. 1.3}$$

where x is the mole fraction, and γ is the activity coefficient, which is a measurement of the deviation from the ideal solution. For a metal deposition, a is reduced to 1. Generally, the activity coefficient of metal chloride is lumped into the standard potential, which gives

$$E_{eq} = E^{ap} + \frac{RT}{nF}\ln(x_{MCl_n}) \qquad \text{Eq. 1.4}$$

where E^{ap} is called the apparent potential, which can be measured experimentally by cyclic voltammetry (CV), chronoamperometry (CA), chronopotentiometry (CP), and electromotive force methods (EMF).

Uranium

Figure 1.3 shows the reported apparent potentials of UCl_3 in LiCl-KCl eutectic at different temperatures without considering the concentration (All the plots of apparent potential, activity coefficient, and diffusion coefficient against temperature do not consider the effect of concentration) [23-36]. They are in pretty good agreement with 60 mV and show a linear relationship with temperature. The data from Hoover et al. [28] and Ghosh et al. [31] have some discrepancy with others, which may be due to the facts that in Hoover et al.'s [28] work, they used higher UCl_3 concentration from 1 to 10 wt%, and for Ghosh et al. [31], the working electrode they used was uranium rod not tungsten or platinum commonly used in other references [23].

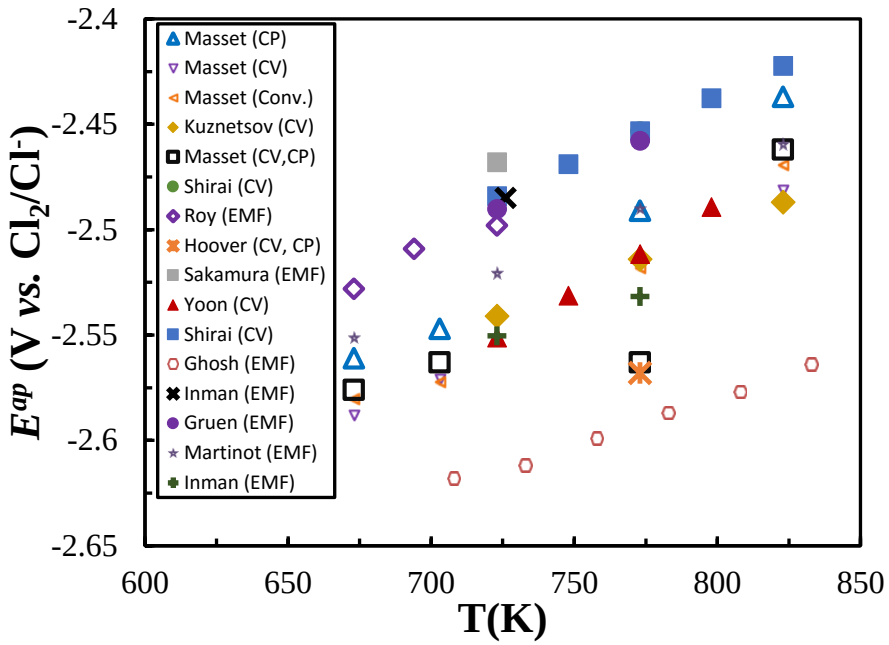

Figure 1.3. The apparent potential of UCl_3 in LiCl-KCl eutectic at different temperatures

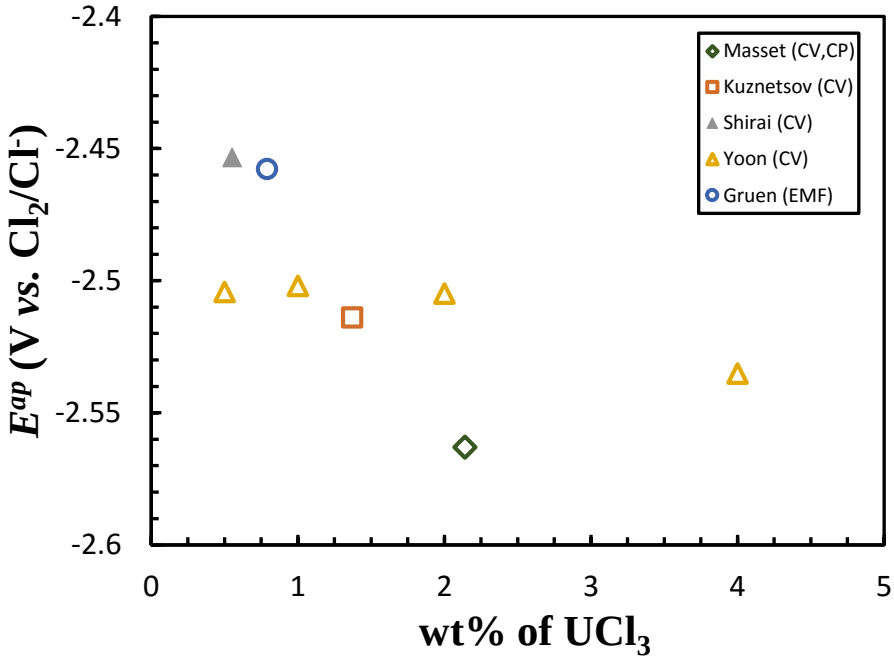

Figure 1.4. The apparent potential of UCl_3 in LiCl-KCl at 773 K with different concentrations

Figure 1.4 plots the concentration dependence of apparent potentials at 773 K. For the EMF method, the cell potential relative to an Ag/AgCl reference electrode can be expressed as

$$E = E^0_{MCl_n} + \frac{RT}{nF}\ln x_{MCl_n} + \frac{RT}{nF}\ln \gamma_{MCl_n} - E^0_{AgCl} - \frac{RT}{F}\ln x_{AgCl}$$
$$= E^{ap} + \frac{RT}{nF}\ln x_{MCl_n} - E^0_{AgCl} - \frac{RT}{F}\ln x_{AgCl} \quad \text{Eq. 1.5}$$

With a given temperature, a series of cell potentials under different concentrations can be measured. The apparent potential can be obtained from the slope of the plot E *vs.* $\log x_{MCl_n}$, which is the general method used to analyze the measured data in literature. Roy et al. [27] derived the standard potential of Ag/AgCl relative to Cl_2/Cl^-

$$E^0_{AgCl} = -1.0910 + 0.0002924T \quad \text{Eq. 1.6}$$

which is commonly used unless otherwise indicated in the present study. On the other hand, under a given concentration, assuming

$$E^0_{MCl_n} = A + BT \quad \text{Eq. 1.7}$$

and

$$E^0_{AgCl} = C + DT \quad \text{Eq. 1.8}$$

Eq. 1.5 could be rewritten as

$$E = (A - C) + (B + \frac{R}{nF}\ln \gamma_{MCl_n} - D + \frac{R}{nF}\ln x_{MCl_n} - \frac{R}{F}\ln x_{AgCl})T \quad \text{Eq. 1.9}$$

Knowing the values of C and D, for example from Eq. 1.6, A and B can be derived from the E *vs.* T plot. Then the apparent potential under given concentration could be calculated. The method was used to reanalyze the literature data to investigate their concentration dependence. The results indicate that the apparent potential has little dependence on the concentration. However, due to the sparse amount of data collected and these works had different electrochemical methods and conditions applied to obtain this data, the concentration dependence may not be revealed comprehensively.

Plutonium

Figure 1.5 shows the apparent potential of $PuCl_3$ in LiCl-KCl at different temperatures [25,26,27,29 ,36,42,43,44]. The data is in accordance with each other being within 60 mV and linearly depending on the temperature. Figure 1.6 plots the apparent potentials of $PuCl_3$ in LiCl-KCl at 773 K with different concentrations. The data reported by Masset et al. [25] and Sakamura et al. [43] are more negative compared to those from Shirai et al. [26,44]. However, due to the large discrepancy between them, a convincing conclusion about the effect of concentration cannot be provided.

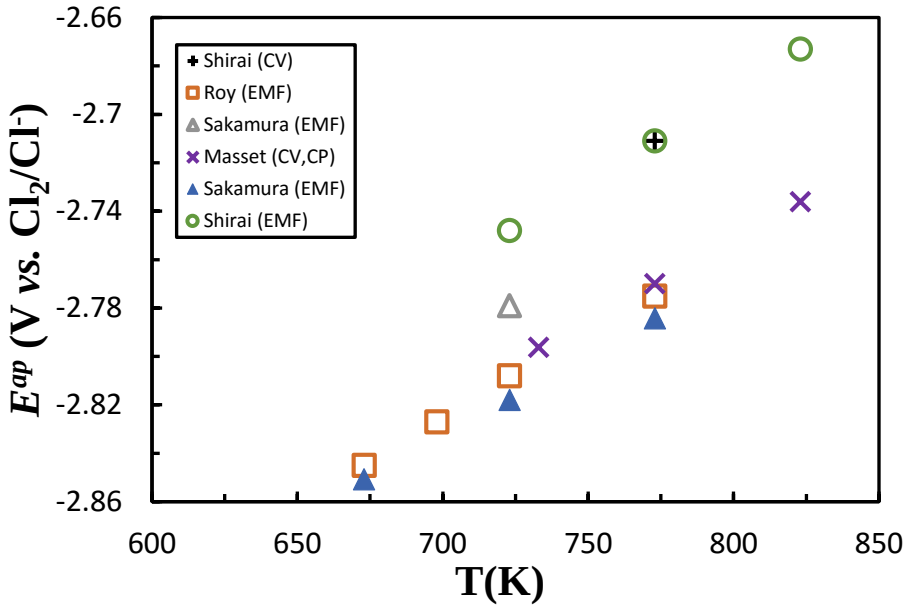

Figure 1.5. The apparent potential of $PuCl_3$ in LiCl-KCl eutectic at different temperatures

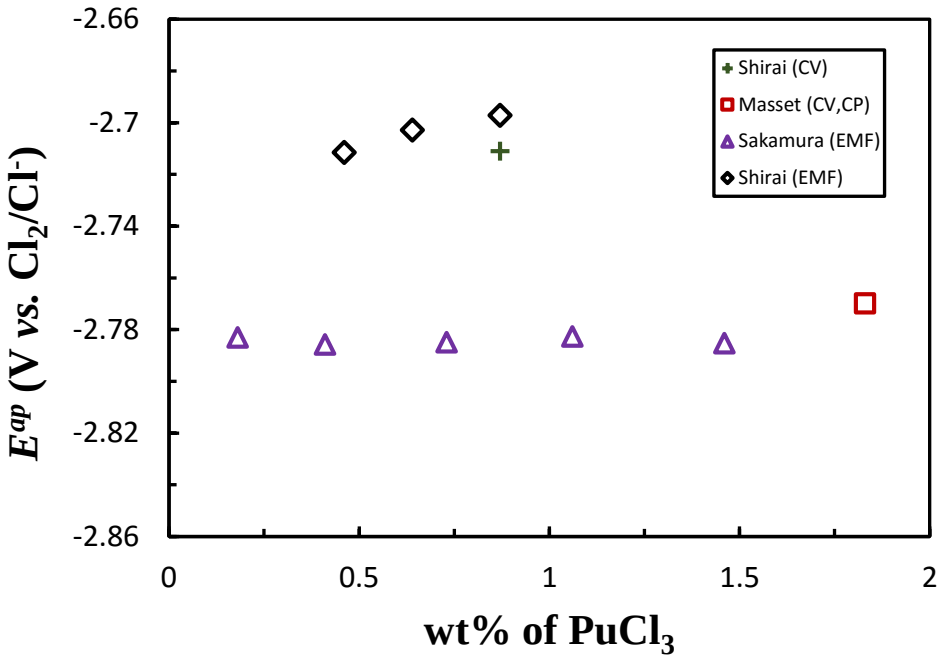

Figure 1.6. The apparent potential of $PuCl_3$ in LiCl-KCl eutectic at 773 K with different concentrations

1.3.1.2 Activity coefficient

The activity coefficient is a measurement of the deviation of a solution to the ideal one. After obtaining the apparent potential, the activity coefficient can be calculated by

$$E^{ap} = E^0 + \frac{RT}{nF}\ln\gamma$$
$$\gamma = \exp[\frac{nF}{RT}(E^{ap} - E^0)] \qquad \text{Eq. 1.10}$$

The value of the activity strongly relies on the accuracy of the standard potential. For the molten salt system, standard potential E^0 is generally taken from the supercooled state of the pure chloride salt, i.e

$$E^0 = \frac{\Delta G^0_{sc}}{nF} \qquad \text{Eq. 1.11}$$

where G^0_{sc} is the Gibbs energy of formation of the supercooled state. It can be calculated by the thermodynamic data [25]

$$\Delta G^0_{sc} = \Delta G^0_s + \int_{T_m}^{T}(C_p^l - C_p^s)dT - T\int_{T_m}^{T}\frac{C_p^l - C_p^s}{T}dT + \Delta H_{f,T_m}(1-\frac{T}{T_m}) \qquad \text{Eq. 1.12}$$

where ΔG^0_s is the standard Gibbs energy of formation in solid state, C_p^s and C_p^l are the heat capacities of solid and liquid states, respectively, at constant pressure. $\Delta H_{f,T_m}$ is the enthalpy of fusion, and T_m is the melting temperature in Kelvin.

Uranium

Only a few of the researchers reporting the apparent potential calculated the activity coefficient, which is plotted in Figure 1.7 [23,24,25,27,28,36,47]. However, these values show a maximum difference up to one order of magnitude. The values from Yoon [47] and Roy et al. [27] are much larger than other values. Figure 1.8 shows the concentration dependence of the activity coefficient at 773 K but no reliable conclusion can be reached based on the limited data points.

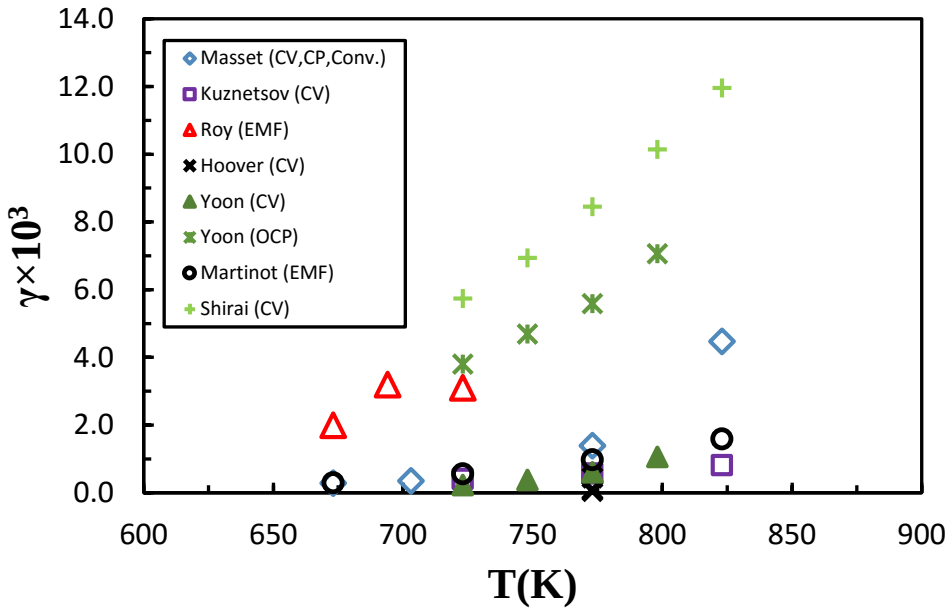

Figure 1.7. Activity coefficient of UCl_3 in LiCl-KCl eutectic at different temperatures

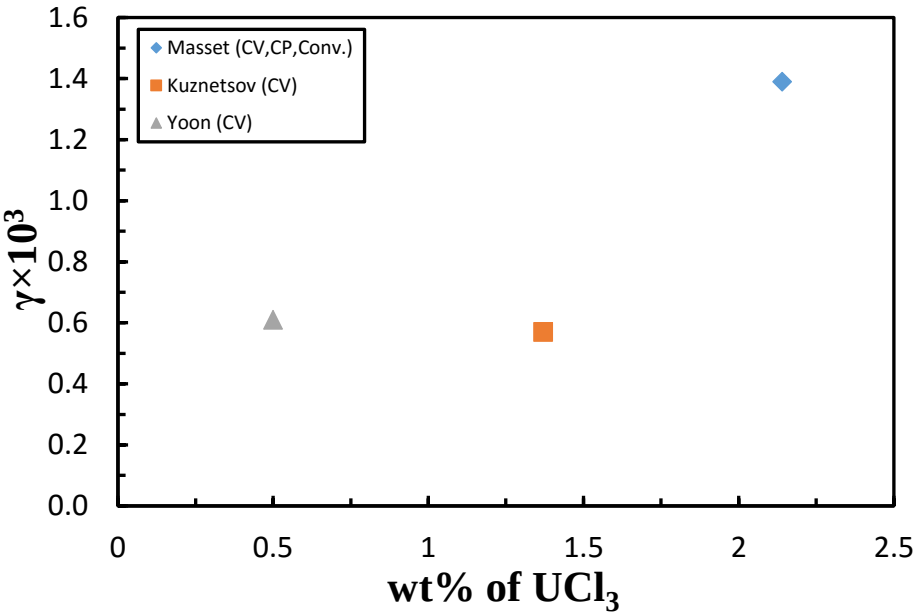

Figure 1.8. Activity coefficient of UCl_3 in LiCl-KCl eutectic at 773 K with different concentrations

Plutonium

Figure 1.9 shows the activity coefficients of $PuCl_3$ in LiCl-KCl eutectic at different temperatures [25,27,42]. When calculating the activity coefficient, Serp et al. [42] retrieved Gibbs energy of supercooled state from two databases, *f*-MPD [48] and NEA-TDP [49]. The results are marked as Serp (CV,CP)_1 and 2, respectively. The first set of data agrees adequately well with values from

other references but the second data set is two to three times larger. The Gibbs energy of the supercooled state has a significant effect on the activity coefficient values. The data is not sufficient to plot against the concentration.

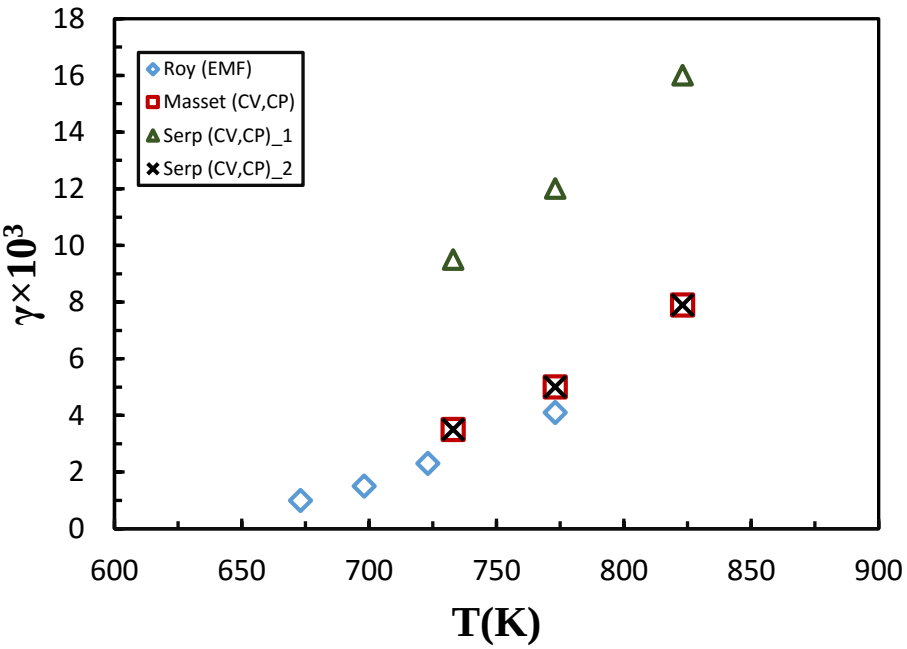

Figure 1.9. Activity coefficient of $PuCl_3$ in LiCl-KCl eutectic at different temperatures

1.3.1.3 Diffusion coefficient

Diffusion coefficients are fundamental data to understand the transport of materials in LiCl-KCl electrolyte by Fick's Law. It is essential to predict the electrorefining performance and efficiency, and also necessary for the model development considering that the diffusion coefficients limit the maximum current allowed in an electrorefiner [50]. Generally, the diffusion coefficient is expressed by the Arrhenius law with the temperature

$$D = D_0 \exp(\frac{-E_a}{RT}) \qquad \text{Eq. 1.13}$$

where D_0 is a pre-exponential factor, and E_a is the activation energy.

Uranium

Figure 1.10 plots the diffusion coefficient of UCl_3 in LiCl-KCl eutectic at various temperatures [23,24,25,28,35,37,38,41,47]. The data basically shows a linear dependence on the temperature but wide scatter appears especially at high temperatures. The reported data from Masset et al. [23,25] show larger values compared to other sources. Figure 1.11 shows the concentration dependence of the UCl_3 diffusion coefficient at 773 K. This data shows good agreement except for Hoover's results [28] from CV method, which gives relatively larger values. The data is widely spread but seems to be affected little by the concentration.

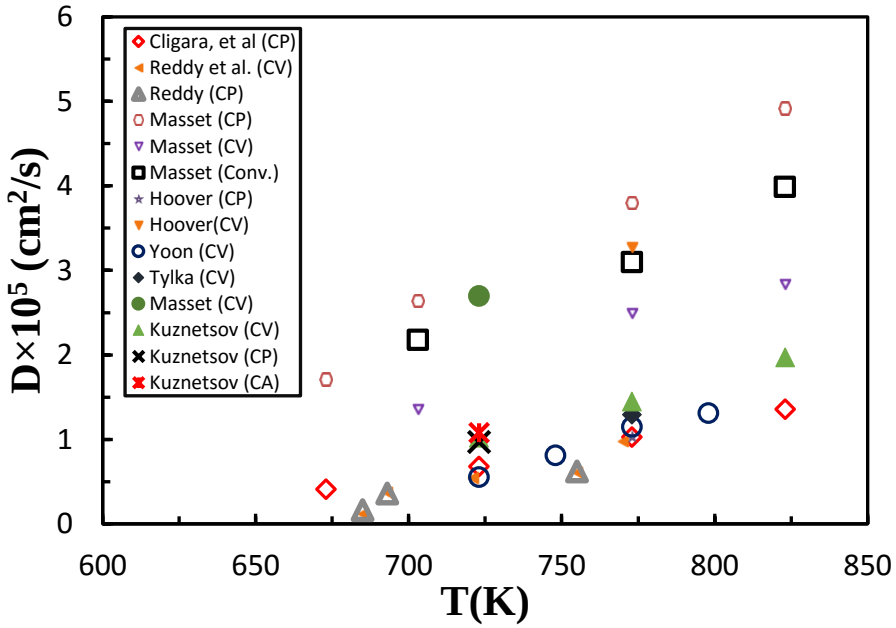

Figure 1.10. Diffusion coefficient of UCl_3 in LiCl-KCl eutectic at different temperatures

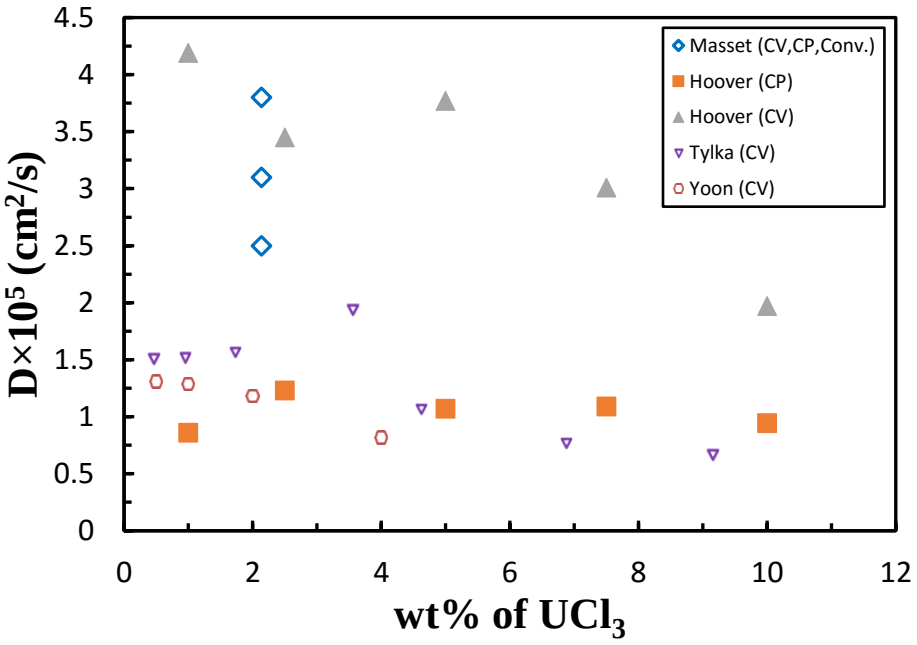

Figure 1.11. Diffusion coefficient of UCl_3 in LiCl-KCl eutectic at 773 K with different concentrations

Plutonium

Figure 1.12 plots the diffusion coefficient of $PuCl_3$ in LiCl-KCl eutectic at different temperatures [25,39,42,44-46]. The diffusion coefficient shows a linear dependence on the temperature. All the data agrees well with each other except those from Shirai et al. [44], which are much larger. Figure

1.13 shows the concentration dependence of the diffusion coefficient. Data from Nissen et al. [45] and Martinot et al. [46] are in agreement with each other. They show little variation with concentration, similarly to the data reported by Shirai et al [44]. However, when these data sets are put together, no obvious conclusion can be claimed due to the large fluctuation.

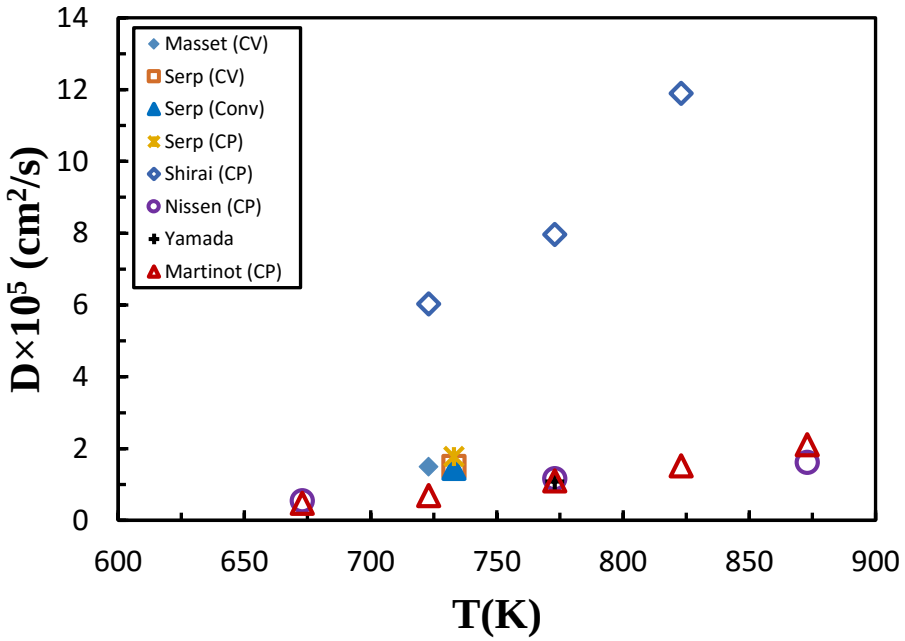

Figure 1.12. Diffusion coefficient of $PuCl_3$ in LiCl-KCl eutectic at 773 K with different temperatures

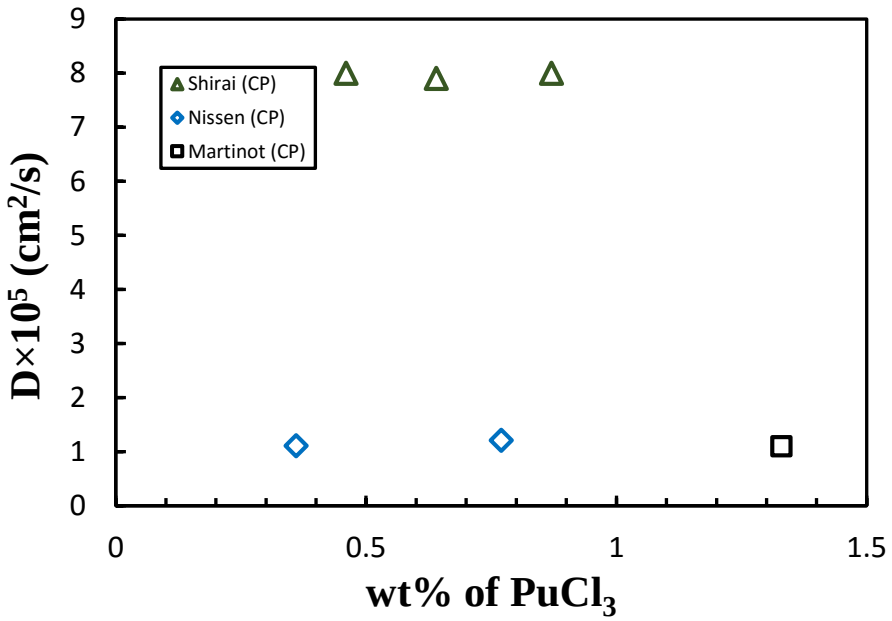

Figure 1.13. Diffusion coefficient of $PuCl_3$ in LiCl-KCl eutectic at 773 K with different concentrations

1.3.1.4 Exchange current

Exchange current is an important measurement of how fast electrons can be transferred in a reaction. Its value represents the half reaction current when a reaction reaches equilibrium. For a soluble-insoluble transition, exchange current can be expressed by

$$j_0 = nFk_0 C_O^{b\,(1-\alpha)} \qquad \text{Eq. 1.14}$$

where k_0 is the rate constant, C_O is the concentration of oxidant. α is the electron transfer coefficient. Before building a kinetic model which considers the Faraday process on the electrode, the parameter has to be evaluated. By different methods, namely CV, Tafel plot, electrochemical impedance spectroscopy (EIS), and linear polarization (LP), the exchange current for the UCl_3 in LiCl-KCl with various concentrations at different temperatures has been studied [51-54]. Figure 1.14 plots the exchange currents at different concentrations and temperatures. This figure basically shows the exchange current increases with the temperature. Figure 1.15 plots the exchange current at different temperatures. It shows a roughly straight line, which indicates a value of zero for α according to Eq. 1.14. However, no references found reported this value. There are no investigations for the exchange current of Pu.

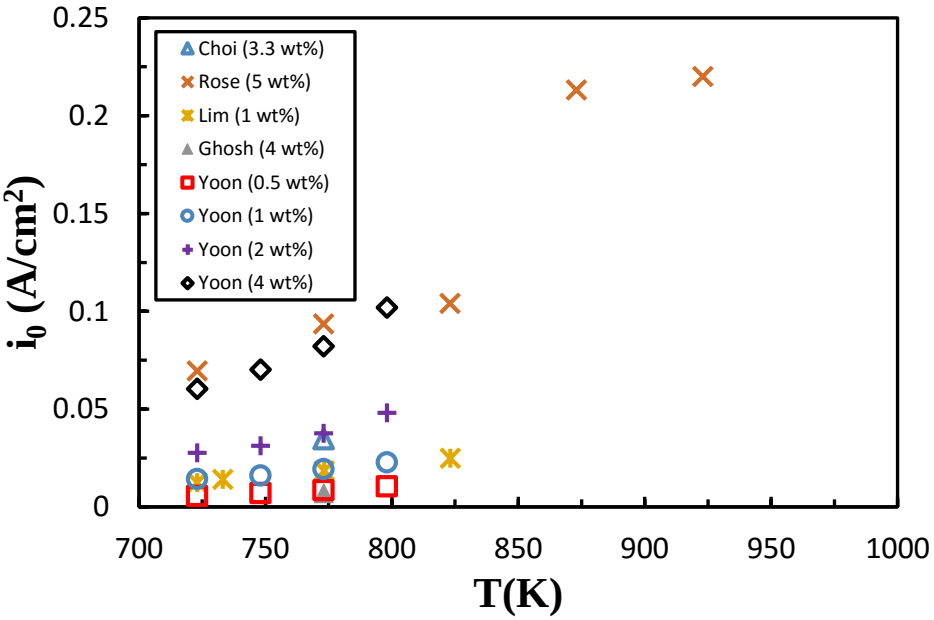

Figure 1.14. Exchange current of UCl_3 in LiCl-KCl eutectic at different temperatures

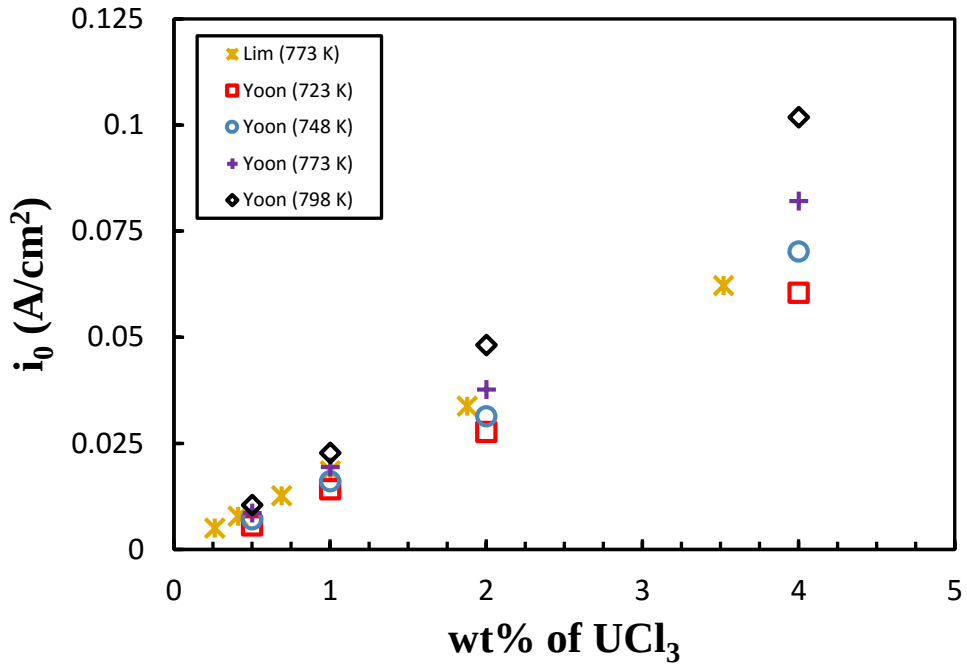

Figure 1.15. Exchange current of UCl_3 in LiCl-KCl eutectic at different concentrations

It can be observed from the above literature review that extensive studies have been conducted on the thermodynamic properties of U and Pu, however these data sometimes have large discrepancies. Usually, several concentrations are involved in each study. However, when analyzing these data, the researchers simply assumed these thermodynamic properties remained constant without considering the effect of the solute concentration. Therefore, most of the reported data actually were the averages among different concentrations, which may only be accurate in dilute solutions. Another issue is that most of these studies only focused on low concentrations (< ~3 wt%) of UCl_3 and $PuCl_3$ but in a pyroprocessing facility, the actinide concentration can be accumulated up to 10 wt% or even more [55,56], where these existing data may not be applicable. Consequently, basic parameter studies for UCl_3 and $PuCl_3$ in LiCl-KCl eutectic are still merited for a widely capable and reliable database, especially at high concentration to investigate their concentration dependence, which is one of the goals in this research.

1.3.2 Safeguards model

Kinetic model development is a promising method for the safeguards. It integrates the basic data and electrochemical theories to predict the material transport in the electrorefiner. The signals from the model include anode and cathode potentials, partial element current, and composition changes in anode, electrolyte, and cathode. Therefore, besides safeguarding the pyroprocessing by tracking the materials via monitoring the composition changes in different batches it can also be used to optimize the facility design, for example, the Pu/U ratio and applied current, and predict the processing performance, like the efficiency and purity of the deposited materials.

Early models based on only the thermodynamic equilibriums between pairs of elements and their oxidants existing at the anode-electrolyte and cathode-electrolyte interfaces were proposed by Johnson et al. [57] and Ackerman et al. [58,59]. Nawada et al. [60] introduced the method to simulate the U and Pu transport in molten salt under 16 conditions, which was enhanced later by Ghosh et al. [61] with a more robust code called PRAGAMAN. Main parameters used in these models are the Gibbs energy and activity coefficient. Basically, at any stage of the electro-transport, the material concentrations in each phase can be calculated by yielding them to the equilibrium equations. Another bunch of models is the diffusion control models. These models assume that all the material diffusing in or out of the electrode react instantly. Kobayashi et al. [62] reported the TRAIL model to study the multicomponent transport in molten salt. In their model, the Nernst's diffusion layer was assumed, whose thickness at different interfaces was determined by polarization experiments. Zhang [63,64] constructed another model based on the diffusion control where the mass transfer coefficient rather than diffusion layer thickness was used as one of the important factors. Therefore the flow conditions can be considered in this model by relating it with the mass transfer coefficient. One of the important assumptions in these models is the reaction equilibrium on the surface so the Nernst equation can be applied at the interface to calculate the electrode potential. However, all the models discussed above only considered the thermodynamic properties and diffusion at the interface but not the kinetic process on the electrode surface. Improved models took into account both the diffusion process in the diffusion layer and the electron transfer process on the electrode by applying the Butler-Volmer equation [65,66,67,68,69,70]. By considering both the diffusion and electron transfer processes, Hoover et al. [65] studied the current and polarization properties of U and Zr under various conditions in Mark-IV. They also reported the anode potential and system resistance with the additional element of Pu [67]. Bae et al. [71] developed the model of REFIN. The model was not only including the diffusion but also the electro-migration. Cumberland [68] developed a comprehensive model of ERAD based on previous REFIN code with a serial of improvements, such as anode passivation layer. The code was then applied to analyze the cyclic voltammogram, diffusion coefficient, and exchange current of UCl_3 in LiCl-KCl electrolyte [70]. A similar model was reported by Ghosh et al. [70] to investigate the cyclic voltammetry, cathodic, and anodic polarization with inert and liquid cadmium yielding different kinds of elements. Generally, steady state was assumed and no accumulation process on the electrode-electrolyte surface in these models, which means the current due to the Butler-Volmer equation is equal to the current due to diffusion. The electrode potential constitutes both the equilibrium potential from the Nernst equation and the overpotential needed to overcome the energy barrier. Recently, commercial computational fluid dynamics (CFD) codes were applied either individually or with the one-dimensional code as another method to assess the pyroprocessing performance [72,73,74,75]. Basically, the system was divided into discrete cells and then the finite element method was applied to solve the governing equations in each cell. They broke the traditional homogeneous setting in 1-D model and could plot the distributions of the diffusion layer, current density, electrode potential, and streamline, in three dimensions. The CFD

models have the advantage to take into account the flow conditions but generally are computationally expensive or only applicable to a specific design [68].

It can be concluded from the above review that previously, extensive studies have been conducted on the electrochemical behaviors of U and Pu in eutectic LiCl-KCl salt. However, almost all of them only focused on the dilute solution, where the thermodynamic properties depend little on solute's concentration. But in pyroprocessing, actinide concentrations can be up to 10 wt% thus the concentration-dependences of these properties have to be considered and studied for a reliable prediction of the separation process and safeguards implementation [76].

In the present work, fundamental data of UCl_3, $LaCl_3$, YCl_3, $ScCl_3$, and $TbCl_3$ in LiCl-KCl molten salt were calculated up to 3 mol% (about 15 wt%) by molecular dynamics (MD) simulation and that of $PuCl_3$ were also calculated via phase diagram development in the range of full composition. Based on the calculated results, a model integrating all the electrorefining, actinide drawdown, and rare earth drawdown processes was developed to predict the partial current of every element, anode and cathode potentials, and concentration profile in different batches in pyroprocessing. The process signals from the model could be used to monitor the material transport and deposition, verify the declared operation of the pyroprocessing facility, and provide insightful information about the diversion of special nuclear materials.

2 Thermodynamic properties of U, La, Y, Sc, and Tb in LiCl-KCl molten salt

2.1 Activity coefficient

The thermodynamic properties mainly focus on the activity coefficient and diffusion coefficient. The former one affects the redox potential of a reaction by Nernst equation and latter one affects the material transport by the Fick's Law. Thermodynamically, the system of LiCl-KCl-MCl_3 (M=U, La, Y, Sc, Tb) can be treated as a homogeneous binary solution because the composition of LiCl-KCl does not change for all the calculations. Therefore, the total Gibbs free energy can be expressed by

$$G_{real} = n_1(\mu_1{}^0 + RTlnx_1 + RTln\gamma_1) + n_2(\mu_2{}^0 + RTlnx_2 + RTln\gamma_2) \quad \text{Eq. 2.1}$$

where $\mu_1{}^0$ and $\mu_2{}^0$ are the chemical potentials of the pure component 1 and 2, R is the gas constant, T is the temperature in kelvin, n_1 and n_2 are the mole numbers of these two components, x_1 and x_2 are the mole fractions of component 1 and 2 respectively, γ_1 and γ_2 are the activity coefficients of component 1 and 2 respectively.

For the ideal solution, the activity coefficient is 1, so the total Gibbs free energy is simplified into

$$G_{ideal} = n_1({\mu_1}^0 + RTlnx_1) + n_2({\mu_2}^0 + RTlnx_2) \quad \text{Eq. 2.2}$$

Thus, the excess Gibbs free energy is

$$G_{excess} = G_{real} - G_{ideal} = n_1 RTln\gamma_1 + n_2 RTln\gamma_2 \quad \text{Eq. 2.3}$$

With respect to the mole number n_1, the partial derivative should be

$$\frac{\partial G_{excess}}{\partial n_1} = RTln\gamma_1 + n_1 RT\frac{\partial ln\gamma_1}{\partial n_1} + n_2 RT\frac{\partial ln\gamma_2}{\partial n_1} = RTln\gamma_1 \quad \text{Eq. 2.4}$$

Hence, the activity coefficient γ_1 can be calculated by the excess Gibbs free energy, which can be derived by the Gibbs energy of the solution and individual component. To reach the Gibbs energy, thermodynamic integration (TI) [77] was applied. It gives the free energy difference between A and B as

$$\Delta F(A \to B) = \int_0^1 < U_B - U_A > d\lambda \quad \text{Eq. 2.5}$$

where U_A and U_B are the interatomic potential of system A and B, respectively. The total Gibbs energy can thus be calculated by

$$G = F + pV \quad \text{Eq. 2.6}$$

After obtaining the excess Gibbs energy, Margules model [78] is was used to fit the values and reach the activity coefficient. The model gives

$$\frac{\partial G_{excess}}{\partial n_M} = RTln\gamma_M = \alpha_2(1 - x_M)^2 + \alpha_3(1 - x_M)^3 + \alpha_4(1 - x_M)^4 + \cdots \quad \text{Eq. 2.7}$$

where α_i is coefficient.

After obtaining activity coefficient, the apparent potential can be calculated by

$$E^{ap} = E^0 + \frac{RT}{nF}\ln\gamma \quad \text{Eq. 2.8}$$

where E^0 is the standard potential

2.1.1 Gibbs energy of solution

For the free energy of solution, the solution was transformed to ideal gas through two steps to get a smooth transformation [79]: first, transform the potential of solution to Gauss potential. Secondly, transform Gauss potential to the null potential of gas. The transformation paths can be expressed by:

$$U_1(\lambda_1) = (1 - \lambda_1)U_{Gauss} + \lambda_1 U_{solution} \quad \text{Eq. 2.9}$$

$$U_2(\lambda_2) = \lambda_2 U_{Gauss} \quad \text{Eq. 2.10}$$

The Gauss potential can be written as:

$$U_{Gauss} = \alpha e^{-\delta r^2} \quad \text{Eq. 2.11}$$

where α and δ are parameters, the value of α and δ are chosen as 21.453 eV and 0.72 Å respectively [80], r is the distance between two particles. When parameter λ_2 varies from 0 to 1, the null potential of ideal gas will transform to Gauss potential, we can get the free energy difference ΔF_2. When parameter λ_1 varies from 0 to 1, Gauss potential will transform to the potential of solution, and then the free energy difference ΔF_1 between these two systems can be calculated. So the Helmholtz free energy of the system is

$$F = F_{id} + \Delta F_1 + \Delta F_2 \quad \text{Eq. 2.12}$$

where F_{id} is the Helmholtz free energy of the ideal gas and can be expressed by [81]

$$F_{id} = \sum_{i}^{n} k_B n_i T ln\left(\rho_i {\zeta_i}^3\right) - N k_B T \quad \text{Eq. 2.13}$$

where k_B is Boltzmann constant, n_i is the atom number of particle i, ρ_i is the number density of particle i, N is the total number of all particles, T is the temperature of the system in kelvin, ζ_i is the de Broglie wavelength and can be expressed by

$$\zeta_i = \frac{h}{(2\pi m_i k_B T)^{1/2}} \quad \text{Eq. 2.14}$$

where m_i is the mass of one particle i, h is the Planck constant and k_B is Boltzmann constant.

2.1.2 Gibbs energy of Supercooled MCl_3

The Gibbs energy of crystal MCl_3 ($G_{crystal,MCl_3}$) is calculated first and that of supercooled state (G_{sc,MCl_3}) is derived by considering Gibbs energy of fusion ($\Delta G_{fusion,MCl_3}$),

$$G_{sc,MCl_3} = G_{crystal,MCl_3} + \Delta G_{fusion,MCl_3} \quad \text{Eq. 2.15}$$

$\Delta G_{fusion,MCl_3}$ could be expressed by

$$\Delta G_{fusion,MCl_3} = \Delta G_{sc,MCl_3} - \Delta G_{c,MCl_3} \quad \text{Eq. 2.16}$$

To calculate the Helmholtz free energy of MCl_3 in solid state, we transform the solid to Einstein crystal by non-equilibrium method of adiabatic switching [82]. A spring force was added by

$$F_{total} = (1-\lambda)F_{solid} + \lambda F_{harm} \quad \text{Eq. 2.17}$$

where F_{solid} is the force due to the interatomic potential of solid, F_{harm} is the force due to spring and λ is the parameter. When λ varies from 0 to 1, the force will transform from F_{harm} to F_{solid} and the free energy difference ΔF can be calculated. The Helmholtz free energy of MCl_3 can be expressed as

$$F = F_{EC} + \Delta F \quad \text{Eq. 2.18}$$

where F_{EC} is the Helmholtz free energy of Einstein crystal. It can be written as [83]

$$\frac{F_{EC}}{N k_B T} = \frac{3}{2}\left(1 - \frac{1}{N}\right)\ln\left(\frac{\beta \Lambda_E \zeta^2}{\pi}\right) + \frac{1}{N}\ln\left(\frac{N\zeta^3}{V}\right) - \frac{3}{2N}\ln(N) \quad \text{Eq. 2.19}$$

where T is temperature, N is atom number, ζ is de Broglie wavelength, V is volume of the system, k_B is Boltzmann constant, Λ_E is the harmonic spring constant, the value of that is $\Lambda_E = 50\ eV/Å^2$, β is expressed by

$$\beta = \frac{1}{k_B T} \qquad \text{Eq. 2.20}$$

where k_B is Boltzmann constant.

2.2 Chemical diffusion coefficient

The self-diffusion coefficient was calculated first by Einstein method, which relates it to the mean squared displacement (MSD) by [84,85]

$$D_s = \frac{1}{6}\lim_{t\to\infty}\frac{d}{dt}(MSD) \qquad \text{Eq. 2.21}$$

where D_s is the self-diffusion coefficient, *t* is time. *MSD* is determined by [85]

$$MSD = \langle (p(t) - p_0)^2 \rangle = \frac{1}{N}\frac{1}{n_t}\sum_{j=0}^{n_t}\sum_{i=0}^{N}(p_i\left(t_{0j} + t\right) - p_i(t_{0j}))^2 \qquad \text{Eq. 2.22}$$

where $p(t)$ is the positon at the time of t and p_0 is the initial position, N is the atom number, n_t is the time origins number, t_{0j} is the initial timestep at time j.

However, what we usually need is the chemical diffusion coefficient. It is different from but can be derived from the self-diffusion coefficient by

$$D_c = D_s(1 + \frac{dln\gamma}{dlnx}) \qquad \text{Eq. 2.23}$$

where D_c is the chemical diffusion coefficient. Obviously, self- and chemical diffusion coefficients are only equal to each other when γ is not dependent on the concentration, which is approximately right for an infinite dilute solution of when molar fraction approaches 1.

2.3 Potential Model

Tosi-Fumi rigid potential model [86] was used in the simulation which is expressed as below

$$U_{ij} = A_{ij}\exp\left(\frac{\sigma_{ij} - r_{ij}}{\rho_{ij}}\right) - \frac{C_{ij}}{{r_{ij}}^6} - \frac{D_{ij}}{{r_{ij}}^8} + \frac{q_i q_j}{4\pi\varepsilon_0 r_{ij}} \qquad \text{Eq. 2.24}$$

where r_{ij} is the distance between the particles i, j. ρ_{ij}, C_{ij} and D_{ij} are the parameters. $\frac{q_i q_j}{4\pi\varepsilon_0 r_{ij}}$ is the Coulomb potential between the particles i, j. All the parameters are given in Table 2.1.

Table 2.1. The parameters used in the simulation [87]

pair	A/eV	ρ/Å	σ/Å	C/eV·Å^6	D/eV·Å^8
Cl^- - Cl^-	0.174084	0.345863	3.340	132.6892	1245.0685
Cl^- - Li^+	0.172894	0.339212	2.570	1.2477	1.5030
Cl^- - K^+	0.17381	0.34140	3.190	29.9336	45.4741
Cl^- - U^{3+}	0.705874	0.293983	2.835	58.0403	100.2000
Cl^- - La^{3+}	0.7755	0.293987	2.842	58.0907	100.393
Cl^- - Y^{3+}	0.73713	0.293987	2.71	24.80299	75.29499
Cl^- - Sc^{3+}	0.80056	0.29399	2.555	17.9435	-50.1967
Cl^- - Tb^{3+}	0.70863	0.29399	2.733	32.2062	-133.8578
Li^+ - Li^+	0.260886	0.337051	1.8	0.0478	0.0167
Li^+ - K^+	0.217637	0.337051	2.42	0.8298	0.5344
Li^+ - U^{3+}	0.002241	0.176390	2.065	1.1403	0.5511
Li^+ - La^{3+}	0.002154	0.17639	2.072	1.14126	0.55216
Li^+ - Y^{3+}	0.00455	0.17639	1.94	0.53777	0.35138
Li^+ - Sc^{3+}	0.01096	0.17639	1.785	0.3944	-0.2175
Li^+ - Tb^{3+}	0.00400	0.17639	1.963	0.6752	-0.4016
K^+ - K^+	0.190113	0.339212	3.04	15.1519	14.9465
K^+ - U^{3+}	6.67E-05	0.176390	2.685	20.7756	15.7982
K^+ - La^{3+}	6.4E-5	0.17639	2.692	20.7936	15.8287
K^+ - Y^{3+}	0.000135	0.17639	2.56	9.7694	10.006
K^+ - Sc^{3+}	0.00033	0.17639	2.405	7.2240	-6.1240
K^+ - Tb^{3+}	0.00012	0.17639	2.583	12.3627	-11.1939
U^{3+} - U^{3+}	0.000748	0.176390	2.330	28.4769	16.7000
La^{3+} - La^{3+}	6.9E-4	0.17639	2.344	28.50	16.7322
Y^{3+} - Y^{3+}	0.003088	0.17639	2.08	6.292	6.693
Sc^{3+} - Sc^{3+}	0.01790	0.17639	1.770	3.4417	-2.5098
Tb^{3+} - Tb^{3+}	0.00238	0.17639	2.126	10.0801	-8.3661

2.4 Simulation Details

For the calculation of the Gibbs free energy of molten LiCl-KCl at the temperatures of 723 K and 773 K, 400 Cl^-, 232 Li^+ and 168 K^+ was performed first. 1-6 MCl_3 were then added to the system separately to create system with different concentrations. With regard to the calculation of Gibbs free energy of eutectic LiCl-KCl and LiCl-KCl-MCl_3, initial configurations with the temperatures of 773 K, 723 K and pressure of 1 bar were set respectively. The simulations were first equilibrated in an NVE ensemble for 10,000 steps, an NVT ensemble for 100,000 steps and then an NPT ensemble for 200,000 steps. During the equilibrium process, the temperature was adjusted from 800 K to 773 K and 723 K respectively for the sake of making simulation results more smooth and

correct. Average volume of the system was obtained by averaging the volume dumped by the 200,000 steps in the NPT ensemble and then used to calculate the free energy in the NVT ensemble at the temperatures of 773 K and 723 K respectively. 10-point Gauss-Legendre quadrature was chosen as λ (coupling parameter of potential transformation) in the process of calculating the free energy by thermodynamic integration method and 2000,000 steps were set in NVT ensemble for every λ. The Gauss potential parameters α and δ used in the simulations were chosen as 21.453 eV and 0.72 Å separately [88]. The time step of all of all simulations was 1 *fs*.

To calculate the Gibbs free energy of MCl_3 in solid state, 200 MCl_3 was created for each system. The structures for the elements calculated are listed in Table 2.2 [89].

Table 2.2. Structure parameters for U, La, Y, Sc, and Tb [89]

	Lattice constant			Angle		
	a/Å	*b*/Å	*c*/Å	α	β	γ
U	7.428	7.428	4.312	90˚	90˚	120˚
La	7.603	7.063	4.375	90˚	90˚	120˚
Y	7.066	6.993	6.993	119.853˚	99.765˚	99.765˚
Sc	7.453	7.453	7.453	51.648˚	51.648˚	51.648˚
Tb	6.531	6.531	11.735	90˚	90˚	90˚

During the process of system equilibrium, the temperature of 800 K and pressure of 1 bar were set as the initial state, then the system ran 10,000 steps in the NVE ensemble, 100,000 steps in the NVT ensemble to adjust the temperature from 800 K to 773 K and 723 K respectively and 500,000 steps in NPT ensemble to obtain the average volume which was used to calculate free energy after that. Thermodynamic integration of adiabatic switching [90] are used in the calculation of free energy, we ran 50,000 steps to equilibrate the system at $\lambda = 0$ and 100,000 steps to vary λ from 0 to 1.

For the calculation of the diffusion coefficient, the trajectory of M^{3+} at different time was tracked and was then used to derive the result of MSD. 1160 Li^+, 840 K^+ and 2000 Cl^- were used in the initial configuration and then 10, 15, 20, 25 30, 35, 40, 45, 50, 55 and 60 MCl_3 were added to the systems respectively to perform the calculations of diffusion coefficients at different concentrations. The simulations were initially ran in NVE ensemble for 50,000 steps and then 500,000 steps in NPT ensemble and 500,000 steps in NVT ensemble eventually. The positions were dumped every 1000 steps in NVT ensemble for 200,000 steps totally and the time step was 1 fs. All the simulation ran in LAMMPS [91,92].

2.5 Results and discussions

Since at temperatures of 723 K and 773 K and the atmosphere pressure, the physical state of MCl_3 is crystal, we need to transfer the Gibbs free energy of crystal MCl_3 to the supercooled MCl_3, which is usually set to the reference state. It can be derived by

$$G_{sc,MCl_3} = G_{crystal,MCl_3} + \Delta G_{fusion,MCl_3} \quad \text{Eq. 2.25}$$

where $G_{crystal,M}$ is the Gibbs energy for crystal MCl_3, $\Delta G_{fusion,MCl3}$ is the Gibbs free energy of fusion for MCl_3 and it can be expressed by

$$\Delta G_{fusion,RECl_3} = \Delta G_{sc,RECl_3} - \Delta G_{c,RECl_3} \quad \text{Eq. 2.26}$$

where $\Delta G_{sc,MCl_3}$ and $\Delta G_{c,MCl_3}$ are Gibbs free energy of formation for the supercooled and crystal status of species MCl_3 respectively. The Gibbs energy of supercooled and crystal states for these elements are shows in Table 2.3.

Table 2.3. Gibbs energy of formation for supercooled and crystal states

	723 K		773 K	
	Supercooled (kJ/mol)	Crystal (kJ/mol)	Supercooled (kJ/mol)	Crystal (kJ/mol)
U	-688.02 [93]	-703.21 [94]	-679.44 [93]	-692.82 [94]
La	-872.976 [95]	-910.7 [96]	-854.87 [95]	-900.8 [96]
Y	-820.979 [95]	-900.0 [95]	810.954 [95]	-892.1 [95]
Sc	-729.047 [97]	754.333 [98]	-719.802 [97]	-743.063 [98]
Tb	-813.517 [99]	-817.842 [98]	-803.678 [99]	-806.165 [98]

2.5.1 Uranium

Table 2.4 lists Gibbs energy of LiCl-KCl-UCl_3 solution. The component of LiCl-KCl-*n* UCl_3 stands for n UCl_3 were added to 116 Li^+, 84 K^+ and 200 Cl^- system.

Table 2.4. Gibbs free energy of LiCl-KCl-UCl_3 mixture solution

T/K	Component	F_{id}	$\Delta F_1 + \Delta F_2$	pV	G_{real}
723 K	LiCl-KCl eutectic	-302.14	-1724.35	0.007259	-2026.48
	LiCl-KCl-1 UCl_3	-564.56	-2952.83	0.013869	-1758.68
	LiCl-KCl-2 UCl_3	-285.72	-1517.87	0.006994	-1803.58
	LiCl-KCl-3 UCl_3	-289.06	-1559.10	0.007048	-1848.15
	LiCl-KCl-4 UCl_3	-292.37	-1600.48	0.007104	-1892.84
	LiCl-KCl-5 UCl_3	-295.59	-1641.78	0.007143	-1937.37
	LiCl-KCl-6 UCl_3	-298.91	-1683.02	0.007211	-1981.92
773 K	LiCl-KCl eutectic	-609.82	-2936.30	0.014097	-3546.11
	LiCl-KCl-1 UCl_3	-308.63	-1509.47	0.007112	-1818.10

	LiCl-KCl-2 UCl_3	-312.20	-1550.60	0.007157	-1862.78
	LiCl-KCl-3 UCl_3	-315.68	-1591.88	0.007194	-1907.56
	LiCl-KCl-4 UCl_3	-319.22	-1632.97	0.007247	-1952.18
	LiCl-KCl-5 UCl_3	-322.80	-1674.04	0.007320	-1996.84
	LiCl-KCl-6 UCl_3	-326.36	-1715.13	0.007388	-2041.49

The calculated results about crystal UCl_3 are shown in Figure 2.1 and Table 2.5. Figure 2.1 shows the integrands in the forward direction (UCl_3 crystal to Einstein crystal) and backward direction (Einstein crystal to UCl_3 crystal) at 723 K. No significant difference was found between them so their average was used in the calculation. Results from 773 K show the same trend. Based on Eq. 2.24 and 2.25, Gibbs energy of supercooled UCl_3 (μ_1^0 in Eq 2.2) can be calculated, which is shown in Table 2.5.

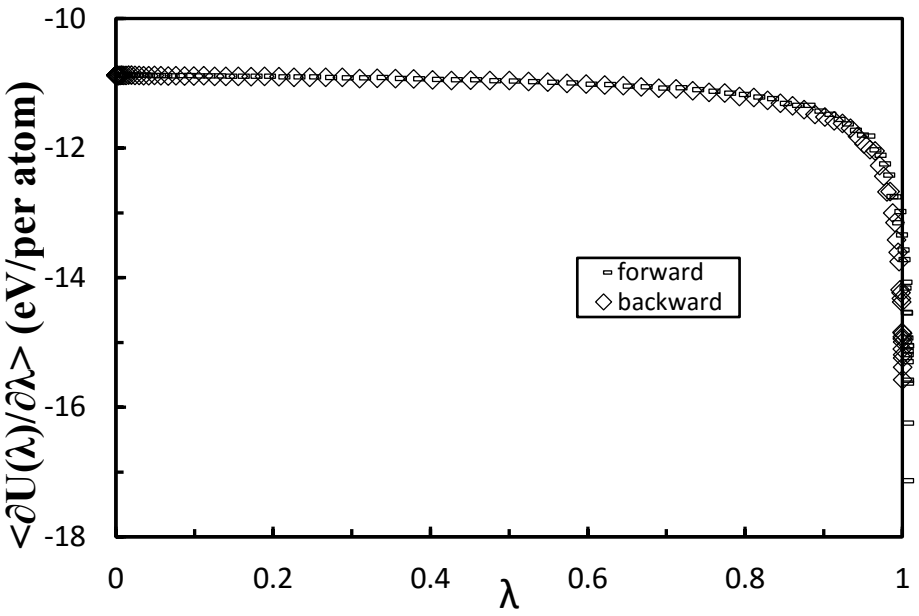

Figure 2.1. Integrands in forward direction (UCl_3 crystal to Einstein crystal) and backward direction (Einstein crystal to UCl_3 crystal) when calculating the free energy of UCl_3 crystal at 723 K

Table 2.5. The Gibbs free energy of supercooled UCl_3 (eV/simulation box)

	ΔF	$F_{Einstein}$	pV	$G_{crystal}$	ΔG_{fusion}	G_{sc}
723 K	-8893.21	44.83	0.01348	-8848.37	31.48	-8816.89
773 K	-8854.08	42.58	0.01357	-8811.50	27.76	-8826.34

Based on all of these results, the molar excess Gibbs energy can be assessed by Eq. 2.1 and 2.3. The values of molar excess Gibbs energy are shown in Table 2.6. Then the Margules model was used to fit the results. Figure 2.2 shows the fitting result of molar excess Gibbs energy. Therefore

the activity coefficient at different concentrations can be obtained based on Eq. 2.7 which is shown in Figure 2.3.

Table 2.6. The molar excess Gibbs energy of UCl_3-LiCl-KCl solution with different concentrations of UCl_3 at 723 K

	x_{UCl_3}(%)	0	0.4975	0.9901	1.4778	1.9608	2.4390	2.9126
723 K	$\bar{G}^{ex}$ (J/mol)	0	-202.78	-289.40	-447.54	-538.34	-644.93	-760.89
773 K	$\bar{G}^{ex}$ (J/mol)	0	-223.27	-304.82	-467.85	-554.03	-667.69	-780.40

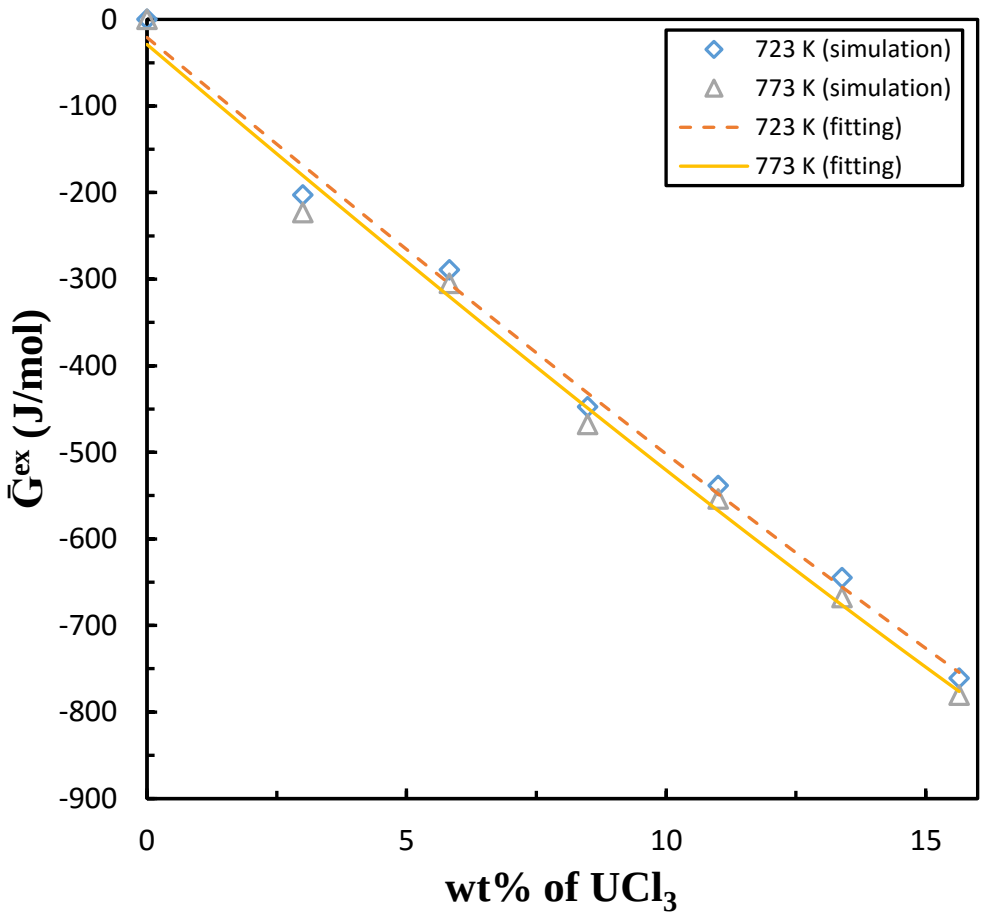

Figure 2.2. Molar excess Gibbs energy and fitting results

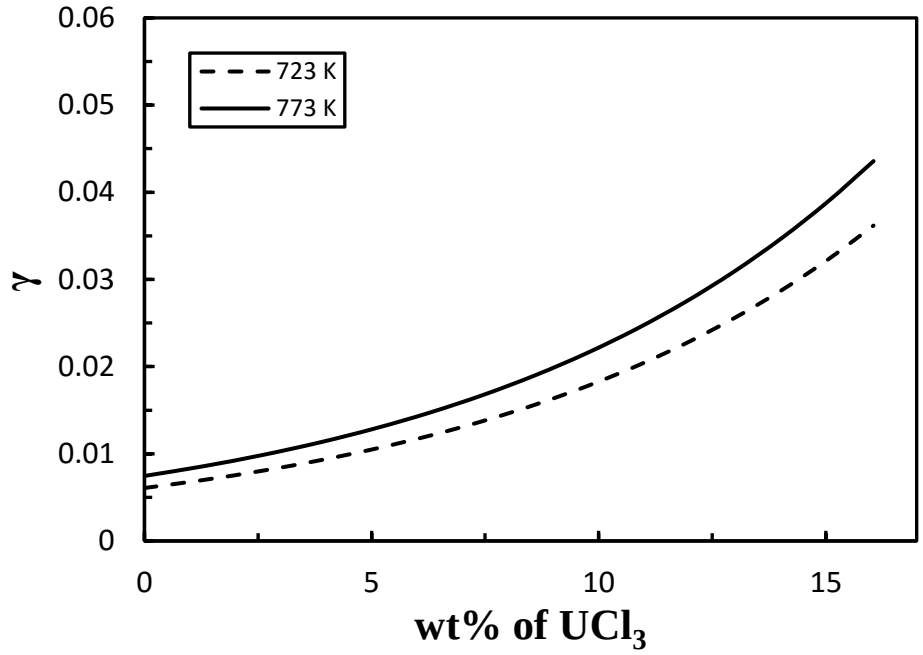

Figure 2.3. Activity coefficient of UCl_3 in LiCl-KCl molten salt

Figure 2.3 shows that the activity coefficient result at 723 and 773 K is in the order of 10^{-3} for dilute cases, which is reasonable and consistent with the available experimental data. The comparison with literature at low concentration plotted in Figure 2.4 shows good agreement. What should most attract our attention is that the result shows the activity coefficient depends strongly on the concentration and increases monotonically with mole fraction. The increasing rate is small at the low concentration but relatively large at high concentration, which is also consistent with the knowledge from literature that the activity coefficient is almost the same at very dilute concentration. Figure 2.3 shows that the activity coefficient increases from 6.08×10^{-3} to 3.62×10^{-2} and 7.46×10^{-3} to 4.36×10^{-2} at 723 K and 773 K, respectively, corresponding to the mole fraction of UCl_3 from around 0.5% to 3.0 %.

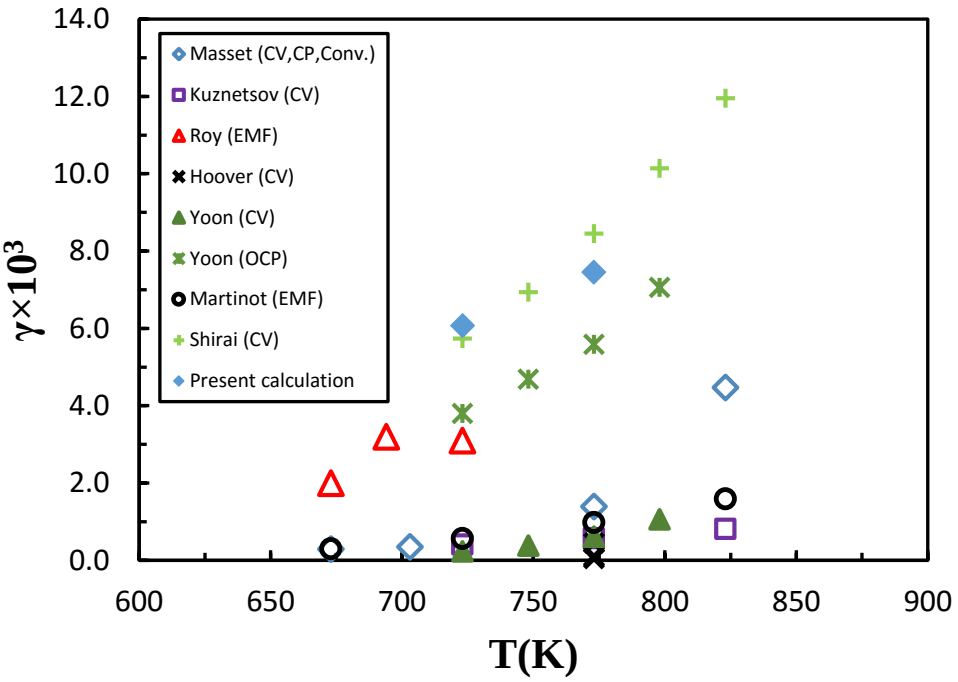

Figure 2.4. Comparison of activity coefficient of UCl_3 in LiCl-KCl molten salt

The comparison also shows that even at the dilute solution, the activity coefficients from experiments have some difference with each other. Plausible explanations include different electrodes, experimental environments, and techniques used. Based on Eq. 2.8, the apparent potential of UCl_3 can be calculated, which is plotted and compared with literature in Figure 2.5. Apparent potentials in literature mainly follow three patterns, which are drawn out on the figure. Present results agree very well with the first pattern. Also, Figure 2.4 and Figure 2.5 indicate that the activity coefficient is very sensitive to the apparent standard potential. A small difference of potential can lead to significant difference in activity coefficient. Most of the apparent potentials in Figure 2.5 range from -2.6 to -2.4 V, and it can be concluded from Eq. 2.8 that 1% difference of apparent potential (or Gibbs energy in our calculation) will result in an increasing factor of around *e* to the activity coefficient because the values of RT/3F at 723 and 773 K are around 0.021 V. Also, Gibbs energy at supercooled state is another sensitive parameter, which can be observed from the review part in Chapter 1.

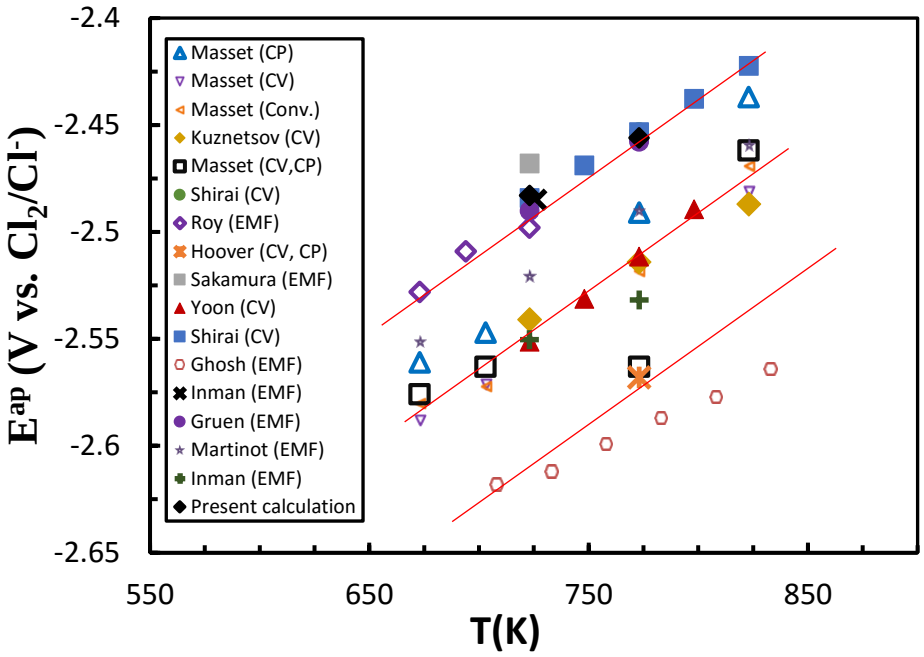

Figure 2.5. Comparison of apparent of UCl_3 in LiCl-KCl molten salt

Eq. 2.21 and 2.22 show that when the simulation time is long enough, the self-diffusivity can be obtained by the slope of MSD *vs.* t plot. Figure 2.6 shows an example of the fitting.

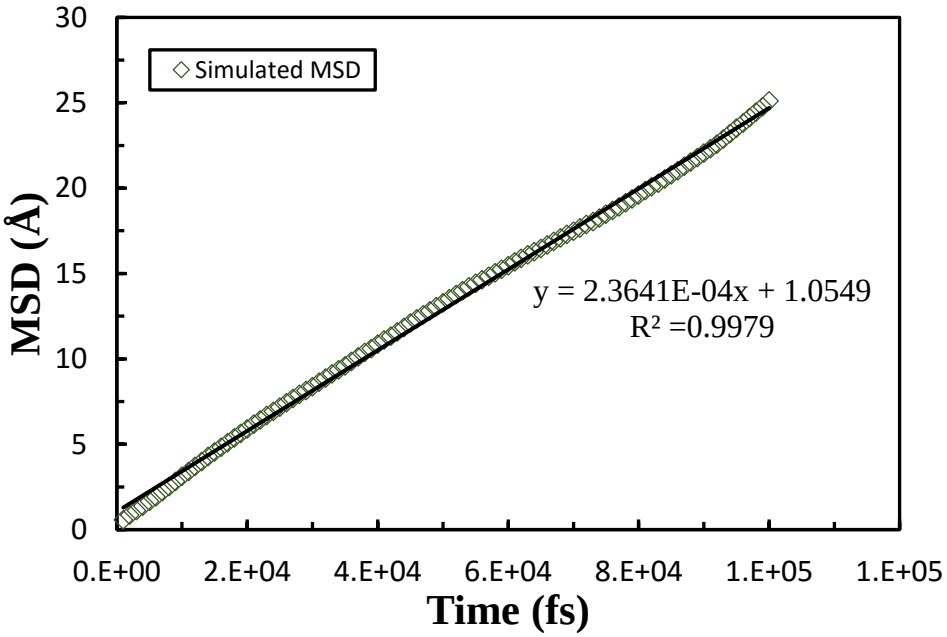

Figure 2.6. MSD vs. t for 5.82 wt% UCl_3 in LiCl-KCl molten salt

Since the MSD was fitted into a linear equation with time, such as

$$MSD(t) = A + Bt \quad \text{Eq. 2.27}$$

where A and B are constant and diffusion coefficient can be derived from B according to Eq. 2.21. The uncertainty of B was calculated through the method described by Talor [100], which gives one sigma error as

$$\sigma_B = \sigma_{MSD}\sqrt{\frac{N}{\Delta}} \quad \text{Eq. 2.28}$$

$$\sigma_{MSD} = \sqrt{\frac{1}{N-2}\sum_{i=1}^{N}(MSD_i - A - Bt_i)} \quad \text{Eq. 2.29}$$

where N is the number of data points, and

$$\Delta = N\sum_{i=1}^{N} t_i^2 - (\sum_{i=1}^{N} t_i)^2 \quad \text{Eq. 2.30}$$

Figure 2.7 shows the self-diffusion coefficient of U^{3+} in LiCl-KCl molten salt at different temperatures and concentrations. It indicates that the self-diffusion coefficient of U^{3+} is a function of both temperature and concentration. It increases with temperature but decreases with concentration.

From the kinetic theory of Einstein relation [101], the self-diffusion coefficient can be expressed by

$$D = \frac{k_B T}{6\pi\eta_s r_a} \quad \text{Eq. 2.31}$$

where k_B is the Boltzmann's constant, η_s is the dynamic viscosity of the solution, and r_a is the radius of the spherical particle. Eq. 2.31 explicitly shows that the diffusion coefficient is related to the temperature, and it may increase with the temperature since generally viscosity becomes smaller when increasing the temperature [102]. However, the concentration dependence is still implicit.

Kim et al [103] studied the viscosity of LiCl-KCl molten salts with actinides and lanthanides dissolved at 773 K by the object falling down method. The experiments were carried out with a maximum concentration of 9 wt% UCl_3 and they reported an increased viscosity in the concentration range. With this result in mind, the self-diffusion coefficient D in Eq. 2.31 is expected to decrease with higher viscosity, which means higher concentration. It supports the present simulation results of self-diffusivity at least qualitatively.

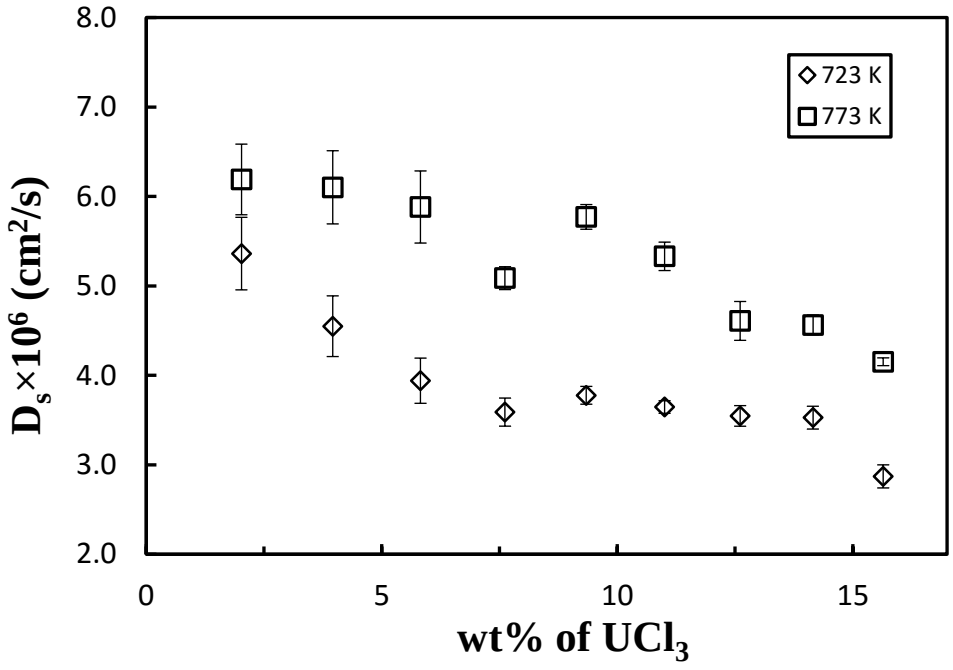

Figure 2.7. Self-diffusion coefficient of U^{3+} in LiCl-KCl

Recalling the Eq. 2.23, chemical diffusion coefficient could be related with self-diffusion coefficient by

$$D_c = D_s(1 + \frac{dln\gamma_i}{dlnx_i}) \quad \text{Eq. 2.32}$$

Due to the relationship of

$$\frac{dln\gamma}{dlnx} = x\frac{dln\gamma}{dx} = \frac{x}{\gamma}\frac{d\gamma}{dx} \quad \text{Eq. 2.33}$$

$(1 + \frac{dln\gamma}{dlnx})$ can be calculated through the fitting curves. Table 2.7 shows the values of $(1 + \frac{dln\gamma}{dlnx})$ at the simulated concentrations, based on which, the chemical diffusion coefficient in Eq. 2.32 can be derived. Figure 2.8 shows the results of the chemical diffusion coefficient at different temperatures and concentrations. The result indicates that the chemical diffusion coefficient is larger with higher temperature. Most importantly, it shows that the chemical diffusivity varies little initially but then increases followed by a decrease with the concentration. The variation range is about 2.5×10^6 cm^2/s. Figure 2.9 shows the comparison of the chemical diffusion with literature under different concentrations at 773 K. Literature data with concentration dependence at 723 K are not enough to compare. Except the data from Hoover by CV method and from Masset, which give larger values compared to all other data, the calculation results agree well with literature. Since the variation of diffusion coefficient is not so dramatic, the average values at 723 K and 773 K are taken to compare with the literature data, which is shown in Figure 2.10. Our results show good agreement with other data reported.

Table 2.7. The values of [1+d(lnγ)/d(ln*x*)] at simulated concentrations

wt%	2.019	3.958	5.822	7.615	9.341	11.003	12.606	14.152	15.645
723 K	1.2162	1.4201	1.6121	1.7927	1.9626	2.1220	2.2715	2.4115	2.5445
773 K	1.2141	1.4158	1.6058	1.7844	1.9523	2.1099	2.2575	2.3958	2.5250

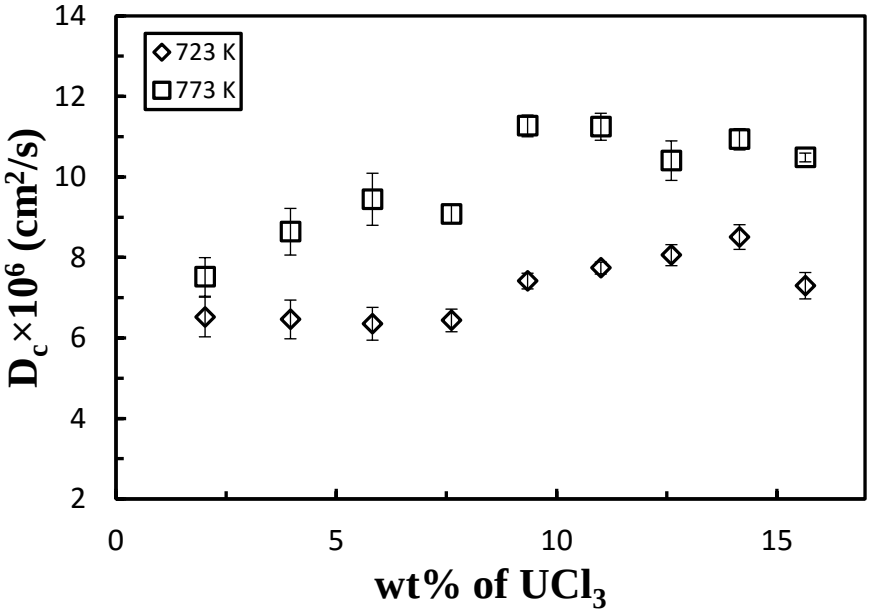

Figure 2.8. Chemical diffusion coefficient of U^{3+} in LiCl-KCl

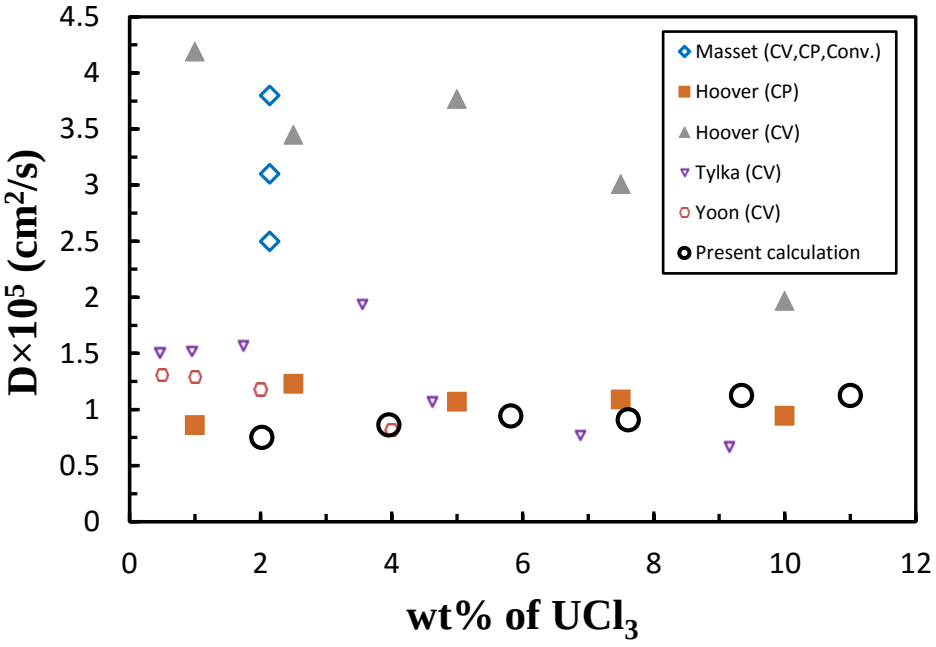

Figure 2.9. Comparison of chemical diffusion coefficient of U^{3+} in LiCl-KCl at 773 K

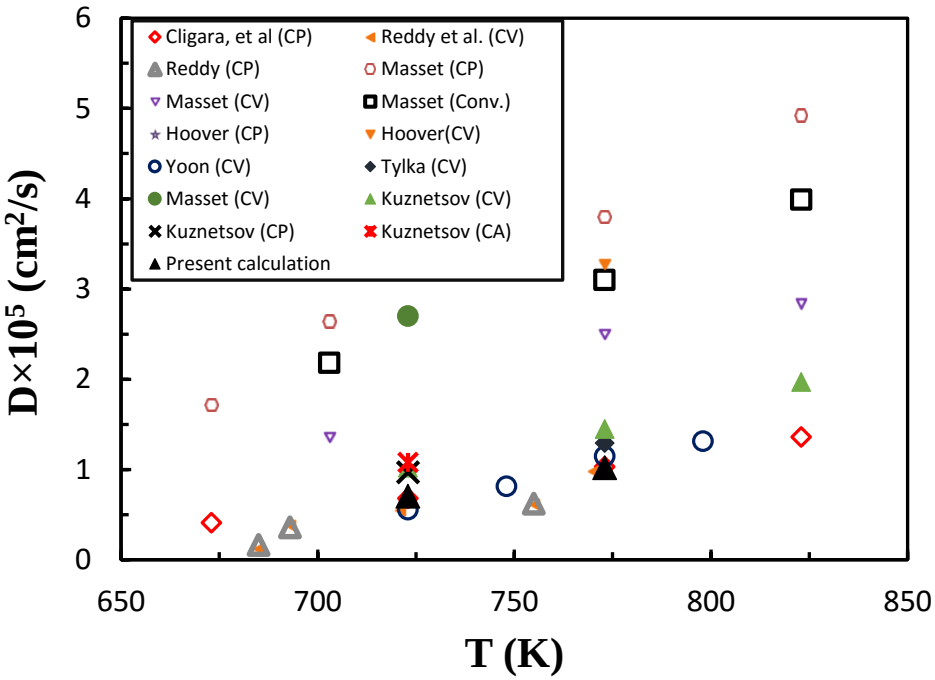

Figure 2.10. Comparison of chemical diffusion coefficient of U^{3+} in LiCl-KCl

2.5.2 Lanthanum

All the results of other elements were analyzed in the similar manner as used for U. The total Gibbs energy for the real solution was obtained and shown in Table 2.8.

Table 2.8. Gibbs free energy of LiCl-KCl-$LaCl_3$ mixture solution

Temperature	Component	F_{id}/eV	$\Delta F_1 + \Delta F_2/eV$	pV/eV	G_{real}/eV
723 K	LiCl-KCl-1 $LaCl_3$	-285.6506	-1517.2685	0.006988	-1802.9122
	LiCl-KCl-2 $LaCl_3$	-289.0637	-1557.8999	0.007077	-1846.9565
	LiCl-KCl-3 $LaCl_3$	-292.2118	-1598.6129	0.007102	-1890.8176
	LiCl-KCl-4 $LaCl_3$	-295.5323	-1639.3944	0.007181	-1934.9195
	LiCl-KCl-5 $LaCl_3$	-298.7167	-1679.9198	0.007227	-1978.6293
	LiCl-KCl-6 $LaCl_3$	-301.9275	-1720.7554	0.007284	-2022.6756
	eutectic LiCl-KCl	-564.5582	-2952.8256	0.013869	-3517.3698
773 K	LiCl-KCl-1 $LaCl_3$	-308.6356	-1508.8986	0.007127	-1817.5271
	LiCl-KCl-2 $LaCl_3$	-311.9753	-1549.4389	0.007128	-1861.4071
	LiCl-KCl-3 $LaCl_3$	-315.6351	-1589.9931	0.007223	-1905.6210
	LiCl-KCl-4 $LaCl_3$	-319.2328	-1630.4524	0.007308	-1949.6779
	LiCl-KCl-5 $LaCl_3$	-322.5984	-1671.0772	0.007336	-1993.6683
	LiCl-KCl-6 $LaCl_3$	-326.0548	-1711.6356	0.007391	-2037.6830
	eutectic LiCl-KCl	-609.8188	-2936.3508	0.014097	-3546.1555

In Table 2.8, p and V are the pressure and volume of the system, F_{id} is the Helmholtz free energy of the ideal gas, ΔF_1 is the free energy difference between Gauss potential fluid and our interesting solution, ΔF_2 is the free energy difference between ideal gas and Gauss potential fluid. The Gibbs free energy of $LaCl_3$ is shown in Table 2.9.

Table 2.9. Gibbs free energy of supercooled $LaCl_3$ at the temperatures of 723 K and 773 K

T/K	$F_{EC}/\ eV$	$\Delta F/\ eV$	pV/eV	$\Delta G_{fusion,\mathrm{LaCl_3}}/\ eV$	$G_{sc,\mathrm{LaCl_3}}/\ eV$
723	54.9053	-8827.6590	0.012654	78.1963	-8694.5447
773	48.0250	-8838.2269	0.012684	95.2062	-8694.9831

In Table 2.9, F_{EC} is Helmholtz free energy of Einstein crystal and ΔF is the free energy difference between the Einstein crystal where the center of mass is fixed and the solid of interest. The results of G_{real} for eutectic LiCl-KCl and $G_{sc,\mathrm{LaCl_3}}$ in Table 2.8 and Table 2.9 respectively are the values of ${n_2\mu_2}^0$ and ${n_1\mu_1}^0$ in the Eq. 2.2, so the Gibbs free energy of ideal solution can be obtained. The total Gibbs free energy for the ideal solution and the excess Gibbs free energy of the system of LiCl-KCl-*n* $LaCl_3$ are presented in Table 2.10.

Table 2.10. The results of total Gibbs free energy of ideal solution, excess Gibbs free energy, mole fraction and molar excess Gibbs free energy of LiCl-KCl-$LaCl_3$ mixture

T/K	Component	G_{real} (eV)	G_{ideal} (eV)	G_{excess} (eV)	x_{La} (%)	$\bar{G}_{excess}$ (J/mol)
723 K	LiCl-KCl-1 $LaCl_3$	-1802.9122	-1802.5502	-0.362	0.4975	-173.7502
	LiCl-KCl-2 $LaCl_3$	-1846.9565	-1846.3294	-0.627	0.9901	-299.5318
	LiCl-KCl-3 $LaCl_3$	-1890.8176	-1890.0764	-0.741	1.4778	-352.3142
	LiCl-KCl-4 $LaCl_3$	-1934.9195	-1933.8024	-1.117	1.9608	-528.3349
	LiCl-KCl-5 $LaCl_3$	-1978.6293	-1977.5131	-1.116	2.4390	-525.3829
	LiCl-KCl-6 $LaCl_3$	-2022.6756	-2021.2115	-1.464	2.9126	-685.7685
773 K	LiCl-KCl-1 $LaCl_3$	-1817.5271	-1816.9724	-0.555	0.4975	-266.2688
	LiCl-KCl-2 $LaCl_3$	-1861.4071	-1860.7750	-0.632	0.9901	-301.9138
	LiCl-KCl-3 $LaCl_3$	-1905.6210	-1904.5431	-1.078	1.4778	-512.3313
	LiCl-KCl-4 $LaCl_3$	-1949.6779	-1948.2889	-1.389	1.9608	-656.9860
	LiCl-KCl-5 $LaCl_3$	-1993.6683	-1992.0181	-1.650	2.4390	-776.6617
	LiCl-KCl-6 $LaCl_3$	-2037.6830	-2035.7343	-1.949	2.9126	-912.7331

In Table 2.10, x_{La} is the mole fraction of $LaCl_3$ in the solution and $\bar{G}_{excess}$ is the molar excess Gibbs free energy. Then the data of mole fraction x_{La} and molar excess Gibbs free energy $\bar{G}_{excess}$ were used to fit a curve by the Margules model [104]. Since the value of $\bar{G}_{excess}$ is 0 when $x_{La} = 0$, so this data point was also used to fit the curve to make the result be more accurate, the fitting result is shown in Figure 2.11. And the activity coefficient can be calculated by Eq.2.2.

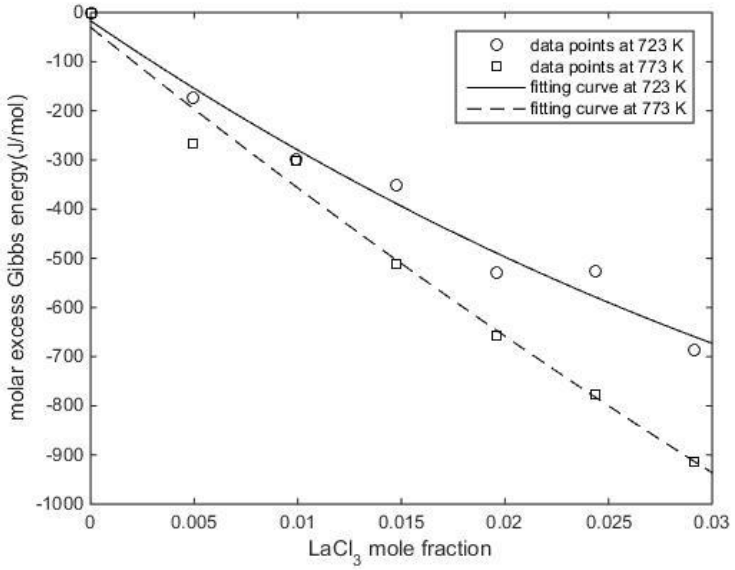

Figure 2.11. The fitting curve of molar excess Gibbs free energy to mole fraction of $LaCl_3$ in the solution

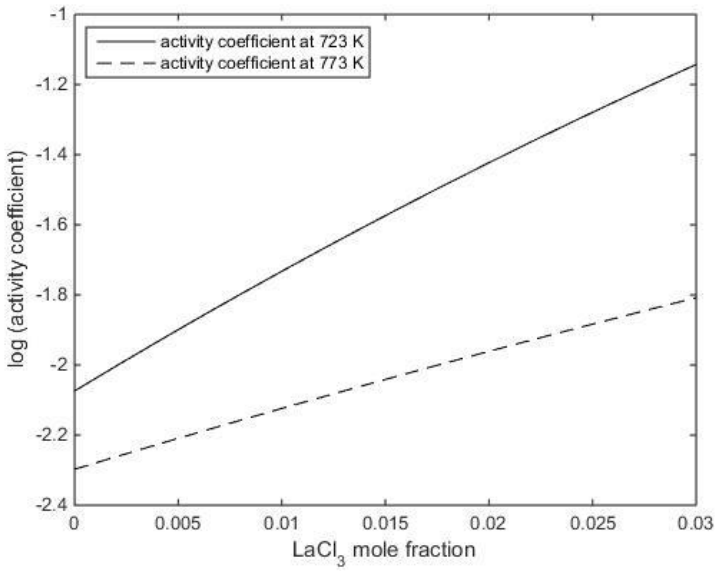

Figure 2.12. Activity coefficient of $LaCl_3$ in eutectic molten salt at the temperatures of 723 K and 773 K

Just as Figure 2.12 shows, the activity coefficient of La^{3+} increases with the mole fraction of La in the eutectic molten salt. Moreover, the values of activity coefficient at the temperature of 723 K are larger than that at the temperature of 773 K, it agrees with trend in literature at the temperature range of 650-870 K [105]. The results we calculated were close to other literature values, and the comparison with other measurement data are shown in Table 2.11.

Table 2.11. Comparison between calculated activity coefficient of $LaCl_3$ and literature values

Temperature	Mole fraction	Calculated activity coefficient[a]	Literature value
723 K	Dilution	8.4×10^{-3} ~ 13.4×10^{-3}	5.4×10^{-3} [95]
	Dilution		4.7×10^{-3} [106]
	Dilution		3.0×10^{-3} [105]
	Dilution		1.4×10^{-3} [107]
	6.4×10^{-3}	14.1×10^{-3}	4.7×10^{-3} [108]
773 K	2.27×10^{-3}	5.5×10^{-3}	1.05×10^{-3} [109]
	Dilution	5.0×10^{-3} ~ 6.4×10^{-3}	1.04×10^{-3} [105]

a: the calculated results corresponding to the mole fraction of 0-0.0058.

Once the activity coefficients have been obtained, apparent standard potential can be calculated by Eq. 2.8. Figure 2.13 presents the calculated results of apparent standard potential at the temperatures of 723 K and 773 K.

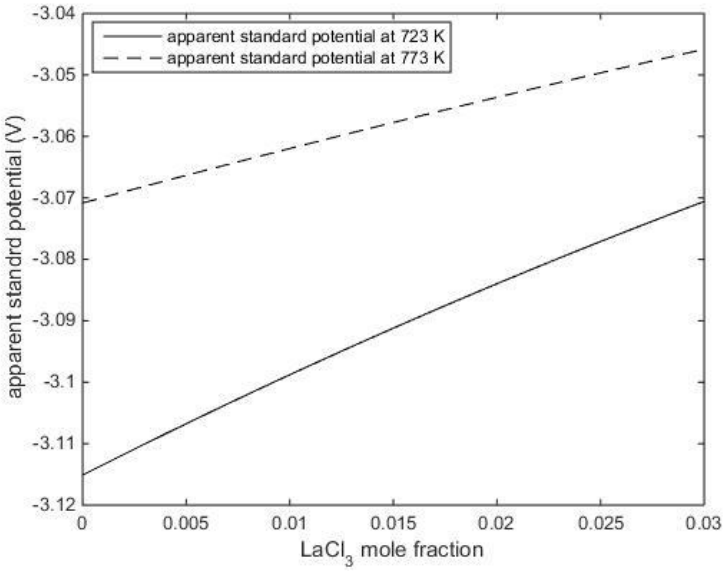

Figure 2.13. Apparent standard potential of $LaCl_3$ at the temperatures of 723 K and 773 K

It can be seen from Figure 2.13 that the apparent standard potential of $LaCl_3$ increases with mole fraction of $LaCl_3$ in eutectic molten salt and apparent standard potential at the temperature 773 K is a little larger than that at the temperature of 723 K. The comparison in Table 2.12 indicates that our calculated results agree well with other literature values.

Table 2.12. Comparison between the calculated apparent standard potential of $LaCl_3$ and literature values

Temperature	Mole fraction	Calculated results (V)[b]	Literature value (V)
723 K	Dilution	-3.1151 ~ -3.1055	-3.136 [105]

	Dilution	-3.1151 ~ -3.1055	-3.124 [95]
	0.0078	-3.1022	-3.208 [110]
	0.004663	-3.1072	-3.267 [111]
	0.00917	-3.1000	-3.143 [112]
773 K	0.004663	-3.0666	-3.216 [111]
	Dilution	-3.0708 ~ -3.0656	-3.106 [105]

b: the calculated results corresponding to the mole fraction of 0-0.0058.

The self-diffusion coefficients and chemical diffusion coefficients at the temperatures of 723 K and 773 K with different mole fractions were also calculated in the present study. It can be seen that there is no big change in self-diffusion coefficient when the mole fraction of $LaCl_3$ increases up to 3 at%. It also should be noticed that the chemical diffusion coefficients slightly depend on the mole fractions and it seems like that with the increase of mole fraction of $LaCl_3$, chemical diffusion coefficients of $LaCl_3$ increase initially and then decrease slightly, however, the dependence is not significant. Moreover, our calculated results show that the chemical diffusion coefficients and self-diffusion coefficients of $LaCl_3$ at 773 K are larger than that at the temperature of 723 K. The comparison between calculated chemical diffusion coefficients and literature values which can be seen in Table 2.13 indicates our calculated results agree well with previous studies.

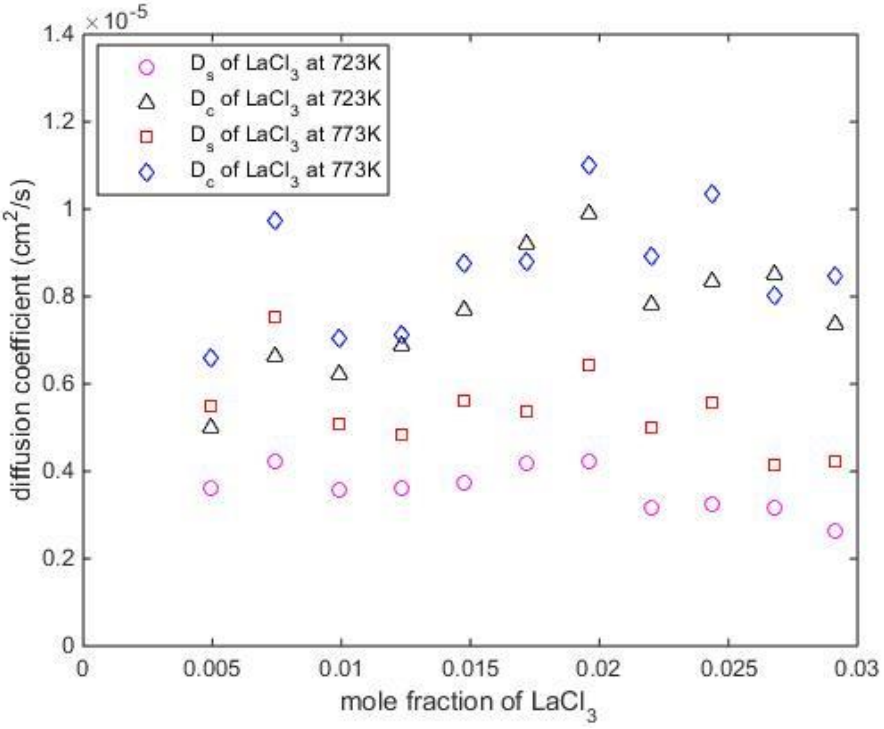

Figure 2.14. Self-diffusion coefficient and chemical diffusion coefficient of $LaCl_3$ at the temperatures of 723 K and 773 K

Table 2.13. Comparison between the calculated chemical diffusion coefficient of $LaCl_3$ and literature values

Temperature	The range of D_c (cm^2/s)[c]	Literature value (cm^2/s)
723 K	5.0196×10^{-6} ~ 9.8964×10^{-6}	$11.5\pm1.2\times10^{-6}$ [113]
		14.7×10^{-6} [110]
		10.0×10^{-6} [111]
773 K	6.5992×10^{-6} ~11.003×10^{-6}	$21\pm5\times10^{-6}$ [114]
		$8\pm1\times10^{-6}$ [115]
		20×10^{-6} [111]

c: the range of D_c corresponding to the mole fraction of 0.004975-0.029126.

2.5.3 Yttrium

The total Gibbs free energy of the real solution is given in Table 2.14

Table 2.14. Gibbs free energy of LiCl-KCl-YCl_3 mixture solution

Temperature	Component	F_{id}/eV	$\Delta F_1 + \Delta F_2/eV$	pV/eV	G_{real}/eV
723 K	LiCl-KCl-1 YCl_3	-285.6113	-1519.1563	0.006988	-1804.7606
	LiCl-KCl-2 YCl_3	-288.8686	-1561.9186	0.007046	-1850.7802
	LiCl-KCl-3 YCl_3	-292.1125	-1604.4875	0.007110	-1896.5929
	LiCl-KCl-4 YCl_3	-295.2237	-1647.1504	0.007142	-1942.3670
	LiCl-KCl-5 YCl_3	-298.4027	-1689.7464	0.007198	-1988.1419
	LiCl-KCl-6 YCl_3	-301.5699	-1732.4175	0.007254	-2033.9801
	eutectic LiCl-KCl	-564.5582	-2952.8256	0.013869	-3517.3698
773 K	LiCl-KCl-1 YCl_3	-308.5892	-1510.7829	0.007127	-1819.3650
	LiCl-KCl-2 YCl_3	-311.9542	-1553.3466	0.007146	-1865.2936
	LiCl-KCl-3 YCl_3	-315.3769	-1595.9625	0.007190	-1911.3322
	LiCl-KCl-4 YCl_3	-319.0461	-1638.1462	0.007305	-1957.1849
	LiCl-KCl-5 YCl_3	-322.2890	-1680.9293	0.007313	-2003.2109
	LiCl-KCl-6 YCl_3	-325.5906	-1723.4216	0.007340	-2049.0048
	eutectic LiCl-KCl	-609.8188	-2936.3508	0.014097	-3546.1555

What Table 2.15 shows is the calculated Gibbs free energy of supercooled YCl_3.

Table 2.15. Gibbs free energy of supercooled YCl_3 at the temperatures of 723 K and 773 K

Temperature	$F_{EC}/\ eV$	$\Delta F/\ eV$	pV/eV	$\Delta G_{fusion,YCl_3}/\ eV$	$G_{sc,YCl_3}/\ eV$
723 K	63.2156	-9187.1730	0.016093	163.7990	-8960.1424
773 K	56.9100	-9204.8284	0.016128	168.2048	-8979.6974

Then the Gibbs free energy of ideal solution was obtained using the same method, total Gibbs free energy of the ideal solution and the excess Gibbs free energy of the systems LiCl-KCl-n YCl_3 are shown in Table 2.16

Table 2.16. The results of total Gibbs free energy of ideal solution, excess Gibbs free energy, mole fraction and molar excess Gibbs free energy of LiCl-KCl-YCl_3 mixture

Temperature	Component	G_{real}/eV	G_{ideal}/eV	G_{excess}/eV	x_Y(%)	$\bar{G}_{excess}(J/mol)$
723 K	LiCl-KCl-1 YCl_3	-1804.7606	-1803.8782	-0.882	0.4975	-423.5670
	LiCl-KCl-2 YCl_3	-1850.7802	-1848.9854	-1.795	0.9901	-857.2989
	LiCl-KCl-3 YCl_3	-1896.5929	-1894.0603	-2.533	1.4778	-1203.7118
	LiCl-KCl-4 YCl_3	-1942.3670	-1939.1144	-3.253	1.9608	-1538.4003
	LiCl-KCl-5 YCl_3	-1988.1419	-1984.1530	-3.989	2.4390	-1877.4345
	LiCl-KCl-6 YCl_3	-2033.9801	-2029.1794	-4.801	2.9126	-2248.5198
773 K	LiCl-KCl-1 YCl_3	-1819.3650	-1818.3960	-0.969	0.4975	-465.1852
	LiCl-KCl-2 YCl_3	-1865.2936	-1863.6221	-1.672	0.9901	-798.3973
	LiCl-KCl-3 YCl_3	-1911.3322	-1908.8138	-2.518	1.4778	-1196.9790
	LiCl-KCl-4 YCl_3	-1957.1849	-1953.9831	-3.202	1.9608	-1514.3400
	LiCl-KCl-5 YCl_3	-2003.2109	-1999.1360	-4.075	2.4390	-1917.9170
	LiCl-KCl-6 YCl_3	-2049.0048	-2044.2758	-4.729	2.9126	-2214.9702

The data of mole fraction and molar excess Gibbs free energy were used to fit a curve which can be seen in Figure 2.15 and the activity coefficients were also calculated by Eq. 2.7. The plot of activity coefficients with mole fractions is shown in Figure 2.16.

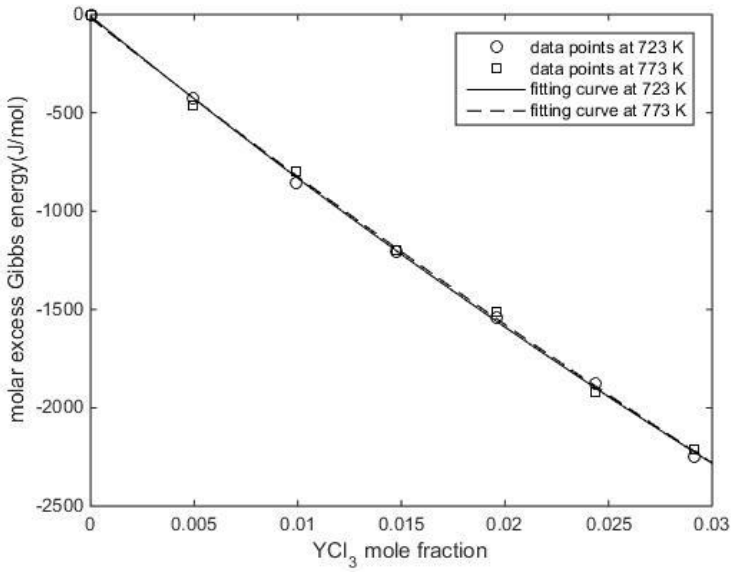

Figure 2.15. The fitting curve of molar excess Gibbs free energy to mole fraction of YCl_3 in the solution

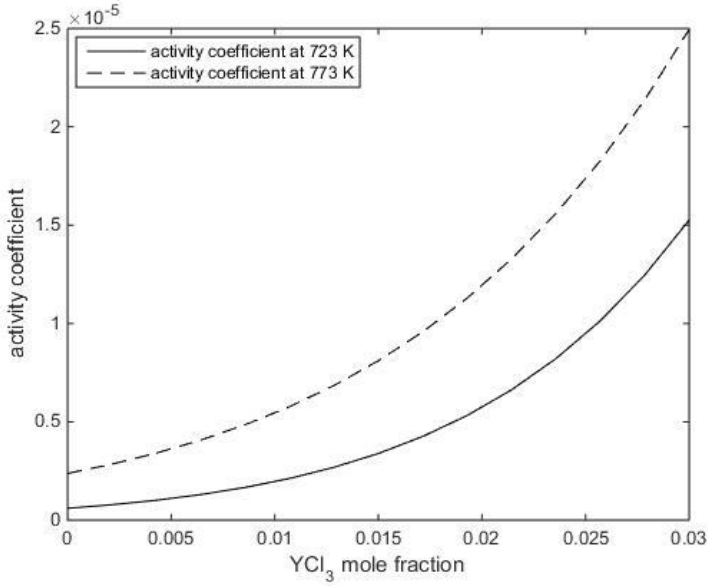

Figure 2.16. Activity coefficient of YCl_3 in eutectic molten salt at the temperatures of 723 K and 773 K

It can be seen from Figure 2.16, the activity coefficient of Y^{3+} increases with mole fraction at the temperatures of 723 K and 773 K. However, different from $LaCl_3$, the value of activity coefficient at 773 K is larger when compared with that at the temperature of 723 K. The comparison in Table 2.17 indicates our calculated results agree well with other literature values.

Table 2.17. Comparison between calculated activity coefficient of YCl_3 and literature values

Temperature	Mole fraction	Calculated activity coefficient[d]	Literature value
723 K	Dilution	0.60348×10^{-6} ~ 1.4390×10^{-6}	2.34×10^{-6} [105]
	Dilution		2.40×10^{-6} [116]
	Dilution		2.06×10^{-6} [95]
773 K	Dilution	2.3760×10^{-6} ~ 4.3749×10^{-6}	5.36×10^{-6} [105]

d: the calculated results corresponding to the mole fraction of 0-0.00729.

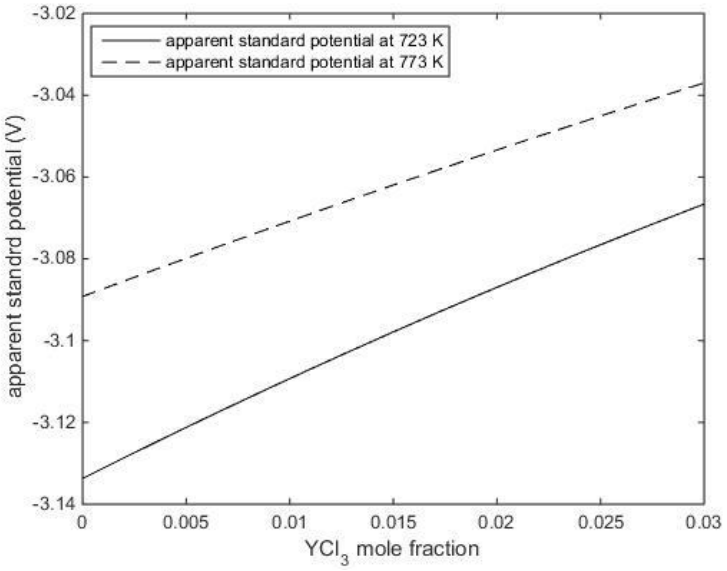

Figure 2.17. Apparent standard potential of YCl_3 at the temperatures of 723 K and 773 K

Figure 2.17 shows the relationships between apparent standard potential and YCl_3 mole fraction, it can be seen that apparent standard potential increases with mole fraction. Moreover, apparent standard potential at 773 K is larger than that at the temperature of 723 K.

Table 2.18 shows the comparisons between the calculated apparent standard potential and literature values and it can be seen our calculated result is quite reasonable.

Table 2.18. Comparison between the calculated apparent standard potential of YCl_3 and literature values

Temperature	Mole fraction	Calculated results (V)[e]	Literature value (V)
723 K	Dilution	-3.1337 ~ -3.1156	-3.106 [105]
	Dilution		-3.108 [95]
	0.00121	-3.1306	-3.126 [112]
773 K	Dilution	-3.0892 ~ -3.0756	-3.071 [105]

e: the calculated results corresponding to the mole fraction of 0-0.00729.

Just as what Figure 2.18 shows, self-diffusion coefficients and chemical diffusion coefficients were also calculated with different mole fractions of YCl_3 at the temperatures of 723 K and 773 K. It can be seen that the self-diffusion coefficients of YCl_3 in molten salt are almost stable although there are some variations with the increase of mole fraction. The overall variation trends in chemical diffusion coefficients of YCl_3 at the temperatures of 723 K and 773 K are similar. They increase firstly and then decrease. Overall, the chemical diffusion coefficients of 773 K are larger than that at 723 K even though there are some exceptions at low mole fractions. The comparison in Table 2.19 shows our calculated chemical diffusion coefficients agree well with other literature values.

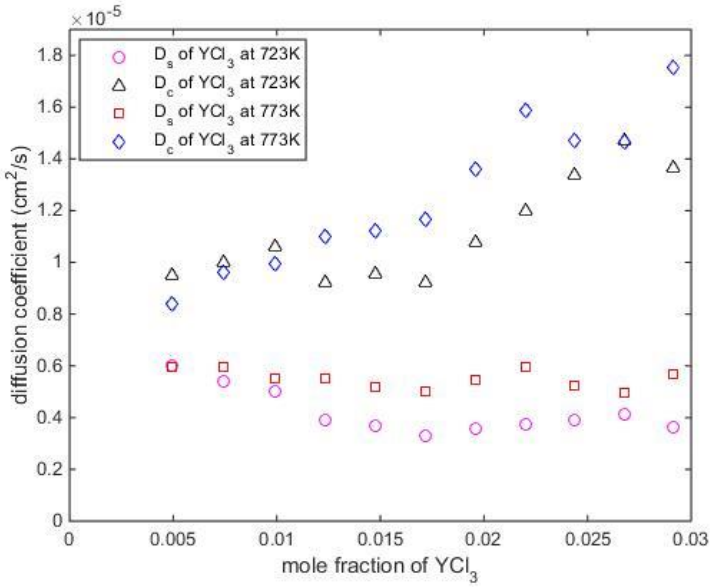

Figure 2.18. Self-diffusion coefficient and chemical diffusion coefficient of YCl_3 at the temperatures of 723 K and 773 K

Table 2.19. Comparison between calculated chemical diffusion coefficient of YCl_3 and literature values

Temperature	The range of D_c (cm^2/s)[f]	Literature value (cm^2/s)
723 K	9.2291×10^{-6} ~ 14.724×10^{-6}	9.14×10^{-6} [117]
		$10\pm1\times10^{-6}$ [113]
773 K	8.3872×10^{-6} ~17.546×10^{-6}	12.9×10^{-6} [117]

f: the range of D_c corresponding to the mole fraction of 0.004975-0.029126.

2.5.4 Scandium

The Gibbs free energy of the mixture solution is shown in Table 2.20

Table 2.20. Gibbs free energy of LiCl-KCl-$ScCl_3$ mixture solution

Temperature	Component	F_{id}/eV	$\Delta F_1 + \Delta F_2/eV$	pV/eV	G_{real}/eV
723 K	LiCl-KCl-1 $ScCl_3$	-285.5381	-1521.5209	0.006986	-1807.0520
	LiCl-KCl-2 $ScCl_3$	-288.7547	-1566.4110	0.007050	-1855.1587
	LiCl-KCl-3 $ScCl_3$	-292.1160	-1611.0155	0.007164	-1903.1243
	LiCl-KCl-4 $ScCl_3$	-295.1832	-1656.0711	0.007202	-1951.2471
	LiCl-KCl-5 $ScCl_3$	-298.3365	-1700.9042	0.007268	-1999.2335
	LiCl-KCl-6 $ScCl_3$	-301.3889	-1745.9329	0.007309	-2047.3144
	eutectic LiCl-KCl	-564.5582	-2952.8256	0.013869	-3517.3698

773 K	LiCl-KCl-1 $ScCl_3$	-308.4145	-1513.1390	0.007098	-1821.5464
	LiCl-KCl-2 $ScCl_3$	-311.8827	-1557.9425	0.007163	-1869.8180
	LiCl-KCl-3 $ScCl_3$	-315.4096	-1602.5921	0.007253	-1917.9945
	LiCl-KCl-4 $ScCl_3$	-318.6696	-1647.4304	0.007278	-1966.0927
	LiCl-KCl-5 $ScCl_3$	-322.2160	-1692.1366	0.007383	-2014.3452
	LiCl-KCl-6 $ScCl_3$	-325.6246	-1736.6496	0.007456	-2062.2667
	eutectic LiCl-KCl	-609.8188	-2936.3508	0.014097	-3546.1555

Table 2.21 shows the calculated Gibbs free energy of supercooled $ScCl_3$.

Table 2.21. Gibbs free energy of supercooled $ScCl_3$ at the temperature of 723 K and 773 K

Temperature	$F_{EC}/\ eV$	$\Delta F/\ eV$	pV/eV	$\Delta G_{fusion,ScCl_3}/\ eV$	$G_{sc,ScCl_3}/\ eV$
723 K	75.9861	-9485.2289	0.013147	52.4143	-9356.8154
773 K	70.5564	-9496.3083	0.013913	48.2160	-9377.5220

The Gibbs free energy of ideal solution and excess Gibbs free energy of the systems of LiCl-KCl-n $ScCl_3$ are presented in Table 2.22.

Table 2.22. The results of total Gibbs free energy of ideal solution, excess Gibbs free energy, mole fraction and molar excess Gibbs free energy of LiCl-KCl-$ScCl_3$ mixture

Temperature	Component	G_{real}/eV	G_{ideal}/eV	G_{excess}/eV	$x_{La}(\%)$	$\bar{G}_{excess}(J/mol)$
723 K	LiCl-KCl-1 $ScCl_3$	-1807.0520	-1805.8616	-1.190	0.4975	-571.4470
	LiCl-KCl-2 $ScCl_3$	-1855.1587	-1852.9521	-2.207	0.9901	-1053.9455
	LiCl-KCl-3 $ScCl_3$	-1903.1243	-1900.0104	-3.114	1.4778	-1480.0146
	LiCl-KCl-4 $ScCl_3$	-1951.2471	-1947.0478	-4.199	1.9608	-1986.1124
	LiCl-KCl-5 $ScCl_3$	-1999.2335	-1994.0698	-5.164	2.4390	-2430.3130
	LiCl-KCl-6 $ScCl_3$	-2047.3144	-2041.0796	-6.235	2.9126	-2920.2349
773 K	LiCl-KCl-1 $ScCl_3$	-1821.5464	-1820.3851	-1.161	0.4975	-557.4775
	LiCl-KCl-2 $ScCl_3$	-1869.8180	-1867.6004	-2.218	0.9901	-1059.2512
	LiCl-KCl-3 $ScCl_3$	-1917.9945	-1914.7812	-3.213	1.4778	-1527.2678
	LiCl-KCl-4 $ScCl_3$	-1966.0927	-1961.9396	-4.153	1.9608	-1964.2790
	LiCl-KCl-5 $ScCl_3$	-2014.3452	-2009.0816	-5.264	2.4390	-2477.3489
	LiCl-KCl-6 $ScCl_3$	-2062.2667	-2056.2105	-6.056	2.9126	-2836.5963

The curve fitted by these data of mole fraction of $ScCl_3$ and molar excess Gibbs free energy is shown in Figure 2.19 and it can be seen the fitting result is quite good.

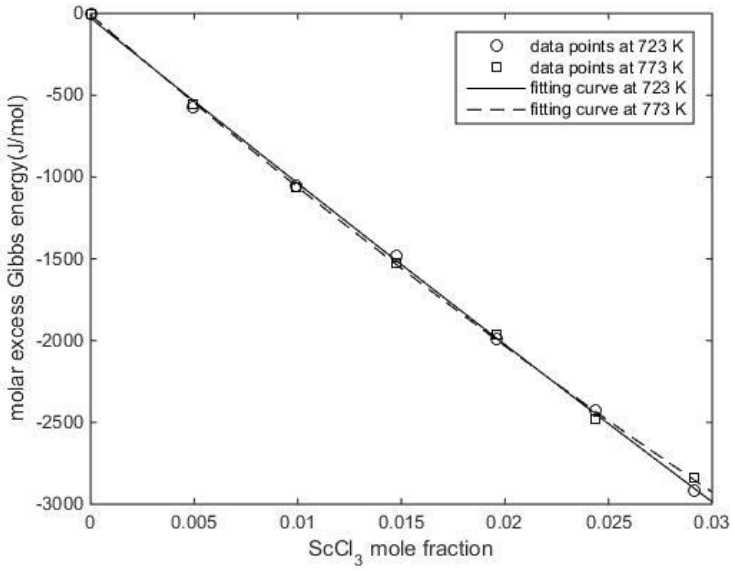

Figure 2.19. The fitting curve of molar excess Gibbs free energy to mole fraction of $ScCl_3$ in the solution

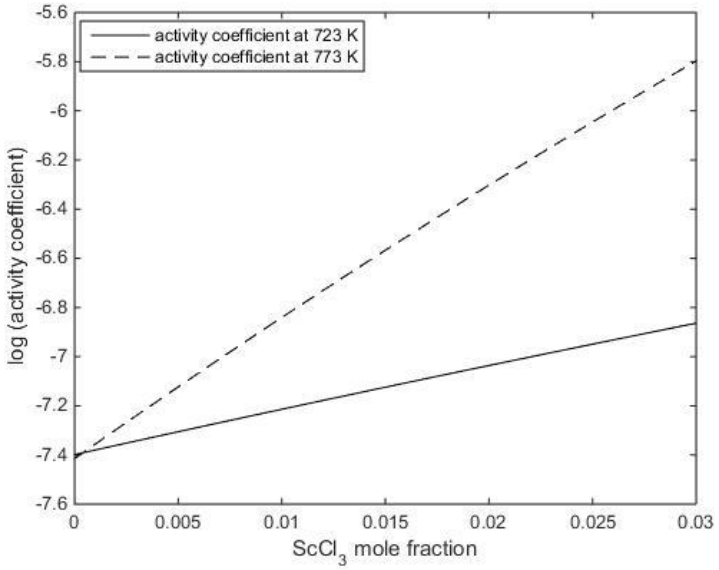

Figure 2.20. Activity coefficient of $ScCl_3$ in eutectic molten salt at the temperatures of 723 K and 773 K

Figure 2.20 shows the relationship between activity coefficient and $ScCl_3$ mole fraction and it can be seen that activity coefficient increases the mole fraction in eutectic molten salt. Besides, the activity coefficient of $ScCl_3$ at 773 K is larger than that at 723 K and this difference gap becomes lager with mole fraction. Table 2.23 shows our calculated activity coefficient agrees well when comparing with other literature values.

Table 2.23. Comparison between the calculated activity coefficient of $ScCl_3$ and literature values

Temperature	Mole fraction	Calculated activity coefficient	Literature value
723 K	4.259×10^{-3}	0.4805×10^{-7}	1.000×10^{-7} [97]
773 K	4.259×10^{-3}	0.6865×10^{-7}	3.981×10^{-7} [97]

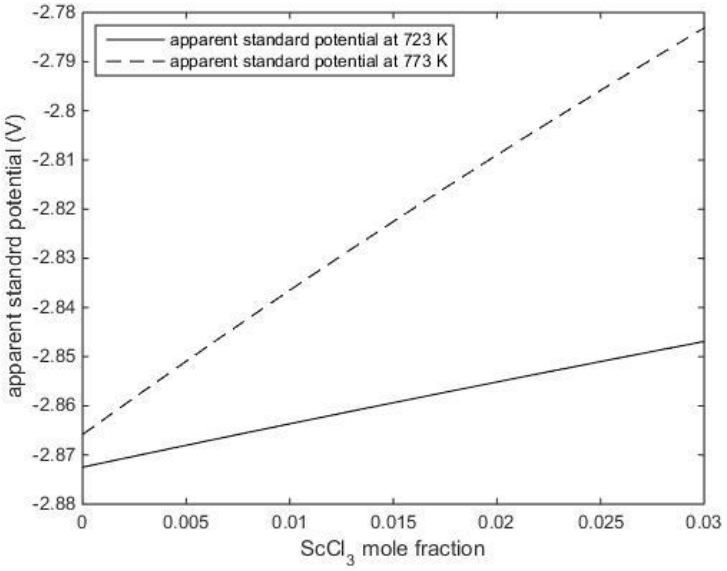

Figure 2.21. Apparent standard potential of $ScCl_3$ at the temperatures of 723 K and 773 K

Figure 2.21 presents that apparent standard potential of $ScCl_3$ increases with the mole fraction and the apparent standard potential at the temperature of 773 K is larger than that at the temperature of 723 K. Table 2.24 shows that our calculated results are quite reasonable when comparing with other literature values.

Table 2.24. Comparison between the calculated apparent standard potential of $ScCl_3$ and literature values

Temperature	Mole fraction	Calculated results (V)	Literature value (V)
723 K	4.259×10^{-3}	-2.869	-2.852 ± 0.009 [97]
773 K	4.259×10^{-3}	-2.853	-2.816 ± 0.012 [97]

The calculated diffusion coefficients were also obtained and shown in Figure 2.22, it can be seen that there are only some small fluctuations in self-diffusion coefficients of $ScCl_3$ with the increase of mole fractions at 723 K and 773 K. The chemical diffusion coefficient with different mole fractions at the temperature of 773 K is larger than that at the temperature of 723 K at the same concentration. There is an increase and then decrease trend in the change of chemical diffusion coefficient with the mole fraction at 723 K and 773 K although the changes at 723 K are not so obvious. The comparisons in Table 2.25 shows our calculated results agree quite well with the literature values.

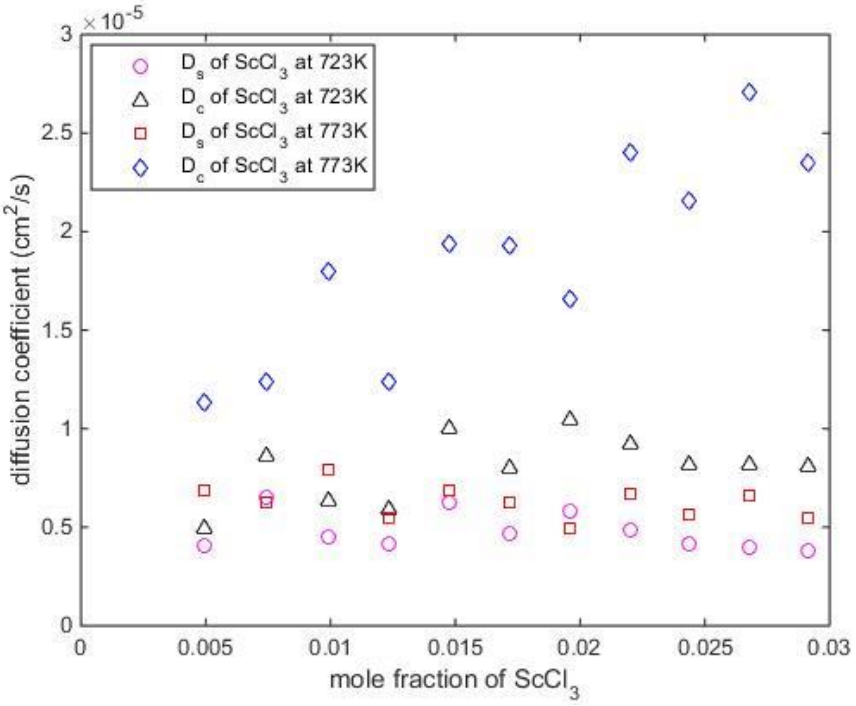

Figure 2.22. Self-diffusion coefficient and chemical diffusion coefficient of $ScCl_3$ at the temperatures of 723 K and 773 K

Table 2.25. Comparison between the calculated chemical diffusion coefficient and literature values

Temperature	The range of D_c (cm^2/s)[g]	Literature value (cm^2/s)
723 K	4.9077×10^{-6} ~ 10.469×10^{-6}	3.0363×10^{-6} ~ 11.079×10^{-6} [97]
773 K	1.1342×10^{-5} ~2.7058×10^{-5}	0.4675×10^{-5} ~ 1.6356×10^{-5} [97]

g: the range of D_c corresponding to the mole fraction of 0.004975-0.029126.

2.5.5 Terbium

For the calculation of the thermodynamic properties of $TbCl_3$, the same method was also used. The total Gibbs free energy of the real solution is shown in Table 2.26

Table 2.26. Gibbs free energy of LiCl-KCl-$TbCl_3$ mixture solution

Temperature	Component	F_{id}/eV	$\Delta F_1 + \Delta F_2/eV$	pV/eV	G_{real}/eV
723 K	LiCl-KCl-1 $TbCl_3$	-285.6147	-1519.3634	0.006974	-1804.9711
	LiCl-KCl-2 $TbCl_3$	-289.0348	-1561.9635	0.007062	-1850.9912
	LiCl-KCl-3 $TbCl_3$	-292.2548	-1604.6750	0.007104	-1896.9228
	LiCl-KCl-4 $TbCl_3$	-295.4718	-1647.4527	0.007151	-1942.9174
	LiCl-KCl-5 $TbCl_3$	-298.7542	-1690.1579	0.007220	-1988.9049
	LiCl-KCl-6 $TbCl_3$	-301.9047	-1732.8904	0.007256	-2034.7879
	eutectic LiCl-KCl	-564.5582	-2952.8256	0.013869	-3517.3698
773 K	LiCl-KCl-1 $TbCl_3$	-308.5055	-1511.0849	0.007089	-1819.5834
	LiCl-KCl-2 $TbCl_3$	-312.1583	-1553.4132	0.007169	-1865.5644
	LiCl-KCl-3 $TbCl_3$	-315.6722	-1596.0311	0.007222	-1911.6961
	LiCl-KCl-4 $TbCl_3$	-319.1141	-1638.6528	0.007262	-1957.7596
	LiCl-KCl-5 $TbCl_3$	-322.5688	-1681.3289	0.007310	-2003.8904
	LiCl-KCl-6 $TbCl_3$	-325.9744	-1723.9534	0.007349	-2049.9205
	eutectic LiCl-KCl	-609.8188	-2936.3508	0.014097	-3546.1555

Gibbs free energy of supercooled $TbCl_3$ is shown in Table 2.27

Table 2.27. Gibbs free energy of supercooled $TbCl_3$ at the temperature of 723 K and 773 K

Temperature	$F_{EC}/\ eV$	$\Delta F/\ eV$	pV/eV	$\Delta G_{fusion,\mathrm{TbCl_3}}/\ eV$	$G_{sc,\mathrm{TbCl_3}}/\ eV$
723 K	52.3963	-9087.2862	0.011915	9.3567	-9025.5213
773 K	45.3407	-9090.8553	0.012097	5.4707	-9040.0318

The Gibbs free energy of ideal solution and excess Gibbs free energy were also calculated, the results can be seen in Table 2.28.

Table 2.28. The results of total Gibbs free energy of ideal solution, excess Gibbs free energy, mole fraction and molar excess Gibbs free energy of LiCl-KCl-$TbCl_3$

Temperature	Component	G_{real}/eV	G_{ideal}/eV	G_{excess}/eV	$x_{La}(\%)$	$\bar{G}_{excess}(J/mol)$
723 K	LiCl-KCl-1 $TbCl_3$	-1804.9711	-1804.2051	-0.766	0.4975	-367.7047
	LiCl-KCl-2 $TbCl_3$	-1850.9912	-1849.6392	-1.352	0.9901	-645.8076
	LiCl-KCl-3 $TbCl_3$	-1896.9228	-1895.0410	-1.882	1.4778	-894.3967
	LiCl-KCl-4 $TbCl_3$	-1942.9174	-1940.4220	-2.495	1.9608	-1180.2419
	LiCl-KCl-5 $TbCl_3$	-1988.9049	-1985.7875	-3.117	2.4390	-1467.2286
	LiCl-KCl-6 $TbCl_3$	-2034.7879	-2031.1408	-3.647	2.9126	-1708.2251
773 K	LiCl-KCl-1 $TbCl_3$	-1819.5834	-1818.6976	-0.886	0.4975	-425.1719
	LiCl-KCl-2 $TbCl_3$	-1865.5644	-1864.2255	-1.339	0.9901	-639.5128
	LiCl-KCl-3 $TbCl_3$	-1911.6961	-1909.7188	-1.977	1.4778	-939.8195
	LiCl-KCl-4 $TbCl_3$	-1957.7596	-1955.1898	-2.570	1.9608	-1215.4260
	LiCl-KCl-5 $TbCl_3$	-2003.8904	-2000.6444	-3.246	2.4390	-1527.7714
	LiCl-KCl-6 $TbCl_3$	-2049.9205	-2046.0858	-3.835	2.9126	-1796.0615

The fitting curves of the excess Gibbs free energy as a function of the mole fraction are given in Figure 2.23. It shows the fitting result is pretty well.

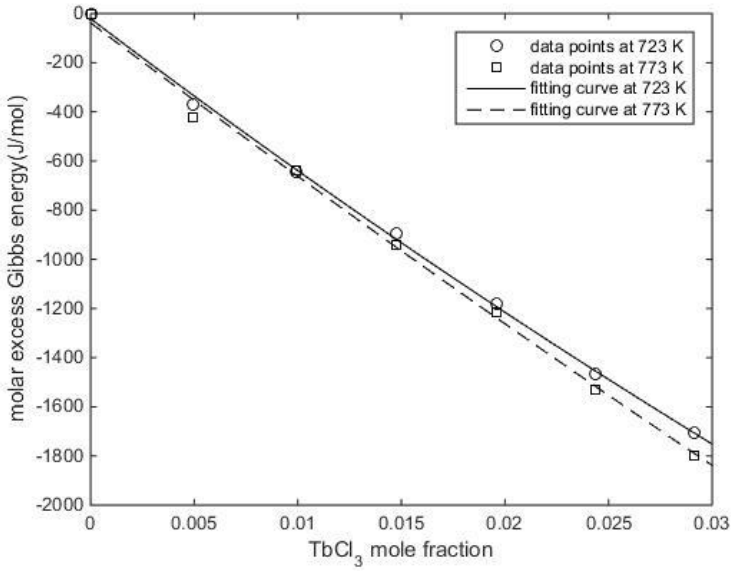

Figure 2.23. The fitting curve of molar excess Gibbs free energy to mole fraction of $TbCl_3$ in the solution

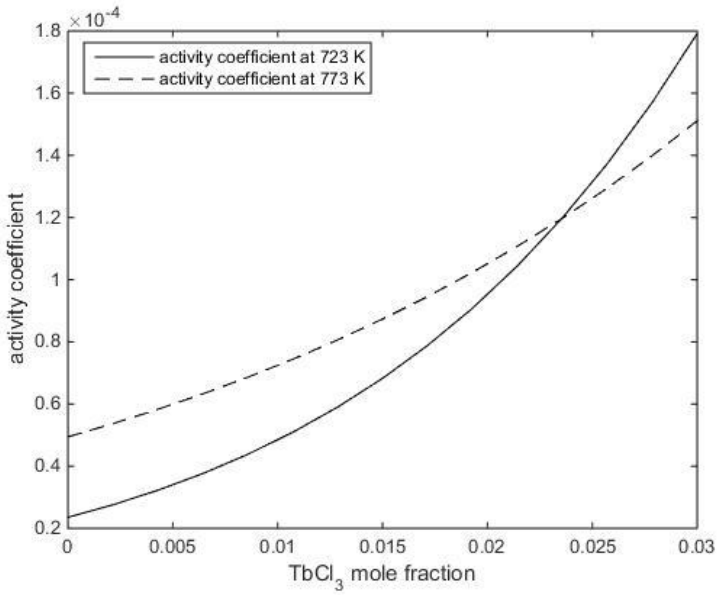

Figure 2.24. Activity coefficient of $TbCl_3$ in eutectic molten salt at the temperature of 723 K and 773 K

It can be seen from Figure 2.24, the activity coefficient of Tb^{3+} increases with $TbCl_3$ mole fraction at 723 K and 773 K. It should be noticed that the activity coefficients at 773 K are larger than that at 723 K for low mole fraction while the activity coefficients at 723 K is larger when the mole fraction is higher than around 0.0235. Table 2.29 shows the calculated results are quite reasonable when comparing with the results from other references.

Table 2.29. Comparison between the calculated activity coefficient of $TbCl_3$ and literature values

Temperature	Mole fraction	Calculated activity coefficient	Literature value
723 K	3.675×10^{-3}	3.0916×10^{-5}	1.7378×10^{-5} [99]
773 K	3.675×10^{-3}	5.7003×10^{-5}	2.4547×10^{-5} [99]

As Figure 2.25 shows, the apparent standard potential of $TbCl_3$ increases with mole fraction. Moreover, the apparent standard potential at 773 K is larger than that at 723 K. The comparisons with the literature values are shown in Table 2.30 and it can be seen our calculated apparent standard potential is quite good.

Table 2.30. Comparison between the calculated apparent standard potential of $TbCl_3$ and literature values

Temperature	Mole fraction	Calculated results (V)	Literature value (V)
723 K	3.675×10^{-3}	-3.026	-3.038 [99]
773 K	3.675×10^{-3}	-2.994	-3.012 [99]

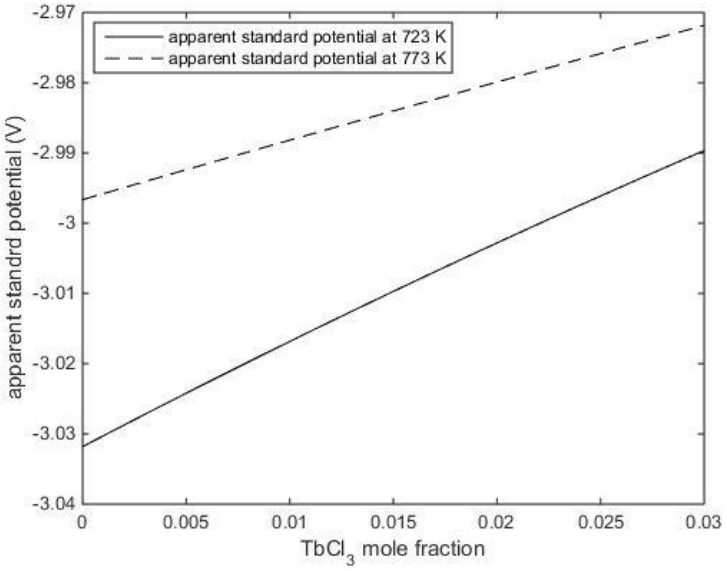

Figure 2.25. Apparent standard potential of $TbCl_3$ at the temperatures of 723 K and 773 K

It can be seen from Figure 2.26 that the self-diffusion coefficients of $TbCl_3$ almost keep stable although there are some fluctuations. The chemical diffusion coefficients slightly depend on the changes of mole fractions of $TbCl_3$ and it increases initially and then decreases with the mole fraction. It should be noticed that just as other three elements talked before, the diffusion coefficients at 773 K are larger than that at the temperature of 723 K. The comparison results are shown in Table 2.31, it can be seen that our calculated chemical diffusion coefficients agree quite well with other literature values.

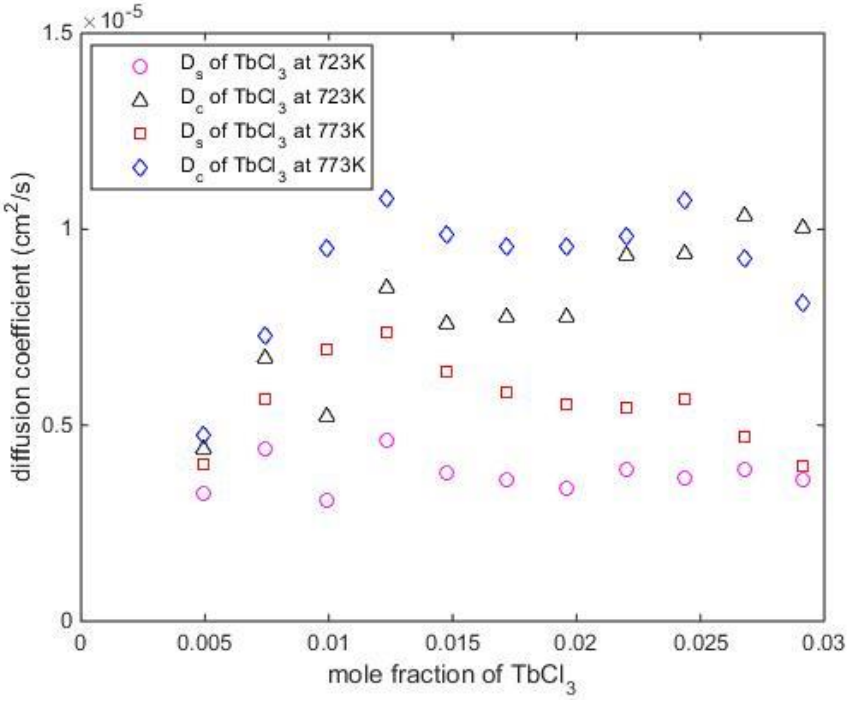

Figure 2.26. Self-diffusion coefficient and chemical diffusion coefficient of $TbCl_3$ at the temperatures of 723 K and 773 K

Table 2.31. Comparison between the calculated chemical diffusion coefficient of $TbCl_3$ and literature values

Temperature	The range of D_c $(cm^2/s)^h$	Literature value (cm^2/s)
723 K	4.7394×10^{-6} ~ 10.345×10^{-6}	3.7653×10^{-6} ~ 10.468×10^{-6} [99]
773 K	4.4103×10^{-6} ~10.722×10^{-6}	5.4836×10^{-6} ~ 14.745×10^{-6} [99]

h: the range of D_c corresponding to the mole fraction of 0.004975-0.029126.

2.6 Conclusions

The thermodynamic and transport properties of Uranium, Lanthanum, Yttrium, Scandium, and Terbium were investigated by the method of molecular dynamics simulation in the present study. The calculation of activity coefficient, apparent standard potential and diffusion coefficient at different concentrations and temperatures can help us identify the effects of concentration and temperature on thermodynamic properties. The comparison between our calculated results and literature values indicates our modelling has a relative high accuracy. This study contributes significantly to the investigation of thermodynamic properties since all of these properties are calculated at different concentrations while most of other available studies are focused on the dilution.

It was found that the activity coefficient and apparent standard potential strongly depend on the element concentration and the relationships between them are positive correlations. However, it seems that the chemical diffusion coefficients are merely slightly depend on the concentrations although it increases for lower concentrations and then decreases slightly when the concentration of MCl_3 in eutectic molten salt is high enough.

Temperature also plays an important role in the thermodynamic properties. This result is same to the previous experimental measurements for diluted molten salt. However, the effects of temperature on the activity coefficient can be different for different elements and the same element at different concentrations. This study indicates that activity coefficients of U^{3+}, Y^{3+} and Sc^{3+} at the temperature of 773 K are larger than that at the temperature of 723 K while La^{3+} appears in the opposite way. It should be noticed that activity coefficient of Tb^{3+} at 773 K is larger than that at 723 K for a low mole fractions while the activity coefficient at 723 K is larger when the mole fraction is higher than around 0.0235. The apparent standard potential at 773 K is less negative than that at temperature of 723 K for all the elements studied. Our calculated results also indicate that generally diffusion coefficient at 773 K is larger than that at 723 K although there are some points which do not satisfy. The activity coefficients of four rare earth elements are also compared which can be seen in Figure 2.27 and Figure 2.28, it shows activity coefficient of $LaCl_3$ is the largest while that of $ScCl_3$ is the smallest.

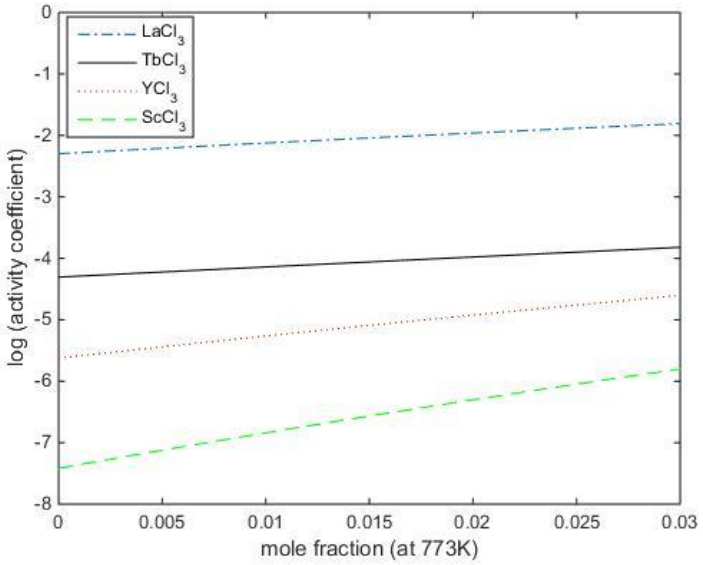

Figure 2.27. Activity coefficients of $LaCl_3$, $TbCl_3$, YCl_3 and $ScCl_3$ in eutectic molten salt at the temperature of 773 K

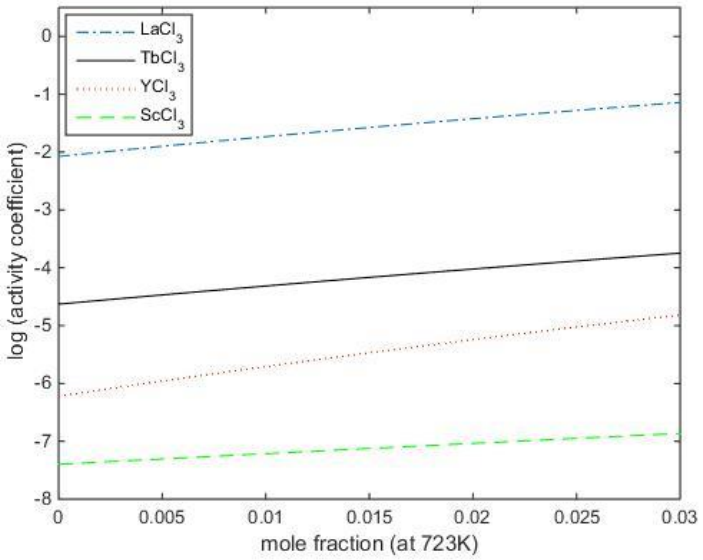

Figure 2.28. Activity coefficient of $LaCl_3$, $TbCl_3$, YCl_3, $ScCl_3$ in eutectic molten salt at the temperature of 723 K

The high accuracy of our calculated results demonstrates the modelling we used is valid so it can be served as a potential method to predict the thermodynamic properties of nuclear elements in the real pyroprocessing of nuclear waste treatment in which the concentration is high and changeable. Also it provides fundamental data in a wide range of composition for our model development.

3 Thermodynamic assessment of LiCl-KCl-$PuCl_3$ system

3.1 Thermodynamic model

The phase diagram is a powerful tool to predict the state of a system under certain conditions. Basically, a phase diagram consists of phase boundaries at which different phases coexist. Key features that can be retrieved from it include phase transitions, intermetallic compounds, liquidus and solidus lines as well as solubility. In the present work, thermodynamic properties of LiCl-KCl-$PuCl_3$ were considered and evaluated by CALPHAD method (Calculation of PHase Diagram). Two-sublattice model for ionic liquid was applied to LiCl-KCl, LiCl-$PuCl_3$, and KCl-$PuCl_3$ binary systems to model their Gibbs energies. The experimental data used included the phase information and enthalpy of mixing from literature. However, for the LiCl-KCl-$PuCl_3$ ternary system, previous studies were limited in electrochemical measurements with a dilute solution. These data can be used but not enough to evaluate the ternary interactions in the system. As a supplementary, an empirical correlation to estimate the enthalpy of mixing for the asymmetric salt system that has been successfully used in the LiCl-KCl-UCl_3 system [118] was applied to calculate the enthalpy

of mixing of the LiCl-KCl-$PuCl_3$. These data combined with the results from binary systems were used as the input to assess the thermodynamic equilibria of the LiCl-KCl-$PuCl_3$ system. After that, the solubility and Gibbs energy of formation of $PuCl_3$ in the typical molten LiCl-KCl used in pyroprocessing were derived from the optimized results.

3.2 CALPHAD method

Phase diagram development is the process to seek the stable or metastable phases and phase boundaries. Proposed by Kaufman and Bernstein [119] in the early 70s, the CALPHAD method has been applied widely within the material research area now, such as alloy design and material performance prediction [120]. Summarized briefly, it is a method connecting existing experimental data about phase information and thermodynamic properties with the phase diagram by thermodynamic functions of Gibbs energy [121]. Basically, under a constant pressure, the thermodynamic functions can be expressed in terms of temperature and chemical compositions with some adjustable parameters. The phase diagram is the manifestation of the thermodynamic properties of a system. All the boundary conditions in a phase diagram can be reflected by the Gibbs energy of the system [122]. For example, the global minimum Gibbs energy corresponds to stable phase and local minimum Gibbs energy to the metastable phase. Also, when two phases coexist, the chemical potential of a species in these two phases should be the same

$$\mu_i^{\varphi 1} = \left(\frac{\partial G_t^{\varphi 1}}{\partial n_i^{\varphi 1}}\right)_{n_{j\neq i},p,T} = \mu_i^{\varphi 2} = \left(\frac{\partial G_t^{\varphi 2}}{\partial n_i^{\varphi 2}}\right)_{n_{j\neq i},p,T} \qquad \text{Eq. 3.1}$$

where $\mu_i^{\varphi j}$ and $n_i^{\varphi j}$ are the chemical potential and mole number of *i* in phase φj, respectively. $G_t^{\varphi j}$ is the total Gibbs energy of phase φj . *p* and *T* are the pressure and absolute temperature, respectively. Therefore, by selecting an appropriate Gibbs energy model, the existing thermodynamic properties of a system can be satisfied and phase information from experiments can also be depicted if these data are self-consistent, by optimizing parameters in the model. Then the phase diagram can be extended to the composition range beyond the experiments and other properties can be also derived from the optimized results. But since it is a method totally based on the experimental data, it is not possible for the CALPHAD to predict completely new phases without input thermodynamic functions. The main flowchart of the CALPHAD is shown in Figure 3.1. Essentially, three steps are involved during the calculation, including Gibbs energy model choice, database compilation, and parameters optimization.

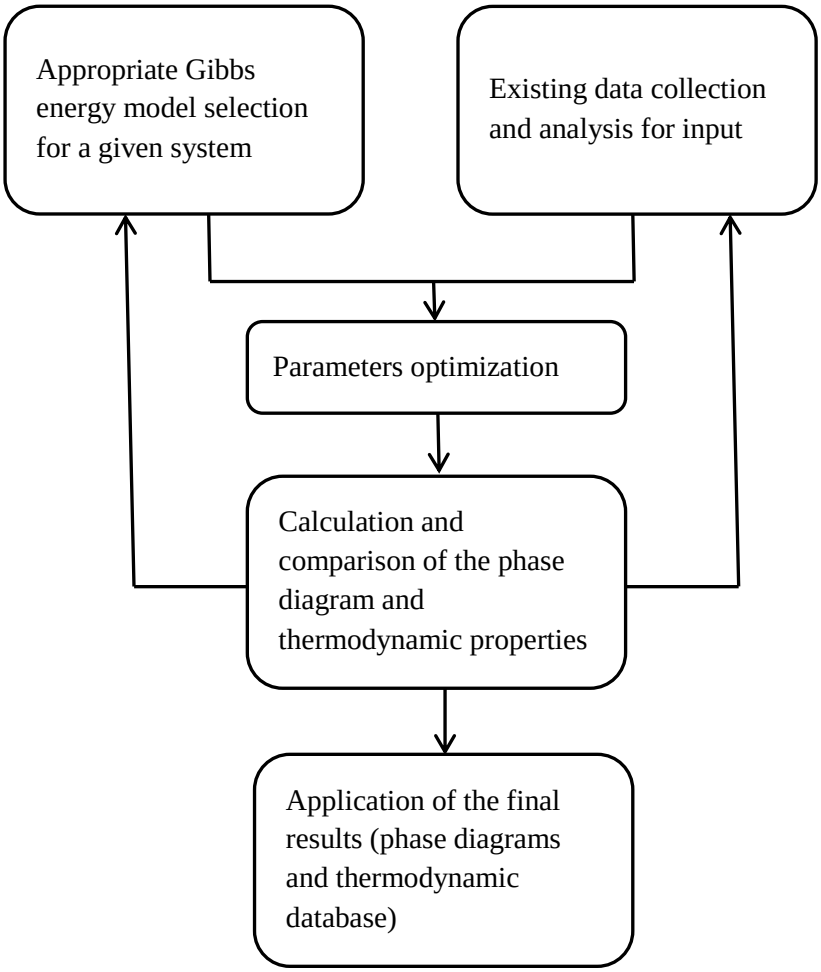

Figure 3.1. Flowchart of the main steps in CALPHAD

3.3 Gibbs energy model

Generally, for a solution phase of a ternary system with components of 1-2-3, the molar Gibbs energy can be expressed by [123]

$$G_m = \sum_{i=1}^{3} x_i G_i^0 + RT \sum_{j=1}^{3} x_j \ln x_j + G_m^{ex}$$
$$= \sum_{i=1}^{3} x_i G_i^0 + RT \sum_{j=1}^{3} x_j \ln x_j + (G_{m,12}^{ex} + G_{m,23}^{ex} + G_{m,13}^{ex} + G_{m,123}^{ex}) \quad \text{Eq. 3.2}$$

where G_i^0 is the standard molar Gibbs energy of i. G_m^{ex} is the molar excess Gibbs energy including the contributions from all sub-binary systems 1-2, 2-3, and 1-3 as well as the ternary system 1-2-

3 in the solution. x_i is the mole fraction of i in the solution phase, R is the gas constant, and T is the temperature in Kelvin. For example, the Redlich-Kister model gives excess Gibbs energy for binary system 1-2 as

$$G_{12}^{ex} = \sum_{\upsilon=0}^{n} (V_{\upsilon,1} + V_{\upsilon,2}T)(x_1 - x_2)^{\upsilon} x_1 x_2 \qquad \text{Eq. 3.3}$$

For the ternary system with 1-2-3, the excess Gibbs can be extrapolated from binary ones as

$$G_{Tern}^{ex} = A_{12}G_{12}^{ex} + A_{13}G_{13}^{ex} + A_{23}G_{23}^{ex} + G_{123}^{ex} \qquad \text{Eq. 3.4}$$

A_{ij} is the coefficient used to extrapolate binary systems to ternary one, which can be a function of composition. Higher order system can be extrapolated analogously. The simplest model is Mugginau model [124] showing

$$A_{12} = A_{13} = A_{23} = 1 \qquad \text{Eq. 3.5}$$

Other models, such as Kaptay model [125] for the binary systems, Kohler, Kohler/Toop, and Muggianu/Toop [126] models for the ternary systems do exist to deal with a variety of systems. An appropriate model is necessary to get a reasonable and meaningful fitting.

3.3.1 Database development

As is discussed above, existing data is the premise of the CALPHAD method. A comprehensive database for a specific system has to be developed before the method can be carried out. The database not only contributes to the selection of the models of Gibbs energy but also is indispensable to fit the parameters in these models. Since the model is about Gibbs energy, any data related to it can be used in the calculation. The main data that can be used as the input are listed in Table 3.1.

Table 3.1. Useful data for calculating the phase diagrams

Data and other information	Comments
Intermediate compounds in the system	Phase diagram calculation is based on the existing data, it can only reflect the compounds we input but cannot generate new compounds itself
Standard Gibbs energy of formation for A, B, C and intermediate compounds	Standard Gibbs energy of formation for liquid and solid should be given for every species. Also, the temperature range of the application and reference states should be defined.
Activity or activity coefficient	Temperature, reference states, and composition of the solution must be recorded for every data point. It is better with data beyond dilute solution.
Enthalpy, entropy, and Gibbs energy of mixing	Temperature, reference states, and composition of the solution must be recorded for every data point.
Chemical potential	Temperature, reference states, and composition of the solution must be recorded for every data point.
Electromotive force	Temperature, reference states, and composition of the solution must be recorded for every data point.
Liquidus and solidus lines or points	Phase boundaries. It also can verify the calculating results
Heat capacity	Heat capacity at constant pressure and the temperature range of application
Possible miscibility gas	In the solid and liquid solution part
Magnetic properties	For example, the critical temperature for magnetic ordering and the Bohr magneton number. Generally for the solid
Eutectic points, congruent melting points, peritectic points, etc	Special points to define a phase diagram

3.3.2 Parameter optimization

Generally, parameters are optimized by minimizing the sum of squared errors through iterations. Algorithms used include Marquardt's, Gauss, and other algorithms [122]. There is several ready-to-use software, such as Thermo-Calc [127], FactSage [128], and Pandat [129].

3.3.3 Gibbs energy model

In the present work, a two-sublattice model [130][131] was applied to describe the excess Gibbs energy of liquid. The model separates anions and cations into different sublattices. There are two intermediate compounds in LiCl-KCl-$PuCl_3$ system, K_2PuCl_5 and K_3PuCl_6 [132] and previous studies showed $PuCl_6^{3-}$ prevails in Pu(III)-containing molten salt [133]. Accordingly, here K_3PuCl_6 was treated as a neutral species in anionic sublattice to deal with the short-range ordering. The model was indicated by

$(K^+, Li^+, Pu^{3+})_p : (Cl^-, K_3PuCl_6)_q$

The parenthesis represents different lattices and the colon is used to separate them. In every parenthesis, there is a constituent array resided in the sub-lattice. *p* and *q* are the site numbers in the corresponding lattice and given by

$$p = y_{Cl^-} \qquad \text{Eq. 3.6}$$

And

$$q = y_{K^+} + y_{Li^+} + 3y_{Pu^{3+}} \qquad \text{Eq. 3.7}$$

where y_i is the site fraction of a particular species *i* on the corresponding sublattice. The molar Gibbs energy of liquid phase was

$$\begin{aligned} G_m^{Liq.} &= y_{Li^+} y_{Cl^-} {}^0G^{Liq.}_{Li^+:Cl^-} + y_{K^+} y_{Cl^-} {}^0G^{Liq.}_{K^+:Cl^-} + y_{Pu^{3+}} y_{Cl^-} {}^0G^{Liq.}_{Pu^+:Cl^-} \\ &+ {}^0G^{Liq.}_{K_3PuCl_6} + RT[\,p(y_{Li^+} lny_{Li^+} + y_{K^+} lny_{K^+} + y_{Pu^{3+}} lny_{Pu^{3+}}) \\ &q(y_{Cl^-} lny_{Cl^-} + y_{K_3PuCl_6} lny_{K_3PuCl_6})] + {}^E G_m^{Liq.} \end{aligned} \qquad \text{Eq. 3.8}$$

where ${}^0G^{Liq.}_{Li^+:Cl^-}$, ${}^0G^{Liq.}_{K^+:Cl^-}$ ${}^0G^{Liq.}_{Pu^{3+}:Cl^-}$, ${}^0G^{Liq.}_{K_3PuCl_6}$ are the standard molar Gibbs energy of LiCl, KCl, $PuCl_3$, and K_3PuCl_6 in liquid status, respectively. ${}^E G_m^{Liq.}$ is the molar excess Gibbs energy. In the manner of Muggianu formalism [134], it is given by

$$\begin{aligned} {}^E G_m^{Liq.} &= y_{Cl^-}(y_{K^+} y_{Li^+} L^{Liq.}_{K^+,Li^+:Cl^-} + y_{K^+} y_{Pu^{3+}} L^{Liq.}_{K^+,Pu^{3+}:Cl^-} + y_{Li^+} y_{Pu^{3+}} L^{Liq.}_{Li^+,Pu^{3+}:Cl^-}) \\ &+ y_{Cl^-} y_{K_3PuCl_6}(y_{K^+} L^{Liq.}_{K^+:Cl^-,K_3PuCl_6} + y_{Li^+} L^{Liq.}_{Li^+:Cl^-,K_3PuCl_6} + y_{Pu^{3+}} y_{K_3PuCl_6} L^{Liq.}_{Pu^{3+}:Cl^-,K_3PuCl_6}) \\ &+ y_{Cl^-} y_{K_3PuCl_6}(y_{K^+} y_{Li^+} L^{Liq.}_{K^+,Li^+:Cl^-,K_3PuCl_6} + y_{K^+} y_{Pu^{3+}} L^{Liq.}_{K^+,Pu^{3+}:Cl^-,K_3PuCl_6} \\ &+ y_{Li^+} y_{Pu^{3+}} L^{Liq.}_{Li^+,Pu^{3+}:Cl^-,K_3PuCl_6}) + y_{K^+} y_{Li^+} y_{Pu^{3+}} y_{Cl^-}(L^{Liq.}_{K^+,Li^+,Pu^{3+}:Cl^-} \\ &+ y_{K_3PuCl_6} L^{Liq.}_{K^+,Li^+,Pu^{3+}:Cl^-,K_3PuCl_6}) \end{aligned} \qquad \text{Eq. 3.9}$$

These interaction parameters *L* for both binary and ternary interactions can be expressed as concentration and temperature dependent. For example, binary interaction parameter $L^{Liq.}_{K^+,Pu^{3+}:Cl^-}$ was expanded as a Redlich-Kister polynomial [135]

$$L^{Liq.}_{K^+,Pu^{3+}:Cl^-} = \sum_{v=0}^{n} {}^v L^{Liq.}_{K^+,Pu^{3+}:Cl^-}(y_{K^+} - y_{Pu^{3+}})^v \qquad \text{Eq. 3.10}$$

And ternary one, for example, can be

$$L^{Liq.}_{Li^+,K^+,Pu^{3+}:Cl^-} = y_{Li^+} L_{Li^+:Cl^-} + y_{K^+} L_{K^+:Cl^-} + y_{Pu^{3+}} L_{Pu^{3+}:Cl^-} \quad \text{Eq. 3.11}$$

Then linear dependence on temperature was applied to these parameters like

$$^{v}L = a_v + b_v T \quad \text{Eq. 3.12}$$

a_v and b_v are the parameters needed to optimize during the calculation. Since there are no heat capacity data for the intermediate compounds K_2PuCl_5 and K_3PuCl_6, their standard Gibbs energies were written according to Neumann–Kopp rule [136] as

$$^{0}G^{state}_{K_mPu_nCl_{m+3n}} = m\,^{0}G^{state}_{KCl} + n\,^{0}G^{state}_{PuCl_3} + A + BT \quad \text{Eq. 3.13}$$

where "state" stands for liquid or solid. A and B are variables related to the enthalpy and entropy of formation of the intermediate compound $K_mPu_nCl_{m+3n}$, respectively. These values were optimized according to experimental data.

The only solid solution considered in the LiCl-KCl-$PuCl_3$ system was the LiCl-KCl mutual terminal solution that is less than 5 mol% reported by Ghosh [118]. The solid solution was also described by two-sublattice model as

$$(Li^+, K^+)_1 : (Cl^-)_1$$

The molar Gibbs energy was

$$G^S_m = y_{K^+}\,^{0}G^S_{K^+:Cl^-} + y_{Li^+}\,^{0}G^S_{Li^+:Cl^-} + RT(y_{K^+}\ln y_{K^+} + y_{Li^+}\ln y_{Li^+}) + {}^{E}G^S_m \quad \text{Eq. 3.14}$$

And excess Gibbs energy was

$${}^{E}G^S_m = y_{Li^+} y_{K^+} \sum_{v=0}^{n} {}^{v}L^S_{Li^+,K^+:Cl^-} (y_{Li^+} - y_{K^+})^v \quad \text{Eq. 3.15}$$

3.4 Database development

For developing the ternary phase diagram based on CALPHAD, experimental data for all the binary systems (LiCl-KCl, LiCl-$PuCl_3$, KCl-$PuCl_3$) and the ternary system are needed. In this section, the database was developed based on previous experimental data.

3.4.1 Binary systems

The LiCl-KCl system has been widely studied. Phase boundary information was investigated by Richards [137], Aukrust [138], Korin [139], and Basin [140] with the methods of heating curves, cooling curves, calorimetric measurements, and oscillation phase analysis. Hersh [141] studied the enthalpy of mixing at the temperature of 1013 K. Recently Ghosh [118] evaluated the LiCl-KCl system with terminal solubility and demonstrated by experiments that the mutual solubility was less than 5 mol%. However, there are only a few studies on LiCl-$PuCl_3$ and KCl-$PuCl_3$. Bjorklund and co-workers [142] studied the phase equilibria of the LiCl-$PuCl_3$ binary system and reported it to be a simple eutectic system without any solid solution or intermediate compounds. The eutectic point occurs at 28% $PuCl_3$ with a temperature of 734 K. The phase diagram of KCl-$PuCl_3$ is a little

more complex compared to the other two binary systems since two intermediate compounds were reported [132]: K_3PuCl_6 and K_2PuCl_5. K_3PuCl_6 melts congruently at 685^0C and the peritectic point related to K_2PuCl_5 melting appears at 35% $PuCl_3$ with a temperature of 611^0C.

3.4.2 Ternary system

Few references were found about the phase diagram or enthalpy about the LiCl-KCl-$PuCl_3$ system, but a variety of experimental measurements have been performed to explore the electrochemical behaviors of $PuCl_3$ in LiCl-KCl eutectic salt as reviewed in Chapter 1. These review data were inputted to the Gibbs energy model to evaluate the ternary interactions.

3.5 Results and discussion

The parameter optimization was carried out in the PARROT module of CALPHAD software Thermo-Calc [127] by minimizing the sum of squared errors through iterations. Data collected in Table 3.2 were edited into an experimental data file to be used as the input. After obtaining the Gibbs energy expressions for different phases in the system, phase diagrams were calculated and plotted accordingly in the POLY module of the same software.

Table 3.2. Gibbs energy database (J/mol) input for the LiCl-KCl-$PuCl_3$ system

Parameters		Functions	Ref.
Liquid	${}^0G^{Liq.}_{Li:Cl}$	$= -395043.11 - 16.124629T - 4.0793198T\ln(T) - 0.071486773T^2$ $+1.4175712\times10^{-5}T^3 - 394814T^{-1}$, 298.15 K < T < 883 K $= -417132.497 + 421.76137T - 73.3062T\ln(T)$ $+0.004715055T^2 - 16535T^{-1}$, 883 K < T < 2000 K	[118]
	${}^0G^{Liq.}_{K:Cl}$	$-427035.9 + 247.546026T - 52.801T\ln(T) + 0.93665\times10^{-3}T^2$ $-2.409027\times10^{-6}T^3 + 97730T^{-1}$, 298.15 K<$T$<750 K $-648588.535 + 3031.321656T - 469.507T\ln(T) + 350.0937\times10^{-3}T^2$ $-57.429763\times10^{-6}T^3 + 22222816T^{-1}$, 750 K<$T$<1045 K $-443361.737 + 404.765951T - 73.3994T\ln(T)$, 1045 K < T < 2000 K	[118]
	${}^0G^{Liq.}_{Pu:Cl}$	$-1037967.35 + 479.21511T - 94.12701T\ln(T) - 0.0135962T^2$ $-6.25\times10^{-10}T^3 - 28380T^{-1} + 63579 - 61.5653437T$, 298.15 K<$T$<1033 K $-1064596.34 + 766.881722T - 133.888T\ln(T) + 63597$ $-61.5653437T$, 1033 K < T < 1500 K	[143]

	${}^{0}G^{Liq.}_{K_3PuCl_6}$	${}^{3}{}^{0}G^{Liq.}_{KCl} + {}^{0}G^{Liq.}_{PuCl_3} - 6700 - 66.7T$	[144]
Solid	${}^{0}G^{S}_{Li:Cl}$	$= 423060.237 + 246.636632T - 44.7048T\ln(T) - 0.0089638T^2$ $-3.1058\times10^{-7}T^3 + 97229T^{-1}$, 289.15 K$<T<$883 K $=490131.802 + 821.73726T - 124.44483T\ln(T) + 0.025420461T^2$ $-1.523016\times10^{-6}T^3 + 9722242T^{-1}$, 883 K $< T <$ 2000 K	[118]
Solid	${}^{0}G^{S}_{K:Cl}$	$-452489.937 + 263.149637T - 51.2948T\ln(T) - 1.40523\times10^{-3}$ $-1731001\times10^{-6}T^3 + 76732T^{-1}$, 298.15 K$<T<$700 K $-487176.143 + 762.308381T - 127.7773T\ln(T)$ $+72.96818\times10^{-3}T^2 - 15.190909\times10^{-6}T^3 + 3002008T^{-1}$, 700 K$<T<$800 K $-729641.417 + 3635.724945T - 553.3953T\ln(T)$ $+406.611005\times10^{-3}T^2 - 63.587069\times10^{-6}T^3$ $+28867854T^{-1}$, 800 K$<T<$1045 K $-9292757.859 + 83732.64789T - 11945.8623451T\ln(T)$ $+7098.951923\times10^{-3}T^2 - 795.735427\times10^{-6}T^3$ $+1229243789T^{-1}$, 1045 K$<T<$1100 K $-469544.033 + 429.820456 - 73.3994T\ln(T)$, 1100 K $< T <$ 2000 K	[118]
	${}^{0}G^{S}_{PuCl_3}$	$-1.37967.35 + 479.21511T - 94.12701T\ln(T) - 0.0135862T^2$ $-6.25\times10^{-10}T^3 - 28380T^{-1}$, 298.15 K$<T<$1033 K $-1064596.34 + 766.881722T - 133.888T\ln(T)$, 1033 K $< T <$ 1500 K	[143]

3.5.1 Binary phase diagrams

3.5.1.1 LiCl-KCl

Figure 3.2 plots the calculated phase diagram of LiCl-KCl. The eutectic point was calculated to be at 58.6 mol% LiCl and 626 K. Due to the similarity of K and Li, a small portion of K atoms can be substituted for Li atoms in LiCl crystal. Then K atoms act as the solute in the matrix of LiCl while LiCl would still keep its structure. The same rule applies to KCl as well. So the two solid solution phases marked as LiCl and KCl at two terminals of the phase diagram in Figure 3.2 are not pure LiCl and KCl but LiCl-structure crystal and KCl-structure crystal, respectively. Or it can be said that these two solid solution phases are two different halite structure crystals.

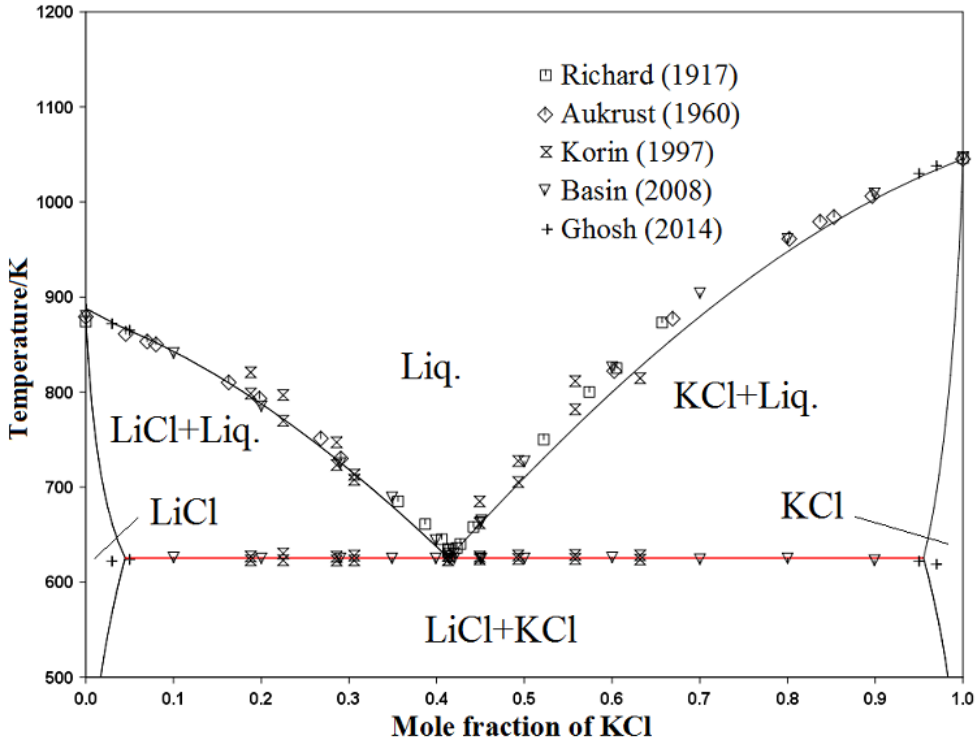

Figure 3.2. Calculated LiCl-KCl phase diagram

3.5.1.2 LiCl-$PuCl_3$

LiCl-$PuCl_3$ was reported as a simple eutectic system with the eutectic point at 28 mol% $PuCl_3$ and 734 K [142]. Figure 3.3 shows our calculated phase diagram. And the eutectic point obtained in this work is at 26.8 mol% and 731 K, which agrees very well with experimental data

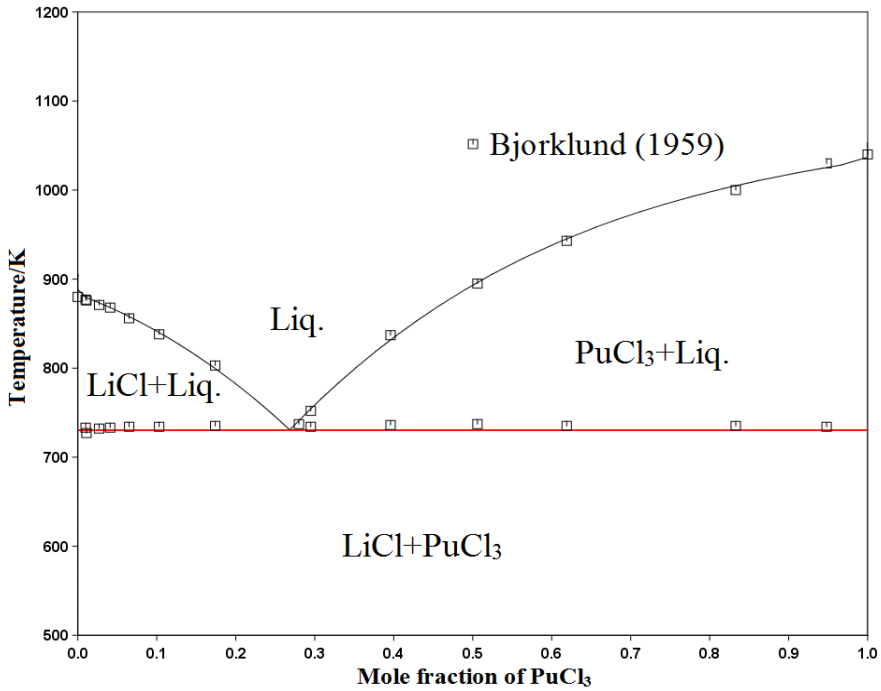

Figure 3.3. Calculated LiCl-$PuCl_3$ phase diagram

3.5.1.3 KCl-$PuCl_3$

KCl-$PuCl_3$ has two intermediate components K_2PuCl_5 and K_3PuCl_6. The calculated phase is shown in Figure 3.4. Calculated melting point of K_3PuCl_6 is at 958 K, compared against the value of 958 K reported by Benz [132]. The peritectic point calculated for K_2PuCl_5 is at 35 mol% KCl and 884 K, while the values of 35 mol% KCl and 884 K reported by Benz [132] as well. Table 3.4 shows the optimized parameters for these binary systems and Table 3.6 is the comparison between the calculated results and the literature data.

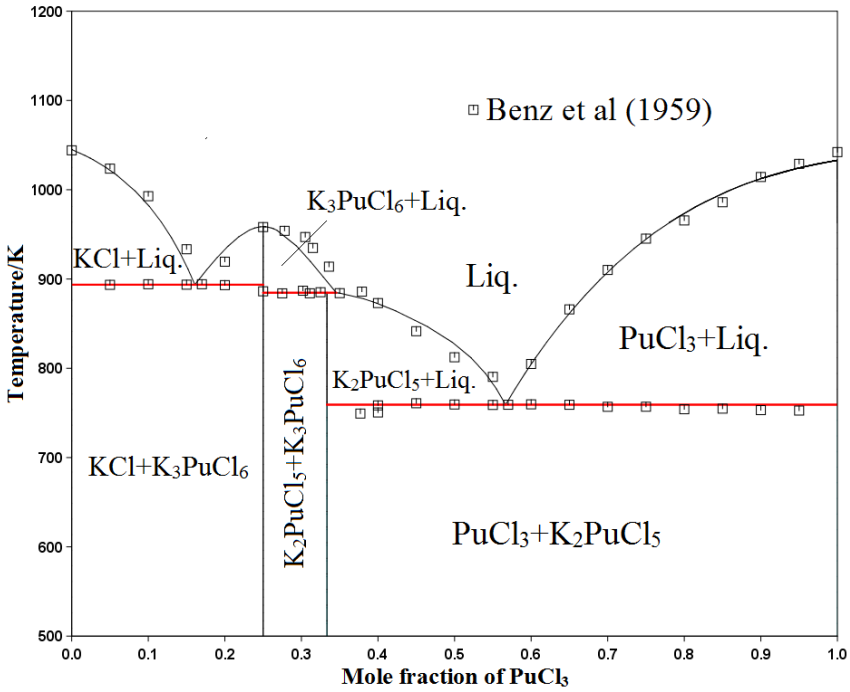

Figure 3.4. Calculated KCl-$PuCl_3$ phase diagram

3.5.2 Ternary phase diagram

There are extensive studies about the electrochemical behaviors of $PuCl_3$ in LiCl-KCl eutectic melt for dilution but no studies reported on the enthalpy or phase information of the LiCl-KCl-$PuCl_3$ ternary system. Here an empirical correlation was derived from the surrounded-ion model, which has been employed in a LiCl-KCl-UCl_3 system [118], and was used to estimate the enthalpy of mixing of the current ternary system. On the basis of this model, the enthalpy of mixing is described by

$$\Delta_{mix}H = \frac{3x_{PuCl_3}x_{LiCl}}{1+2x_{PuCl_3}}\left[\frac{1}{3}\left(\frac{x_{LiCl}}{1+2x_{PuCl_3}}\right)\Delta\overline{H}^{\infty}_{PuCl_3(LiCl)} + \left(1-\frac{x_{LiCl}}{1+2x_{PuCl_3}}\right)\Delta\overline{H}^{\infty}_{LiCl(PuCl_3)}\right]$$
$$+\frac{x_{LiCl}x_{KCl}}{1+2x_{PuCl_3}}\left[\frac{x_{KCl}}{1+2x_{PuCl_3}}\Delta\overline{H}^{\infty}_{LiCl(KCl)} + \left(1-\frac{x_{KCl}}{1+2x_{PuCl_3}}\right)\Delta\overline{H}^{\infty}_{KCl(LiCl)}\right] \qquad \text{Eq. 3.16}$$
$$+\frac{3x_{KCl}x_{PuCl_3}}{1+2x_{PuCl_3}}\left[\frac{3x_{PuCl_3}}{1+2x_{PuCl_3}}\Delta\overline{H}^{\infty}_{KCl(PuCl_3)} + \left(1-\frac{3x_{PuCl_3}}{1+2x_{PuCl_3}}\right)\frac{1}{3}\Delta\overline{H}^{\infty}_{PuCl_3(KCl)}\right]$$

where x_i is the mole fraction of species *i* and $\Delta\overline{H}^{\infty}_{i(j)}$ represents partial enthalpy of mixing at infinite dilution for component *i* in the *i*-*j* binary system. Figure 3.5 shows the calculated enthalpy of

mixing for these three binary systems at 1200 K. The similar structure of the LiCl and KCl is indicated by the pretty symmetric curve. What should attract one's attention most is that the minimum value of enthalpy of mixing of KCl-$PuCl_3$ system is present at $PuCl_3$-rich side with around 0.63 mole fraction of $PuCl_3$. This is unexpected because the only two compounds existing in the system are K_2PuCl_5 and K_3PuCl_6, which are both KCl-rich. This phenomenon could be due to the effects of some local ordering [145,146]. But further experiments, for example, by X-ray diffraction method, are merited to investigate it and provide more insightful information. Based on the plot of enthalpy of mixing, these $\Delta\overline{H}^{\infty}_{i(j)}$ in Eq. 3.16 were obtained, which are shown in Table 3.3. Based on the model, the enthalpy of mixing of LiCl-KCl-$PuCl_3$ system at 1200 K with $x(\mathrm{LiCl}) : x(\mathrm{KCl}) = 0.586 : 0.414$ was estimated and is indicated in Figure 3.5, which was used as the input to extrapolate the binary systems to ternary one based on the Muggianu formalism with ternary interactions described by Eq. 3.8 to Eq. 3.12 [134].

Table 3.3. Partial enthalpies at infinite dilution at 1200 K

i	*j*	$\Delta\overline{H}^{\infty}_{i(j)}$ (kJ/mol)	$\Delta\overline{H}^{\infty}_{j(i)}$ (kJ/mol)
LiCl	KCl	-15.33	-15.77
LiCl	$PuCl_3$	-40.48	-33.84
KCl	$PuCl_3$	-99.66	-53.86

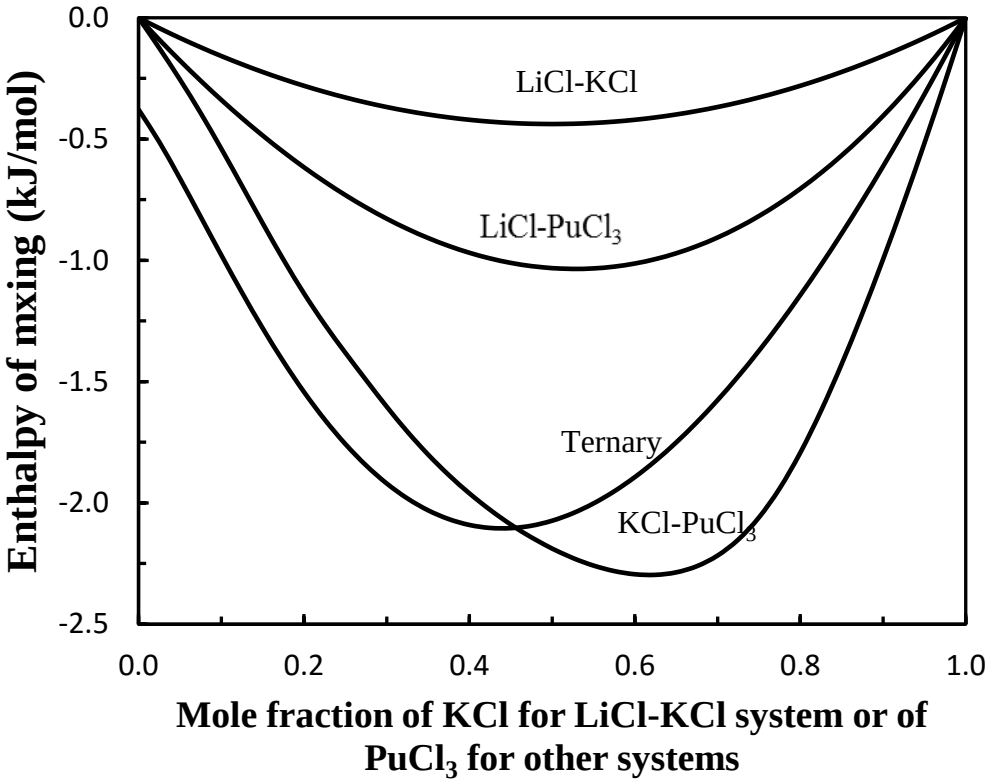

Figure 3.5. Calculated enthalpy of mixing for LiCl-KCl, LiCl-$PuCl_3$, KCl-$PuCl_3$, and LiCl-KCl-$PuCl_3$ ternary system with x(LiCl):x(KCl)=0.586:0.414 at 1200 K

The optimized parameters are shown in Table 3.4. The obtained results for A and B in Eq. 10 indicate that the enthalpy and entropy of formation are -48.16 kJ/mol and 23.92 J/mol/K, respectively, for K_2PuCl_5 crystal and -21.25 kJ/mol and 78.80 J/mol/K for K_3PuCl_6 crystal. Based on the equilibrium information, the apparent potential of $PuCl_3$ ($E^{ap}_{PuCl_3}$ vs Cl_2/Cl^-) in LiCl-KCl eutectic was calculated for an infinite dilute solution and can be compared with the data from the literature reviewed. The reported values in literature and calculated results are plotted in Figure 3.6. The fitted correlations are listed in Table 3.5. As seen from the comparison, the present work is in good agreement with the literature. The maximum difference of 9% should be reasonable when considering the difference of $PuCl_3$ mole fraction in the salt, electrode reference, and electrochemical methods used in experiments [118].

Table 3.4. Optimized parameters for the LiCl-KCl-$PuCl_3$ system

Phase	Parameters
Solid	${}^0L_{Li^+,K^+:Cl^-} = 17467.15$
	${}^0G^s_{K_2PuCl_5} = 2{}^0G^s_{KCl} + {}^0G^s_{PuCl_3} - 48155.48 - 23.92T$
	${}^0G^s_{K_3PuCl_6} = 3{}^0G^s_{KCl} + {}^0G^s_{PuCl_3} - 21250.17 - 78.80T$
Liquid	${}^0L_{Li^+,K^+:Cl^-} = -17523.74$
	${}^0L_{Pu^{3+},Li^+:Cl^-} = -41287.45 + 29.33T$
	${}^1L_{Pu^{3+},Li^+:Cl^-} = 4617.38 - 6.59T$
	${}^0L_{K^+,Pu^{3+}:Cl^-} = -125404.78 + 40.40T$
	${}^1L_{K^+,Pu^{3+}:Cl^-} = -18196.78$
	${}^0L_{K^+:Cl^-,K_3PuCl_6} = -37469.98$
	${}^0L_{Pu^{3+}:Cl^-,K_3PuCl_6} = -107125.88$
	${}^0L_{Li^+,K^+,Pu^{3+}:Cl^-} = -316741.85$
	${}^1L_{Li^+,K^+,Pu^{3+}:Cl^-} = 5046.88$
	${}^2L_{Li^+,K^+,Pu^{3+}:Cl^-} = 61450.10$

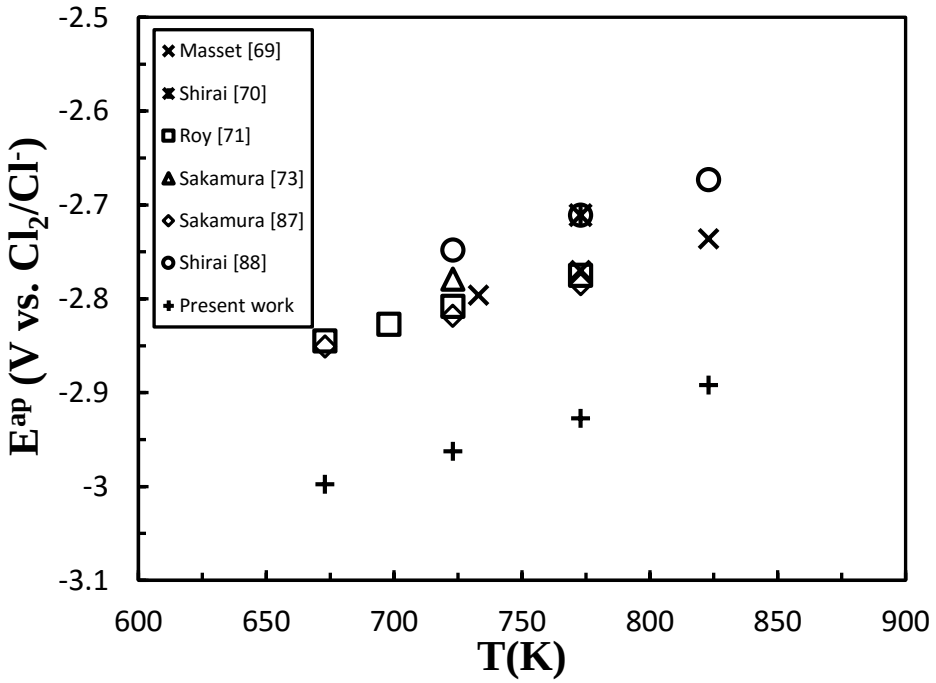

Figure 3.6. Comparison of apparent potential for $PuCl_3$ in LiCl-KCl eutectic

Table 3.5. Comparison of apparent potential for $PuCl_3$ in LiCl-KCl eutectic

Apparent potential (V *vs.* Cl_2/Cl^-)	Temperature (K)	Reference
$E^{ap}_{PuCl_3} = -3.3048 + 6.910\times10^{-4}T$	733-823	[25]
$E^{ap}_{PuCl_3} = -3.2980 + 7.600\times10^{-4}T$	723-823	[26]
$E^{ap}_{PuCl_3} = -3.3187 + 7.044\times10^{-4}T$	673-773	[27]
$E^{ap}_{PuCl_3} = -3.3048 + 6.910\times10^{-4}T$	733-823	[42]
$E^{ap}_{PuCl_3} = -3.2950 + 6.594\times10^{-4}T$	673-773	[43]
$E^{ap}_{PuCl_3} = -3.2904 + 7.500\times10^{-4}T$	723-823	[44]
$E^{ap}_{PuCl_3} = -3.4727 + 7.058\times10^{-4}T$	673-823	Present work

Figure 3.7 is the calculated isothermal section at 773 K, which is the general temperature pyroprocessing operates at. Figure 3.8 shows the calculated liquidus projection. It indicates two eutectics and one quasi-peritectic. One eutectic (E1) involving LiCl, $PuCl_3$, and K_2PuCl_5 occurs at 616 K and another one (E2) involving LiCl, KCl, and K_3PuCl_6 at 589 K. The quasi-peritectic involving K_2PuCl_5, K_3PuCl_6, and LiCl appears at 658 K. There is also a monovariant eutectic involving LiCl and K_2PuCl_5 at 690 K. All these phase reactions have been presented in Table 3.6.

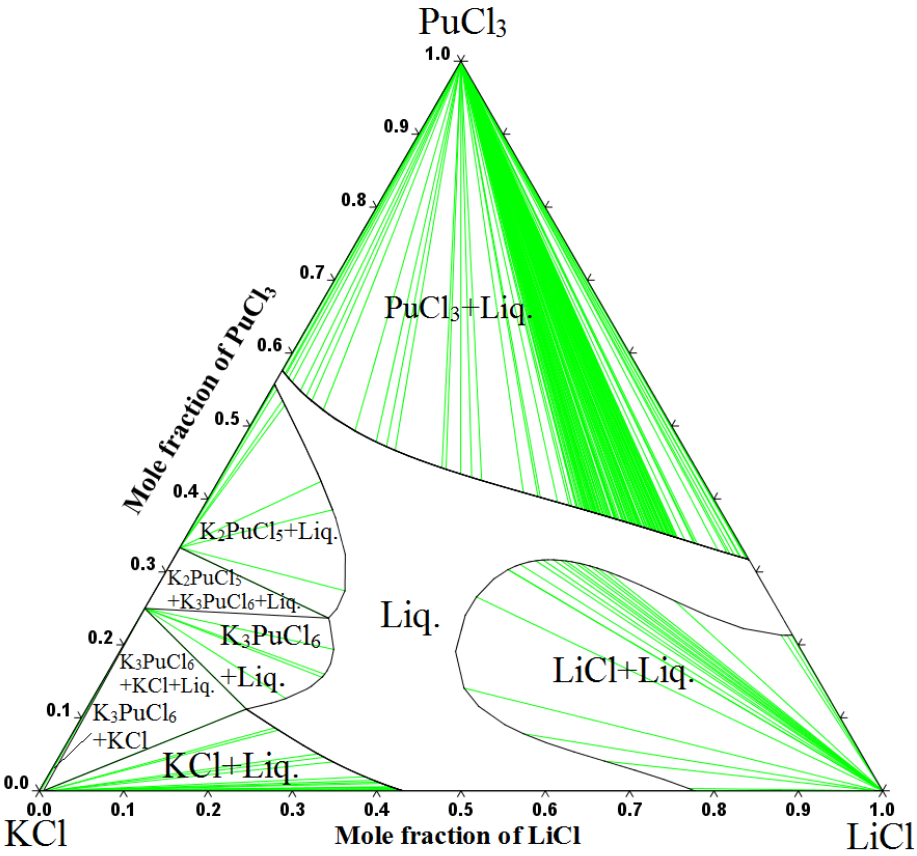

Figure 3.7. Calculated isothermal section of LiCl-KCl-$PuCl_3$ at 773 K

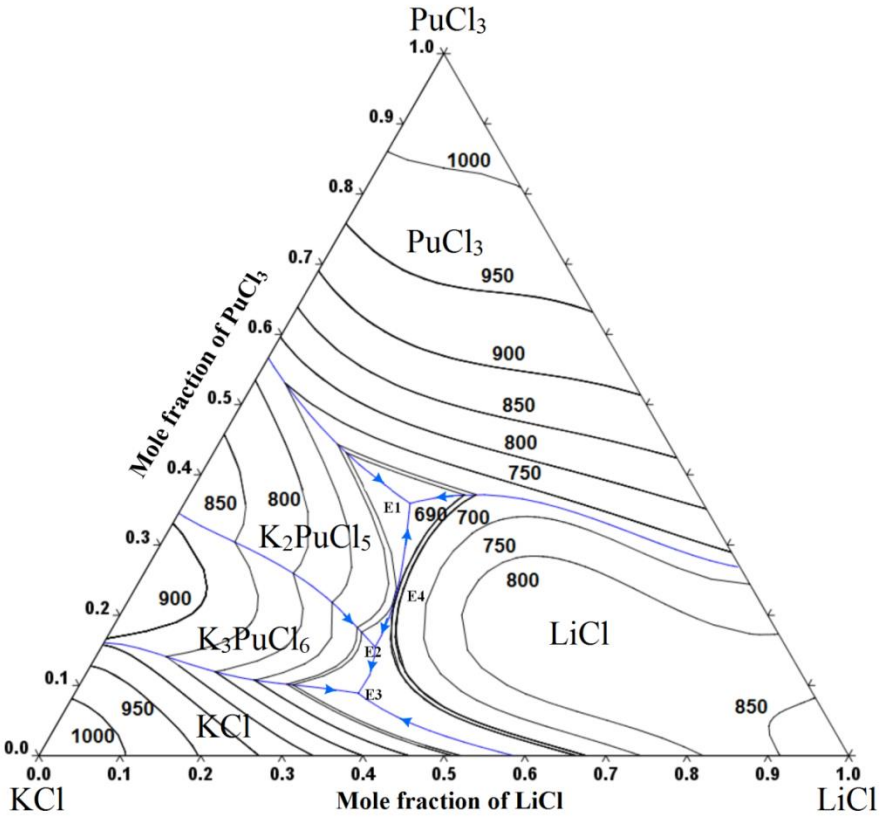

Figure 3.8. Calculated liquidus projection for LiCl-KCl-$PuCl_3$ system

Table 3.6. Phase reactions in LiCl-KCl-$PuCl_3$ system

Phase reaction	Reaction type	Composition of liquid		T/K	Reference
		x_{LiCl}	x_{PuCl_3}		
Binary					
Liquid ⇌ LiCl + KCl	Eutectic	0.586	-	626	This work
		0.585± 0.003	-	628±3	[118, 137-140]
Liquid ⇌ LiCl + $PuCl_3$	Eutectic	-	0.268	731	This work
		-	0.28	734	[142]
Liquid ⇌ KCl + K_3PuCl_6	Eutectic	-	0.161	895	This work
		-	0.17	894	[132]
Liquid ⇌ K_3PuCl_6	Congruent	-	0.250	958	This work
		-	0.250	958	[132]
Liquid + K_3PuCl_6 ⇌ K_2PuCl_5	Peritectic	-	0.350	884	This work
		-	0.35	884	[132]
Liquid ⇌ $PuCl_3$ + K_2PuCl_5	Eutectic	-	0.564	759	This work
		-	0.57	759	[132]

Ternary					
Liquid ⇌ LiCl + KCl + K_3PuCl_6	Eutectic	0.350	0.089	589	This work
Liquid + K_2PuCl_5 ⇌ K_3PuCl_6 + LiCl	Quasi-peritectic	0.338	0.155	658	This work
Liquid ⇌ LiCl + $PuCl_3$ + K_2PuCl_5	Eutectic	0.279	0.359	616	This work
Liquid ⇌ LiCl + K_2PuCl_5	Eutectic	0.324	0.225	690	This work

3.5.3 Solubility and apparent potential

Three temperatures of 723, 773, and 823 K were analyzed in detail. Figure 3.9 shows the calculated liquidus projection under these three temperatures. The dashed line stands for the compositions with $x(\mathrm{LiCl}) : x(\mathrm{KCl}) = 0.586 : 0.414$. The squares represent where the solid first appears and the circles represent where $PuCl_3$ starts to become solid, which should be the limit of solubility of $PuCl_3$ in LiCl-KCl eutectic salt at different temperatures. The mole fractions of $PuCl_3$ at these positions are listed in Table 3.7. Generally, the solubility S_{PuCl_3} in the unit of mole fraction can be expressed by [147]

$$\log S_{PuCl_3} = a + \frac{b}{T} \qquad \text{Eq. 3.17}$$

which was used to fit the calculated data in Table 3.7. Figure 3.10 shows the fitting result, which gives the correlation of

$$\log S_{PuCl_3} = 0.2415 - \frac{478.37}{T} \qquad \text{Eq. 3.18}$$

Figure 3.11 shows the Gibbs energy of formation of $PuCl_3$ in LiCl-KCl eutectic up to 5 mol% at different temperatures. The Gibbs energy change at 4.3 mol% $PuCl_3$ at 723 K is due to the precipitation of LiCl in the liquid. It shows that the Gibbs energy is dependent on the concentration and increases with it, which should be noted but is not well reported in literature.

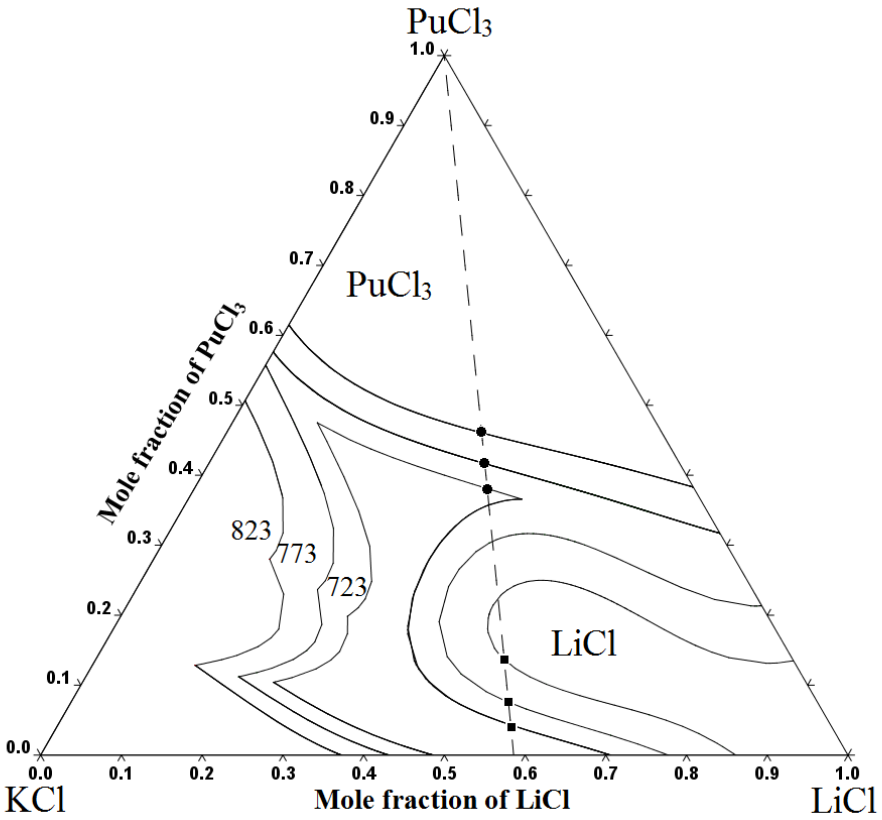

Figure 3.9. Calculated liquidus projection for LiCl-KCl-$PuCl_3$ system at 723, 773, and 823 K

Table 3.7. Mole fraction of $PuCl_3$ at the squares and circles in Figure 3.9

	723 K	773 K	823 K
Squares	0.043	0.076	0.137
Circles	0.382	0.415	0.460

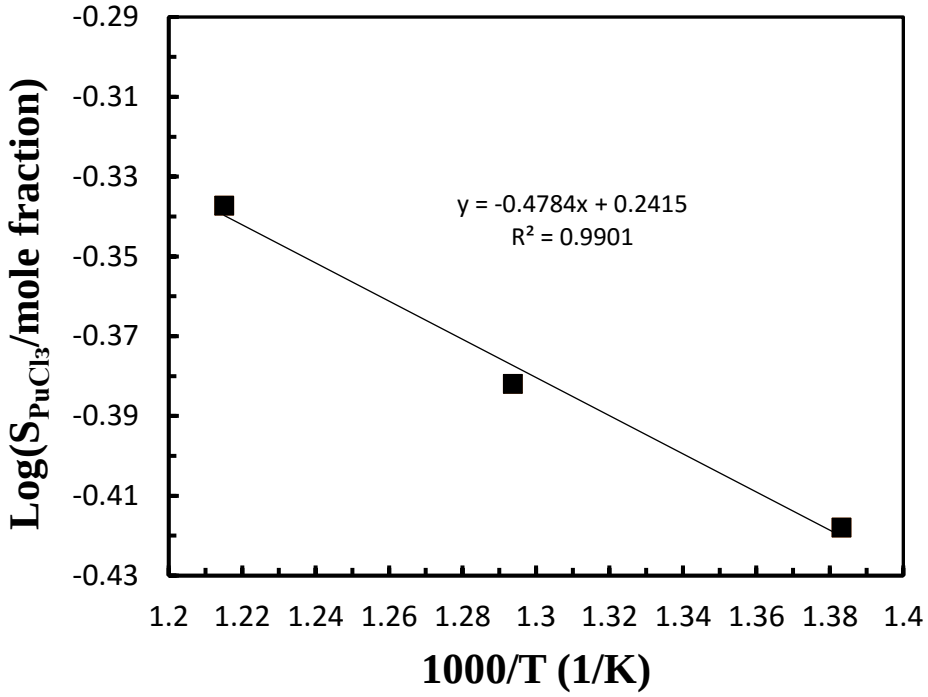

Figure 3.10. Calculated solubility of $PuCl_3$ in LiCl-KCl eutectic and the fitting curve

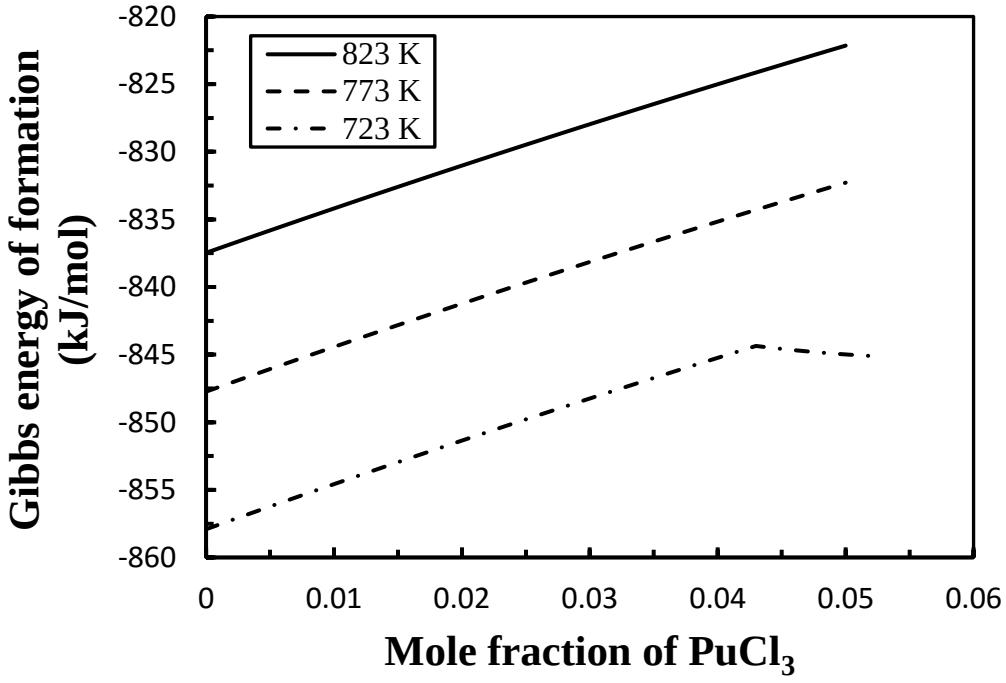

Figure 3.11. Calculated Gibbs energy of formation of $PuCl_3$ in LiCl-KCl eutectic at 723, 773, and 823 K

3.6 Conclusions

Thermodynamic assessment for the LiCl-KCl-$PuCl_3$ ternary system has been carried out by the CALPHAD method using a two-sublattice model. Binary systems of LiCl-KCl, LiCl-$PuCl_3$, and KCl-$PuCl_3$ were primarily evaluated based on available phase information and enthalpy of mixing. The calculated results show good agreement with experimental data. The enthalpy of mixing of LiCl-KCl-$PuCl_3$ was estimated by an empirical correlation for the asymmetric ionic salt system. The estimation combined with the output from binary systems and previous electrochemical studies were used as the input to extrapolate to the ternary system.

The solubility and Gibbs energy of formation of $PuCl_3$ in LiCl-KCl eutectic were obtained from the optimized results. Other interesting thermodynamic properties can be derived from it as well. This study helps to evaluate the salt states and $PuCl_3$ properties during pyroprocessing and will also contribute to the evaluation of other salt systems with more components. Also, the properties of $PuCl_3$ in a full range of compositions may benefit the safeguards of pyroprocessing of detecting the concentration of $PuCl_3$ in the electrorefining batches.

4 Integrated model development and case studies

4.1 Introduction

As was reviewed in Chapter 1, a kinetic model not only has the ability to safeguard the pyroprocessing but also can be used to monitor the separation processing and instruct the operation of pyroprocessing facilities via its output signals, mainly with the potential, current, and species concentration. The potential determines the quality of the deposition on the cathode. When the potential is more negative than the redox potential of an element, the element can be reduced at the cathode. Sudden decrease or increase of the potential at the cathode indicates new elements generated and may serve as a signal of SNM diversion. By adjusting the potential, purity of the deposition can be controlled. Current can be used to measure the quantity of deposition by integrating it with respect to the time. So the deposition amount and throughput can be predicted. Current is also an indicator of material transport and can be used to verify the material distribution obtained by other methods. Species concentration in the molten salt is the direct variable to determine the material balance. Monitoring of it is the most straightforward method to detect any scenario of SNM diversion, thus to safeguard the pyroprocessing facilities. In this Chapter, we focus on developing the kinetic model to predict the material transport in the electrorefiner. The model was validated by existing experimental data and then new cases were run to investigate the separation performance under different conditions to provide the safeguards signature for the pyroprocessing.

4.2 Model construction

Considering a half reaction of reduction involving soluble-soluble transition on the cathode during the electrorefining

$$O^{n+} + ne^{-} = R \qquad \text{Eq. 4.1}$$

The current density is defined by the difference of forward and backward reactions as

$$j = nF(k_f C_O^s - k_b C_R^s) \qquad \text{Eq. 4.2}$$

where k_f and k_b are the forward and backward rate constants, respectively, C_O^s and C_R^s are the surface concentrations of oxidant and reductant on the electrode, respectively. These rate constants can be expressed in terms of the electrode potential

$$k_f = k_0 \exp[-\frac{\alpha nF}{RT}(E - E^f)] \qquad \text{Eq. 4.3}$$

$$k_b = k_0 \exp[\frac{(1-\alpha)nF}{RT}(E - E^f)] \qquad \text{Eq. 4.4}$$

where k_0 is the standard rate constant, α is the transfer coefficient, R is the gas constant, T is the temperature in Kelvin, E is the electrode potential, and E^f is the formal potential, n is the number of electrons involved. Then the Butler-Volmer equation is derived as

$$j = nFk_0\{C_O^s \exp[-\frac{\alpha nF}{RT}(E - E^f)] - C_R^s \exp[\frac{(1-\alpha)nF}{RT}(E - E^f)]\} \qquad \text{Eq. 4.5}$$

When the reaction is at equilibrium the current density should be zero, which gives

$$j_0 = nFk_0 C_O^b \exp[-\frac{\alpha nF}{RT}(E_{eq} - E^f)] = nFk_0 C_R^b \exp[\frac{(1-\alpha)nF}{RT}(E_{eq} - E^f)] \qquad \text{Eq. 4.6}$$

where j_0 is defined as the exchange current and E_{eq} is the equilibrium potential, C_O^b and C_R^b are the bulk concentrations because surface and bulk concentration should be the same at equilibrium. Nernst equation shows

$$E_{eq} = E^f + \frac{RT}{nF}\ln\frac{C_O^b}{C_R^b} \qquad \text{Eq. 4.7}$$

Plugging Eq. 4.7 into Eq. 4.6, one has the exchange current in the form of

$$j_0 = nFk_0 C_O^{b\,(1-\alpha)} C_R^{b\,\alpha} \qquad \text{Eq. 4.8}$$

Introducing Eq. 4.8 to Eq. 4.5, Butler-Volmer equation can be expressed in another manner as

$$j = j_0\{\frac{C_O^s}{C_O^b}\exp[-\frac{\alpha nF}{RT}\eta] - \frac{C_R^s}{C_R^b}\exp[\frac{(1-\alpha)nF}{RT}\eta]\} \qquad \text{Eq. 4.9}$$

where η is the over-potential defined by

$$\eta = E - E_{eq} \qquad \text{Eq. 4.10}$$

Above is the discussion of kinetic process on the electrode surface. For the diffusion process, the current density can be expressed by

$$j = nFK_O(C_O^b - C_O^s) = nFK_R(C_R^s - C_R^b) \qquad \text{Eq. 4.11}$$

where K_O and K_R are the mass transfer coefficients of oxidant and reductant, respectively, which can be determined by the flow conditions. The third term is because the reductant is produced on the electrode surface so its surface concentration is larger than the bulk concentration. Then the limiting currents of diffusions are

$$j_L^c = nFK_O C_O^b \quad \text{Eq. 4.12}$$

and

$$j_L^a = -nFK_R C_R^b \quad \text{Eq. 4.13}$$

j_L^c and j_L^a are the cathodic and anodic limiting currents, respectively. Taking the ratios of Eq. 4.12 and Eq. 4.13 to Eq. 4.11, relations between surface concentration, bulk concentration, and limiting current can be obtained

$$\frac{C_O^s}{C_O^b} = 1 - \frac{j}{j_L^c} \quad \text{Eq. 4.14}$$

$$\frac{C_R^s}{C_R^b} = 1 - \frac{j}{j_L^a} \quad \text{Eq. 4.15}$$

Combining Eq. 4.14, Eq. 4.15, and Eq. 4.9, the Butler-Volmer equation coupled with mass transfer is written as

$$j = \frac{j_0\{\exp[-(\alpha nF/RT)\eta] - \exp[(1-\alpha)(nF/RT)\eta]\}}{1 + \frac{j_0}{j_L^c}\exp[-(\alpha nF/RT)\eta] - \frac{j_0}{j_L^a}\exp[(1-\alpha)(nF/RT)\eta]} \quad \text{Eq. 4.16}$$

It is shown that when η is extremely negative, j will approach j_L^c. And when η is extremely positive, j will approach j_L^a.

4.2.1 Solid cathode

For the solid cathode, the reductant exists as the metal. Basically, there is no diffusion for the reductant, for example U metal. And its concentration is set to unity. Therefore, at the solid anode and molten salt interface, one has

$$j = nFK_O^{ms,c}(C_O^{b,ms} - C_O^{s,ms}) \quad \text{Eq. 4.17}$$

$$j_L^c = nFK_O^{ms,c} C_O^{b,ms} \quad \text{Eq. 4.18}$$

$$\frac{C_O^s}{C_O^b} = 1 - \frac{j}{j_L^c} \quad \text{Eq. 4.19}$$

Combining them with the Eq. 4.9, the following equation could arrive

$$j = \frac{j_0^s\{\exp[-(3\alpha F/RT)\eta] - \exp[(1-\alpha)(3F/RT)\eta]\}}{1 + \frac{j_0^s}{j_L^c}\exp[-(3\alpha F/RT)\eta]} \quad \text{Eq. 4.20}$$

The equilibrium potential now is

$$E^{eq} = E^{0} + \frac{RT}{nF} \ln \gamma^{ms} X^{ms} \qquad \text{Eq. 4.21}$$

4.2.2 Solid anode

The situation differs in solid spent fuel anode. Previous studies about the dissolution behavior of U-Pu-Zr found that a dense salt layer consisting of Zr powder and salt exists around the dissolved fuel [148,149,150]. Before dissolving into the electrolyte, oxidized Pu and U ions need to pass through this layer, which is a fibrous or cottonlike microstructure [149]. Therefore, another diffusion layer of porous Zr was considered for the dissolution of U-Pu-Zr alloys. The model is shown in Figure 4.1. Steady state was assumed considering the long time needed for the electrorefining.

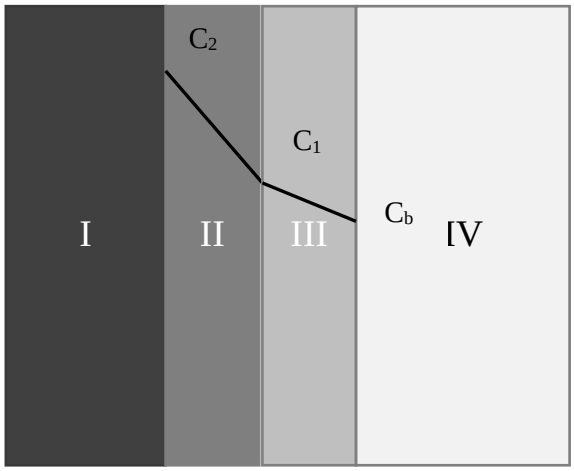

Figure 4.1. Diffusion model in U-Pu-Zr anode. I is the undissolved alloy, II is the porous Zr, III is the diffusion layer on the molten salt side, IV is the molten salt electrolyte.

Therefore, Eq. 4.22 was established for each actinide.

$$nFD_{porous\_Zr} \frac{(C_2 - C_1)}{L_{porous\_Zr}} = nFK_O^{ms,a}(C_1 - C_b) = j \qquad \text{Eq. 4.22}$$

where L_{porous_Zr} is the thickness of porous Zr layer and $K_O^{ms,a}$ is the mass transfer coefficient in molten salt.

Even though the redox potentials of other actinides and active fission products are much lower than U, it is assumed that they would not be oxidized until the surrounding U has dissolved considering U is the major component of used fuel and other elements are embedded inside. They would not be contacting with the molten salt sufficiently to react before the dissolution of U. Basically, these active elements were assumed to be co-dissolved with U with a current related to the current of U.

$$i_{Ac} = \frac{n_{AE} x_{AE}}{n_U x_U} i_U \qquad \text{Eq. 4.23}$$

The subscript AE represents the active metals. In the alloy, initially, only active metals dissolve to support the current. The radius of the undissolved alloy decreases while porous Zr increases. When the surface concentrations of the metal ions exceed their solubility limits in molten salt, as shown by Eq. 4.24, Zr from outside of the porous Zr layer starts to dissolve to compensate for the current. The thickness of the layer then decreases correspondingly.

$$C_2 > C_k^{slb} \qquad \text{Eq. 4.24}$$

where C_k^{slb} is the solubility of element *k* in mol/cm^3. There was no diffusion in porous Zr layer for Zr ions since it was assumed that Zr only dissolves from the most outside. The thickness change of porous Zr layer during the dissolution can be derived from Eq. 4.25 and Eq. 4.26

$$\begin{aligned} \frac{[\pi R_a^2 H - \pi(R_a - \Delta l_{alloy})^2 (H_a - \Delta l_{alloy})]\rho_a W_U}{100} &= N_{dis}^U m_U \\ \frac{[\pi R_a^2 H - \pi(R_a - \Delta l_{p\_Zr})^2 (H_a - \Delta l_{p\_Zr})]\rho_a W_{Zr}}{100} &= N_{dis}^{Zr} m_{Zr} \end{aligned} \qquad \text{Eq. 4.25}$$

where R_a and H_a are the initial radius and length of the alloy, respectively. Δl_{alloy} and Δl_{porous_Zr} are the thickness decreased due to the dissolution of U and Zr, respectively. *W* represents the weight percent of each element in the alloy, N_{dis} is the total mole number of elements dissolved into the electrolyte, and *m* is the molar weight of elements. Then the thickness of porous Zr layer is

$$L_{porous\_Zr} = \Delta l_{alloy} - \Delta l_{porous\_Zr} \qquad \text{Eq. 4.26}$$

The Butler-Volmer equation is still written as

$$j = \frac{j_0^s \{\exp[-(3\alpha F / RT)\eta] - \exp[(1-\alpha)(3F / RT)\eta]\}}{1 + \frac{j_0^s}{j_L^c} \exp[-(3\alpha F / RT)\eta]} \qquad \text{Eq. 4.27}$$

But the current is controlled by both Eq. 4.22 and Eq. 4.27.

4.2.3 Liquid cadmium electrode

Liquid cadmium is used sometimes for the intention to co-deposit all the actinides. The high activity coefficient of uranium and low activity coefficients of other actinides in cadmium make their formal potential very close [27]. It is hard for one actinide element to be decontaminated from others because they are reduced basically simultaneously. When Pu and other minor actinides are accumulated in molten salt to some designated criteria with the deposition of U, the solid electrode is switched to a liquid one to deposit out remaining actinides. That is why some researchers claim that pyroprocessing has the intrinsic barriers for proliferation [151,152]. Actually, small amounts

of lanthanide fission products are also collected in liquid cadmium, which actually benefits to the safeguards because of its high radioactivity [153]. Taking the cathode cadmium as an example, when the reduced metals are dissolving into the cadmium, one has two diffusion processes. One is at the molten salt side and another at the cadmium side.

$$j = nFK_O^{ms}(C_O^{b,ms} - C_O^{s,ms}) = nFK_R^{Cd}(C_R^{s,Cd} - C_R^{b,Cd}) \quad \text{Eq. 4.28}$$

$$j_L^c = nFK_O^{ms}C_O^{b,ms} \quad \text{Eq. 4.29}$$

and

$$j_L^a = -nFK_R^{Cd}C_R^{b,Cd} \quad \text{Eq. 4.30}$$

Combining these equations to the Butler-Equation, one now has

$$j = \frac{j_0^{Cd}\{\exp[-(3\alpha F/RT)\eta] - \exp[(1-\alpha)(3F/RT)\eta]\}}{1 - \frac{j_0^{Cd}}{j_L^c}\exp[-(3\alpha F/RT)\eta] + \frac{j_0^{Cd}}{j_L^a}\exp[-(3\alpha F/RT)\eta]} \quad \text{Eq. 4.31}$$

The sign change at the denominators of Eq. 4.31 is because that the oxidant is produced at the anode and its surface concentration should be larger than the bulk concentration. And the reductant needs to diffuse from bulk liquid cadmium to the surface so its bulk concentration should be larger than the surface concentration. The equilibrium potentials at the anode are

$$E^{Cd,eq} = E^0 + \frac{RT}{nF}\ln\frac{\gamma^{ms}X^{ms}}{\gamma^{Cd}X^{Cd}} \quad \text{Eq. 4.32}$$

In the cadmium, the solubility of metals has to be considered, for example, when the concentration of Pu exceeds its solubility, $PuCd_6$ is formed and precipitates at the bottom. When metals reach their solubility and form $AECd_z$, in a time step of Δt, Eq. 4.33 should be satisfied, which can be rearranged as Eq. 4.34

$$\sum_k z_k[V(t-\Delta t)S_k - V(t)S_k + \frac{i_k\Delta t}{n_kF}]m_{cd}/\rho_{cd} = V(t-\Delta t) - V(t) \quad \text{Eq. 4.33}$$

$$\frac{dV_{Cd}}{dt} = \frac{V(t)-V(t-\Delta t)}{\Delta t} = \frac{m_{Cd}\sum_k \frac{i_k z_k}{n_k F}}{m_{Cd}\sum_k C_k^{slb}z_k - \rho_{Cd}} \quad \text{Eq. 4.34}$$

where m_{Cd} is the molar weight of Cd, ρ_{Cd} is the density of Cd. Then the distribution of species in anode, electrolyte, and cathode is derived numerically as

$$N_k^a(t+\Delta t) = N_k^a(t) - \frac{j_k^a\Delta t A_a}{n_kF} \quad \text{Eq. 4.35}$$

$$N_k^{ms}(t+\Delta t) = N_k^{ms}(t) - \frac{(j_k^cA_c - j_k^aA_a)\Delta t}{n_kF} \quad \text{Eq. 4.36}$$

$$N_k^c(t+\Delta t) = N_k^c(t) + \frac{j_k^c\Delta t A_c}{n_kF} \quad \text{Eq. 4.37}$$

4.3 Parameters identification

For the model validations, only three elements Zr (IV), U(III), and Pu(III), were involved. But for the application of the model, totally 7 species were studied, such as Zr(IV), U(III), Pu(III), Am(II), Gd(III), Ce(III), and La(III). The potential of Zr is the between U and other noble metals. All the noble metals will be retained in the anode if the dissolution of Zr is avoided. Am is the actinide whose potential is next to the lanthanide species and Gd is the lanthanide whose potential is closest to the actinides [154]. Therefore, the separation performance of Zr, Am, and Gd can represent how the noble metals, actinides, and lanthanides are separated from each other. U and Pu are the actinides mostly concerned for the safeguards and Ce and La represent other lanthanides. Basically, all parameters for these 7 elements needed to be collected.

4.3.1 Density of LiCl-KCl molten salt and liquid cadmium

Several kinds of molten salt electrolytes have been considered for the electrorefining, including LiCl-KCl (42 mol % KCl), NaCl-KCl (50 mol % KCl), BeF_2-LiF (67 mol % LiF), and CaF_2-LiF (77 mol % LiF) [155], but generally LiCl-KCl is recognized as the best candidate due to its lower eutectic melting temperature [155]. Cd is commonly used as the liquid electrode. Based on the work from Janz [156], the density of LiCl-KCl was reached in the form of

$$\rho_{ms}[g/cm^3] = 1.9397 - 4.9422\times10^{-4}T \qquad \text{Eq. 4.38}$$

Zhang [20] reported the density of Cd as

$$\rho_{Cd}[g/cm^3] = 8.7504 - 1.251\times10^{-3}T \qquad \text{Eq. 4.39}$$

4.3.2 Diffusion coefficient in molten salt

As the diffusion coefficient significantly affects the material transport when multiple literature sources are found for an element the correlation compiled by Zhang [105], based on previous studies, was used to obtain an "average value". As was reviewed in Chapter 1, diffusion coefficient was widely studied for the U and Pu. Calculated result of 1.02×10^{-5} cm^2/s at 773 K for the UCl_3 was applied in the model. By averaging literature data, Zhang [105] obtained the correlation for Pu, Gd, La as

$$D_{Pu}^{ms} = 1.66322\times10^{-3}\exp(-\frac{32128.8}{RT}),\quad 650-873\,\mathrm{K} \qquad \text{Eq. 4.40}$$

$$D_{Gd}^{ms} = 1.1812\times10^{-3}\exp(-\frac{32485}{RT}),\quad 673-873\,\mathrm{K} \qquad \text{Eq. 4.41}$$

$$D_{La}^{ms} = 2.16\times10^{-3}\exp(-\frac{30010}{RT}),\quad 653-863\,\mathrm{K} \qquad \text{Eq. 4.42}$$

Diffusion coefficients of Zr, Am, and Ce were reported by Yamada et al. [157], Serp et al. [158], and Marsden et al [159], respectively.

$$D_{Zr}^{ms} = 3.58\times10^{-3}\exp(-\frac{37000}{RT}),\quad 723-873\,\mathrm{K} \qquad \text{Eq. 4.43}$$

$$D_{Am}^{ms} = 1.7211\times10^{-2}\exp(-\frac{44747.6}{RT}),\quad 733-823\,\mathrm{K} \qquad \text{Eq. 4.44}$$

$$D_{Ce}^{ms} = 3.965\times10^{-3}\exp(-\frac{35791.8}{RT}),\quad 673-973\,\mathrm{K} \qquad \text{Eq. 4.45}$$

4.3.3 Diffusion coefficients in porous Zr layer

For a species in same solution, diffusion coefficient in porous media is a function of that in open space solution as

$$D_{porous} = \frac{\theta\phi}{\tau} D_{open} \qquad \text{Eq. 4.46}$$

where θ is the constrictivity factor, φ is the effective transport-through porosity, τ is the tortuosity factor. In our model, we set that

$$D_{porous} = k_d D_{ms} \qquad \text{Eq. 4.47}$$

It is reasonable considering these parameters above are unknown to us

4.3.4 Diffusion coefficient in liquid cadmium

Zhang et al. [160] reported the diffusion coefficient of U in Cd in the form of

$$D_{U}^{Cd} = 2.160\times10^{-4}\exp(-\frac{17100}{RT}) \qquad \text{Eq. 4.48}$$

Diffusion coefficient of Pu was evaluated by Murakami et al. [161]

$$D_{Pu}^{Cd} = 1.67\times10^{-4}\exp(-\frac{19122}{RT}),\quad 723-823\,\mathrm{K} \qquad \text{Eq. 4.49}$$

Murakami et al. [162] measured the diffusion coefficients of Gd and La

$$D_{Gd}^{Cd} = 3.739\times10^{-5}\exp(-\frac{14703}{RT}),\quad 723-823\,\mathrm{K} \qquad \text{Eq. 4.50}$$

$$D_{La}^{Cd} = 2.23\times10^{-4}\exp(-\frac{28712}{RT}),\quad 723-823\,\mathrm{K} \qquad \text{Eq. 4.51}$$

No values of diffusion coefficients were found for Zr, Am, or Ce. Values of Zr and Am were taken as the same with U in the calculation. Ce was assumed to have the same values as Gd.

4.3.5 Apparent potential in LiCl-KCl molten salt

The apparent potentials of U and Pu were taken from the present calculation. They are changing with the concentration. The potential of other elements were treated as constant considering the scarcity of data and low concentration in the electrolyte. The potential of Am was taken from results by Serp et al. [158]. They gave the correlation as

$$E_{Am}(vs.\,Cl_2/Cl^-) = -3.2331 + 4.4048\times10^{-4}T,\ \ 722-823\ \mathrm{K} \qquad \text{Eq. 4.52}$$

Caravaca et al. [163] reported the apparent potential of Gd in LiCl-KCl molten salt to be

$$E_{Gd}(vs.\,Cl_2/Cl^-) = -3.5204 + 6.7023\times10^{-4}T,\ \ 723-873\ \mathrm{K} \qquad \text{Eq. 4.53}$$

Based previous sources, Zhang [105] obtained the correlation of

$$E_{La}(vs.\,Cl_2/Cl^-) = -3.575 + 6.064\times10^{-4}T,\ \ 650-870\ \mathrm{K} \qquad \text{Eq. 4.54}$$

Marsden et al. [159] measured the apparent potential of Ce as

$$E_{Ce}(vs.\,Cl_2/Cl^-) = -3.5338 + 5.923\times10^{-4}T,\ \ 673-973\ \mathrm{K} \qquad \text{Eq. 4.55}$$

Very few studies were reported about the apparent potential of Zr(IV). Only four values at 773 K were found from the references [68,149,154], namely -2.08, -2.20 V vs. Cl_2/Cl^- and -0.838, -0.85 V vs. 1wt% Ag/AgCl. The average value was used in the calculation.

4.3.6 Exchange current in on solid and liquid electrode

For liquid electrode, exchange current has the expression of

$$j_0 = nFk_0C_O^{b\ (1-\alpha)}C_R^{b\ \alpha} \qquad \text{Eq. 4.56}$$

For solid electrode

$$j_0 = nFk_0C_O^{b\ (1-\alpha)} \qquad \text{Eq. 4.57}$$

In the calculation, all the electron transfer coefficients, α, were assumed as 0.5. Thus the only unknown parameter is k_0, which is different for different electrodes and species. After being validated by one literature result, k_0 of U, Pu, Zr on solid and liquid electrodes were obtained. All other k_0 was derived by setting them as the same with U

4.3.7 Mass transfer coefficient in molten salt and liquid cadmium

The mass transfer coefficient determines the limiting current one species can support. Generally, the electrolyte and liquid electrode will be stirred, and the solid electrode will be rotated to strengthen the mass transfer rate in the experiments. The most common relation used for cylinder electrode is the Eisenburg equation [164]

$$K = 0.0791U^{0.7}d^{-0.3}v^{-0.344}D^{0.644} \qquad \text{Eq. 4.58}$$

where U is the flow velocity ($U=\pi dw$), d is the electrode diameter, v is the kinematic viscosity of the molten salt ($v=\mu/\rho$), μ is the dynamic viscosity. It can be concluded that for the same flow conditions and electrode, mass transfer coefficient of a species is proportional to $D^{0.644}$. Previous models setting the same Nernst diffusion layers for all the species seems to be unreasonable [62,149]. Because

$$K = \frac{D}{\delta} \qquad \text{Eq. 4.59}$$

where δ is the Nernst diffusion layer. The same Nernst diffusion layer indicates the mass transfer coefficient is proportional to D. Even though previous studies showed that the solute concentration effected the dynamic viscosity of molten salt [103], here we only considered it to be a function of temperature due to lack of the data. Zhang [147] reported the correlations for the dynamic viscosity of LiCl-KCl and Cd as

$$\mu_{ms}[g/(cm\cdot s)] = 8.61\times10^{-4}\exp(\frac{20926.3}{RT}) \quad \text{Eq. 4.60}$$

$$\mu_{Cd}[g/(cm\cdot s)] = 0.003\exp(\frac{10900}{RT}) \quad \text{Eq. 4.61}$$

For the application of the model to seven species, the mass transfer coefficient of other species was derived from that of uranium via below equation [164], which was applied to both molten salt and Cd.

$$K_i = (\frac{D_i}{D_U})^{0.644} K_U \quad \text{Eq. 4.62}$$

Once given the flow conditions, mass transfer coefficient for every species can be calculated accurately.

4.3.8 Solubility in eutectic LiCl-KCl molten salt

The solubility of species and mass transfer coefficient together determine the maximum transport rate of a species. Here only the solubility of U, Pu, and Zr were considered because concentrations of other species in electrolyte were very low, they can rarely reach their solubility. Solubility can be derived from the phase diagrams. Thermodynamic assessment of LiCl-KCl-UCl_3 system has been reported previously [118]. According to the optimized results, the liquidus projections of the system at 773, 823, and 873 K are plotted in Figure 4.2. The red line indicates the eutectic LiCl-KCl composition (mol% LiCl: mol% KCl=0.586:0.414). The black dots stand for the composition where UCl_3 starts to be precipitated and represent UCl_3 solubility limits at different temperatures. Table 4.1 lists the mole fractions of UCl_3 at these points. Generally, solubility in mole fraction can be correlated with the temperature as [165]

$$log(S_{UCl_3}) = A + \frac{B}{T} \quad \text{Eq. 4.63}$$

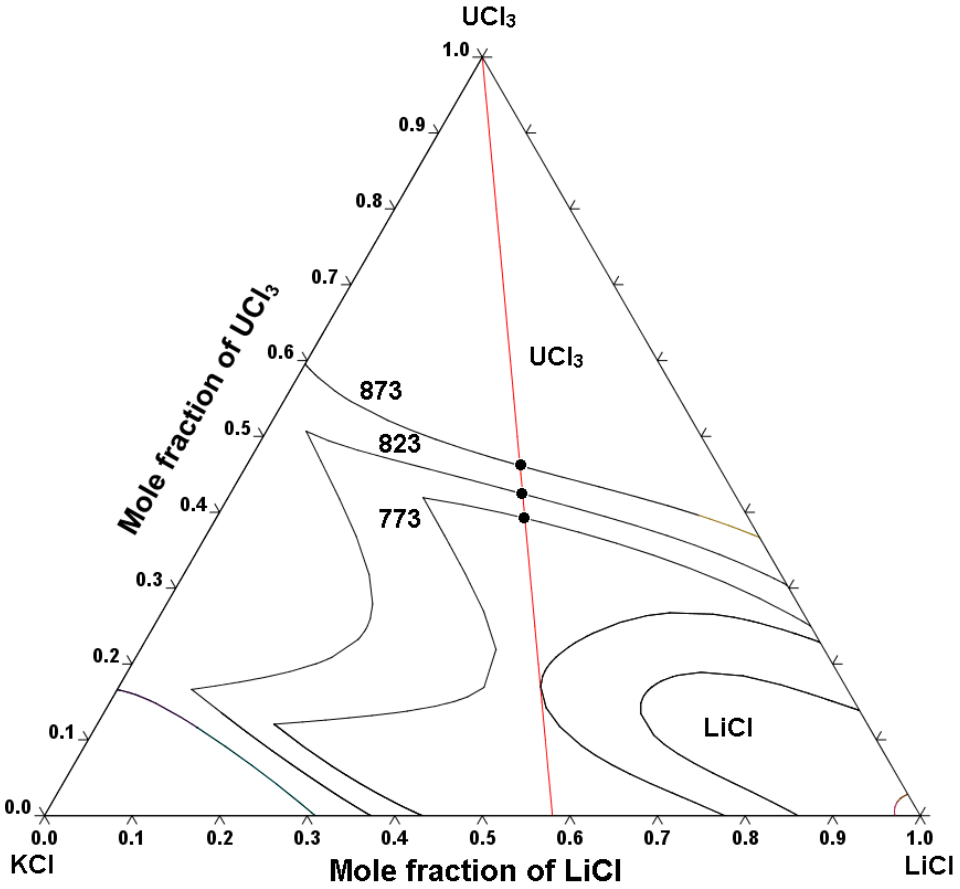

Figure 4.2. Liquidus projection of LiCl-KCl-UCl_3 system with temperatures of 773, 823, 873 K [118]

Table 4.1. UCl_3 solubility at different temperatures

Temperature (K)	773	823	873
Mole fraction	0.394	0.427	0.462

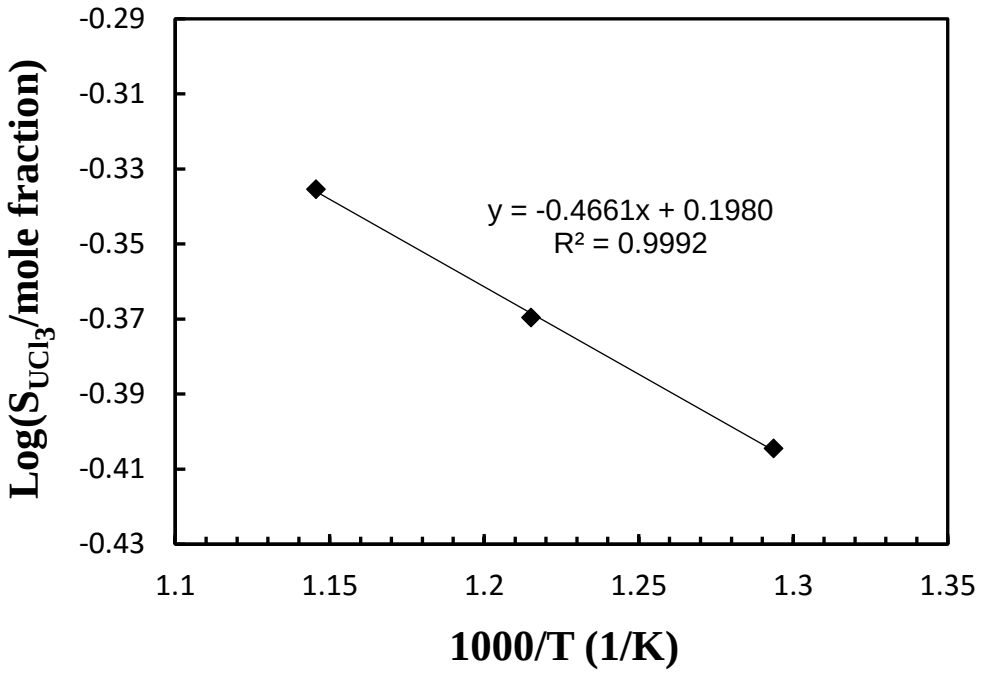

Figure 4.3. Correlation before solubility and temperature

Figure 4.3 shows that solubility of UCl_3 in LiCl-KCl-UCl_3 can be expressed by

$$log(S_{UCl_3}) = 0.1980 - \frac{466.14}{T} \qquad \text{Eq. 4.64}$$

The solubility of $PuCl_3$ in LiCl-KCl has been calculated from the phase diagram assessment in chapter 2, which gives

$$log(S_{PuCl_3}) = 0.2415 - \frac{478.37}{T} \qquad \text{Eq. 4.65}$$

LiCl-KCl-$ZrCl_4$ phase diagram has not been assessed but its solubility was reported to be 0.013 in mole fraction at 773 K [166].

4.3.9 Activity coefficient, solubility, compounds formed in Cd

According to Eq. 4.32, activity coefficients of elements in liquid Cd have to be obtained in order to calculate their formal potentials. Murakami et al. [167] measured the activity coefficient of Zr in Cd from 723 to 784 K and reported a value of 0.51 at 773 K. Activity coefficients of other elements were compiled by Zhang [160]. When an element reaches its solubility, its concentration will keep constant and other elements' concentration may increase if they are not saturated due to the decrease of Cd to form the compounds. The activity coefficients, solubility, and compounds formed of these elements concerned in present study are listed is Table 4.2

Table 4.2. Activity coefficients, solubility, and the compounds formed when elements reach their solubility at 773 K [160]

Element	Activity coefficient	Solubility (at%)	Compound
Zr [167]	0.51	0.24 wt% (0.296 at%)	Cd_2Zr ($ZrCd_2$)
U	89	1.11	U (UCd_0)
Pu	2.34×10^{-4}	1.86	$PuCd_6$
Am	8.00×10^{-5}	0.029	$AmCd_6$
Gd	4.40×10^{-7}	1.38	$GdCd_6$
Ce	9.19×10^{-9}	0.60	$CeCd_{11}$
La	3.36×10^{-9}	0.322	$LaCd_{11}$

4.3.10 Activity of U in porous Zr

The previous studies of the dissolution of U-Zr alloy reported that a small amount of U remained in the porous Zr even after electrorefining of about two days [168]. Therefore, the activity of U was approximated to compensate for the effects. An approximation of exponential decrease from previous diffusion model [149] was selected to describe the activity. Actually, the remaining U in porous Zr layer was not simulated. The activity approximation was more like a virtual compensation to reflect the experimental phenomenon.

$$a[U] = f + e^{-gL_{porous\_Zr}} \qquad \text{Eq. 4.66}$$

where *f* and *g* are the parameters. The activity coefficient of Zr is taken a one.
All the simulations were running at the temperature of 773 K. All these parameters used in the simulation are summarized in Table 4.3.

Table 4.3. Parameters used in the simulation

Molten salt and Cd							
Parameter		Eutectic LiCl-KCl				Liquid Cd	
ρ (g/cm^3)		1.5575				7.4446	
μ (g/(cm·s))		0.0223				0.0164	
Elements in salt and Cd							
	Zr	U	Pu	Am	Gd	Ce	La
D_{ms} ×10^6(cm^2/s)	11.31	10.2	11.22	16.29	7.54	15.12	20.25
D_{Cd} ×10^6(cm^2/s)	15.1	15.1	8.52	15.1	3.79	3.79	2.56
E_{ms}^{ap} (V vs. Ag/AgCl)	-0.88	*	*	-1.6585	-1.7681	-1.8418	-1.8720
Solubility in molten salt (mol%)	0.013	39.4	41.5	-	-	-	-

Solubility in Cd (mol%)	0.296	1.11	1.86	0.029	1.38	0.60	0.322
γ in Cd	0.51	89	2.34×10^{-4}	8.00×10^{-5}	4.40×10^{-7}	9.19×10^{-9}	3.36×10^{-9}

* Data used in from present calculation, they vary with concentration

4.4 Model validation

Because of scarce amount of data for the experiments from liquid cadmium anode to liquid cadmium cathode, the model was only validated in three cases, including liquid cadmium anode to solid cathode, solid anode to liquid cadmium cathode, and solid anode to solid cathode.

4.4.1 Liquid anode to solid cathode

Transport of the liquid anode to solid cathode was validated by the experiments carried out by Tomczuk [169] in ANL to study the behaviors of U and Pu. Table 4.4 lists the conditions for the experiments

Table 4.4. Conditions for the experiments [169]

Parameters		Parameters	
T (K)	773	Current (A)	1.5
Molten salt volume (cm^3)	1868	Molten salt weight (g)	3023
Cadmium volume (cm^3)	2049	Cadmium wight (g)	16500
Initial U in molten salt (wt%)	1.61	Initial U in Cd (wt%)	1.01
Initial Pu in molten salt (wt%)	1.82	Initial Pu in Cd (wt%)	0.59
Anode area (cm^2)	83.4	Cathode area (cm^2)	181.5

This experiment is the only one found in the literature to have potential change as well as the composition changes in anode, electrolyte, and cathode with time. The rate constants of U and Pu on the solid and liquid electrodes were fitted and used in the remaining simulation. For a parameter vector

$$\mathbf{p} = [p_1, p_2, p_3, ..., p_n] \qquad \text{Eq. 4.67}$$

Then the squared residuals could be expressed in terms of this vector

$$S(\mathbf{p}) = \sum_{i=1}^{l} [sim_i(\mathbf{p}) - \exp_i]^2 \qquad \text{Eq. 4.68}$$

where l is the number of the experimental data points. The nonlinear least squares algorithm of Trust Region [170] was used to search the n-dimensional parameter space to find the optimum values that minimized the squared residuals. Figure 4.4 to Figure 4.7 shows the comparison of simulation results with experimental data. The results show the model predicts the material

distribution in electrorefining cell very well. The small mismatch can be due to current applied since in the experiment, the author just mentioned the applied current is 1-2 A but did not present the exact current pattern. In the molten salt, weight percent of U decreased because only U gradually deposited on the solid cathode initially. The increase of Pu in molten salt was due to the supplement from the anode. Because of their close redox potentials, basically U and Pu were oxidized at the same time from liquid cadmium anode, which explains their decreases in the anode. Figure 4.6 shows that Pu would not deposit until 48 hours, which is corresponding to the step increase of the cell potential.

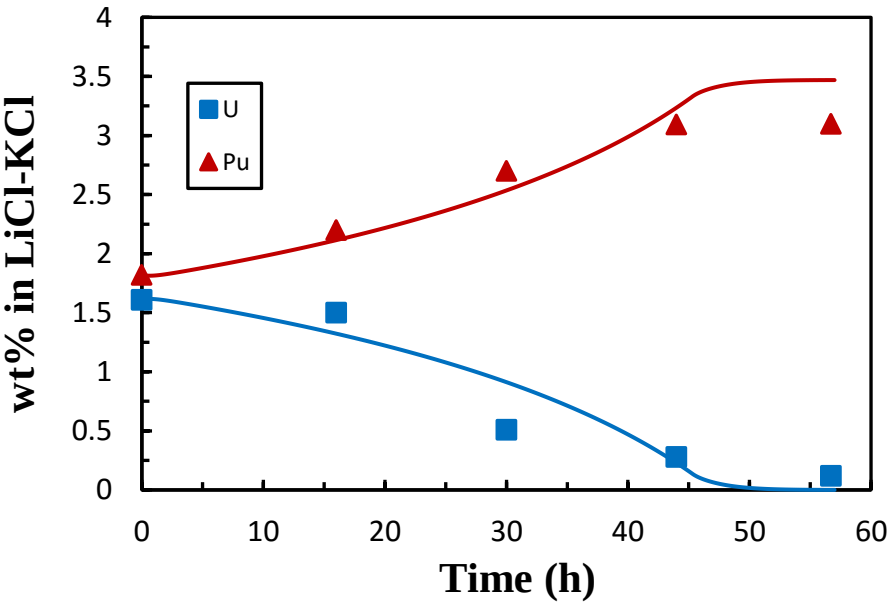

Figure 4.4. Weight percent of U and Pu in LiCl-KCl molten salt electrolyte

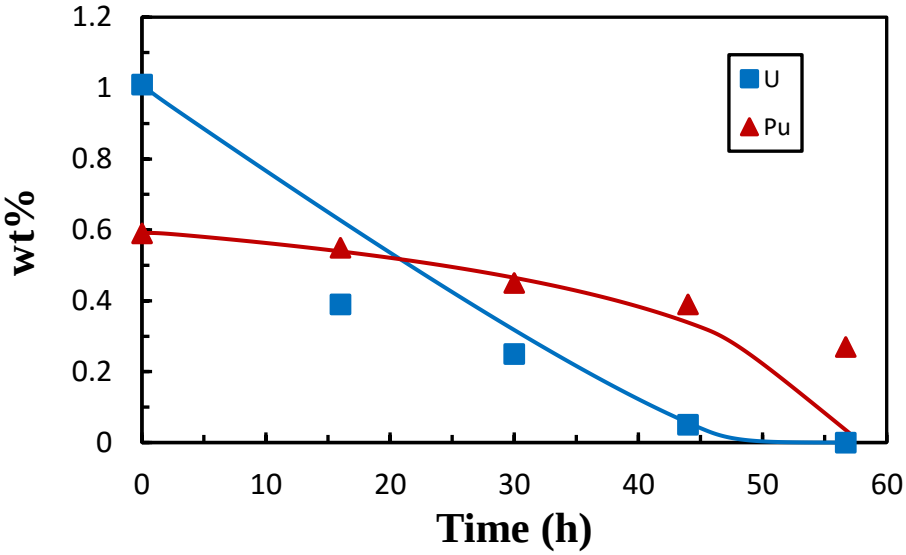

Figure 4.5. Weight percent of U and Pu in liquid cadmium cathode

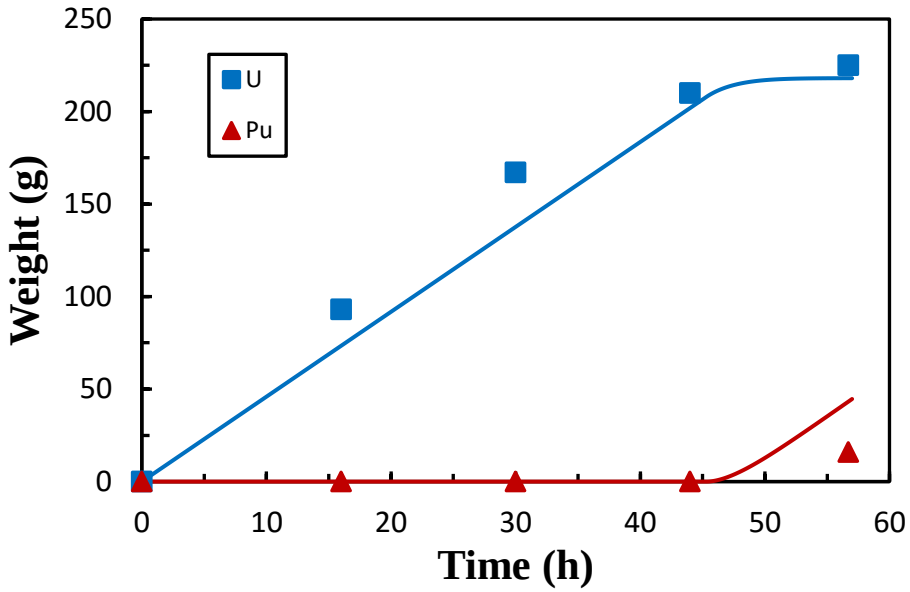

Figure 4.6. Amount of U and Pu deposited on the solid cathode

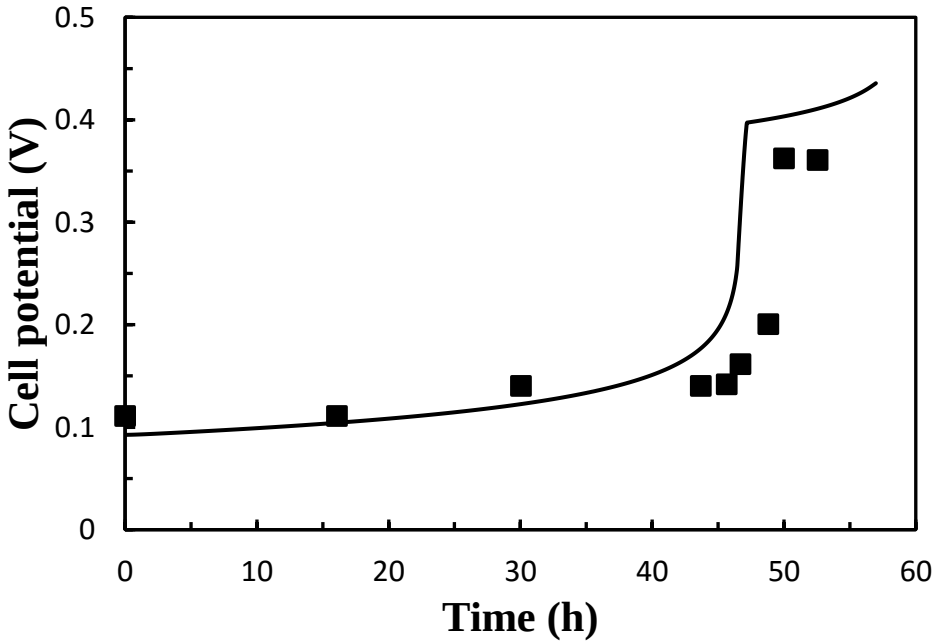

Figure 4.7. Cell potential of the electrorefining cell

Table 4.5. Fitting results for rate constants and mass transfer coefficients

$k^{s}_{0,U}$ (cm/s)	$k^{s}_{0,Pu}$ (cm/s)	$k^{l}_{0,U}$ (cm/s)	$k^{l}_{0,Pu}$ (cm/s)
1.31e-5	1.67e-6	2.40e-3	1.09e-2

$K_{0,U}^{ms}$ (cm/s)	$K_{0,Pu}^{ms}$ (cm/s)	$K_{0,U}^{Cd}$ (cm/s)	$K_{0,Pu}^{Cd}$ (cm/s)
7.0e-3	5.4e-3	5.03e-3	5.03e-3

Table 4.5 shows the fitting results of the rate constants of U and Pu on solid and liquid electrodes as well as the mass transfer coefficients in molten salt and liquid cadmium. Then according to the Eq. 4.8, Exchange currents of U and Pu at solid and liquid cadmium electrode can be evaluated. Figure 4.8 shows the comparison of the exchange current of U on the solid electrode from the present simulation and literature. It can be observed that present results agree well with the literature data. The result is not a straight line because α was not equal to 0 but 0.5 in the present simulation. Figure 4.9 shows the exchange current of Pu on the solid. It follows the same trend with U but is an order of magnitude smaller. No reported values are found to compare with. For the exchange current on the liquid cadmium electrode, both the concentrations of oxidant of reductant are well defined. The exchange current is

$$j_0 = nFk_0 C_O^{b\ (1-\alpha)} C_R^{b\ \alpha} \qquad \text{Eq. 69}$$

where the concentration is the value at the equilibrium. Here the exchange current on the liquid electrode is not reported because given an oxidant concentration in molten salt, the activity coefficient of $CdCl_2$ needs to know to calculate C_R^b at equilibrium [171]. To our knowledge, the value has not been measured in literature. However, once one has the value, the exchange current is ready to be calculated with the rate constants obtained in this study.

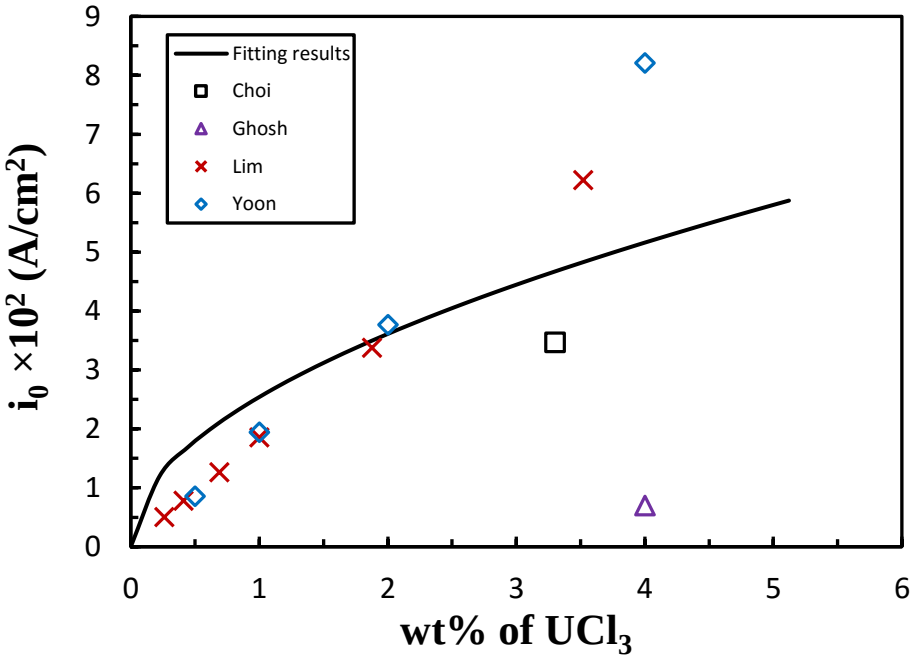

Figure 4.8. Comparison of exchange current of U on the solid cathode with literature [51-54]

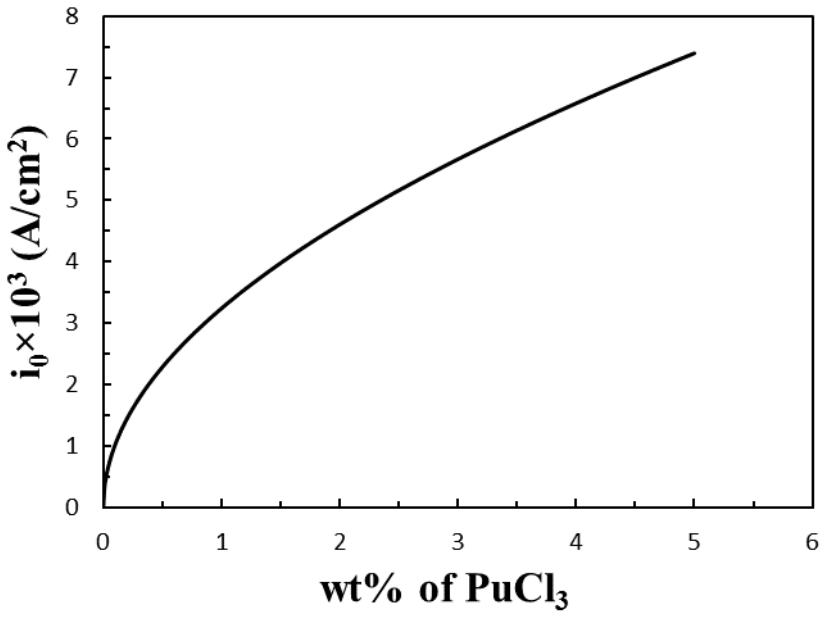

Figure 4.9. Exchange current of Pu on the solid electrode at 773 K

4.4.2 Solid used fuel anode to solid cathode

The experiment result was taken from the work by Koyama et al. [150]. In the run #4, they used unirradiated metal alloy fuel of U-20Pu-10Zr as the anode and solid steel as the cathode. Its density was assumed as the same with that of U-19Pu-10Zr, which is 15.9 g/cm^3 [149]. The diameter of the cylinder was stated as 0.48 cm by other researchers [149], which yielded a length of 3.34 cm. The molar volumes were calculated as 21.39, 76.75, 57.37 cm^3/mol for U, Pu, and Zr, respectively, in the alloy. The electrorefiner conditions in the study are shown in Table 4.6. Table 4.7 shows the mass transfer coefficient of U and other parameters used to have a good agreement with the experiments. Mass transfer coefficients of Pu and Zr were restricted by Eq. 4.62. f, g, and k_d were not changing in other simulations but mass transfer coefficients did change due to different flow conditions in different experiments.

Table 4.6. Conditions in run #4 [150]

UPuZr charged	9.6 g	Current	0.4 A	Quantity of electricity	8680 C
Cathode diameter	1.8 cm	Cathode length	8 cm	Molten salt	1000 g
Initial composition of U, Pu, and Zr in molten salt (wt%)					
U	0.73	Pu	3.1	Zr	0.003

Table 4.7. Parameters by trial and error method

K_U^a (cm/s)	2.00×10^{-4}	K_U^c (cm/s)	7.8×10^{-3}
k_{Zr}^s (cm/s)	2.2×10^{-7}	f	6×10^{-6}
g (cm^{-1})	10000	k_d	2.6×10^{-2}

Figure 4.10 shows the comparison of anode potential, which indicates the simulation results agree well with the experimental data. There are two plateaus for the anode potential. The fluctuation between them in experiments can be caused by the non-uniform porous layer during electrorefining. The first plateau corresponds to the dissolution of U and Pu. The sudden increase to another one represents the beginning dissolution of Zr, which can be taken from Figure 4.11, Figure 4.12, and Figure 4.13. Figure 4.11 shows U and Pu co-dissolved from the anode initially. After passing around 850 C, Zr started to dissolve. The thickness of porous Zr grew with the dissolution of U and Pu but decreased after Zr dominated the dissolution, as shown in Figure 4.12. Figure 4.13 shows the current almost kept constant before around 850 C and after around 2000 C. The later one can be due to the solubility limits of actinides at the surface of the undissolved alloy.

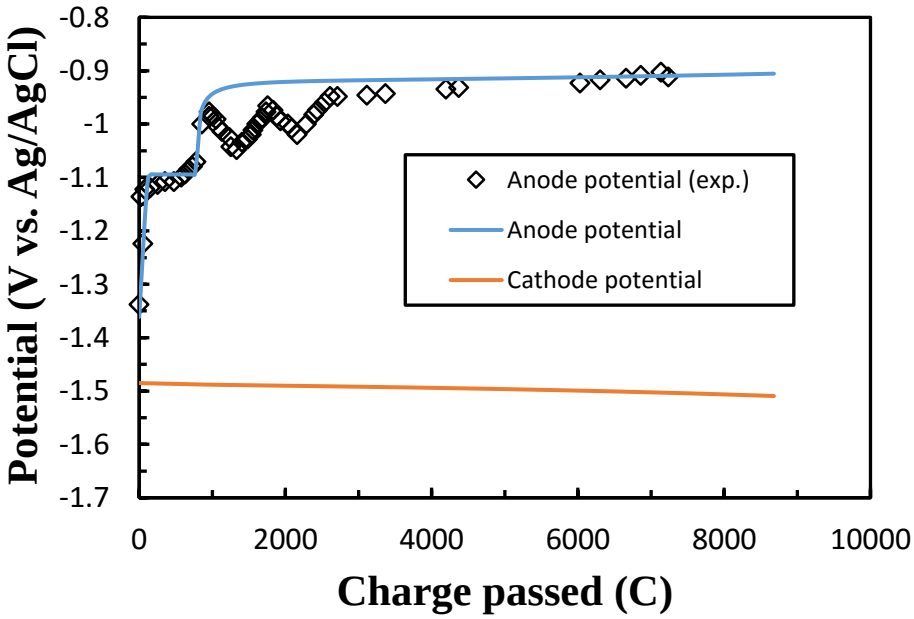

Figure 4.10. Anode and cathode potentials

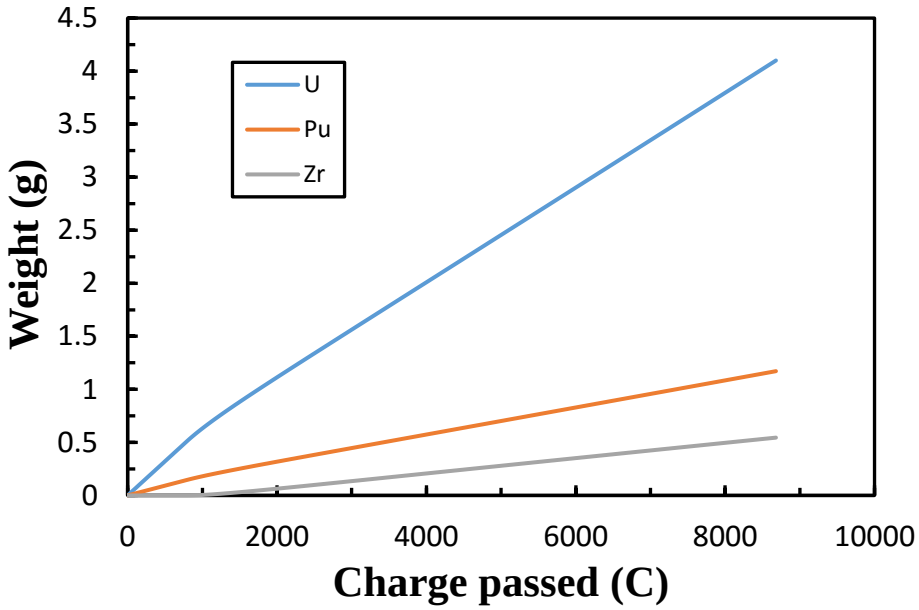

Figure 4.11. Weight dissolved from anode

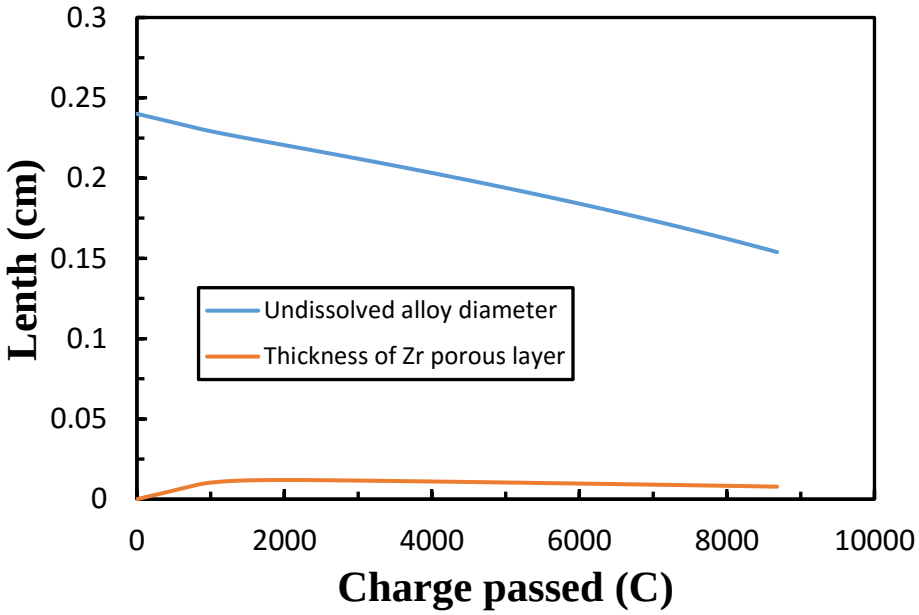

Figure 4.12. Thickness of porous Zr and diameter of remaining alloy

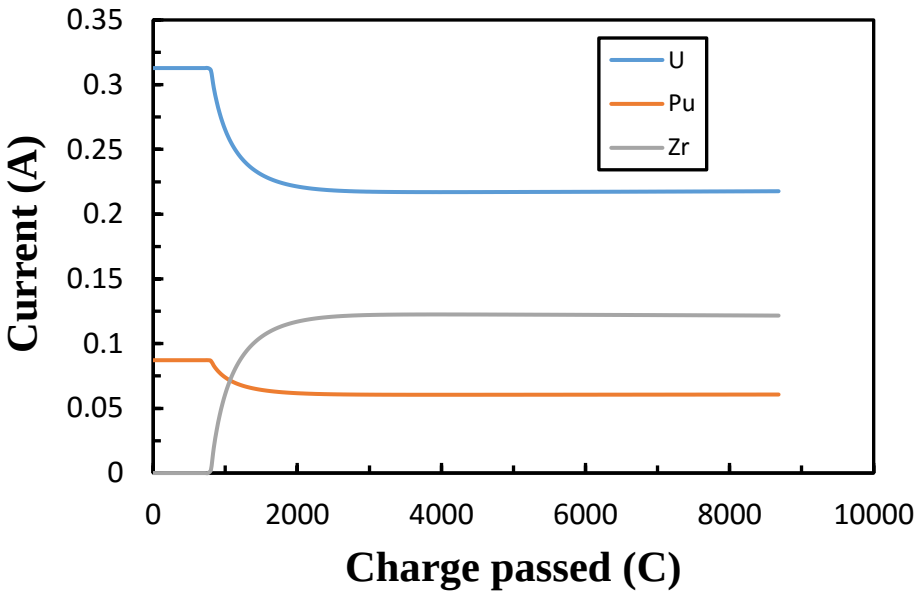

Figure 4.13. Anode current of each element

Table 4.8 lists the comparisons of the amount of U, Pu, and Zr in the electrolyte and solid cathode at the end of the experiments and simulation. It shows that the data of U and Pu agree quite well with each other while Zr in the electrolyte was overestimated. It makes sense when considering low concentration is hard to be detected accurately. Figure 4.14 shows an increase of Pu and decrease of U in electrolyte because while both U and Pu dissolved from anode, the U dominated the deposition on the cathode. Also, Figure 4.15 and Figure 4.16 shows Zr co-deposited with U due to its high redox potential but low concentration in the electrolyte and no Pu was found on the cathode, which corresponds to the flat cathode potential in Figure 4.10. Considering the material balance, there should be some Zr reduced on the cathode in experiments even though it was not determined because Zr dissolved from the anode while its final concentration in electrolyte decreased.

Table 4.8. Amount of elements in electrolyte and cathode at the end of experiments and simulation

		Experiments	Simulation
Electrolyte	U (wt%)	0.45	0.51
	Pu (wt%)	3.3	3.22
	Zr (wt%)	0.001	0.033
Cathode	U (g)	6.8	6.28
	Pu (g)	<0.01	0
	Zr (g)	Not determined	0.248

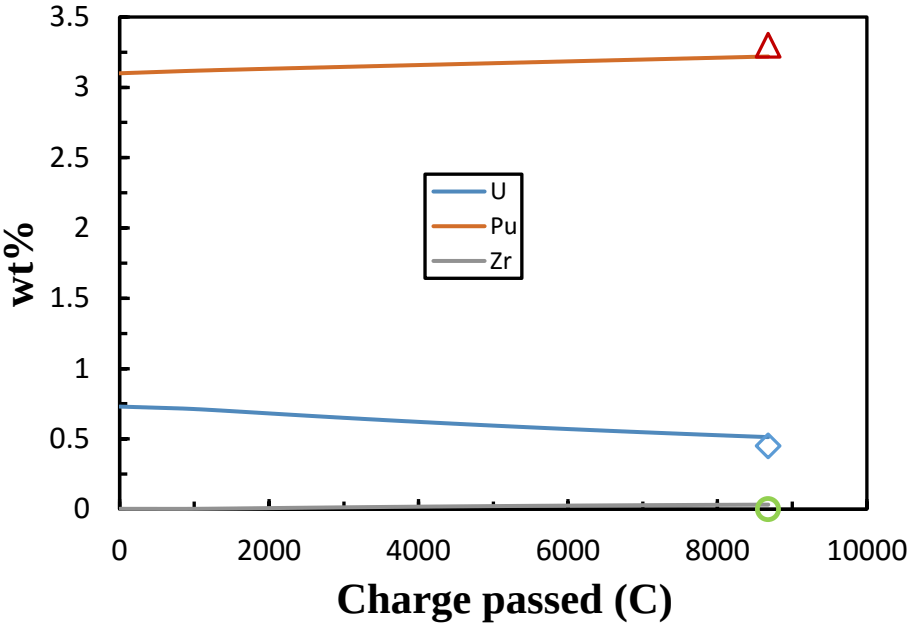

Figure 4.14. Concentration in the molten salt, markers represent the final concentrations of the species in experiments denoted by the line with the same color.

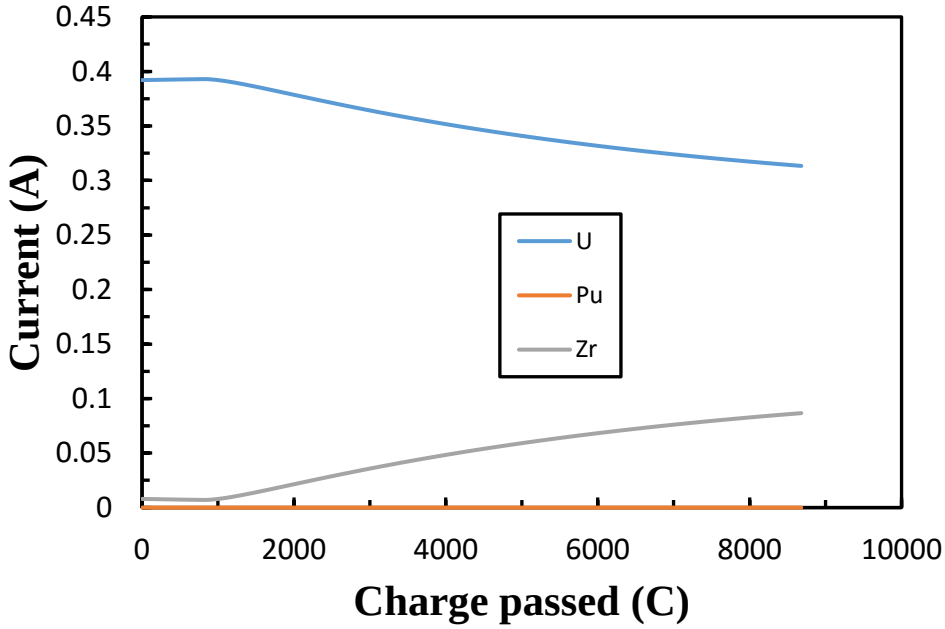

Figure 4.15. Cathode current of each element

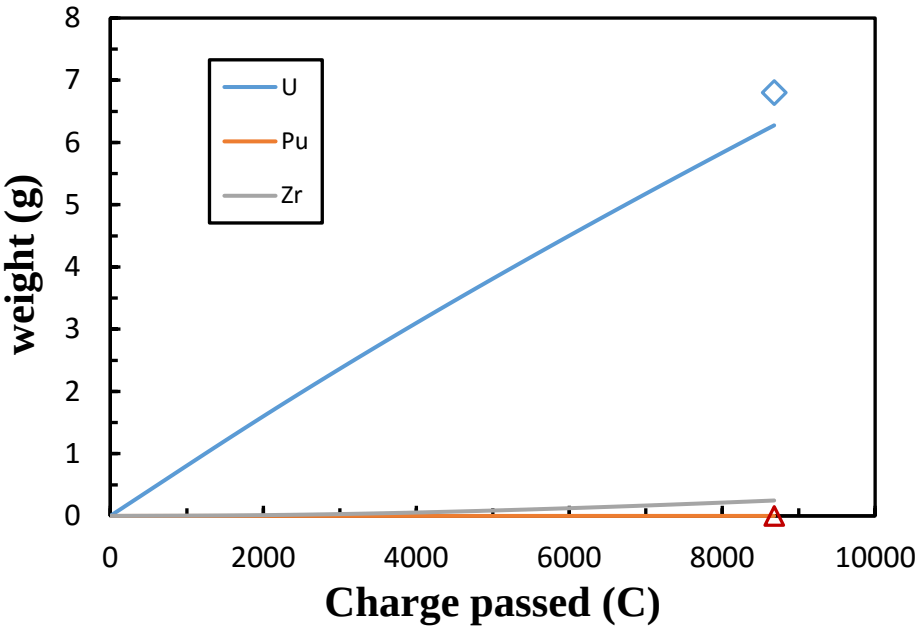

Figure 4.16. Weight deposited on the cathode, markers represent the final concentrations of the species in experiments denoted by the line with the same color.

4.4.3 Solid used fuel anode to liquid cadmium cathode

The transport from the solid anode to liquid cathode was validated by the run #2 carried out by Koyama et al. [150]. The experiments conditions are listed in Table 4.9. Table 4.10 shows the mass transfer coefficients at the cathode.

Table 4.9. Conditions in run #2 [150]

UPuZr charged	13.2 g	Current	0.4 A	Quantity of electricity	8100 C
Anode diameter	0.48 cm	Cathode diameter	3.5 cm	Molten salt	1000 g
Initial composition of U, Pu, and Zr in molten salt (wt %)					
U	0	Pu	3.5	Zr	0

Table 4.10. Parameters by trial and error method

$K_U^{a,ms}$ (cm/s)	1.00×10^{-3}	$K_U^{c,Cd}$ (cm/s)	1.11×10^{-3}
$K_U^{c,ms}$ (cm/s)	8.30×10^{-4}	k_{Zr}^{Cd} (cm/s)	2.30×10^{-3}

Figure 4.17 to Figure 4.24 plot the results from simulation. Figure 4.17 indicates that the potential was predicted very well. There is a sudden increase-decrease-increase pattern for the anode potential. That is due to the competition between the dissolution of Zr and actinides, which is also

shown in Figure 4.20. With the dissolution of Zr, it would deposit on the cathode simultaneously, which resulted in an increase in the cathode potential, as is shown in the tail of the plot in Figure 4.17. The pattern changes of the anode and cathode currents at the beginning and end shown in Figure 4.20 and Figure 4.22 are due to the fact that the current applied is 0.3 A but not 0.4 A during that period in the experiment.

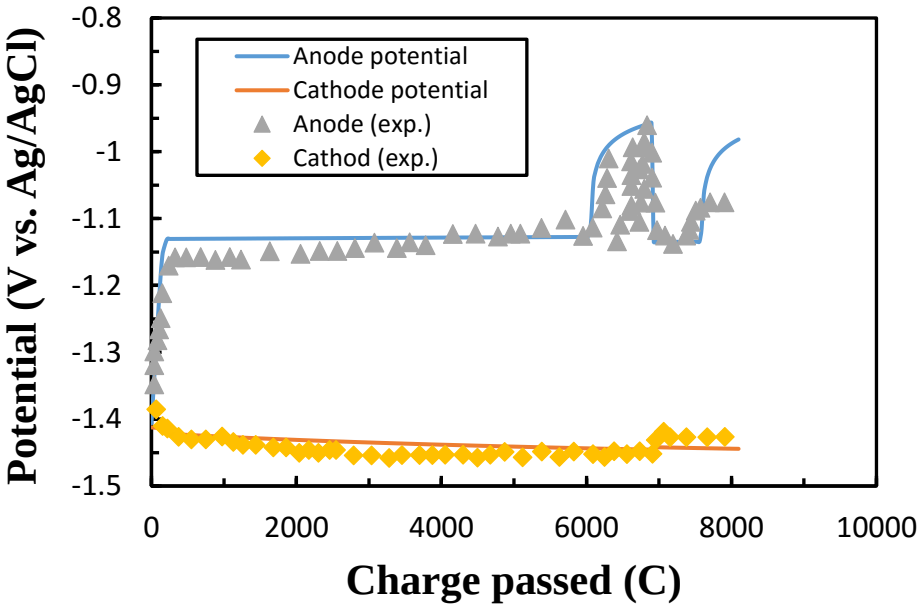

Figure 4.17. Anode and cathode potentials

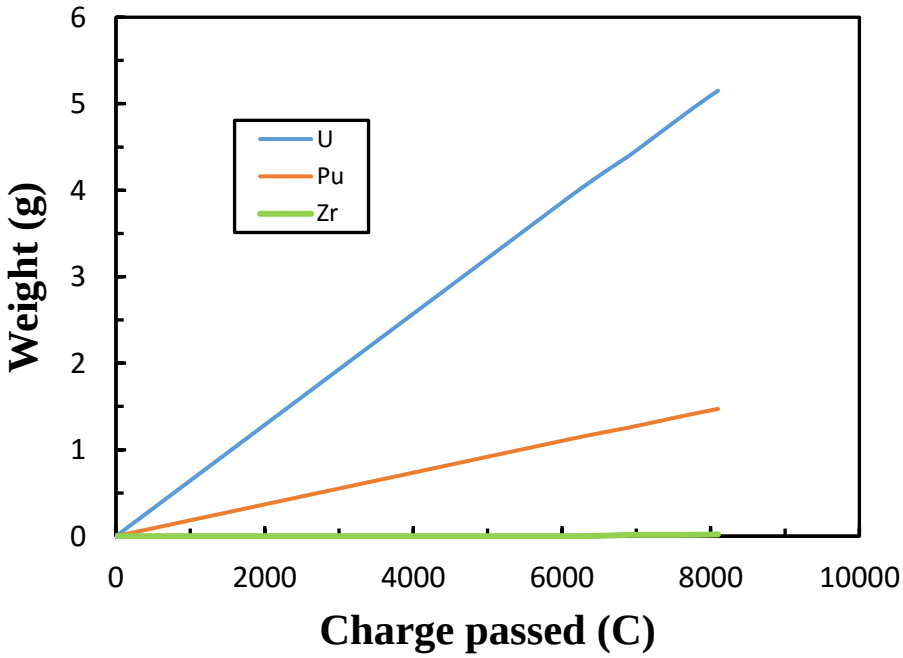

Figure 4.18. Weight dissolved from anode

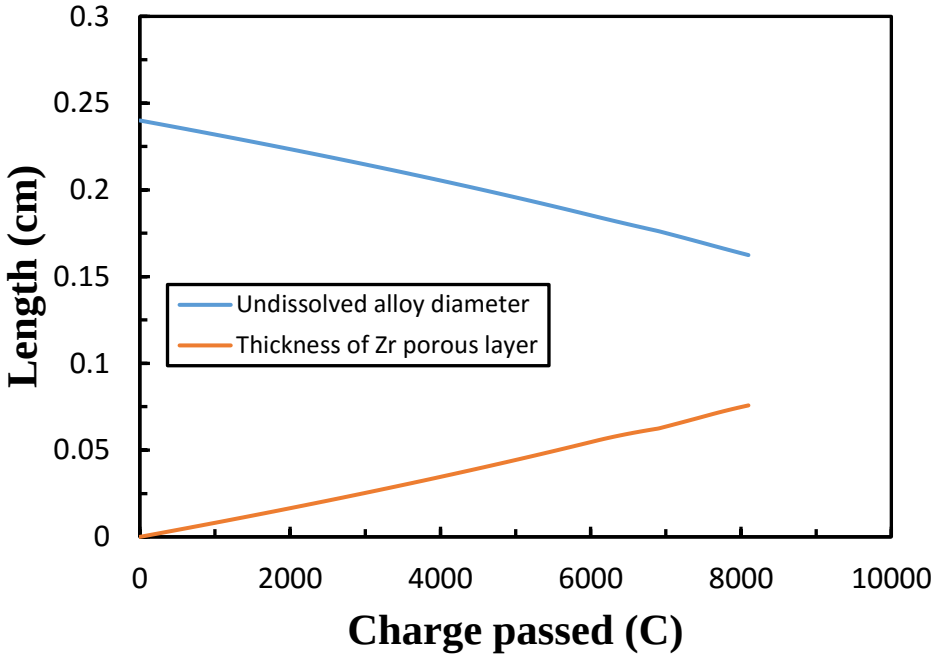

Figure 4.19. Thickness of porous Zr and diameter of remaining alloy

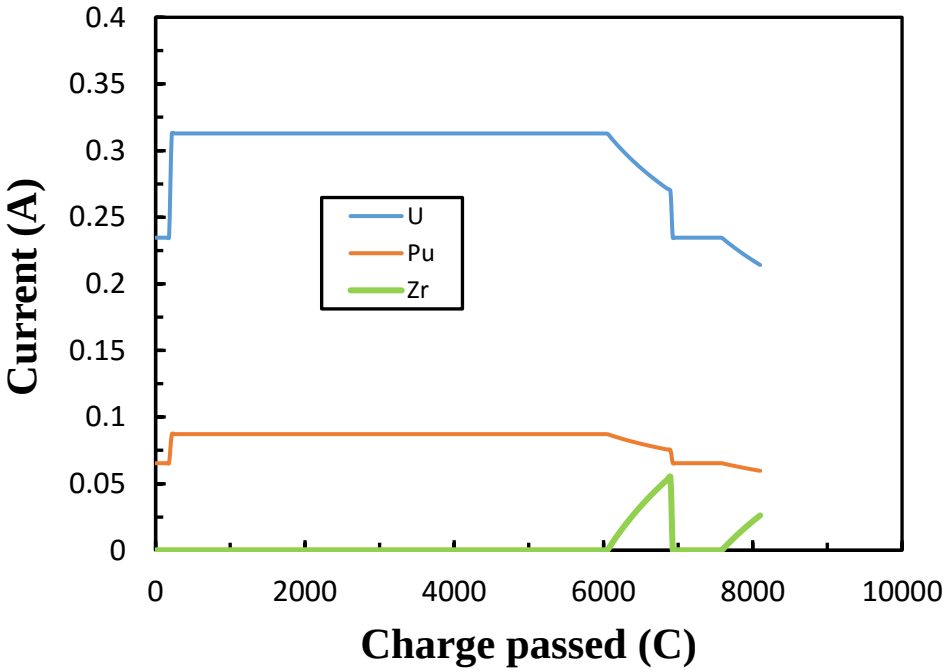

Figure 4.20. Anode current of each element

Table 4.11 lists the compositions of electrolyte and liquid cadmium at the end of experiment and simulation. The concentration of UCl_3 in LiCl-KCl molten salt is higher but overall the agreement is pretty good. What should be noted is that 6.0 wt% deposition of Pu in liquid cadmium has

exceeded its solubility, as is shown in Figure 4.25. The concentration of Pu kept constant after its saturation, which should be taken into account in any simulation.

Table 4.11. Amount of elements in electrolyte and cathode at the end of experiments and simulation

		Experiments	Simulation
Electrolyte	U (wt%)	0.19	0.46
	Pu (wt%)	3.4	3.09
	Zr (wt%)	0	0.002
Cathode	U (wt%)	0.62	0.63
	Pu (wt%)	6.0	6.14
	Zr (wt%)	0.003	0.001

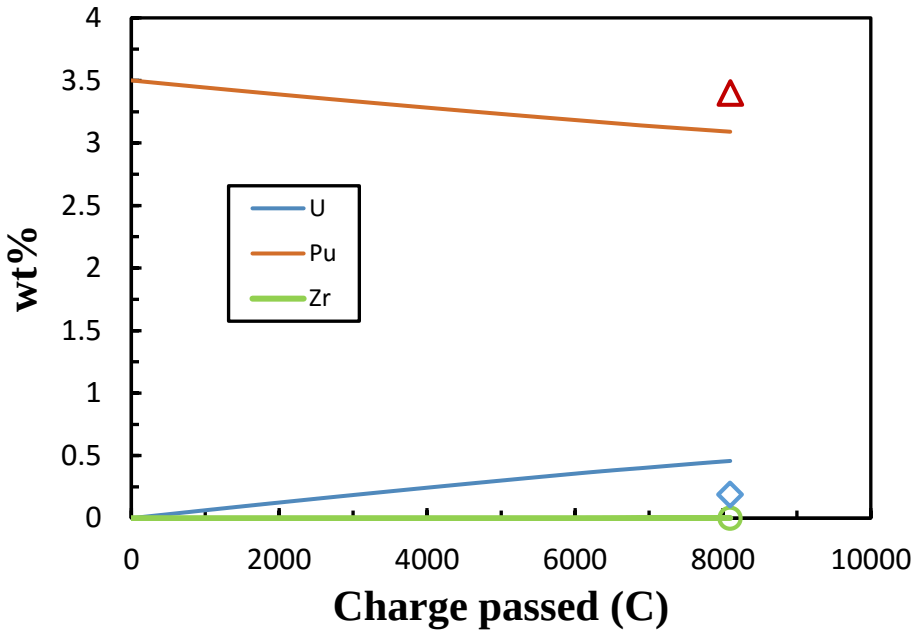

Figure 4.21. Concentration in the molten salt, markers represent the final concentrations of the species in experiments denoted by the line with the same color.

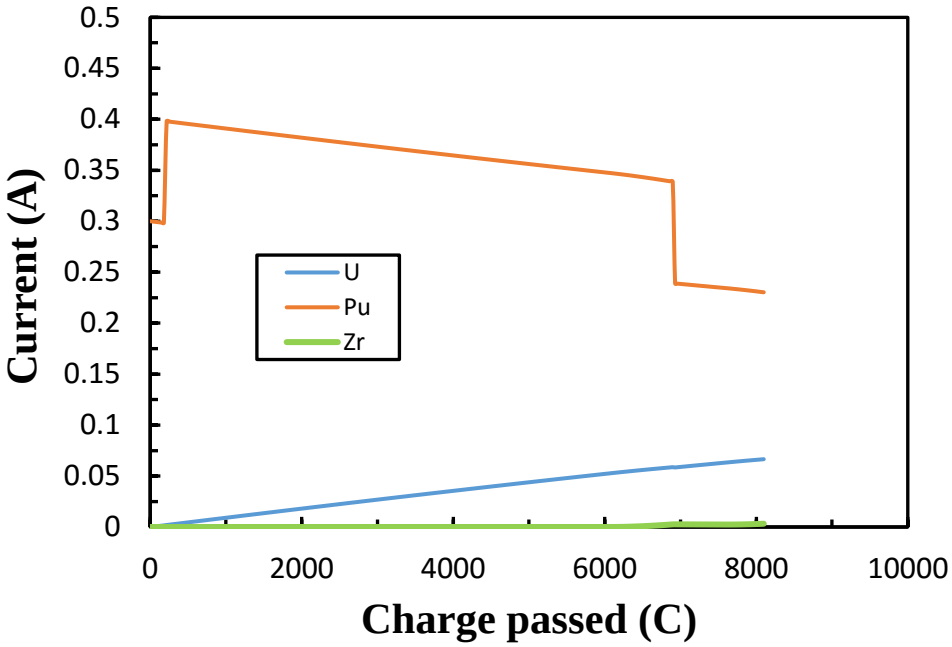

Figure 4.22. Cathode current of each element

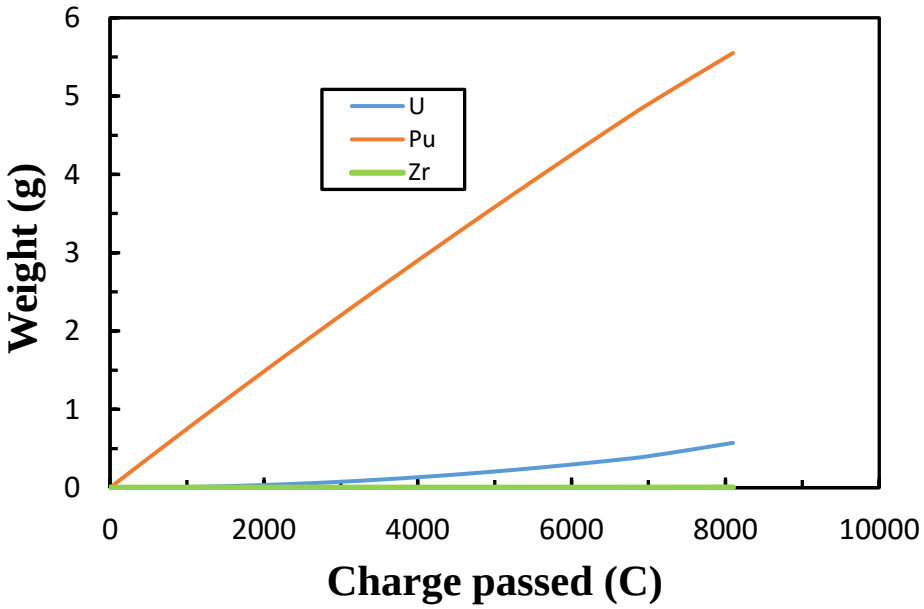

Figure 4.23. Weight deposited on the cathode

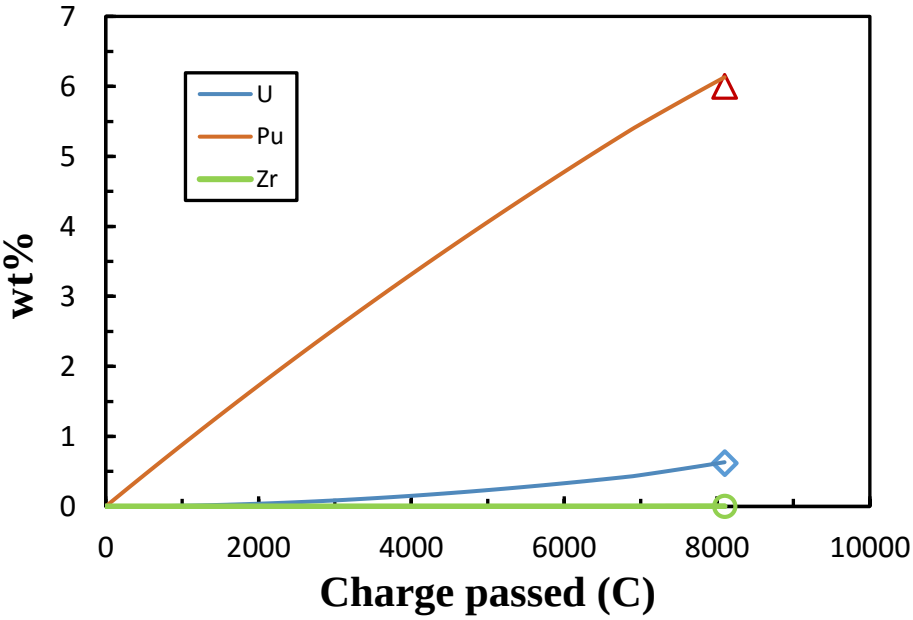

Figure 4.24. Weight percent in the cathode, markers represent the final concentrations of the species in experiments denoted by the line with the same color.

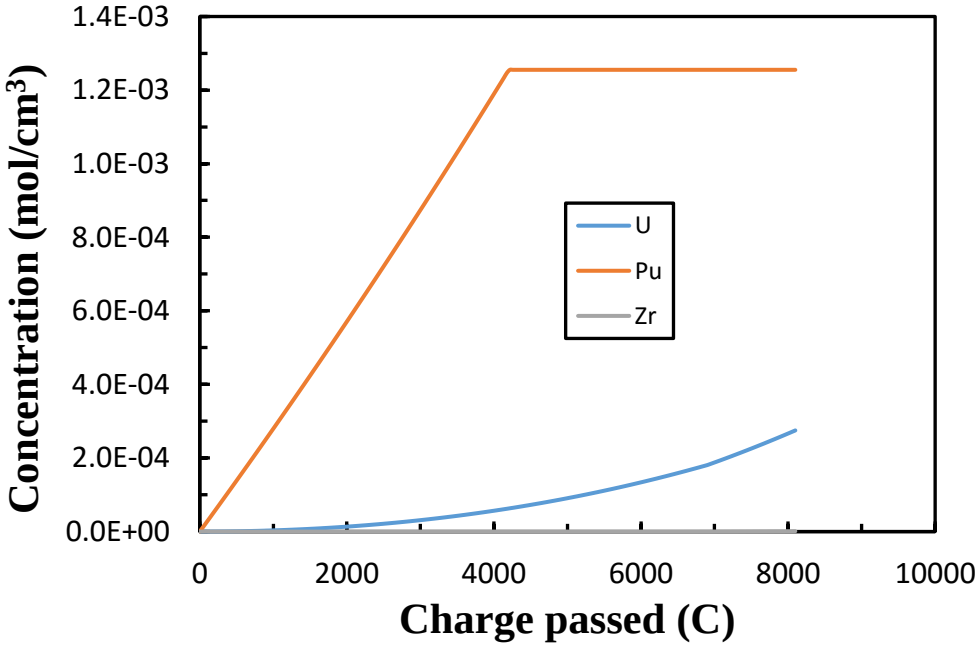

Figure 4.25. Concentrations of elements in liquid cadmium cathode

4.5 Application of electrochemical model

The validation above indicates that model is robust to predict the material transport and distribution in the electrorefiner. In this part, the model would be applied to electrorefining, actinide drawdown,

and rare earth drawdown processes to investigate its performance under different conditions. Here all the anodes were solid used fuel anodes because they are the most ready-to-use form after the fuel is discharged from the fast reactor or obtained by reducing the fuel from LWR. Seven species, namely Zr, U, Pu, Am, Gd, Ce, and La were considered. Their composition in used fuel is shown in Table 4.12 in accordance to their composition in EBR-II used driver fuel shown in Ref. 47. The Am was set to 0.5 wt% here.

Table 4.12. Composition used in this study

Elements	Zr	U	Pu	Am	Gd	Ce	La
wt%	10.81	80.60	0.413	0.5	0.005	0.542	0.284

4.5.1 Solid anode to solid cathode

The transport from the solid anode to solid cathode has been studied in the last section. However, Zr would be dissolved from the anode and deposit on the cathode, which needs to be avoided. Here the emphasis was placed on the behavior of Pu and how to avoid the dissolution of Zr. Table 4.13 shows the conditions applied. When the applied current is 0.4 A, the limiting concentration of U to support the current alone can be calculated by

$$C_{U,\lim}^{ms} = \frac{i}{nFK_{U,ms}^{c}A_c} \qquad \text{Eq. 4.70}$$

which is 3.67×10^{-5} mol/cm^2 (0.557 wt%). Therefore, basically, two sets of initial concentration of U and Pu at molten salt, namely 0.6 wt% and 0, 0.6 wt% and 6 wt%, respectively, were set to study whether Pu deposits with U up to a high Pu/U of 10. Recall Eq. 4.58 and Eq. 4.62, the mass transfer coefficients of other elements can be calculated based the value of U by

$$K_i = \left(\frac{D_i}{D_U}\right)^{0.644} K_U \qquad \text{Eq. 4.71}$$

According to the optimized results in Table 4.7, mass transfer coefficients of other elements at anode and cathode are listed in Table 4.14

Table 4.13. Conditions of electrorefining

anode charged	9.6 g	Current	0.4 A	time	9.7 h
Cathode diameter	1.8 cm	Cathode length	8 cm	Molten salt	1000 g
Initial U in molten salt	0.6 wt%	Initial Pu in molten salt	0/6 wt%		

Table 4.14. Mass transfer coefficients of elements concerned

Elements	Zr	U	Pu	Am	Gd	Ce	La
$K^a \times 10^4$ (cm/s)	2.14	2.00	2.13	2.70	1.65	2.58	3.11
$K^c \times 10^4$ (cm/s)	8.41	7.87	8.37	10.60	6.48	10.10	12.20

For the first set of initial composition, Figure 4.26 plots the anode current. During the simulation, Zr started to dissolve after about half an hour and all other elements dissolved with U from the beginning. However, as Figure 4.27 shows, only U deposited on the cathode initially and then it co-deposited with Zr after the dissolution of Zr from the anode. Even Pu, whose potential is closest to U, did not deposit. Elements except U were accumulated in molten salt as Figure 4.28. Figure 4.29 shows the deposition amounts on the solid cathode. Figure 4.30 is the anode and cathode potentials. The gradual increase of the anode potential at the end of the plot is because of exhausting of metal materials in the anode and more positive potential was needed to drive the reaction.

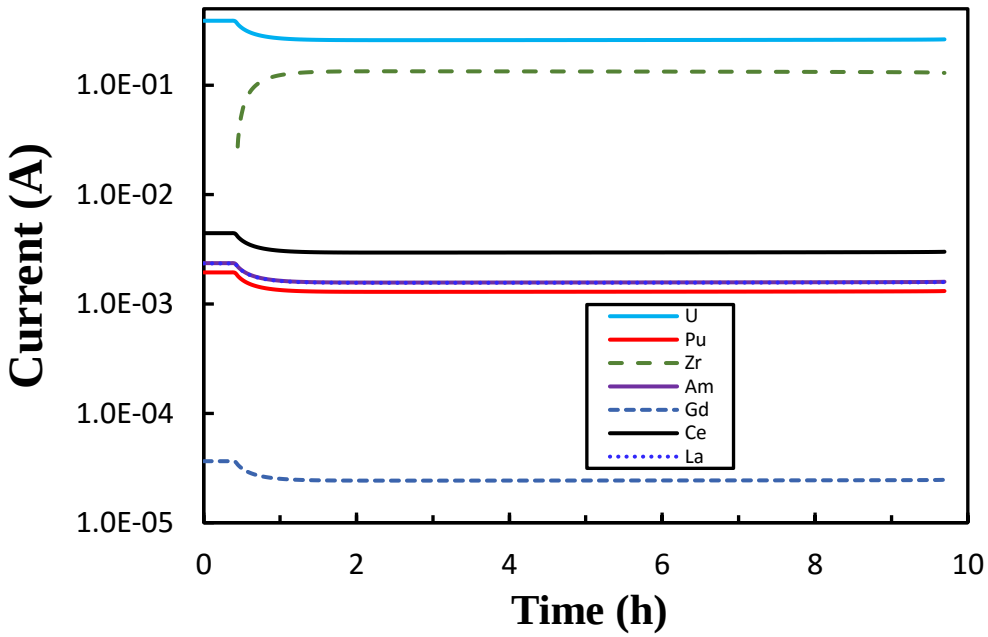

Figure 4.26. Anode current

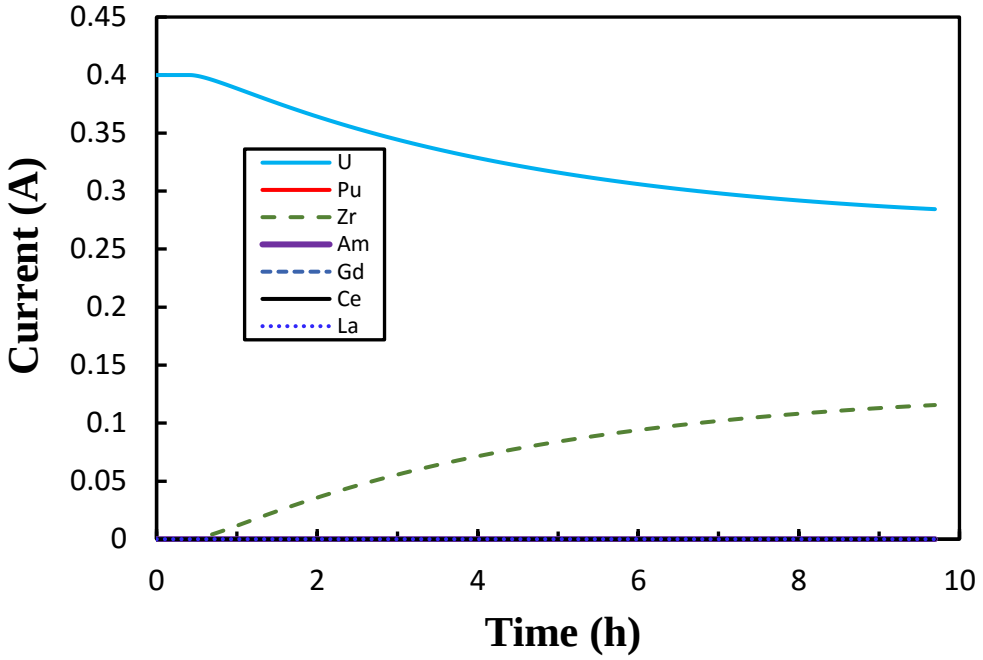

Figure 4.27. Cathode current

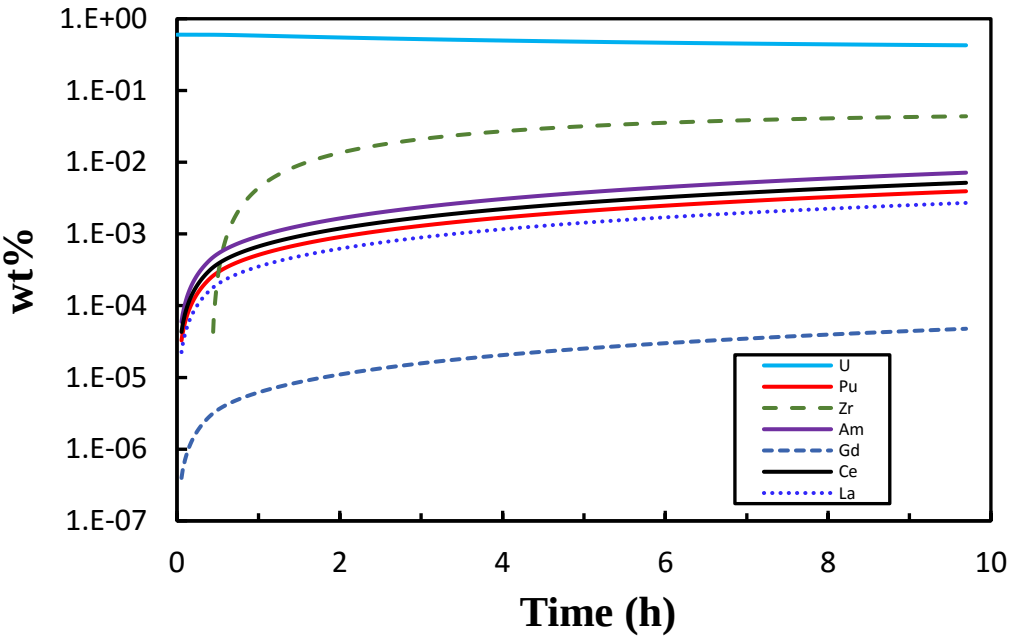

Figure 4.28. Concentration in molten salt electrolyte

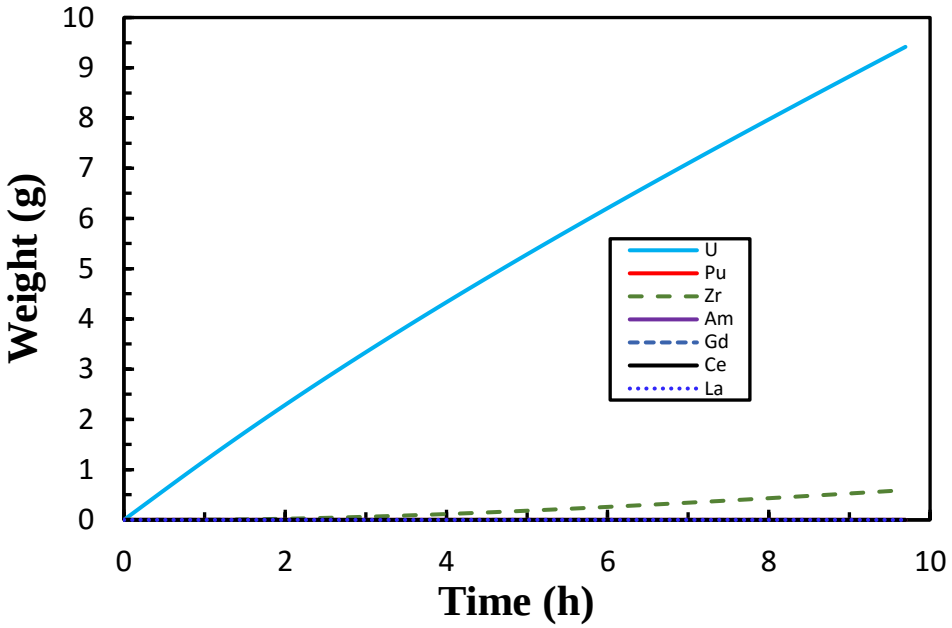

Figure 4.29. Deposition of species on the solid cathode

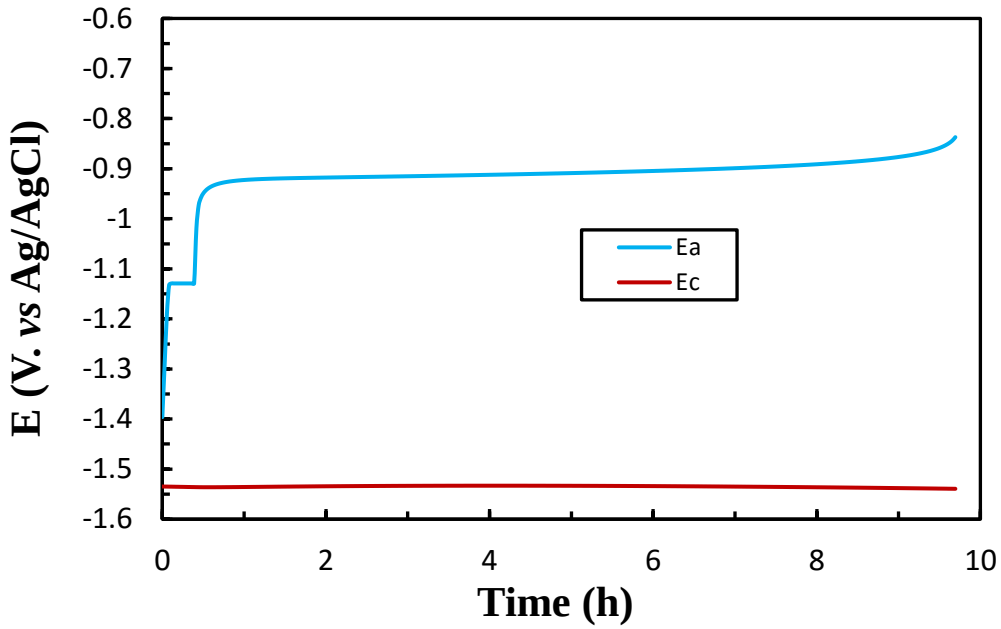

Figure 4.30. Anode and cathode potential

When the initial electrolyte included 0.6 wt% U and 6 wt% Pu, the results were pretty similar. There was still only U and Zr depositing on the solid cathode electrode, as is indicated by their cathode current in Figure 4.31.

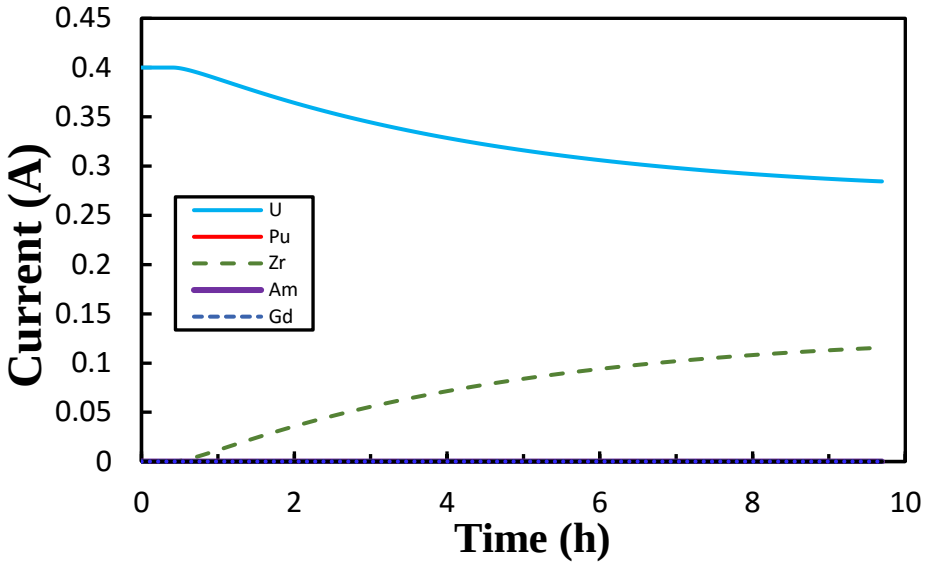

Figure 4.31. Cathode current with initial concentrations of U and Pu in LiCl-KCl molten salt is 0.6 wt% and 6 wt%, respectively.

Now the problem is that Zr would be dissolved from the anode. As is shown in Figure 4.32, Zr was exhausting simultaneously with U, which would inevitably result in the deposition of Zr on the solid cathode due to its high redox potential.

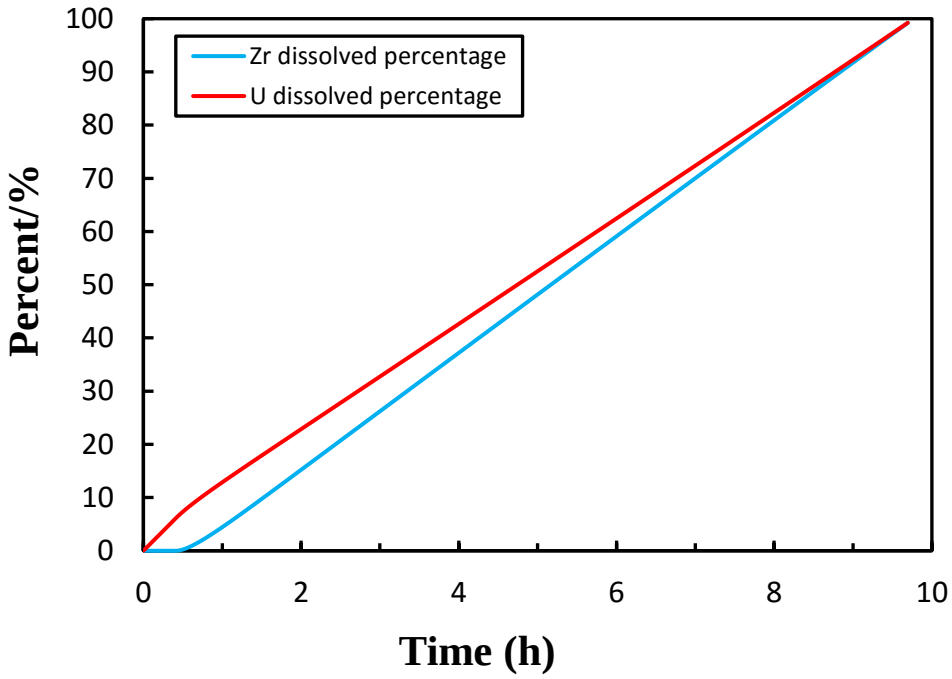

Figure 4.32. Zr and U dissolved percentage with initial concentrations of U and Pu in LiCl-KCl molten salt is 0.6 wt% and 0 respectively.

One of the methods to avoid this is to use the stepwise current. Whenever Zr needs to dissolve to compensate for the current, the current is decreased by a factor (d_c) and kept constant until to next decrease, i.e.

$$i(t_1) = (1 - d_c) i(t_0) \qquad \text{Eq. 4.72}$$

For the initial composition with only 0.6 wt% U in LiCl-KCl, the stepwise current was applied by decreasing 10% each time just before Zr started to dissolve. Figure 4.33 and Figure 4.34 show the anode and cathode current, respectively, which indicates Zr did not dissolve from the anode and only U deposited on the cathode. The pattern of applied current should be the same with the cathode current. Both the anode and cathode currents decrease stepwise. Figure 4.35 plots the composition changes in the LiCl-KCl molten salt electrolyte. There was no Zr in the molten salt. And the concentration of U should decrease because U supported all the current in cathode while only part of the current in anode.

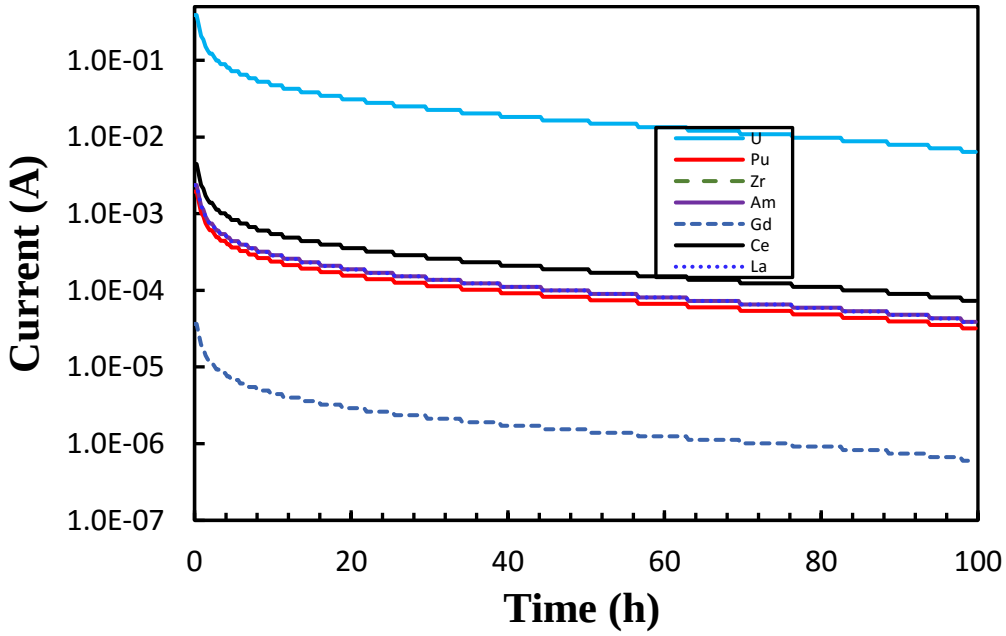

Figure 4.33. Anode current

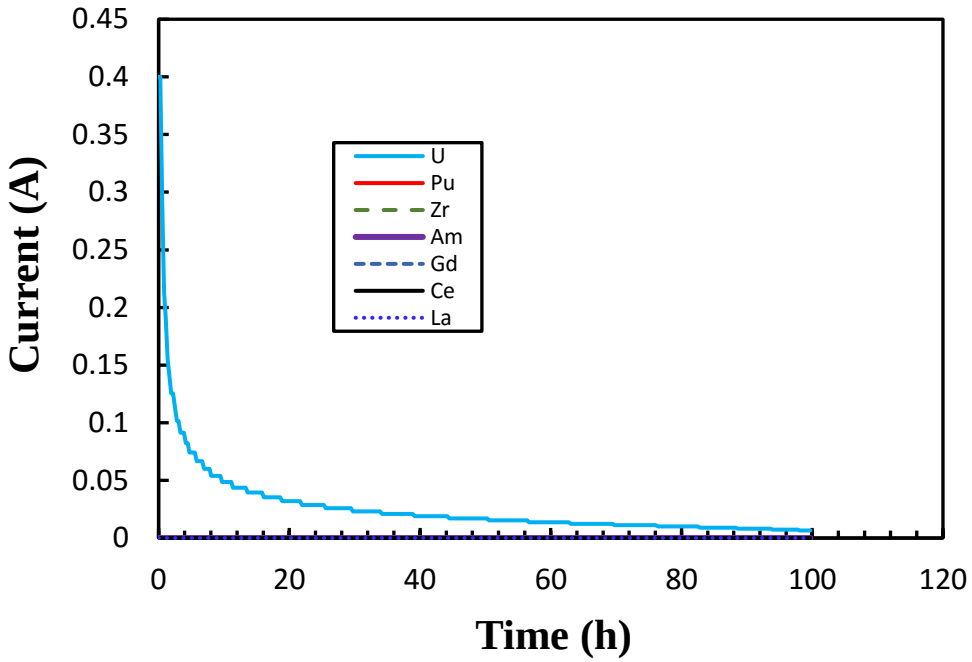

Figure 4.34. Cathode current

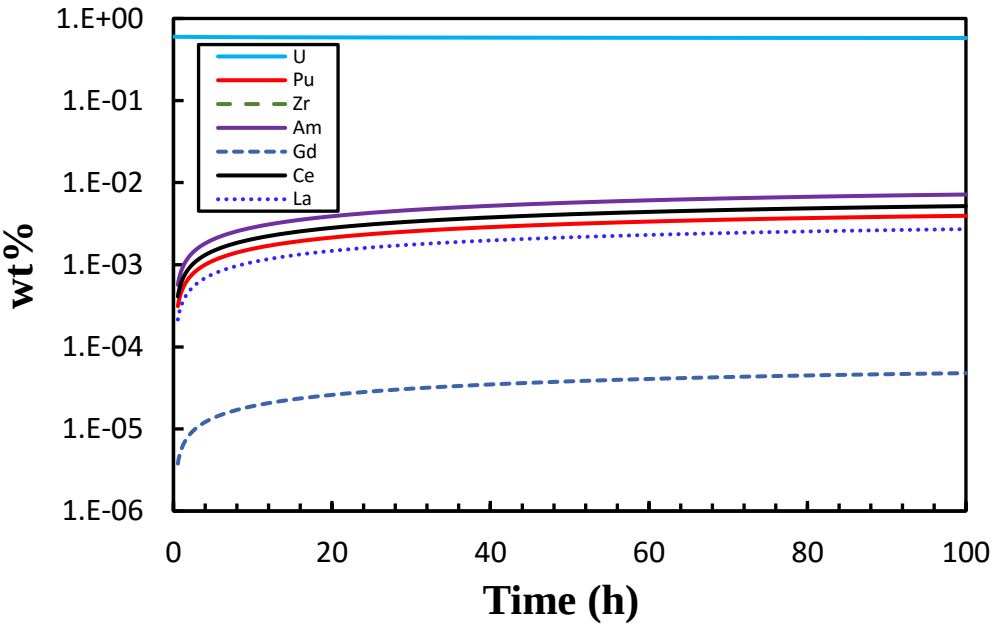

Figure 4.35. Weight percent of species in LiCl-KCl electrolyte

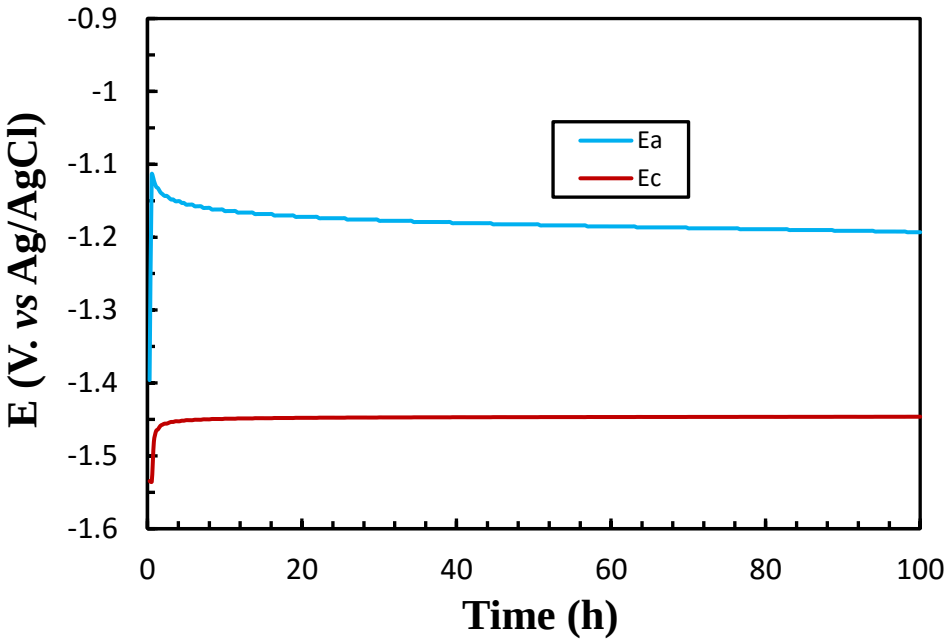

Figure 4.36. Anode and cathode potentials

Figure 4.36 plots the anode and cathode potentials. Both anode and cathode potentials almost keep constant because of no dissolution or deposition of Zr. It can be easily imagined that a smaller decreasing factor will yield a larger average current and shorten the time needed to dissolve all the U. However, a smaller decreasing factor will require more frequent decreases to avoid the dissolution of Zr, which may be too complicated and hard to control. Four decreasing factors, namely 5%, 10%, 15%, and 20% were tested to dissolve 99% U in the anode. Figure 4.37 and Figure 4.38 show the time needed to dissolve 99% U and current decreasing frequency during the dissolution, respectively under different decreasing factors. It can be observed that the time needed approximately increases linearly with the decreasing factor. And the decreasing frequency decreases rapidly at small decreasing factor but slowly at large decreasing factor. Basically, the smallest decreasing factor that can be controlled should be selected in practice to increase the transport efficiency.

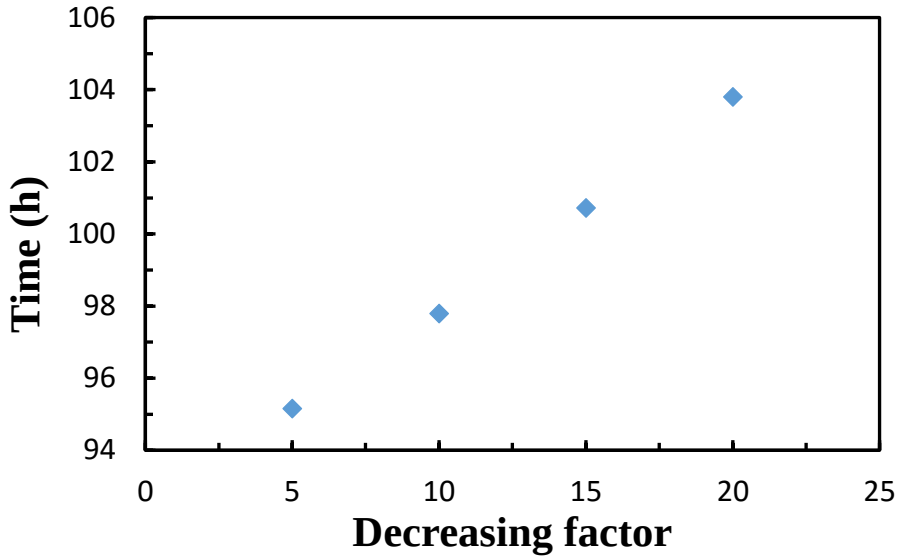

Figure 4.37. Time needed to dissolve 99% U using different decreasing factor

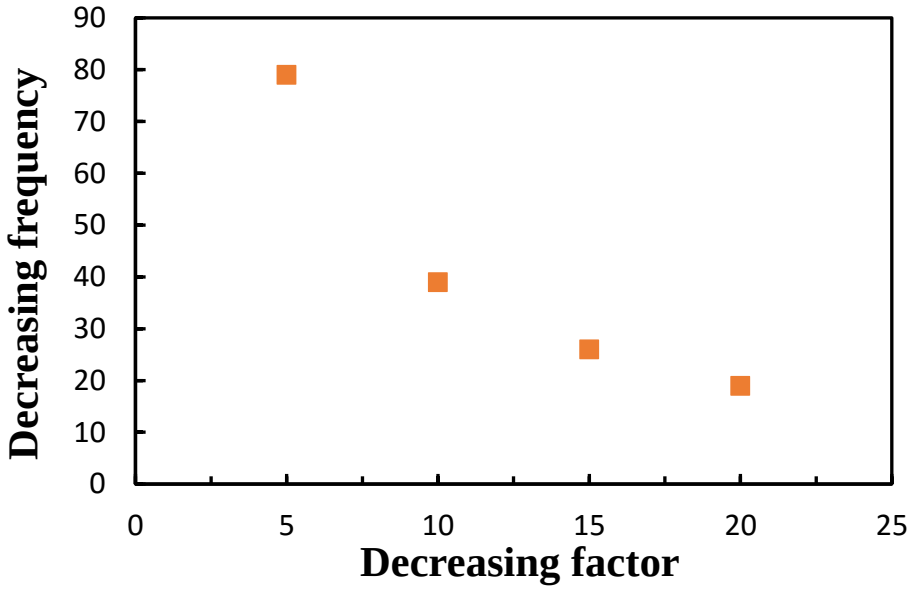

Figure 4.38. Current decreasing frequency to dissolve 99% U using different decreasing factors

4.5.2 Solid anode to liquid cadmium cathode

Generally, the solid cathode electrode is switched to a liquid cadmium one when Pu is accumulated to a designated concentration, for example, 3 wt% in the electrolyte, to reduce the Pu with other elements. Table 4.15 shows the conditions applied in this study. Two cadmium masses were used, namely 100 g and 1000 g. U and Pu would be saturated when using 100 g Cd but not for 1000 Cd after electrorefining for 5 hours. The effect of the saturation can be identified. Also, two initial U concentrations in electrolyte were used to determine how the concentration of U affects their

deposition behaviors. Table 4.16 lists the mass transfer coefficients for all of the elements based on the value of U obtained in the model validation and Eq. 4.71.

Table 4.15. Conditions of electrorefining

anode charged	13.2 g	Current	0.4 A	time	5 h
Cathode diameter	3.5 cm	Cadmium mass/g	100/1000	Molten salt/g	1000
Initial U in molten salt	0.6/1.5 wt%	Initial Pu in molten salt	3 wt%		

Table 4.16. Mass transfer coefficients of elements concerned

Elements	Zr	U	Pu	Am	Gd	Ce	La
$K_{ms}^{a} \times 10^4$ (cm/s)	10.69	10.00	10.63	13.52	8.23	12.89	15.55
$K_{ms}^{c} \times 10^4$ (cm/s)	8.87	8.30	8.82	11.22	6.83	10.69	12.91
$K_{Cd}^{c} \times 10^4$ (cm/s)	11.10	11.10	7.69	11.10	4.56	4.56	3.54

Figure 4.39 plots the anode current during the dissolution. Zr would dissolve into molten salt since the decreasing factor was not applied. It should be noted from Figure 4.40 all the elements deposited into liquid cadmium cathode due to their close redox potentials, which is different from their behaviors on a solid cathode. U and Pu were the main products and constituted more than 99.5% of the deposition as is shown in Figure 4.41. U and Pu showed a final concentration of 1.44 wt% and 3.64 wt%, respectively, which both exceed their solubility (solubility is 1.11 wt% and 1.86 wt% for U and Pu, respectively). Figure 4.42 shows the anode and cathode potentials. When 1000 g Cd was applied to the simulation, the behavior of the dissolution and deposition was pretty similar. Figure 4.43 shows the deposition amount of U and Pu in saturated and unsaturated Cd. Slightly more Pu while less U was deposited into unsaturated Cd. The depositions for Pu and U in saturated and unsaturated cadmium were 3.83 g, 3.86 g and 1.52 g and 1.50 g, respectively. The difference can be larger when more UNF is loaded in anode. Avoiding the saturation helps the deposition of Pu to some degree. When 1.5 wt% U and 3 wt% Pu in the electrolyte were used for the initial conditions, the deposition still included more than 99.5% U and Pu. However, U increased while Pu decreased significantly, as plotted in Figure 4.44. Before switching to the liquid electrode, U concentration should be kept as low as possible to deposit out more Pu. As is discussed in the last section, U concentration could be kept just above the concentration needed to support the current when using the solid cathode due to the large gaps between the redox potentials of elements on the solid cathode. And the best method for this step is using inert anode to conduct electrolysis.

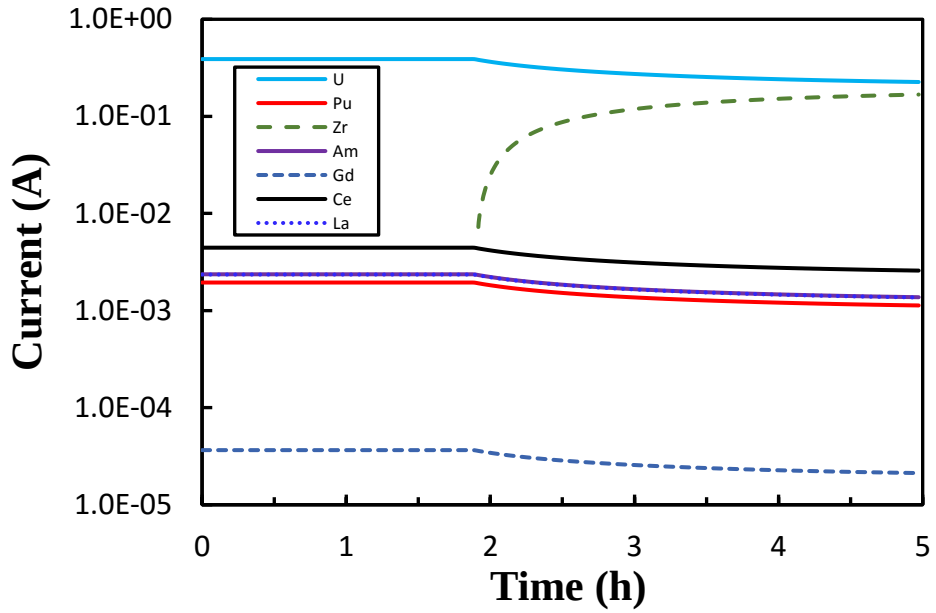

Figure 4.39. Anode current

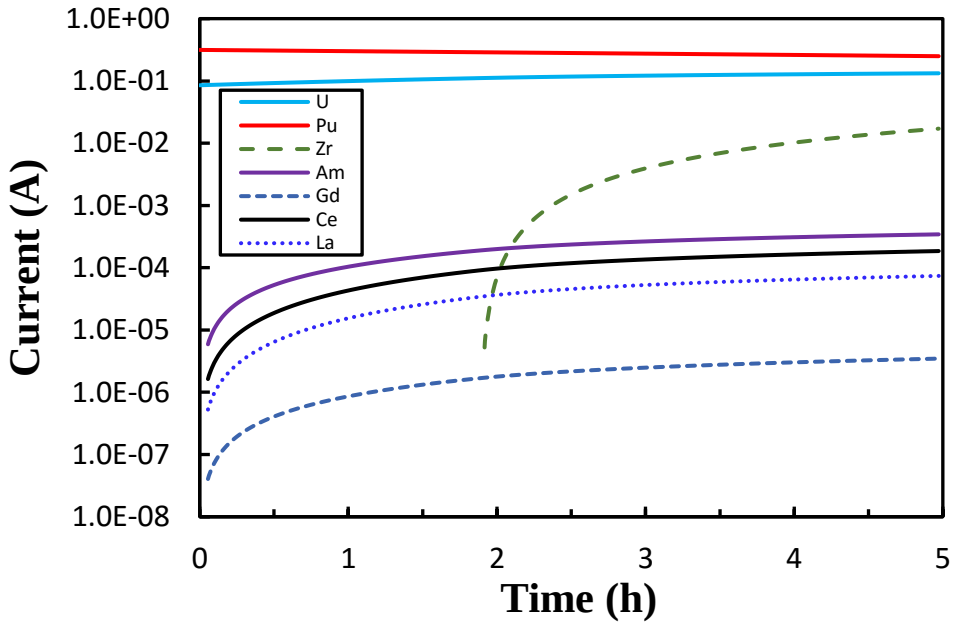

Figure 4.40. Cathode current

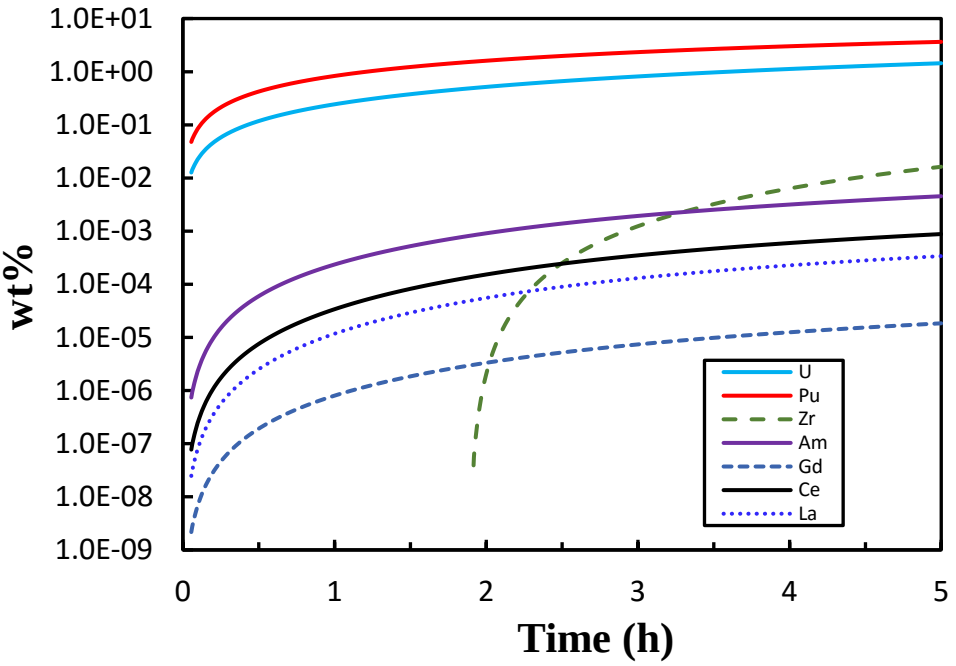

Figure 4.41. Weight percent of elements in liquid cadmium cathode.

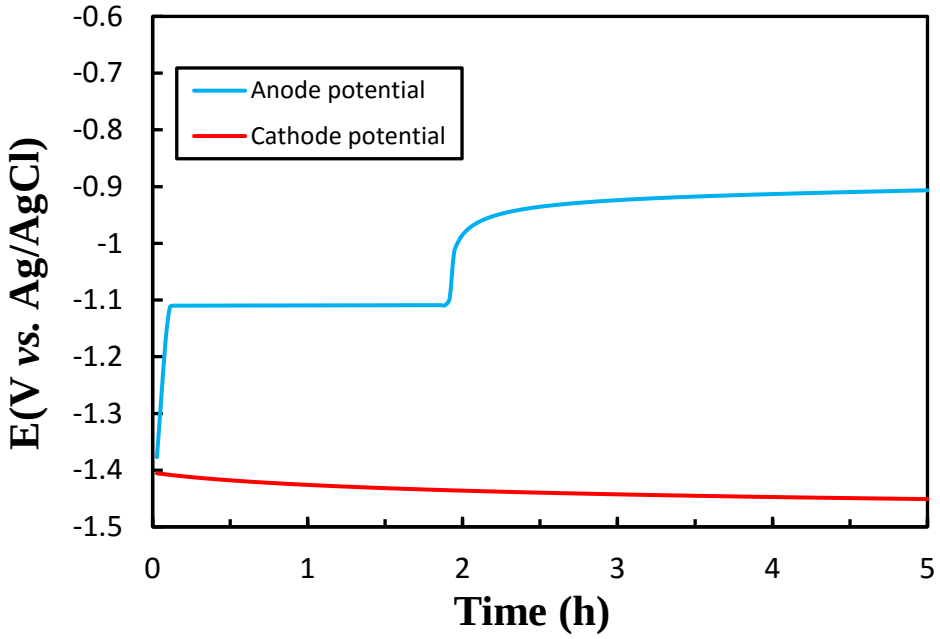

Figure 4.42. Anode and cathode potential

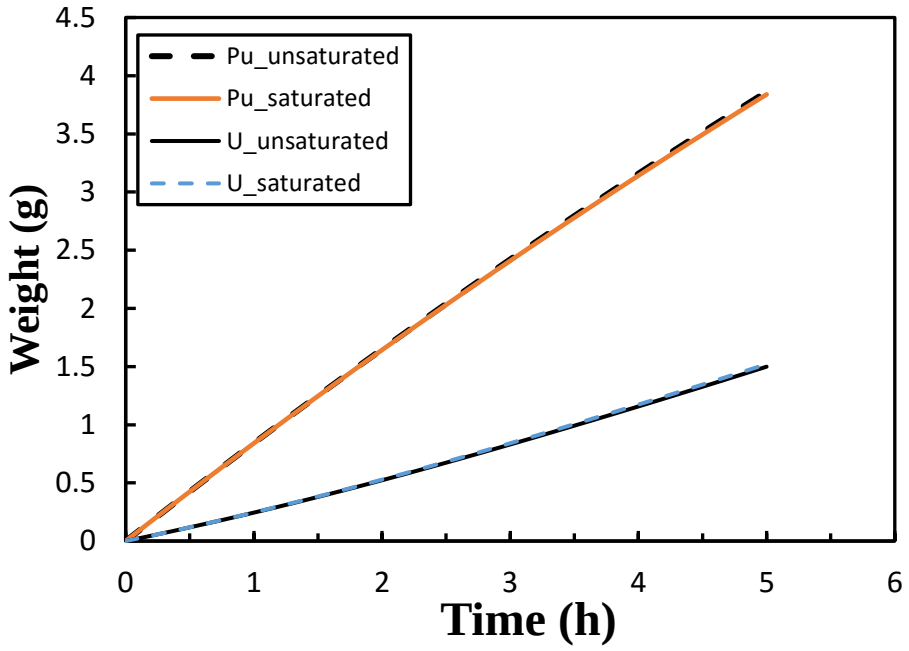

Figure 4.43. Deposition of U and Pu into saturated and unsaturated Cd

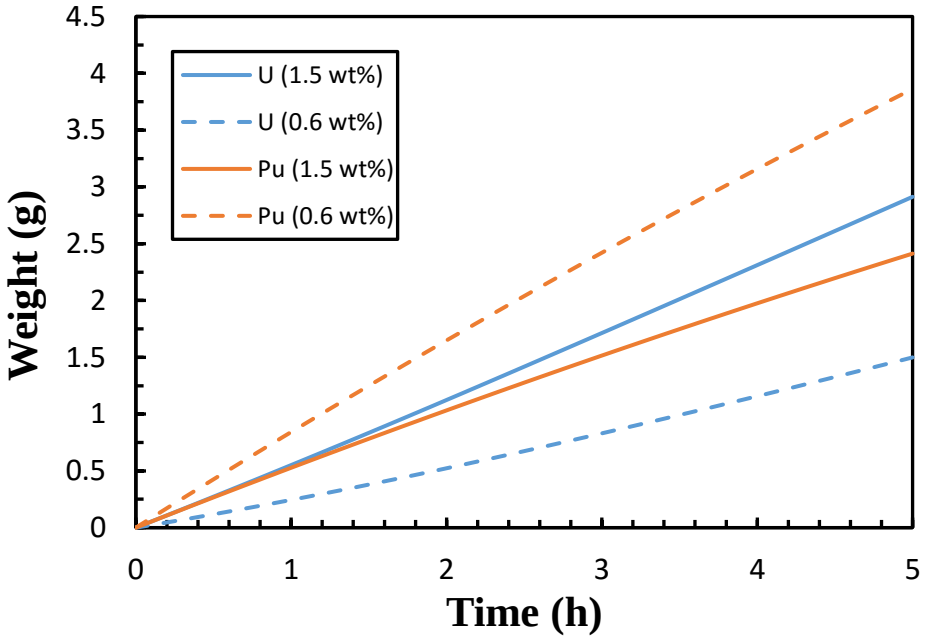

Figure 4.44. Deposition of U and Pu into unsaturated Cd with two different initial conditions, i.e 0.6 wt% U and 1.5 wt% U

4.5.3 Actinide and rare earth drawdown

The purpose of actinide and rare earth drawdown is to decontaminate the molten salt and reduce the actinide and rare earth elements into two groups. Therefore, the solid cathode was considered.

The current can be applied. However due to the lack of supply from the anode when doing the electrolysis, the current may need to be adjusted continuously to make sure it can be supported by the ions. Here studies mainly focused on the potential control of applying a constant potential. The initial concentrations of U and Pu were set to 0.6 wt% and 1 wt%, respectively. Concentrations of other element were set according to their ratios to Pu in EBR used driver fuel (The composition of Am in fuel was set to 0.5%). The composition is listed in Table 4.17. Their equilibrium potentials under these conditions are listed in Table 4.18. But considering the overpotential, a more negative potential than its equilibrium potential is needed to deposit an element out.

Table 4.17. Initial composition of LiCl-KCl electrolyte before electrolysis

Elements	U	Pu	Am	Gd	Ce	La
wt%	0.6	1.0	1.211	0.012	1.312	0.688

Table 4.18. Equilibrium potential corresponding to the initial composition

Elements	U	Pu	Am	Gd	Ce	La
E^{eq} (V vs. Ag/AgCl)	-1.405	-1.704	-1.853	-1.990	-1.957	-2.002

A potential of -2.1 V was tested first. Figure 4.45 shows the current of each species, which decreases with time. Figure 4.46 and Figure 4.47 plot the deposition amount on the cathode and composition changes in the electrolyte. Figure 4.48 shows the separation factor, which is defined to be the percentage of an element removed from the molten salt. Almost all of the U and Pu were deposited out. Around 98% of Am was reduced. However, the product included large amounts of rare earth elements. The redox potential of Am is next to these of rare earth elements, if it is decontaminated in a high degree, the rare earth will inevitably be reduced simultaneously.

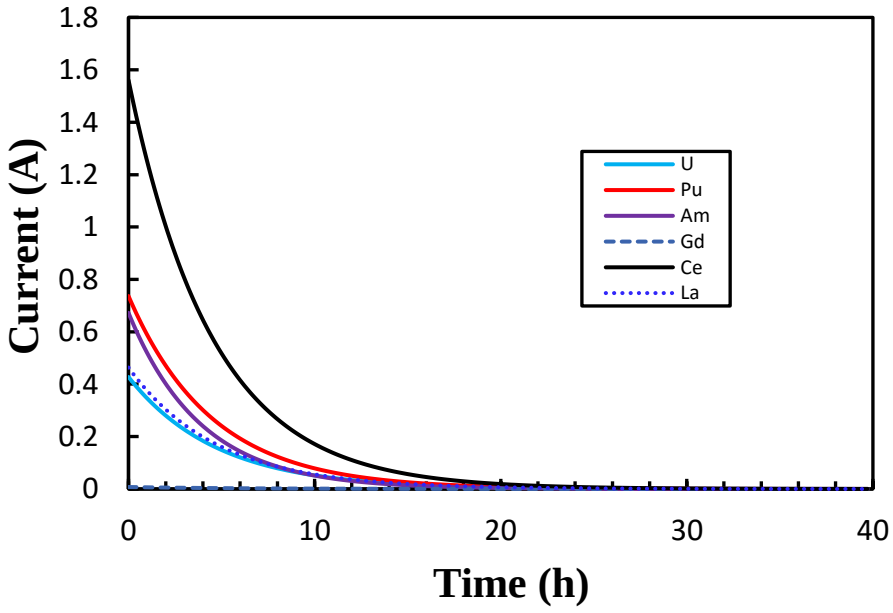

Figure 4.45. Current of each species

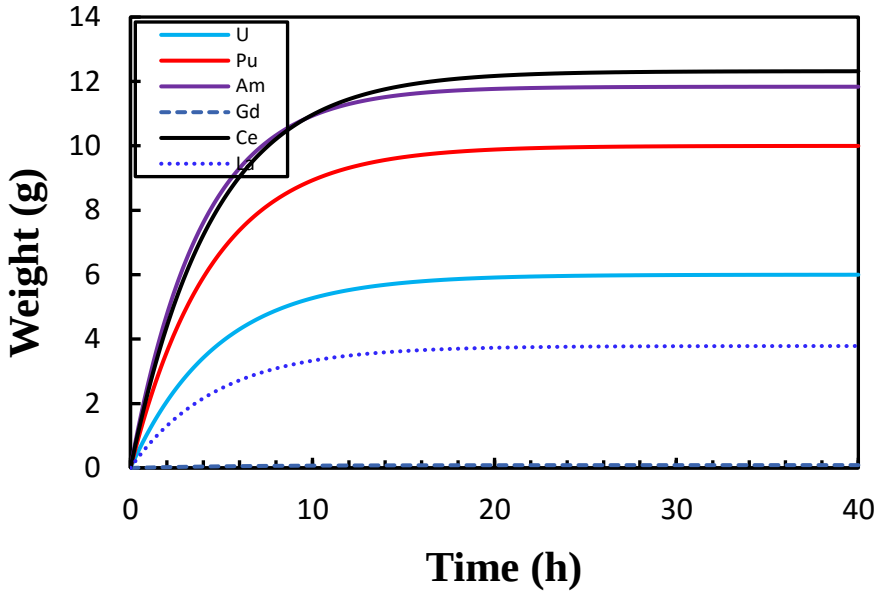

Figure 4.46. Deposition on the cathode

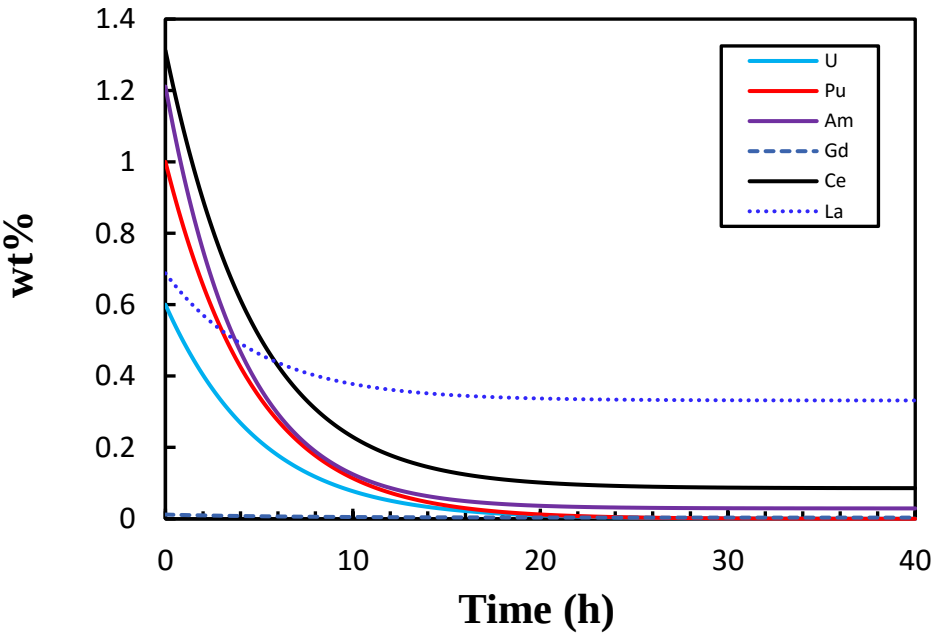

Figure 4.47. Concentration in molten salt electrolyte

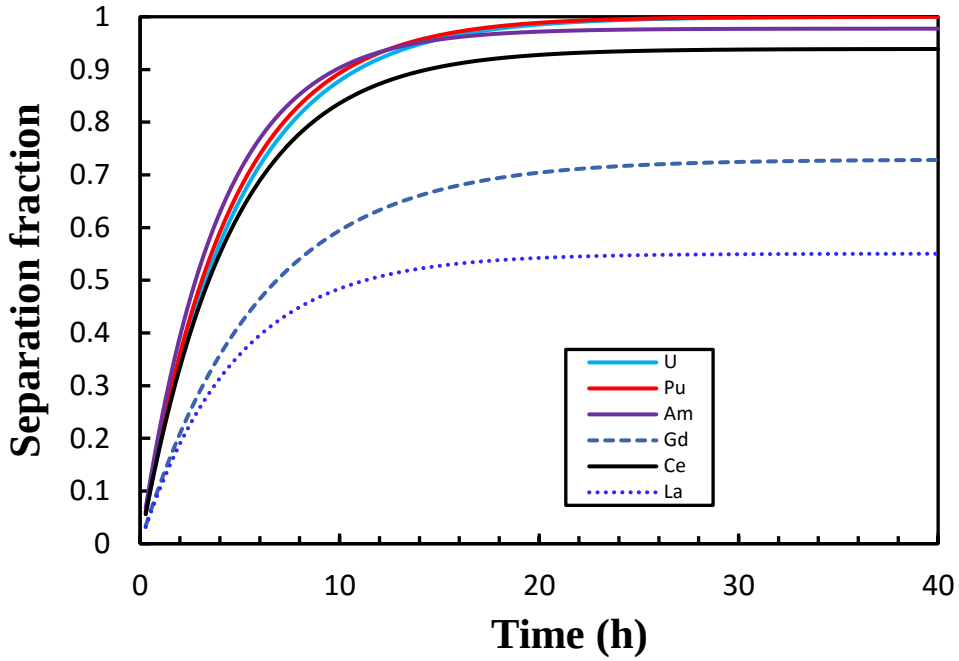

Figure 4.48. Separation factor

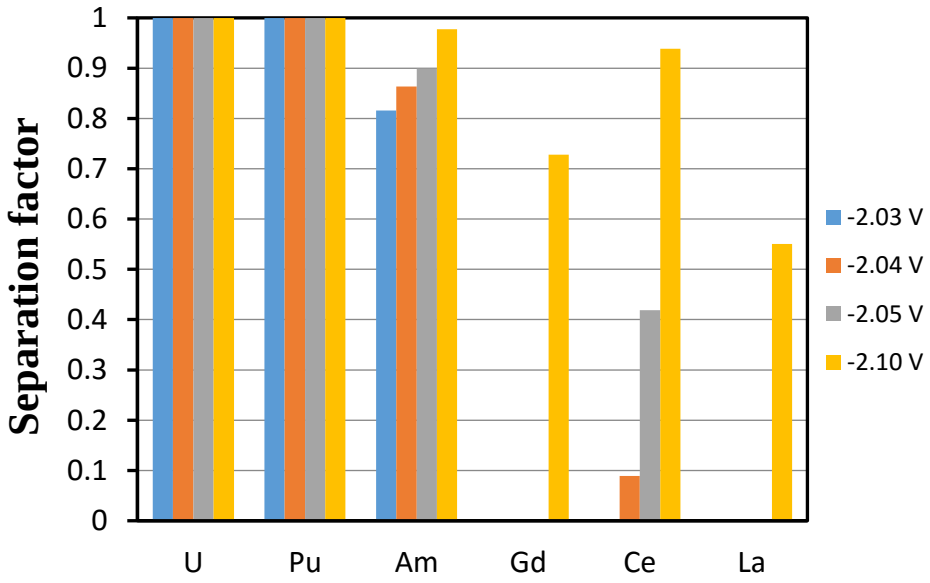

Figure 4.49. Separation factor at different potentials

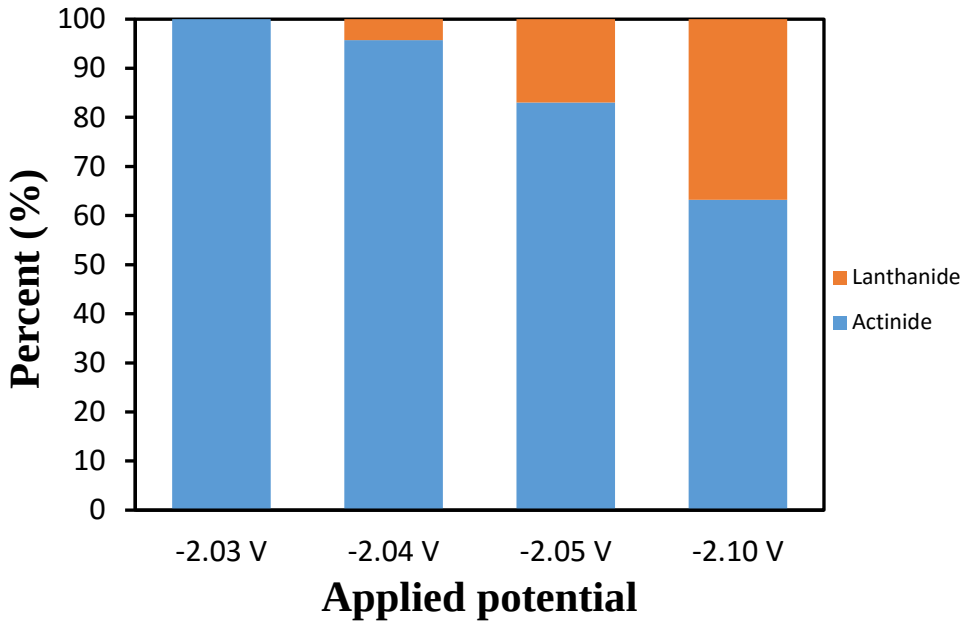

Figure 4.50. Deposition product composition

Figure 4.49 and Figure 4.50 plot the separation factors and deposition product composition at different applied potentials. It indicates that without the deposition of lanthanides, Am could only have a separation factor of around 82% under current conditions. More Am is separated; more lanthanide would be in the product. After the decontamination of actinide, apply a potential just above the redox potential of Li^+/Li (-2.38 vs. Ag/AgCl [172]), all the lanthanides could be deposited out, as shown in Figure 4.51

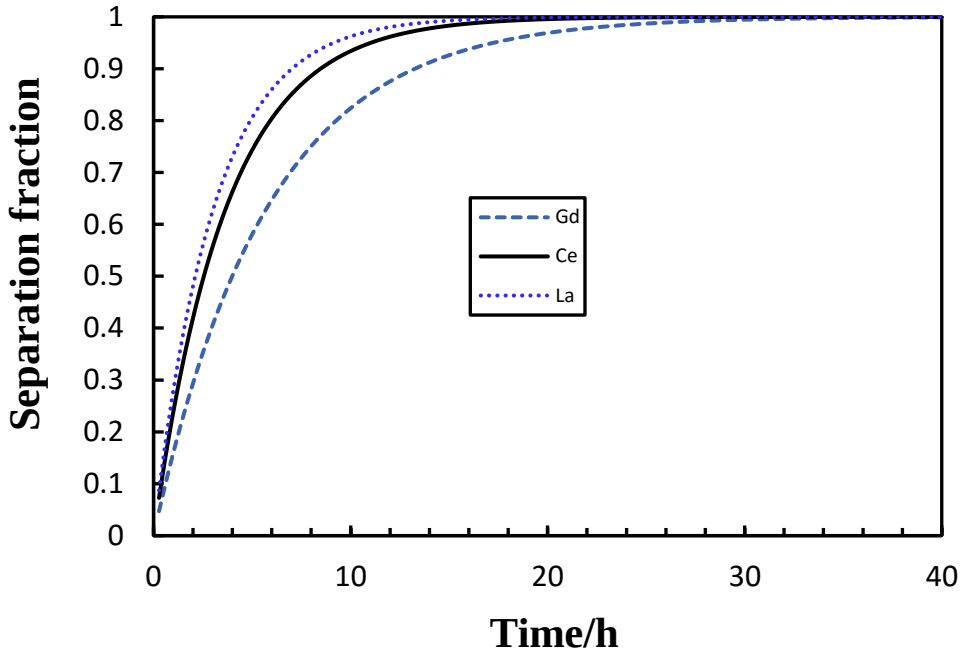

Figure 4.51. Separation factor of lanthanides when applying a potential of -2.38 V

4.5.4 Integrated model construction and case study

The final objective is to construct an integrated model for safeguarding the pyroprocessing facility. Figure 4.52 shows the schematic flow of the model, which mainly includes U deposition on a solid cathode, U/TRU separation into the liquid cathode, actinide and rare earth drawdown processes. Initially, the electrolyte composition, anode and cathode properties, current applied, flow conditions, and fundamental data are provided to conduct the electrorefining of depositing U on a solid electrode. Different criteria can be used to switch the solid electrode to liquid cadmium electrode for the U/TRU separation, i.e. cycle number and $PuCl_3$ concentration. One cycle number stands for the exhaustion of U in one anode basket. After the decontamination of the majority of the U and Pu, the molten salt is electrolyzed to draw down the remaining actinides. An applied potential or required separation factors need to be provided in this step due to incomplete separation of Am without deposition of rare earth elements. Finally, the rare earth elements are collected by applying a negative enough potential following the removal of the actinides. Basically, the output from the last step is used as the input of next one. During all the simulations, essentially, dissolution fraction of the anode, composition changes in the electrolyte and liquid cadmium, deposition amount in the cathode, anode and cathode potential, partial current of each element, and separation factors are recorded to be used as the safeguards signatures. When the measurements and signals from the processing do not follow the same route as the simulation, an alarm is triggered to alert the inspectors to stop the processing and close the material balance to detect possible diversions of U and Pu.

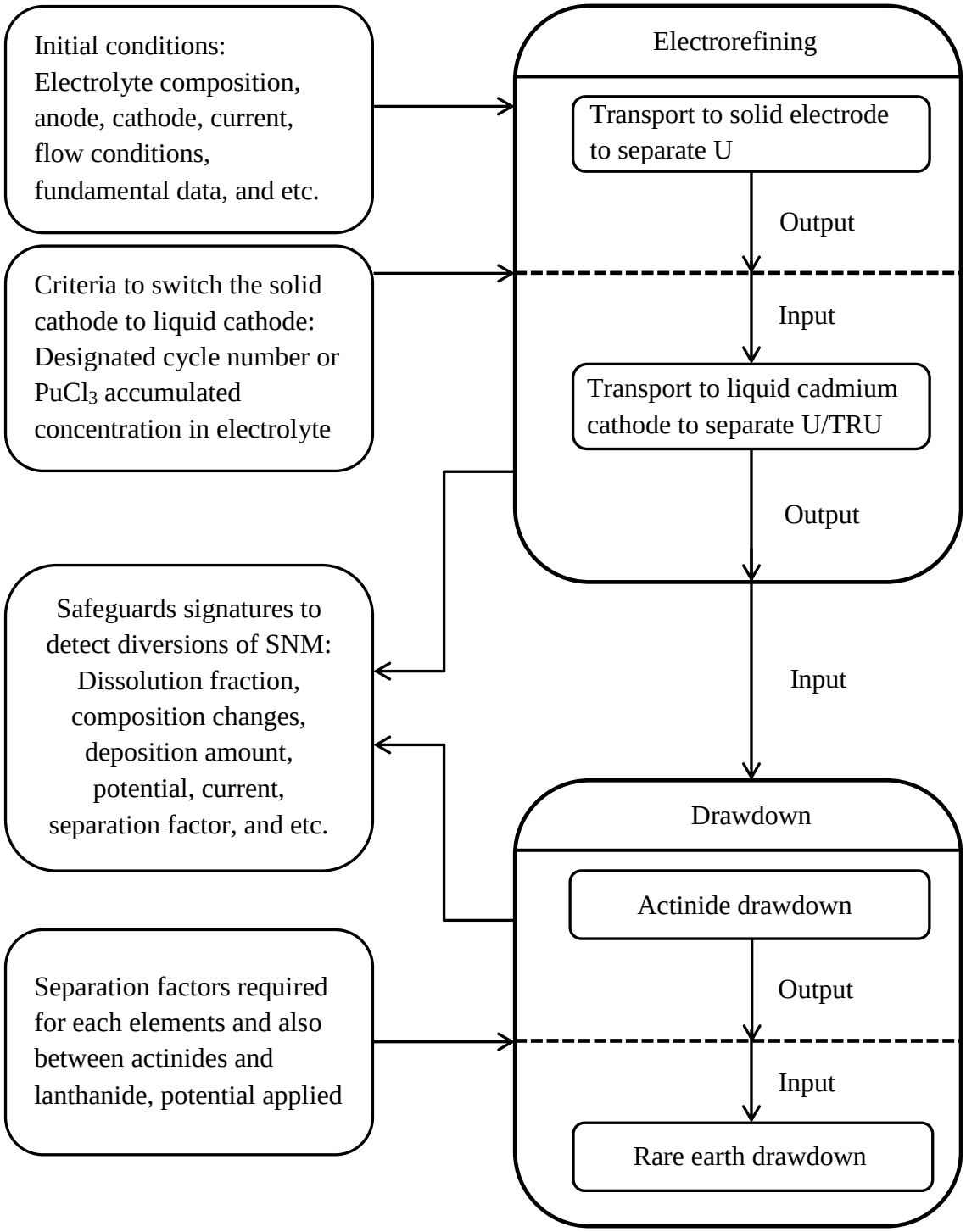

Figure 4.52. Schematic flow of the integrated model

An example was studied as below. To transport U to the solid cathode, the current was set to 100 A and the anode loading contains 250 fuel segments. Each segment was 9.6 g and totally weight was 2.4 kg. When the concentration of Pu in LiCl-KCl electrolyte reached 3 wt%, the solid cathode was switched to liquid cadmium cathode to co-deposit the Pu with other actinides. The process was run with three cycles with 100 hours for each cycle to dissolve all the U in the anode. The initial concentration of U was 6 wt% for each cycle. The current was decreased by 5% each time when the actinide could not support the current, to avoid the dissolution and deposition of Zr. Figure 4.53 and Figure 4.54 shows the anode and cathode current, respectively, in three cycles. Only U deposited on the solid cathode by controlling the current as indicated in Figure 4.55. Figure 4.56 plots the anode and cathode potentials. Basically, they keep almost constant due to the lack of dissolution and deposition of Zr. The concentrations of species are shown in Figure 4.57 and listed in Table 4.19, which was used as the input when switching to liquid cadmium cathode.

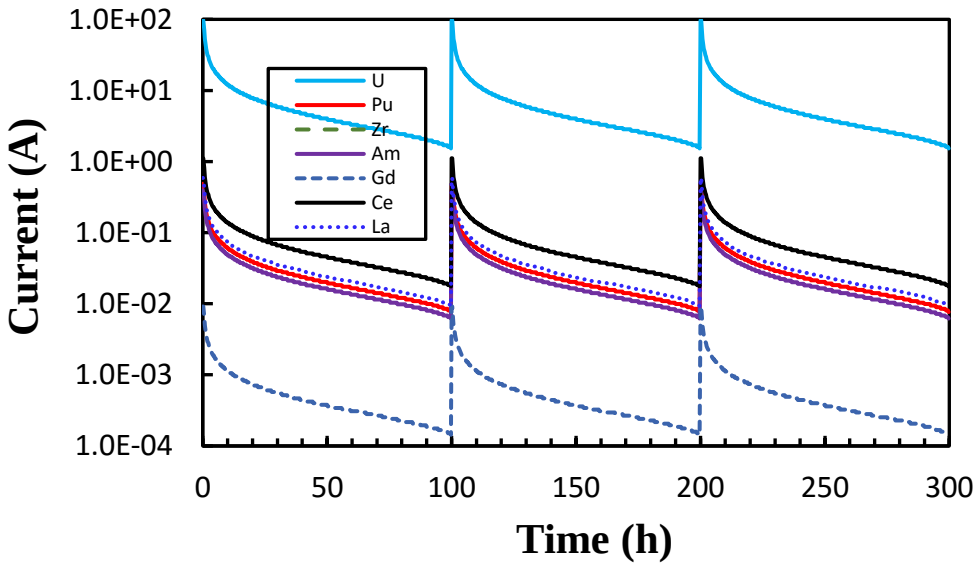

Figure 4.53. Anode current

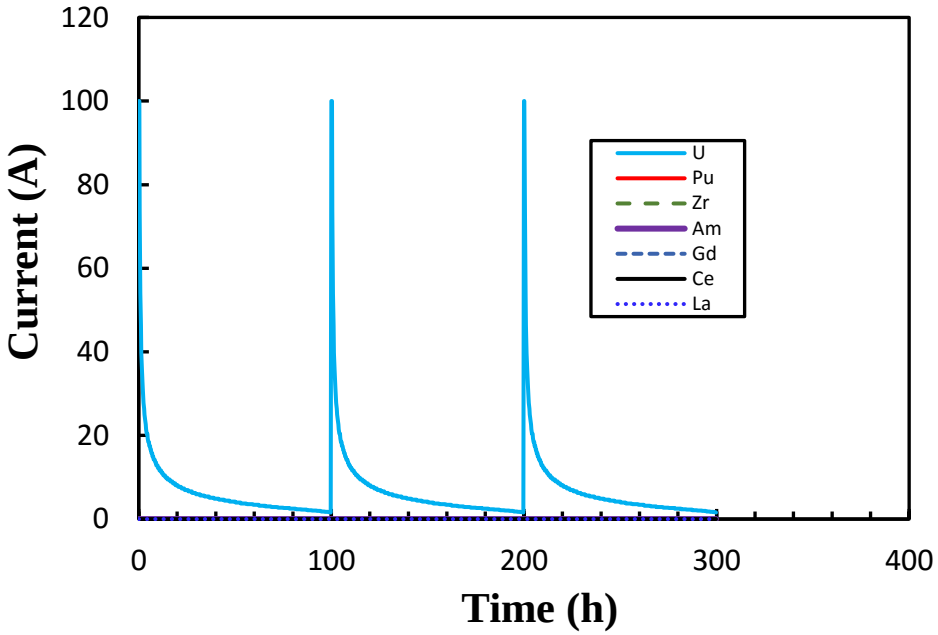

Figure 4.54. Cathode current

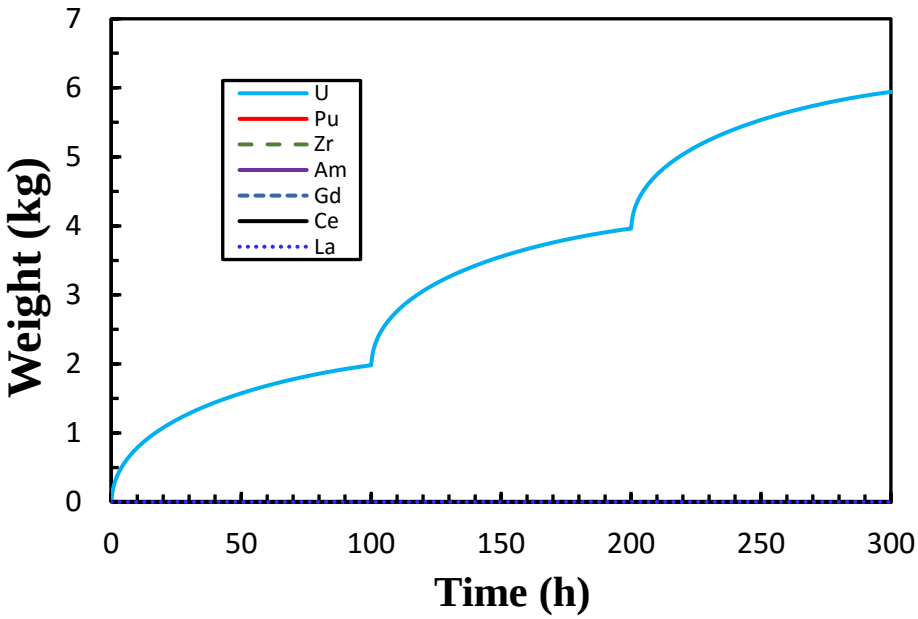

Figure 4.55. Deposition on the cathode

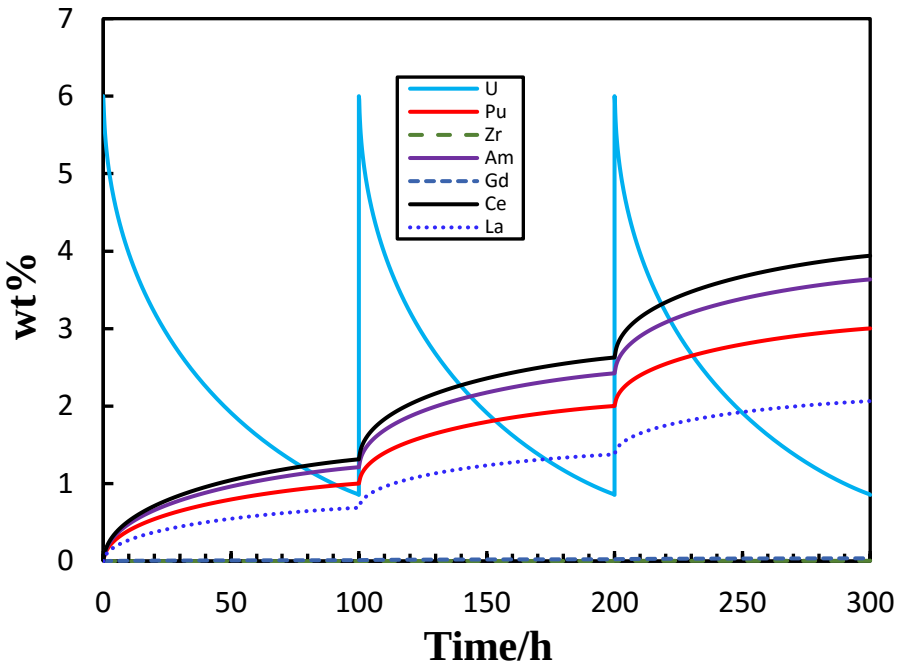

Figure 4.56. Concentration in electrolyte

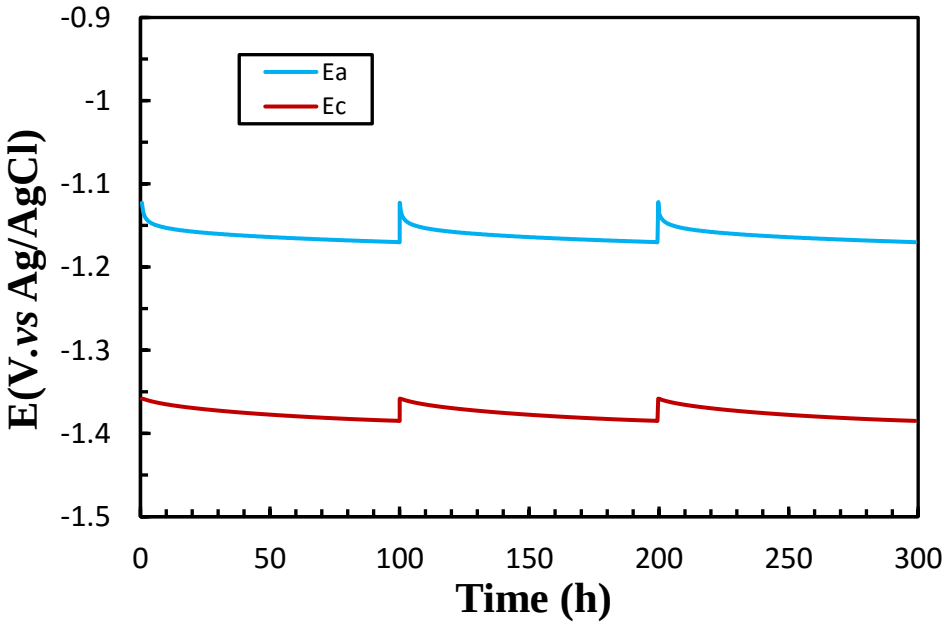

Figure 4.57. Anode and cathode potential

Table 4.19. Concentration of each species in electrolyte after three cycles

Elements	Zr	U	Pu	Am	Gd	Ce	La
wt%	0	0.855	3.003	3.635	0.036	3.940	2.065

For electrorefining using liquid cadmium, according to section 4.5.2, the most efficient method is using an inert anode electrode to stop the U supply from the anode so that Pu can be removed efficiently. Here all the conditions were set as the section 4.5.2 and the mass of Cd was 1000 g to avoid any saturation. The simulation duration was 35 h because of the rapid deposition of Ce after that. Figure 4.58 shows the cathode current. It can be observed that the main deposition was the Pu, Am, and U, which can also be seen from Figure 4.59. Figure 4.60 plots the concentration of each species in the molten salt electrolyte. Figure 4.61 is the cathode potential. It almost kept constant because all of the species started to deposit on the cathode at the beginning. Table 4.20 lists the concentrations of species at the end of the simulation

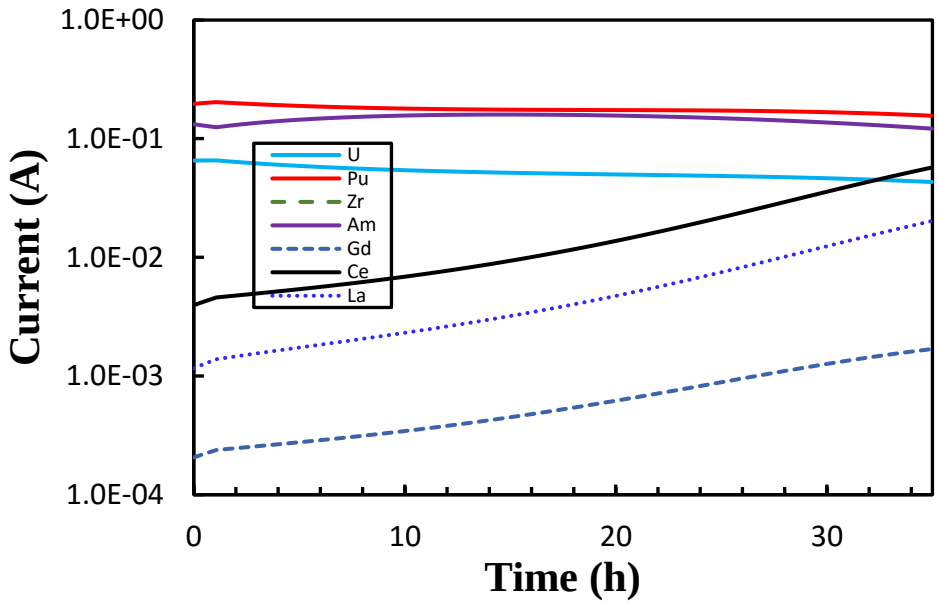

Figure 4.58. Cathode current

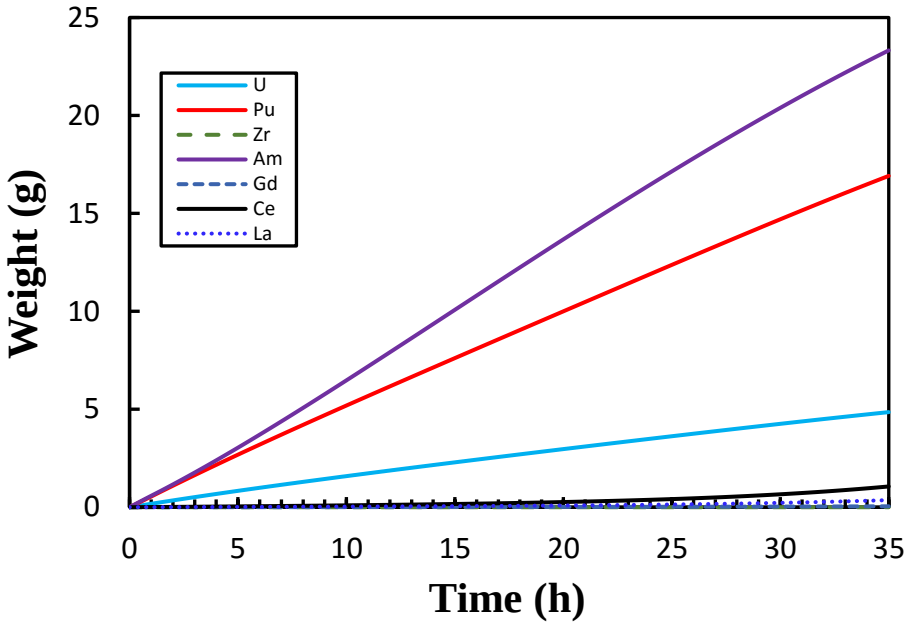

Figure 4.59. Deposition on the cathode

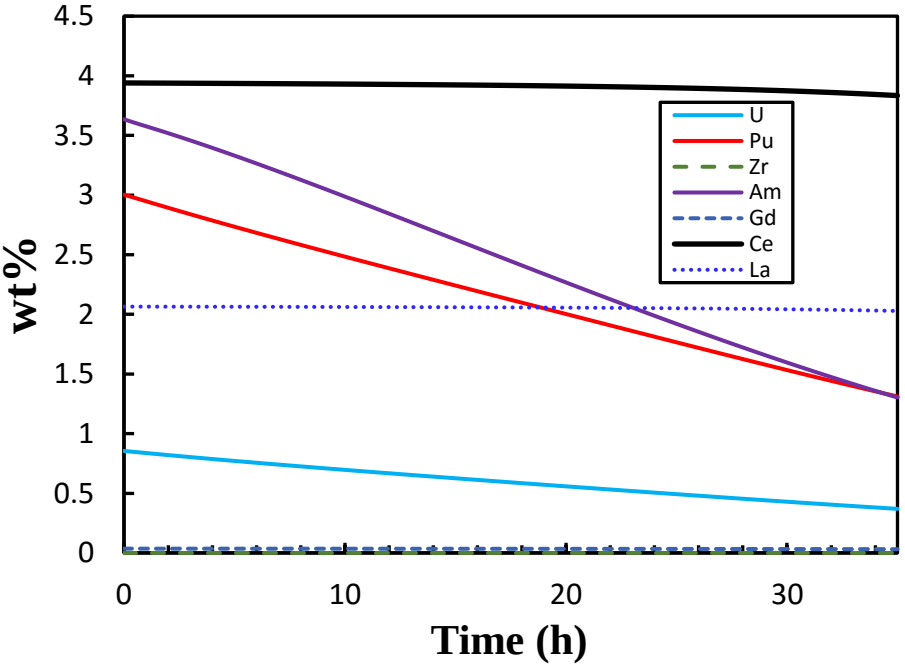

Figure 4.60. Concentration in electrolyte

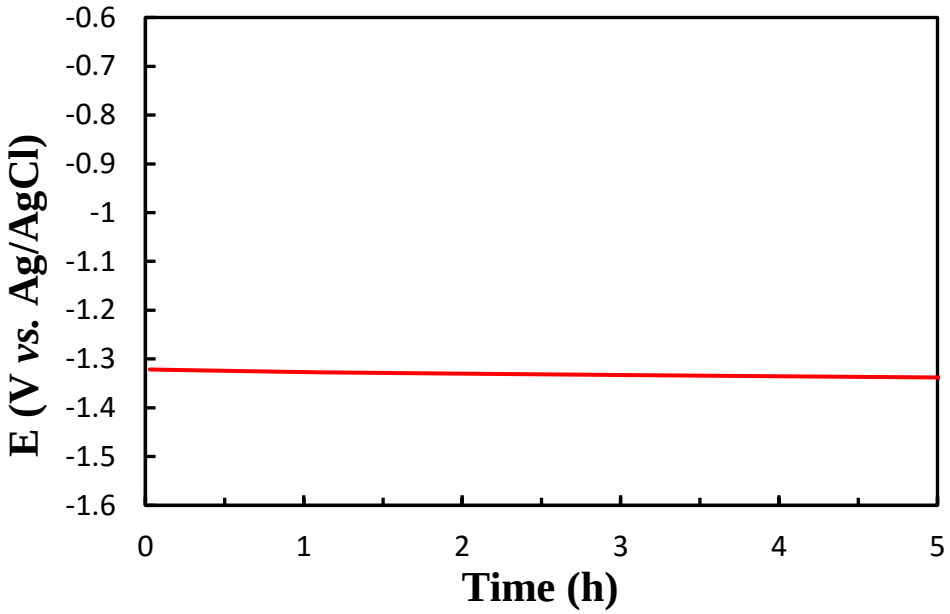

Figure 4.61. Cathode potential

Table 4.20. Concentration of each species in electrolyte after removal of Pu

Elements	Zr	U	Pu	Am	Gd	Ce	La
wt%	0	0.370	1.312	1.303	0.031	3.834	2.029

The separation factor for each species and the composition of the deposition product are shown in Figure 4.62. More than half the actinides were deposited into the liquid cadmium cathode. The deposition product was a mixture of actinides and a small amount of lanthanide, which was around 3 wt% totally.

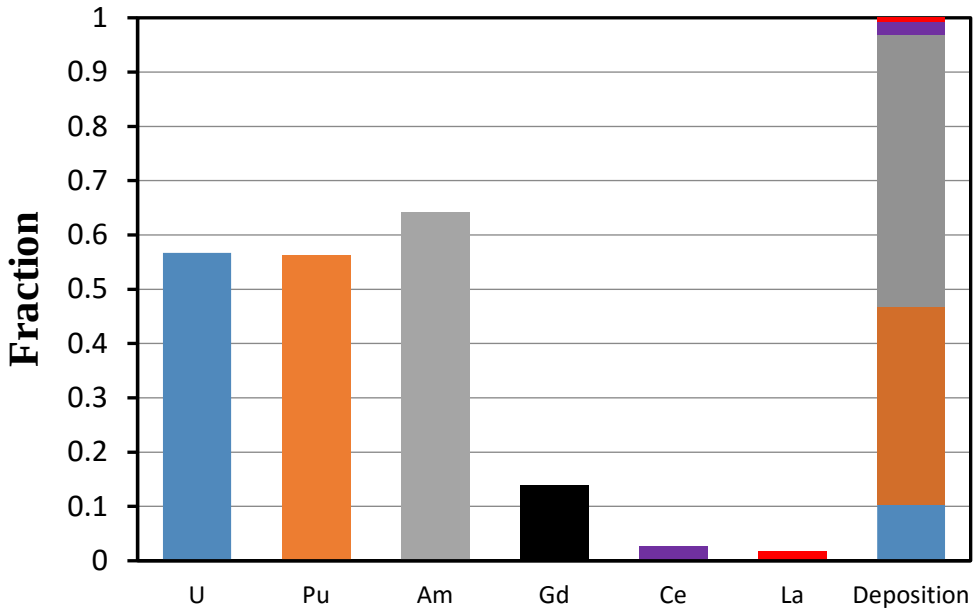

Figure 4.62. Separation factor of each species and the composition of deposition product

Then the molten salt with lanthanides and residue actinides was electrolyzed to draw down the actinides first. The applied potential was -2.015 V to maximize the separation of Am and minimize the separation of lanthanides. Other conditions were the same as section 4.5.3. Figure 4.63 shows the cathode current. Ce but not Gd would deposit with the actinides. That is due to the high concentration of Ce, which increases its redox potential. Figure 4.64 and Figure 4.65 give the deposition amount at the cathode and concentration in the molten salt electrolyte, respectively. Figure 4.66 plots the separation factor of each species and the composition of deposition product. All the U and Pu, while only 73 wt% of Am, were separated. The deposition product was comprised of 95% actinides and 5% lanthanides. If a more positive potential is applied, actinides and lanthanides can each be separated better while more Am will be left in the molten salt. Table 4.21 lists the concentration of each species after actinide drawdown which was used as the input for lanthanide drawdown.

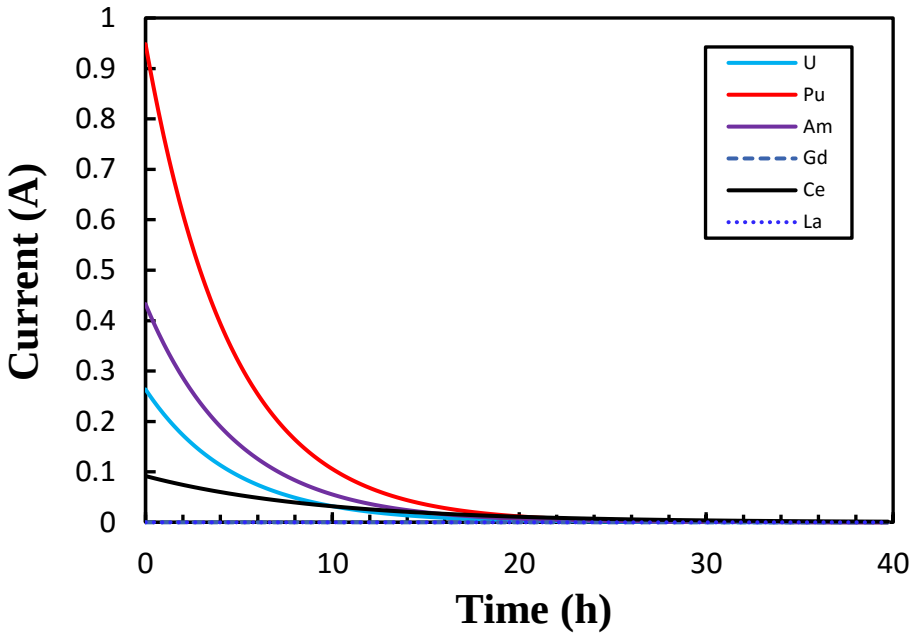

Figure 4.63. Cathode current

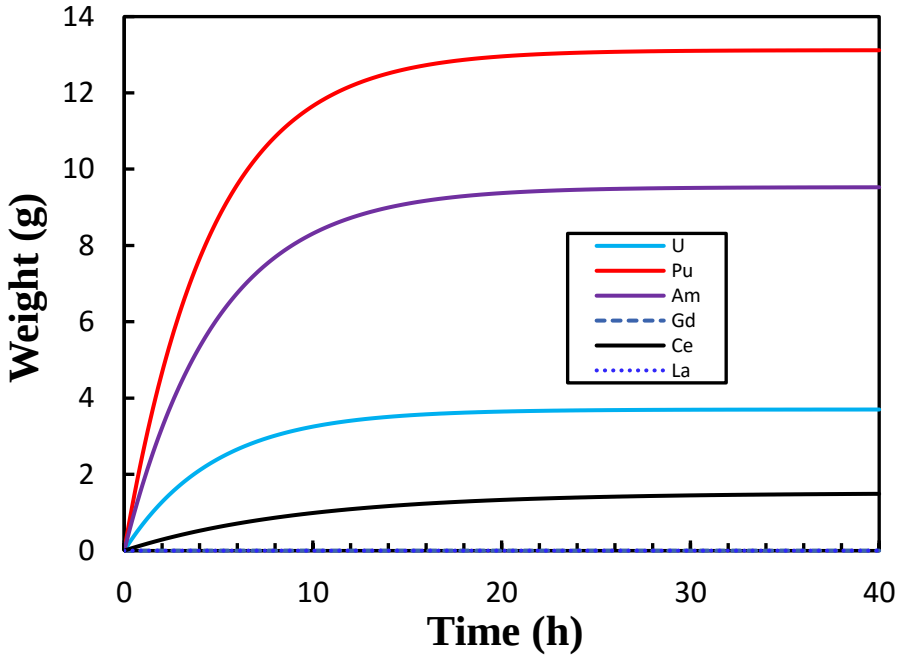

Figure 4.64. Deposition on the cathode

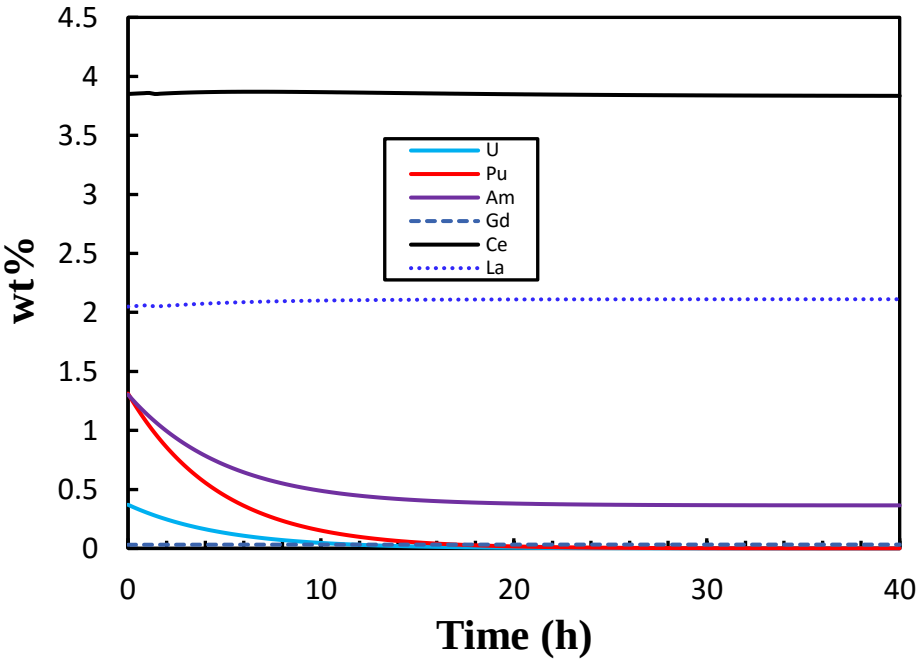

Figure 4.65. Concentration in the molten salt electrolyte

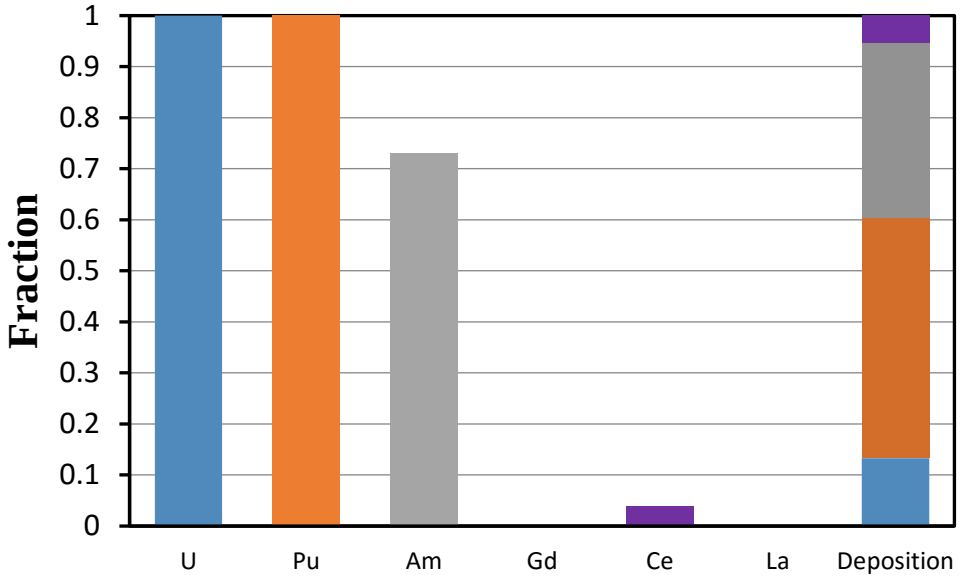

Figure 4.66. Separation factor of each species and the composition of deposition product

Table 4.21. Concentration of each species after actinide drawdown

Elements	Zr	U	Pu	Am	Gd	Ce	La
wt%	0	0	0	0.350	0.031	3.685	2.029

For the lanthanide drawdown, a negative enough potential of -2.38 V, which is just above the Li+/Li reduction potential was applied. All other conditions were the same as in the section 4.5.3. Figure 4.67 shows the cathode current. Figure 4.68 and Figure 4.69 give the deposition amount on the cathode and concentration in the electrolyte. Basically, all the remaining Am, Gd, Ce, and La were separated completely from the molten salt.

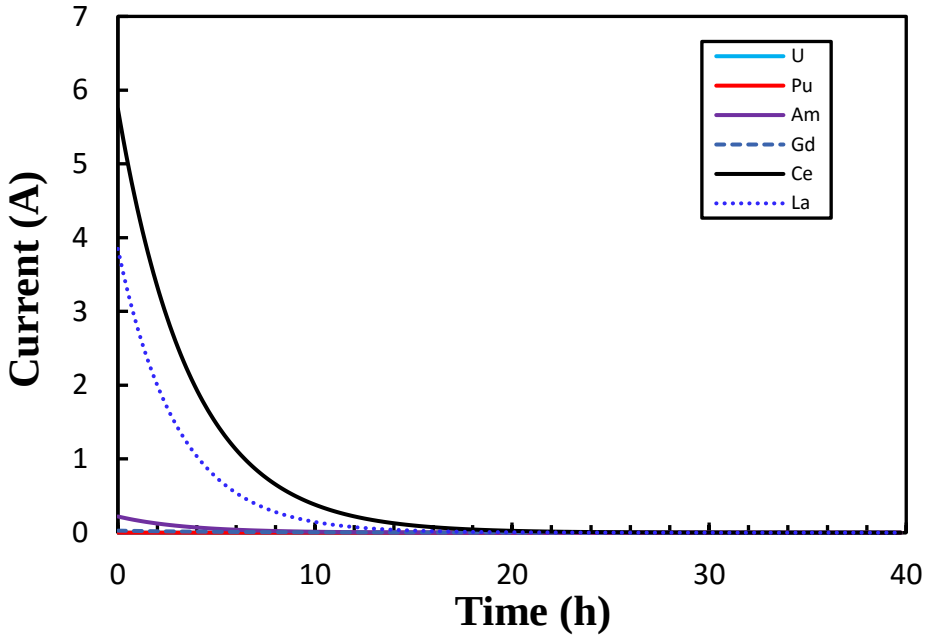

Figure 4.67. Cathode current

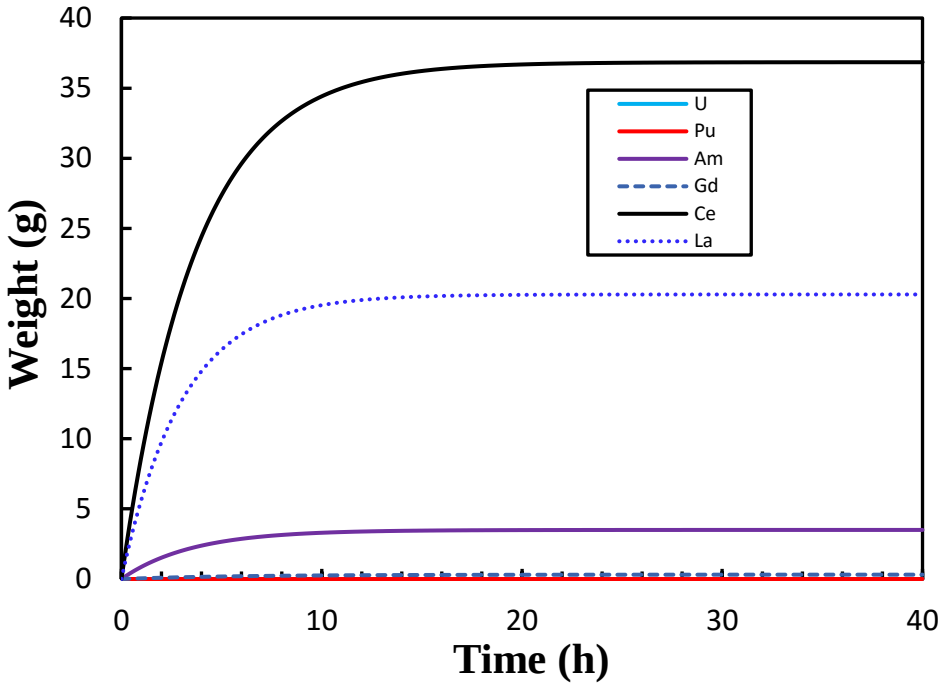

Figure 4.68. Deposition on the cathode

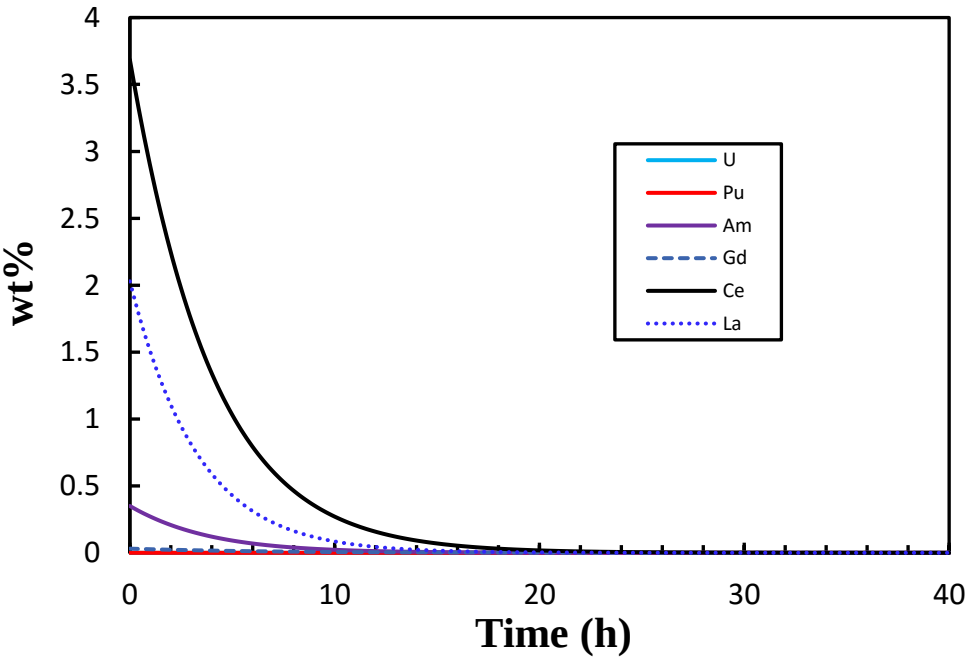

Figure 4.69. Concentration in molten salt electrolyte

4.6 Conclusions

In this chapter, integrating all the previous calculation data, an integrated model was developed to predict the electrorefining performance during the pyroprocessing. The model was validated by literature data. Then under different cases, the model was used to predict the material transport and separation for the electrorefining, actinide and rare earth. In order to avoid dissolution and deposition of Zr, stepwise current can be applied. When the cathode is switched to liquid cathode from solid cathode, a lower concentration of U and unsaturated Cd benefit the deposition of Pu. The most efficient method to remove Pu is using an electrolysis model to stop the supplement of U from the anode. In the drawdown process, Am cannot be separated completely without the co-deposition of lanthanides. All the lanthanides can be decontaminated with a negative potential just above Li+/Li reduction potential. The integrated model shows the very promising capability to simulate each process in pyroprocessing to provide safeguards signatures.

5 Summary and future work

5.1 Summary

In the present study, the MD method was applied to calculate the fundamental properties of UCl_3 in eutectic LiCl-KCl molten salt, namely activity coefficient, apparent potential, and diffusion coefficient to a high concentration up 3 mol%. Attention was focused on their concentration dependence as researchers have seldom addressed this in previous literature. The calculated results indicate that the activity coefficient and apparent increased with concentration. The diffusion coefficient showed little variation at low concentration but it increased and then decreased with higher concentrations, even though the variation of the range of diffusivity was not very significant.

In the meantime, properties of the LiCl-KCl-$PuCl_3$ system were evaluated by the CALPHAD method. The isotherm sections and liquidus projection of this system were plotted. The solubility of $PuCl_3$ was found to be 41.5 mol% at 773 K and its apparent potential also showed a trend of increase with the concentration. Our calculation sheds light on the understanding of the elements' behavior in LiCl-KCl molten salt and provides reference data at high concentrations, which will benefit the safeguards of pyroprocessing.

Integrating all the calculated results and electrochemical theories, a kinetic model was constructed considering the diffusion in the electrolyte, diffusion in anode used fuel, and Faraday process on the electrode surface. The model was validated by literature experiments and showed the robust ability to predict the material transport in different batches in an electrorefiner. Then under different conditions, the model was studied to evaluate the performance of electrorefining, actinide drawdown, and rare earth drawdown processes. The results show that for the solid used fuel anode,

Zr would co-dissolve with U but a stepwise current could be a method to resolve this problem. However, a longer time was needed to dissolve the same quantity of U. And frequent current change could bring some technical problems. When using liquid cadmium as the cathode, Pu, U, and even lanthanides were inevitably deposited simultaneously into the cathode. The unsaturated state of Cd and low initial concentration of U in electrolyte benefit the deposition of Pu. For the actinide drawdown, complete separation of Am from the molten salt was impossible without the deposition of lanthanides due to its low redox potential. After the actinide drawdown, basically, all the lanthanides could be reduced when applying a potential just above the redox potential of Li+/Li.

Given the conditions of a pyroprocessing, the model could be run to simulate the separation process, based on which, safeguard signatures can be provided to detect any scenario of SNM diversion. When the current, potential, and other signals measured have a large discrepancy with the predictions of the model, an alert should be given to stop the facility and close the material balance.

5.2 Future work

Some suggestions of future work include investigations on the:

- Electron transfer coefficients and exchange currents of the elements.
- Effects of solute concentration on the fundamental data and species interference with each other in a multicomponent system.
- How the anode dissolution limits the material transport
- Nucleation process during cathode deposition
- Effect of uranium dendrite on the deposition

References

[1] Chang, Yoon I. "The integral fast reactor." *Nuclear Technology* 88.2 (1989): 129-138.

[2] Miller, William E., and Zygmunt Tomczuk. "Pyroprocess for processing spent nuclear fuel." U.S. Patent No. 6,461,576. 8 Oct. 2002.

[3] Chang, Yoon II, "Integral Fast Reactor and Associated Fuel Cycle System: Part 3. Status of Pyroprocess Development", IAEA/ICTP School on Physics and Technology of Fast Reactor Systems, Trieste, Italy, November 9-20, 2009

[4] Choi, Eun-Young, and Sang Mun Jeong. "Electrochemical processing of spent nuclear fuels: an overview of oxide reduction in pyroprocessing technology." *Progress in Natural Science: Materials International* 25.6 (2015): 572-582.

[5] An Experimental Study of Molten Salt Electrorefining of Uranium Using Solid Iron Cathode and Liquid Cadmium Cathode for Development of Pyrometallurgical Reprocessing

[6] Inoue, Tadashi, and Tadafumi Koyama. "An Overview of CRIEPI Pyroprocessing Activities." *Actinide and Fission Product Partitioning and Transmutation*: 187.

[7] Jang, Jun-Hyuk, et al. "Development of continuous ingot casting process for uranium dendrites in pyroprocess." *Journal of Radioanalytical and Nuclear Chemistry* 295.3 (2013): 1743-1751.

[8] Williamson, M. A., and J. L. Willit. "Pyroprocessing flowsheets for recycling used nuclear fuel." *Nuclear Engineering and Technology* 43.4 (2011): 329-334.

[9] Simpson, Michael F. "Developments of Spent Nuclear Fuel Pyroprocessing Technology at Idaho National Laboratory." *Idaho National Laboratory, INL/EXT-12-25124, Idaho Falls, ID, USA* (2012).

[10] Kessler, Günter. *Sustainable and safe nuclear fission energy: Technology and safety of fast and thermal nuclear reactors*. Springer Science & Business Media, p255, 2012.

[11] Gao, Fanxing, et al. "Criticality safety evaluation of materials concerning pyroprocessing." *Journal of nuclear science and technology* 48.6 (2011): 919-928.

[12] Iizuka, Masatoshi, et al. "Development of Plutonium Recovery Process by Molten Salt Electrorefining with Liquid Cadmium Cathode." *6th Information Exchange Meeting on Actinide and Fission Product P&T, Madrid, Spain*. 2000.

[13] Cipiti, Benjamin B., et al. "Modeling and design of integrated safeguards and security for an electrochemical reprocessing facility." *Sandia National Labs, Albuquerque* (2012).

[14] INFCIRC, IAEA. "153." The structure and content of agreements between the Agency and States required in connection with the treaty on the non-proliferation of nuclear weapons (1971).

[15] Glossary, IAEA Safeguards. "Edition, IAEA, Vienna, Austria, June 2002." (2001).

[16] Bekiert, W., et al. "Safeguarding Pyroprocessing Related Facilities in the Republic of Korea (ROK)."

[17] Cipiti, Benjamin B., et al. "Modeling and design of integrated safeguards and security for an electrochemical reprocessing facility." *Sandia National Laboratories, SAND2012-9303, Albuquerque, NM, USA* (2012).

[18] Rappleye, Devin. "Developing Safeguards for Pyroprocessing: Detection of a Plutonium Co-deposition on Solid Cathode in an Electrorefiner by Applying the Signature-Based Safeguards Approach." Master thesis, North Carolina State University, Raleigh, North Carolina (2012).
[19] Wigeland, R., T. Bjornard, and B. Castle. *The concept of goals-driven safeguards*. No. INL/EXT-09-15511. Idaho National Laboratory (INL), 2009.
[20] Zhang, Jinsuo. "Kinetic model for electrorefining, part II: Model applications and case studies." *Progress in Nuclear Energy* 70 (2014): 287-297.
[21] Lafreniere, Philip. Identification of Electrorefiner and Cathode Processing Failure Modes and Determination of Signature-Significance for Integration into a Signature Based Safeguards Framework for Pyroprocessing, The University of New Mexico, Albuquerque, New Mexico (2015).
[22] Durst, Philip C., et al. *Advanced safeguards approaches for new reprocessing facilities*. No. PNNL-16674. Pacific Northwest National Laboratory (PNNL), Richland, WA (US), 2007.
[23] Masset, Patrick, et al. "Electrochemistry of uranium in molten licl-kcl eutectic." *Journal of The Electrochemical Society* 152.6 (2005): A1109-A1115.
[24] Kuznetsov, S. A., et al. "Electrochemical behavior and some thermodynamic properties of UCl4 and UCl3 dissolved in a LiCl-KCl eutectic melt." *Journal of the Electrochemical Society* 152.4 (2005): C203-C212.
[25] Masset, Patrick, et al. "Thermochemical properties of lanthanides (Ln= La, Nd) and actinides (An= U, Np, Pu, Am) in the molten LiCl–KCl eutectic." *Journal of Nuclear Materials* 344.1 (2005): 173-179.
[26] Shirai, Osamu, Hajimu Yamana, and Yasuo Arai. "Electrochemical behavior of actinides and actinide nitrides in LiCl–KCl eutectic melts." *Journal of alloys and compounds* 408 (2006): 1267-1273.
[27] Roy, J. J., et al. "Thermodynamic Properties of U, Np, Pu, and Am in Molten LiCl-KCl Eutectic and Liquid Cadmium." *Journal of the Electrochemical Society* 143.8 (1996): 2487-2492.
[28] Hoover, Robert O., et al. "Electrochemical studies and analysis of 1–10wt% UCl 3 concentrations in molten LiCl–KCl eutectic." *Journal of Nuclear Materials* 452.1 (2014): 389-396.
[29] Sakamura, Y., et al. "Measurement of standard potentials of actinides (U, Np, Pu, Am) in LiCl–KCl eutectic salt and separation of actinides from rare earths by electrorefining." *Journal of alloys and compounds* 271 (1998): 592-596.
[30] Shirai, Osamu, et al. "Electrode Reaction of the U^{3+}/U Couple at Liquid Cd and Bi Electrodes in LiCl-KCl Eutectic Melts." *Analytical Sciences/Supplements* 17.0 (2002): i959-i962.
[31] Ghosh, Suddhasattwa, et al. "Experimental investigations and thermodynamic modelling of KCl–LiCl–UCl_3 system." *Calphad* 45 (2014): 11-26.
[32] Inman, D., and J. O'M. Bockris. "The reversible electrode potential of the system U/UCl_3 in molten chloride solvents." *Canadian Journal of Chemistry* 39.5 (1961): 1161-1163.
[33] Gruen, Dieter M., and Robert A. Osteryoung. "MEASUREMEKT OF THE URANIUM-URANIUM (III) POTENTIAL IN LiCl-KCl EUTECTIC." *Annals of the New York Academy of Sciences* 79.1 (1960): 897-907.

[34] Inman, D., et al. "Electrode reactions in molten salts: the uranium+ uranium trichloride system." *Transactions of the Faraday Society* 55 (1959): 1904-1914.
[35] Kuznetsov, S. A., et al. "Determination of uranium and rare-earth metals separation coefficients in LiCl–KCl melt by electrochemical transient techniques." *Journal of nuclear materials* 344.1 (2005): 169-172.
[36] Martinot, L. "Some thermodynamic properties of dilute solutions of actinide chlorides in (Li-K) Cl and in (Na- K) Cl eutectics." *Journal of Inorganic and Nuclear Chemistry* 37.12 (1975): 2525-2528.
[37] Caligara, F., L. Martinot, and G. Duyckaerts. "Chronopotentiometric determination of U (III), U (IV), UO_2 (VI) and Np (IV) in molten LiCl-KCl eutectic." *Journal of Electroanalytical Chemistry and Interfacial Electrochemistry* 16.3 (1968): 335-340.
[38] Reddy, B. Prabhakara, et al. "Electrochemical studies on the redox mechanism of uranium chloride in molten LiCl–KCl eutectic." *Electrochimica Acta* 49.15 (2004): 2471-2478.
[39] Yamada, Daichi, et al. "Diffusion behavior of actinide and lanthanide elements in molten salt for reductive extraction." *Journal of Alloys and Compounds* 444 (2007): 557-560.
[40] Kobayashi, Tsuguyuki, et al. "Polarization effects in the molten salt electrorefining of spent nuclear fuel." *Journal of Nuclear Science and Technology* 32.7 (1995): 653-663.
[41] Tylka, M. M., et al. "Application of voltammetry for quantitative analysis of actinides in molten salts." *Journal of The Electrochemical Society* 162.12 (2015): H852-H859.
[42] Serp, J., et al. "Electrochemical behaviour of plutonium ion in LiCl–KCl eutectic melts." *Journal of Electroanalytical Chemistry* 561 (2004): 143-148.
[43] Sakamura, Y., et al. "Distribution behavior of plutonium and americium in LiCl–KCl eutectic/liquid cadmium systems." *Journal of Alloys and Compounds* 321.1 (2001): 76-83.
[44] Shirai, Osamu, Masatoshi Iizuka, and I. W. A. I. Takashi. "Electrode reaction of Pu^{3+}/Pu couple in LiCl-KCl eutectic Melts: Comparison of the electrode reaction at the surface of liquid Bi with that at a solid Mo electrode." *Analytical sciences* 17.1 (2001): 51-57.
[45] Nissen, D. A. "Electrochemistry of plutonium (III) in molten alkali chlorides." *Journal of Inorganic and Nuclear Chemistry* 28.8 (1966): 1740-1743.
[46] Martinot, L., and G. Duyckaerts. "Electrochemistry of Pu (III) in Molten LiCl-KCl Eutectic." Analytical Letters 4.1 (1971): 1-11.
[47] Yoon, Dalsung. "Electrochemical Studies of Cerium and Uranium in LiCl-KCl Eutectic for Fundamentals of Pyroprocessing Technology." Ph.D. Thesis, Virginia Commonwealth University, Richmond, VA (2016).
[48] Konings, R. J. M. "The ITU Material Property Data Base for f-elements and Compounds, f-MPD, 2002. Available from:< http." *www. f-elements. net*.
[49] Lemire, Robert J. *Chemical thermodynamics of neptunium and plutonium*. Vol. 4. Elsevier, 2001.
[50] Zhang, Jinsuo. "Kinetic model for electrorefining, part I: Model development and validation." *Progress in nuclear energy* 70 (2014): 279-286.
[51] Choi, Inkyu, et al. "Determination of Exchange Current Density of U^{3+}/U Couple in LiCl-KCl Eutectic Mixture." (2009).

[52] Rose, M. A., M. A. Williamson, and J. Willit. "Determining the exchange current density and Tafel constant for uranium in LiCl/KCl eutectic." *ECS Electrochemistry Letters* 4.1 (2015): C5-C7.
[53] Lim, Keun Hong, Seung Park, and Jong-Il Yun. "Study on Exchange Current Density and Transfer Coefficient of Uranium in LiCl-KCl Molten Salt." *Journal of The Electrochemical Society* 162.14 (2015): E334-E337.
[54] Ghosh, Suddhasattwa, et al. "Anodic dissolution of U, Zr and U–Zr alloy and convolution voltammetry of Zr 4+| Zr 2+ couple in molten LiCl–KCl eutectic." *Electrochimica Acta* 56.24 (2011): 8204-8218.
[55] Davies, Kim, and Shelly X. Li. "Simplified reference electrode for electrorefining of spent nuclear fuel in high temperature molten salt." *GLOBAL 2007* (2007).
[56] Fujii, Toshiyuki, et al. "Quantitative analysis of trivalent uranium and lanthanides in a molten chloride by absorption spectrophotometry." *Journal of Radioanalytical and Nuclear Chemistry* 296.1 (2013): 255-259.
[57] Johnson, Irving. "The thermodynamics of pyrochemical processes for liquid metal reactor fuel cycles." *Journal of Nuclear Materials* 154.1 (1988): 169-180.
[58] Ackerman, JOHN P., and Terry R. Johnson. "Partition of Actinides and Fission Products Between Metal and Molten Salt Phases–Theory, Measurement and Application to IFR Pyroprocess Development." *Int. Conf. Actinides*. Vol. 93. 1993.
[59] Ackerman, John P., and Jack L. Settle. "Distribution of plutonium, americium, and several rare earth fission product elements between liquid cadmium and LiCl□ KCl eutectic." *Journal of alloys and compounds* 199.1-2 (1993): 77-84.
[60] Nawada, H. P., and N. P. Bhat. "Thermochemical modelling of electrotransport of uranium and plutonium in an electrorefiner." *Nuclear engineering and design* 179.1 (1998): 75-99.
[61] Ghosh, Suddhasattwa, et al. "PRAGAMAN: A computer code for simulation of electrotransport during molten salt electrorefining." *Nuclear Technology*170.3 (2010): 430-443.
[62] Kobayashi, Tsuguyuki, and Moriyasu Tokiwai. "Development of TRAIL, a simulation code for the molten salt electrorefining of spent nuclear fuel."*Journal of alloys and compounds* 197.1 (1993): 7-16.
[63] Zhang, Jinsuo. "Kinetic model for electrorefining, part I: Model development and validation." *Progress in Nuclear Energy* 70 (2014): 279-286.
[64] Zhang, Jinsuo. "Kinetic model for electrorefining, part II: Model applications and case studies." *Progress in Nuclear Energy* 70 (2014): 287-297.
65 Gonzalez, M., et al. "Application of a One-Dimensional Transient Electrorefiner Model to Predict Partitioning of Plutonium from Curium in a Pyrochemical Spent Fuel Treatment Process." *Nuclear Technology* 192.2 (2015): 165-171.
[66] Hoover, Robert, et al. "A Computational Model of the Mark-IV Electrorefiner: Phase I—Fuel Basket/Salt Interface." *Journal of Engineering for Gas Turbines and Power* 131.5 (2009): 054503.
[67] Hoover, Robert O., et al. "Development of computational models for the mark-IV electrorefiner-Effect of uranium, plutonium, and zirconium dissolution at the fuel basket-salt interface." *Nuclear technology* 171.3 (2010): 276-284.

[68] Cumberland, Riley M., and Man-Sung Yim. "Development of a 1D transient electrorefiner model for pyroprocess simulation." *Annals of Nuclear Energy*71 (2014): 52-59.
[69] Cumberland, Riley M., and Man-Sung Yim. "A computational meta-analysis of UCl3 cyclic voltammograms in LiCl-KCl electrolyte." *Journal of The Electrochemical Society* 161.4 (2014): D147-D149.
[70] Ghosh, Suddhasattwa, et al. "Exchange Current Density and Diffusion Layer Thickness in Molten LiCl-KCl Eutectic: A Modeling Perspective for Pyroprocessing of Metal Fuels." *Nuclear Technology* 195.3 (2016): 253-272.
[71] Bae, Judong, et al. "A Time-Dependent Electrochemical Model of Pyrochemical Partitioning for Waste Transmutation" Proc. Global 2003, New Orleans, Louisiana (2003): 784
[72] Bae, Judong, et al. "Numerical assessment of pyrochemical process performance for PEACER system." *Nuclear Engineering and Design* 240.6 (2010): 1679-1687.
[73] Choi, Sungyeol, et al. "Three-dimensional multispecies current density simulation of molten-salt electrorefining." *Journal of Alloys and Compounds*503.1 (2010): 177-185.
[74] Krishna Srihari, B., et al. "Modeling the Molten Salt Electrorefining Process for Spent Metal Fuel Using COMSOL." *Separation Science and Technology*50.15 (2015): 2276-2283.
[75] Bae, Judong, et al. "Numerical assessment of pyrochemical process performance for PEACER system." *Nuclear Engineering and Design* 240.6 (2010): 1679-1687.
[76] Bagri, Prashant, and Michael F. Simpson. "Determination of activity coefficient of lanthanum chloride in molten LiCl-KCl eutectic salt as a function of cesium chloride and lanthanum chloride concentrations using electromotive force measurements." *Journal of Nuclear Materials* 482 (2016): 248-256.
[77] Frenkel, Daan, and Berend Smit. *Understanding molecular simulation: from algorithms to applications*. Vol. 1. Academic press, 2001.
[78] Shpil'rain, E. E., et al. "Activity of the components of binary alloys of alkali metals: Na–K system." *High temperature* 40.1 (2002): 33-43.
[79] Rodrigues P C R, Fernandes F M S S. Phase diagrams of alkali halides using two interaction models: A molecular dynamics and free energy study[J]. The Journal of chemical physics, 2007, 126(2): 024503.
[80] Kato T, Inoue T, Iwai T, et al. Separation behaviors of actinides from rare-earths in molten salt electrorefining using saturated liquid cadmium cathode[J]. Journal of Nuclear materials, 2006, 357(1): 105-114.
[81] Zhou, Wentao, and Jinsuo Zhang. "Direct Calculation of Concentration-Dependent Activity Coefficient of UCl3 in Molten LiCl-KCl." Journal of The Electrochemical Society 162.10 (2015): E199-E204.
[82] Watanabe M, Reinhardt W P. Direct dynamical calculation of entropy and free energy by adiabatic switching[J]. Physical review letters, 1990, 65(26): 3301.
[83] Aragones J L, Valeriani C, Vega C. Note: Free energy calculations for atomic solids through the Einstein crystal/molecule methodology using GROMACS and LAMMPS[J]. The Journal of chemical physics, 2012, 137(14): 146101.
[84] Allen M P, Tildesley D J. Computer simulation of liquids[M]. Oxford university press, 1989.

[85] Croteau T, Patey G N. Structures and rearrangements of LiCl clusters. The Journal of chemical physics, 2006, 124(24): 244506-244506.
[86] Tosi M P, Fumi F G. Ionic sizes and born repulsive parameters in the NaCl-type alkali halides—II: The generalized Huggins-Mayer form[J]. Journal of Physics and Chemistry of Solids, 1964, 25(1): 45-52.
[87] Salanne M, Simon C, Turq P, et al. Calculation of activities of ions in molten salts with potential application to the pyroprocessing of nuclear waste[J]. The Journal of Physical Chemistry B, 2008, 112(4): 1177-1183.
[88] Kato T, Inoue T, Iwai T, et al. Separation behaviors of actinides from rare-earths in molten salt electrorefining using saturated liquid cadmium cathode. Journal of Nuclear materials, 2006, 357(1): 105-114.
[89] Jain, Anubhav, et al. "Commentary: The Materials Project: A materials genome approach to accelerating materials innovation." *Apl Materials* 1.1 (2013): 011002.
[90] Watanabe M, Reinhardt W P. Direct dynamical calculation of entropy and free energy by adiabatic switching[J]. Physical review letters, 1990, 65(26): 3301.
[91] Plimpton, Steve. "Fast parallel algorithms for short-range molecular dynamics." *Journal of computational physics* 117.1 (1995): 1-19.
[92] http://lammps.sandia.gov/index.html
[93] Shirai, Osamu, et al. "Electrode Reaction of the U 3+/U Couple at Liquid Cd and Bi Electrodes in LiCl-KCl Eutectic Melts." *Analytical Sciences/Supplements* 17.0 (2002): i959-i962.
[94] Pankratz, L. B. *Thermodynamic properties of halides*. WA: US Department of the Interior, Bureau of Mines, 1984. p730
[95] Castrillejo Y, Bermejo M R, Barrado E, et al. Solubilization of rare earth oxides in the eutectic LiCl–KCl mixture at 450 C and in the equimolar CaCl 2–NaCl melt at 550 C. Journal of Electroanalytical Chemistry, 2003, 545: 141-157.
[96] Fusselman S P, Roy J J, Grimmett D L, et al. Thermodynamic properties for rare earths and americium in pyropartitioning process solvents. Journal of the Electrochemical Society, 1999, 146(7): 2573-2580.
[97] Castrillejo Y, Hernández P, Rodriguez J A, et al. Electrochemistry of scandium in the eutectic LiCl–KCl. Electrochimica Acta, 2012, 71: 166-172.
[98] Pankratz L B. Thermodynamic properties of halides. United States Department of the Interior, Bureau of Mines, 1984.
[99] Bermejo M R, Gómez J, Martínez A M, et al. Electrochemistry of terbium in the eutectic LiCl–KCl. Electrochimica Acta, 2008, 53(16): 5106-5112.
[100] Taylor, John R., and E. R. Cohen. "An introduction to error analysis: the study of uncertainties in physical measurements." University Science Books; 2nd edition (1997). P 193-200
[101] Einstein, A. "Über die von der molekularkinetischen Theorie der Wärme geforderte Bewegung von in ruhenden Flüssigkeiten suspendierten Teilchen". *Annalen der Physik* (in German) 322.8 (1905) 549–560
[102] Janz, George J., et al. "Molten salts: Volume 4, part 2, chlorides and mixtures—electrical conductance, density, viscosity, and surface tension data." *Journal of Physical and Chemical Reference Data* 4.4 (1975): 871-1178.
[103] Kim, Jong-Yun, et al. "High-Temperature Viscosity Measurement of LiCl-KCl Molten Salts Comprising Actinides and Lanthanides." *Bull. Korean Chem. Soc*33.11 (2012): 3871.

[104] Shpil'rain E E, Shkermontov V I, Skovorod'ko S N, et al. Activity of the components of binary alloys of alkali metals: Na–K system. High temperature, 2002, 40(1): 33-43.
[105] Zhang J. Electrochemistry of actinides and fission products in molten salts—Data review. Journal of Nuclear Materials, 2014, 447(1): 271-284.
[106] Johnson I, Yonco R M. Thermodynamics of cadmium-and zinc-rich alloys in the Cd− La, Cd− Ce, Cd− Pr, Zn− La, Zn− Ce and Zn− Pr systems. Metallurgical Transactions, 1970, 1(4): 905-910.
[107] Konings R J M, Malmbeck R, Serp J. Evaluation of thermochemical and electrochemical data for the pyrochemical partitioning process. Journal of Nuclear Science and Technology, 2002, 39(sup3): 906-909.
[108] H. Miyashiro, in: Proc. Information Exchange Meeting on Actinide and Fission Product Separation and Transmutation, OECD Nuclear Energy Agency, Mito City, Japan, November 6–8, 1990.
[109] Sridharan K, Martin S, Mohammadian M, et al. Thermal properties of LiCl-KCl molten salt for nuclear waste separation. Transactions of the American Nuclear Society, 2012, 106: 1240-1241.
[110] Lantelme F, Berghoute Y. Electrochemical Studies of LaCl3 and GdCl3 Dissolved in Fused LiCl-KCl[J]. Journal of the Electrochemical Society, 1999, 146(11): 4137-4144.
[111] Fabian C P, Luca V, Chamelot P, et al. Experimental and simulation study of the electrode reaction mechanism of La3+ in LiCl-KCl eutectic molten salt. Journal of The Electrochemical Society, 2012, 159(4): F63-F67.
[112] Fusselman S P, Roy J J, Grimmett D L, et al. Thermodynamic properties for rare earths and americium in pyropartitioning process solvents. Journal of the Electrochemical Society, 1999, 146(7): 2573-2580.
[113] Castrillejo Y, Bermejo M R, Martínez A M, et al. Electrochemical behavior of lanthanum and yttrium ions in two molten chlorides with different oxoacidic properties: The eutectic LiCl-KCl and the equimolar mixture CaCl2-NaCl. Journal of Mining and Metallurgy, Section B: Metallurgy, 2003, 39(1-2): 109-135.
[114] Matsumiya M, Matsumoto S. Electrochemical studies on lanthanum ions in molten LiCl-KCl-eutectic mixture. Zeitschrift für Naturforschung A, 2004, 59(10): 711-714.
[115] Masset P, Konings R J M, Malmbeck R, et al. Thermochemical properties of lanthanides (Ln= La, Nd) and actinides (An= U, Np, Pu, Am) in the molten LiCl–KCl eutectic. Journal of Nuclear Materials, 2005, 344(1): 173-179.
[116] Iizuka M. Studies on electrorefining and electroreduction processes for nuclear fuels in molten chloride systems. 2010.
[117] Y. Castrillejo, M.R. Bermejo, A.M. Martinez, P.D. Arocas, J. Min. Metall. 39 (1–2) (2003) 109–135.
[118] S. Ghosh, B.P. Reddy, K. Nagarajan and K.H. Kumar. "Experimental investigations and thermodynamic modelling of KCl–LiCl–UCl 3 system." *Calphad* 45 (2014): 11-26.
[119] Kaufman, Larry, and Harold Bernstein. "Computer calculation of phase diagrams. With special reference to refractory metals." (1970).
[120] Campbell, F. C. "Phase Diagram Applications." (2012).
[121] Ohtani, Hiroshi, and Kiyohito Ishida. "Application of the CALPHAD method to material design." *Thermochimica acta* 314.1 (1998): 69-77.

[122] H.L. Lukas, S.G. Fries and B. Sundman. *Computational thermodynamics: the Calphad method*. Vol. 131. Cambridge: Cambridge university press, 2007.
[123] U.R. Kattner. "The thermodynamic modeling of multicomponent phase equilibria." *JOM* 49.12 (1997): 14-19.
[124] Y.-M. Muggianu, M. Gambino, and L.P. Bros, *J. Chim. Phus.*, 72 (1975), pp. 85-88.
[125]Kaptay, George. "A new equation for the temperature dependence of the excess Gibbs energy of solution phases." *Calphad* 28.2 (2004): 115-124.
[126] Pelton, Arthur D. "A general "geometric" thermodynamic model for multicomponent solutions." *Calphad* 25.2 (2001): 319-328.
[127] J.O. Andersson, T. Helander, L. Höglund, P. Shi and B. Sundman. "Thermo-Calc & DICTRA, computational tools for materials science." *Calphad* 26.2 (2002): 273-312.
[128] C. W. Bale, E. Bélisle, P. Chartrand, S. A. Decterov, G. Eriksson, A.E. Gheribi, K. Hack, I. H. Jung, Y. B. Kang, J. Melançon, A. D. Pelton, S. Petersen, C. Robelin. J. Sangster and M-A. Van Ende, *FactSage Thermochemical Software and Databases* - 2010 - 2016, Calphad, vol. 54, pp 35-53, 2016 <www.factsage.com>
[129] Cao, Weisheng, et al. "PANDAT software with PanEngine, PanOptimizer and PanPrecipitation for multi-component phase diagram calculation and materials property simulation." *Calphad* 33.2 (2009): 328-342.
[130] M. Hillert, B. Jansson, B. Sundman. "A two-sublattice model for molten solutions with different tendency for ionization." *Metallurgical Transactions A* 16.1 (1985): 261-266.
[131] B. Sundman. "Modification of the two-sublattice model for liquids." *Calphad*15.2 (1991): 109-119.
[132] R. Benz, M. Kahn and J.A. Leary. "Phase Equilibria of the Binary System PuCl3− KCl." *The Journal of Physical Chemistry* 63.11 (1959): 1983-1984.
[133] V.Y. Buz'ko, G.Y. Chuiko and K.B. Kushkhov. "DFT study of the structure and stability of Pu (III) and Pu (IV) chloro complexes." *Russian Journal of Inorganic Chemistry* 57.1 (2012): 62-67.
[134] Y. M. Muggianu, M. Gambino, J. P. Bros, Enthalpies of formation of liquid alloys, *J. Chim. Phys*., 72 (1975): 83–88
[135] O. Redlich and A.T. Kister. "Algebraic representation of thermodynamic properties and the classification of solutions." *Industrial & Engineering Chemistry* 40.2 (1948): 345-348.
[136] H. Kopp. "Investigations of the specific heat of solid bodies."*Philosophical Transactions of the Royal Society of London* (1865): 71-202.
[137] T.W. Richards and W.B. Meldrum. "THE MELTING POINTS OF THE CHLORIDES OF LITHIUM, RUBIDIUM AND CAESIUM, AND THE FREEZING POINTS OF BINARY AND TERNARY MIXTURES OF THESE SALTS, INCLUDING ALSO POTASSIUM AND SODIUM CHLORIDE."*Journal of the American Chemical Society* 39.9 (1917): 1816-1828.
[138] E. Aukrust, B. Björge, H. Flood and T. Førland. "ACTIVITIES IN MOLTEN SALT MIXTURES OF POTASSIUM-LITHIUM-HALIDE MIXTURES: A PRELIMINARY REPORT."*Annals of the New York Academy of Sciences* 79.11 (1960): 830-837.

[139] E. Korin and L. Soifer. "Thermal analysis of the system KCl-LiCl by differential scanning calorimetry." *Journal of thermal analysis* 50.3 (1997): 347-354.
[140] A.S. Basin, A.B. Kaplun, A.B. Meshalkin and N.F. Uvarov. "The LiCl-KCl binary system." *Russian Journal of Inorganic Chemistry* 53.9 (2008): 1509-1511.
[141] L.S. Hersh and O.J. Kleppa. "Enthalpies of mixing in some binary liquid halide mixtures." *The Journal of Chemical Physics* 42.4 (1965): 1309-1322.
[142] C.W. Bjorklund, J.G. Reavis, J.A. Leary and K.A. Walsh. "Phase Equilibria in the Binary Systems PuCl3–NaCl and PuCl3–LiCl." *The Journal of Physical Chemistry* 63.10 (1959): 1774-1777.
[143] Thermo-Calc Software Database SSUB5, (Accessed 3/20/2016)
[144] R. Benz. "Thermodynamic properties of the system PuCl3-KCl", Dissertation, The University of New Mexico, 1958.
[145] Mallett, J. J., et al. "Underpotential codeposition of Cu–Au alloys." *Electrochemical and solid-state letters* 12.8 (2009): D57-D60.
[146] Alkire, R. C., Philip N. Bartlett, and Jacek Lipkowski. "Electrochemical engineering across scales: from molecules to processes." *Advances in electrochemical science and engineering* 15 (2015), p.86-87.
[147] J. Zhang. "Kinetic model for electrorefining, part II: Model applications and case studies." *Progress in Nuclear Energy* 70 (2014): 287-297.
[148] Iizuka, Masatoshi, Kensuke Kinoshita, and Tadafumi Koyama. "Modeling of anodic dissolution of U–Pu–Zr ternary alloy in the molten LiCl–KCl electrolyte." *Journal of Physics and Chemistry of Solids* 66.2 (2005): 427-432.
[149] Iizuka, Masatoshi, and Hirotake Moriyama. "Analyses of anodic behavior of metallic fast reactor fuel using a multidiffusion layer model." *Journal of nuclear science and technology* 47.12 (2010): 1140-1154.
[150] Koyama, Tadafumi, et al. "Study of Molten Salt Electrorefining ofU-Pu-Zr Alloy Fuel." *Journal of Nuclear Science and Technology* 39.sup3 (2002): 765-768.
[151] Laidler, J. J., et al. "Development of pyroprocessing technology." *Progress in Nuclear Energy* 31.1-2 (1997): 131-140.
[152] BarP, R., et al. "Proliferation Risk Reduction Study ofAlternative Spent Fuel Processing." (2009).
[153] Uozumi, Koichi, et al. "Electrochemical behaviors of uranium and plutonium at simultaneous recoveries into liquid cadmium cathodes." *Journal of nuclear materials* 325.1 (2004): 34-43.
[154] R.O. Hoover, "Uranium and Zirconium Electrochemical Studies in LiCl-KCl Eutectic for Fundamental Applications in Used Nuclear Fuel Reprocessing," Ph.D. Thesis, University of Idaho, Idaho Falls, ID (2014).
[155] Yoon, Dalsung. "Electrochemical Studies of Cerium and Uranium in LiCl-KCl Eutectic for Fundamentals of Pyroprocessing Technology." Ph.D. Thesis, Virginia Commonwealth University, Richmond, VA (2016).

[156] Janz, George J., et al. Physical properties data compilations relevant to energy storage. II. Molten salts: data on single and multi-component salt systems. No. NSRDS-NBS-61 (Pt. 2). Rensselaer Polytechnic Inst., Troy, NY (USA). Cogswell Lab., 1979.
[157] Yamada, Daichi, et al. "Diffusion behavior of actinide and lanthanide elements in molten salt for reductive extraction." *Journal of Alloys and Compounds* 444 (2007): 557-560.
[158] Serp, J., et al. "Electrochemical behaviour of americium ions in LiCl–KCl eutectic melt." *Electrochimica acta* 51.19 (2006): 4024-4032.
[159] Marsden, K. C., and B. Pesic. "Evaluation of the electrochemical behavior of CeCl3 in molten LiCl-KCl eutectic utilizing metallic Ce as an anode." *Journal of The Electrochemical Society* 158.6 (2011): F111-F120.
[160] Zhang, Jinsuo, Erik A. Lahti, and Wentao Zhou. "Thermodynamic properties of actinides and rare earth fission products in liquid cadmium." *Journal of Radioanalytical and Nuclear Chemistry* 303.3 (2015): 1637-1648.
[161] Murakami, T., et al. "Electrochemical measurement of diffusion coefficient of Pu in liquid Cd." *Journal of The Electrochemical Society* 161.7 (2014): D3057-D3060.
[162] Murakami, Tsuyoshi, and Tadafumi Koyama. "Application of electrochemical method to measure diffusion coefficient in liquid metal." *Journal of The Electrochemical Society* 158.8 (2011): F147-F153.
[163] Caravaca, C., et al. "Electrochemical behaviour of gadolinium ion in molten LiCl–KCl eutectic." *Journal of Nuclear Materials* 360.1 (2007): 25-31.
[164] Gabe, D. R. "The rotating cylinder electrode." *Journal of Applied Electrochemistry* 4.2 (1974): 91-108.
[165] Zhang, Jinsuo. "Kinetic model for electrorefining, part II: Model applications and case studies." *Progress in Nuclear Energy* 70 (2014): 287-297.
[166] Sakamura, Yoshiharu, et al. "Conversion of oxide into metal or chloride for the pyrometallurgical partitioning process." *Actinide and Fission Product Partitioning & Transmutation Eighth Information Exchange Meeting, Las Vegas, 9À11 November*. 2004.
[167] Murakami, Tsuyoshi, and Tetsuya Kato. "Electrochemical behavior of Zr on a liquid Cd electrode in LiCl–KCl eutectic melts." *Journal of The Electrochemical Society* 155.7 (2008): E90-E95.
[168] Iizuka, Masatoshi, Takashi Omori, and Takeshi Tsukada. "Behavior of U-Zr alloy containing simulated fission products during anodic dissolution in molten chloride electrolyte." *Journal of nuclear science and technology* 47.3 (2010): 244-254.
[169] Tomczuk, Zygmunt, et al. "Uranium transport to solid electrodes in pyrochemical reprocessing of nuclear fuel." *Journal of the Electrochemical Society* 139.12 (1992): 3523-3528.
[170] Conn, Andrew R., Nicholas IM Gould, and Ph L. Toint. *Trust region methods*. Vol. 1. Siam, 2000.
[171] Cohen, William, et al. "Molten fluoride salt and liquid metal multistage extraction model." *Progress in Nuclear Energy* 97 (2017): 214-219.
[172] Gaune-Escard, Marcelle, and Kenneth R. Seddon, eds. *Molten salts and ionic liquids: never the twain?*. John Wiley & Sons, 2012. P272-273

Part II: Technical report from the Virginia Commonwealth University

--Cerium and Uranium Electrochemical Separations in LiCl-KCl Eutectic Systems

Dalsung Yoon and Supathorn Phongikaroon

Mechanical and Nuclear Engineering, Virginia Commonwealth University
Richmond, Virginia, 23284

LIST OF ABBREVIATIONS AND SYMBOLS

Abbreviations	Meaning
ANL	Argonne national laboratory
CPE	Constant phase element
CP	Chronopotentiometry
CV	Cyclic voltammetry
EBR-II	Experimental breeder reactor-II
EIS	Electrochemical impedance spectroscopy
ER	Electrorefiner
ICP-MS	Inductively coupled plasma-mass spectrometry
INL	Idaho national laboratory
LCC	Liquid cadmium cathode
LP	Linear polarization
MA	Minor actinide
OCC	Open circuit chronopotentiometry
OCP	Open circuit potential
PUREX	Plutonium uranium redox extraction
Redox	Reduction-oxidation
RSS	Radiation safety section
SNM	Special nuclear material
UNF	Used nuclear fuel
VCU	Virginia Commonwealth University

Symbols	Physical meaning	Unit
a	Activity	
α	Transfer coefficient	
C	Concentration	mol cm^{-3}
C_p	Heat capacity	kJ mol^{-1} K^{-1}

D	Diffusion coefficient	$cm^2\ s^{-1}$
D_0	Pre-exponential factor for diffusivity	$cm^2\ s^{-1}$
E	Equilibrium potential	V
E_a	Activation energy	$kJ\ mol^{-1}$
E^0	Standard reduction potential	V
E^{0*}	Apparent standard reduction potential	V
E_p	Peak potential in CV	V
E_{cp}	Cathodic peak potential in CV	V
$E_{p/2}$	Half peak potential in CV	V
F	Faraday's constant	$C\ mol^{-1}$
ΔG^0	Standard Gibbs free energy	$J\ mol^{-1}\ K^{-1}$
ΔG^{0*}	Partial molar Gibbs free energy	$J\ mol^{-1}\ K^{-1}$
ΔG^{sc}	Gibbs free energy at super cooled state	$kJ\ mol^{-1}\ K^{-1}$
$\Delta G^{Formation}$	Gibbs free energy for the formation	$kJ\ mol^{-1}\ K^{-1}$
ΔG^{Fusion}	Gibbs free energy for fusion	$kJ\ mol^{-1}\ K^{-1}$
γ	Activity coefficient	
ΔH^{Fusion}	Enthalpy of fusion	$kJ\ mol^{-1}$
i	Current	A
i_p	Peak current	A
i_0	Exchange current density	$A\ cm^{-2}$
I_0	Pre-exponential factor for exchange current density	$A\ cm^{-2}$
k^0	Rate constant	$cm\ s^{-1}$
N	Number of electrons transferred	
R	Universal gas constant	$J\ mol^{-1}\ K^{-1}$
R_{ct}	Charge transfer resistance	ohm
R^2	Coefficient of determination	
S	Working electrode surface area	cm^2
ΔS^{Fusion}	Entropy of fusion	$kJ\ mol^{-1}\ K^{-1}$
T	Absolute temperature	K
T_m	Melting temperature	K
υ	Scan rate in CV	$V\ s^{-1}$
X	Mole fraction	

EXECUTIVE SUMARRY

Understanding the characteristics of special nuclear materials in LiCl-KCl eutectic salt is extremely important in terms of effective system operation and material accountability for safeguarding pyroprocessing technology. By considering that uranium (U) is the most abundant and important element in the used nuclear fuel, measurements and analyses of U properties were performed in LiCl-KCl eutectic salt. Therefore, the electrochemical techniques such as cyclic voltammetry (CV), open circuit potential (OCP), Tafel, linear polarization (LP), and electrochemical impedance spectroscopy (EIS) were conducted under different experimental conditions to explore the electrochemical, thermodynamic, and kinetic properties of U in LiCl-KCl eutectic. The ultimate goal of this study was to develop proper methodologies for measuring and analyzing the exchange current density (i_0) of U^{3+}/U reaction, which has not been fully studied and understood in literature.

In the preliminary study, cerium (Ce) was selected as a surrogate material for uranium and its behavior was being explored with the developments of experimental methods. CV was performed to evaluate Ce properties such as the diffusion coefficients (D), apparent standard reduction potential (E^{0*}), Gibbs free energy (ΔG), and activity coefficient (γ). In addition, EIS methods were adapted and specific experimental procedures were established for the proper i_0 measurements providing repeatable and reproducible data sets. The i_0 values for Ce^{3+}/Ce pair were ranging from 0.0076 A cm^{-2} to 0.016 A cm^{-2}, depending on the experimental conditions. These preliminary results give insight in developing the experimental setups and methods to evaluate the properties of U in LiCl-KCl. Plus, Ce is one of the lanthanide (Ln) fission products in electrorefiner (ER) system; therefore, the resulting data values yield useful information of the fundamental behaviors of Ln elements in the system.

Based on these developed methodologies, the experimental designs and routines were established to explore the main properties (e.g., D, E^{0*}, etc.) of UCl_3 in LiCl-KCl eutectic salt under different concentrations (0.5 wt% to 4 wt% UCl_3) and temperatures (723 K to 798 K). Specially, the i_0 values of U^{3+}/U were evaluated via EIS, LP, Tafel, and CV methods. All i_0 values had linear trends with the change of concentration and temperature; however, these values measured by LP, Tafel, and CV methods were greatly influenced by the change in electrode surface area. Overall, the i_0 values agreed within 33% relative error range with the EIS method being the most consistent and accurate in comparison to reported literature values. The measured values of i_0 were ranging from 0.0054 A cm^{-2} to 0.102 A cm^{-2}. Therefore, an extremely reliable database for i_0 was provided and it is feasible to anticipate the i_0 kinetics in other experimental conditions by using the provided equation models. Furthermore, $GdCl_3$ was added to the LiCl-KCl-UCl_3 system to explore the effects of other elements on the U properties such as the diffusion coefficients, thermodynamic properties, and i_0 kinetics. The diffusion coefficient was generally decreased by 12 ~ 35% with addition of $GdCl_3$ in LiCl-KCl-UCl_3; however, the apparent standard potentials and exchange current density follow the same trends with data obtained without $GdCl_3$ additions. Hence, the results indicate that the thermodynamic and kinetic values for U^{3+}/U reaction in LiCl-KCl eutectic salt are not greatly influenced by the presence of $GdCl_3$.

1 Introduction

Nuclear power produces a significant portion of electricity worldwide nowadays. The reported number of commercial nuclear power plants operating in 2014 was 438 with a global generating capacity of 376.2 GW(e) [1]. Seventy of reactors were under the construction [1] and continuous expansion of nuclear power is expected in the future with increasing demand of energy. As the nuclear power production has increased, the management of the used nuclear fuel (UNF) became an important issue due to the political, economic, and societal concerns in the nuclear industry [2]. The total amount of UNF cumulatively generated worldwide by 2014 was 204,421 tHM, and it increases from year to year [3]. The used fuel storage capacity in 2014 was 201,722 tHM and the global reprocessing capacity was only 3,800 tHM/year [3]. Therefore, in terms of saving fuel resources and solving the issue of storage capacity, the significance of recovering components from the used fuel will continue to grow in the future [2].

Reprocessing UNF can be more invaluable when it is considered that 96 percent of uranium remains after the fuel is permanently removed from reactor, which can be re-used after suitable retreatments [2, 4]. Two methods have been widely investigated and implemented for the reprocessing of the nuclear fuel, which are referred as aqueous reprocessing and pyroprocessing [4]. The aqueous reprocessing utilizes a method known as PUREX (Pu-U recovery extraction), which is the most common and well developed technique. In the PUREX process, pure U and Pu are separated through chemical adjustments and several cycles of solvent extractions by using highly concentrated nitric acid [4, 5, 6]. By experiencing the renaissance of nuclear energy worldwide, pure U and Pu productions gave rise to several concerns about proliferation of nuclear materials. From the safeguarding aspect of reprocessing UNF, pyroprocessing technology has been considered as an alternative method for future reprocessing [2, 4, 6, 7].

Pyroprocessing was originally developed by the Argonne National Laboratory (ANL) and currently is operated at Idaho National Laboratory (INL) to treat used metallic fuels from Experimental Breeder Reactor-II (EBR-II) [8-10]. This technology uses molten salt electrolytes as a media instead of using acid solutions or organic solvents [4, 9]. In these electrolytes, U, Pu, and minor actinides (MAs) can be recovered by electrochemical reduction on cathode electrodes. In comparison to the conventional aqueous methods which have superior maturity to date, pyroprocessing technology provides the following unique benefits: 1) intrinsic proliferation-resistant features by Pu recovery as a mixture, 2) compact facilities for fuel recovery and fabrication, 3) critically-safe condition for processing high enriched fuel, and 4) rapid on-site support for fast reactor fuel cycle [6, 11]. In addition, a low radiation sensitivity of the salt electrolyte allows the early reprocessing of UNF after discharge [2], which will minimize the chance of a loss of coolant accidents in the spent fuel pool [12]. With these noble features, the main purpose of pyroprocessing technology is not only to treat the irradiated nuclear fuels, but to reduce volume of the nuclear waste, recycle actinides, and close the fast reactor fuel cycle [13]. Therefore, there are considerable ongoing research and development on pyroprocessing technologies in many countries [4]. For example, the research teams in South Korea have constructed and operated an engineering scale demonstration facility with non-radioactive

materials for the purpose of pyroprocessing research [14]. On another aspect, Russia has already demonstrated the production of mixed oxide fuels through pyroprocessing technology and plans to use the technology for the development of a closed fuel cycle by 2020 [4].

1.1 Pyroprocessing

Pyroprocessing technology, also known as electrochemical process, electrometallurgical reprocessing, or pyrochemical technology, has been considered as a promising way to treat metal/oxide form of UNF from the nuclear fuel cycle [8-10]. Figure 1.1 illustrates schematically the flow sheet of the process [5, 6]. Despite of its original development purpose, oxide form of used fuels from light water reactor can also be treated through the head-end process, known as electrolytic oxide reduction. In the electrolytic oxide reduction process, the used oxide fuel is loaded into a cathode basket in a molten LiCl-Li_2O salt at 923 K and chemically reduced into metal form by the reaction with Li metal, which is electrochemically deposited on the cathode [15]. In 2006, INL successfully converted 50 g of the used light water reactor (LWR) fuel into metal form in their hot cell facility [16]. Then, the metal fuels are transferred into the anode basket of an electrorefiner (ER). While U, Pu, MAs, and rare earth materials are anodically dissolved into the LiCl-KCl eutectic salt from the anode basket, only U is recovered on the solid cathode by controlling the voltage applied on the cathode. After that, the residual U, Pu, and MAs are simultaneously collected by using a liquid cadmium cathode (LCC) due to the fact that activity of the elements get very small in liquid metal [17, 18]. The deposits (U and U-Pu-MA mixtures) from the cathode electrodes go to the cathode processor. The process is basically in a high temperature vacuum furnace where the adhering salt or cadmium are evaporated and pure metal product are left [10]. The ingot products from the cathode processor are fabricated into new metal fuel in an injection casting furnace [8] which can be used in fast reactors. The electrolyte salt from the ER system is recycled by removing actinides through the ion exchange method and the separated fission products (Cs, Rb, Sr, Ba, Br, I, Y, Sm, Eu, etc.) are immobilized into ceramic waste forms [10]. After operating the ER system, zirconium and noble metal fission products are left in the anode basket, which are processed into alloy metal waste form for the disposal [10].

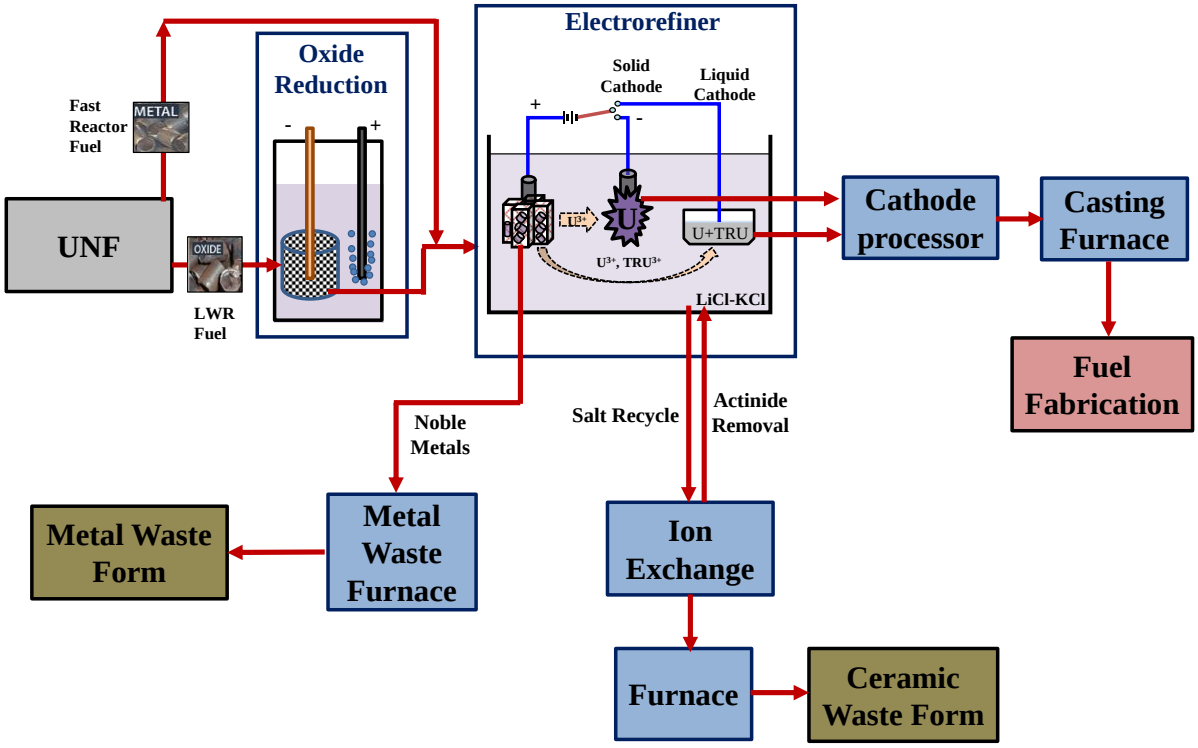

Figure 124.1 Schematic flowchart of pyroprocessing based on spent fuel treatment.

1.2 Electrorefiner (ER)

The ER is the key component in pyroprocessing technology, in which the primary separation of U and MAs from fission products is being performed [18, 19]. The system contains a LiCl-KCl eutectic salt (44.2 wt% LiCl and 55.8 wt% KCl), and the operating temperature ranges from 723 K to 773 K [4]. There are two engineering scale ERs (Mark IV and Mark V) at INL (U.S.) which are currently operated to treat the metallic used driver and blanket fuels, respectively, from EBR-II [19]. Figure 1.2 shows the drawings of both INL ERs, which have similar size but Mark V has an upgraded electrode design [19]. The Mark IV ER has been used to treat the driver fuels (highly enriched uranium at about 63% of U-235), whereas Mark V ER treats the blanket fuels (which contains depleted uranium) [20]. To date, 830 kg of heavy metals have been processed via Mark IV ER and numerous studies have been performed and reported in the literature [19]. Technical issues which are currently of concern include current efficiency, uranium recovery efficiency, zirconium recovery, and understanding of cadmium effects [19].

Here, UNFs are loaded in the anode basket and lowered into the LiCl-KCl molten salt. As current is applied through the cell, U metal is oxidized into U^{3+} ions from the anode basket [19]. Fission products, which have more negative redox potential than that of U, are being oxidized together (these products are referred as active products) whereas noble metals which have more positive redox potential than U stay in the anode basket [19]. The general contents of the driver

fuel are summarized in Table 1.1 [21, 22-25]. Therefore, the main goal is to dissolve as much U as possible from the used fuels on the anodic side with minimal oxidation of the noble metals into the salt [19] and collect uranium metal on the cathode side. Li and Simpson in 2005 [20] reported that 99.7 % of U from fission products could be dissolved into the salt over several runs, but it caused Zr and noble metal co-dissolution into the salt. Table 1.2 lists the weight percent of dissolved fission products into the LiCl-KCl salt from EBR-II used fuel (loaded in anode basket). For the cathode electrodes, there are two types of electrode: 1) solid electrode (typically stainless steel) and the LCC. By using the solid electrode, selective deposition of pure U is possible by controlling the applied potential. On the other hand, reduction potentials of actinide elements including Pu and U become very close on the LCC, so that MAs are inevitably recovered along with U and Pu into the LCC process [17]. The U has a tendency to be deposited in form of a dendrite [18, 19] which prevents the co-deposition of MA on LCC. Therefore, several studies have been performed to develop the LCC structures for avoiding dendrite formation on LCC [18, 26, 27]. Overall, the main reaction schemes in an electrorefiner can be described as follows [28]:

Anode: $$\mathrm{U\,(anode) \rightarrow U^{3+}\,(salt) + 3e^-} \quad (1\text{-}1)$$

Cathode: $$\mathrm{U^{3+}\,(salt) + 3e^- \rightarrow U\,(cathode)} \quad (1\text{-}2)$$

Net reaction: $$\mathrm{U\,(anode) \rightarrow U\,(cathode)} \quad (1\text{-}3)$$

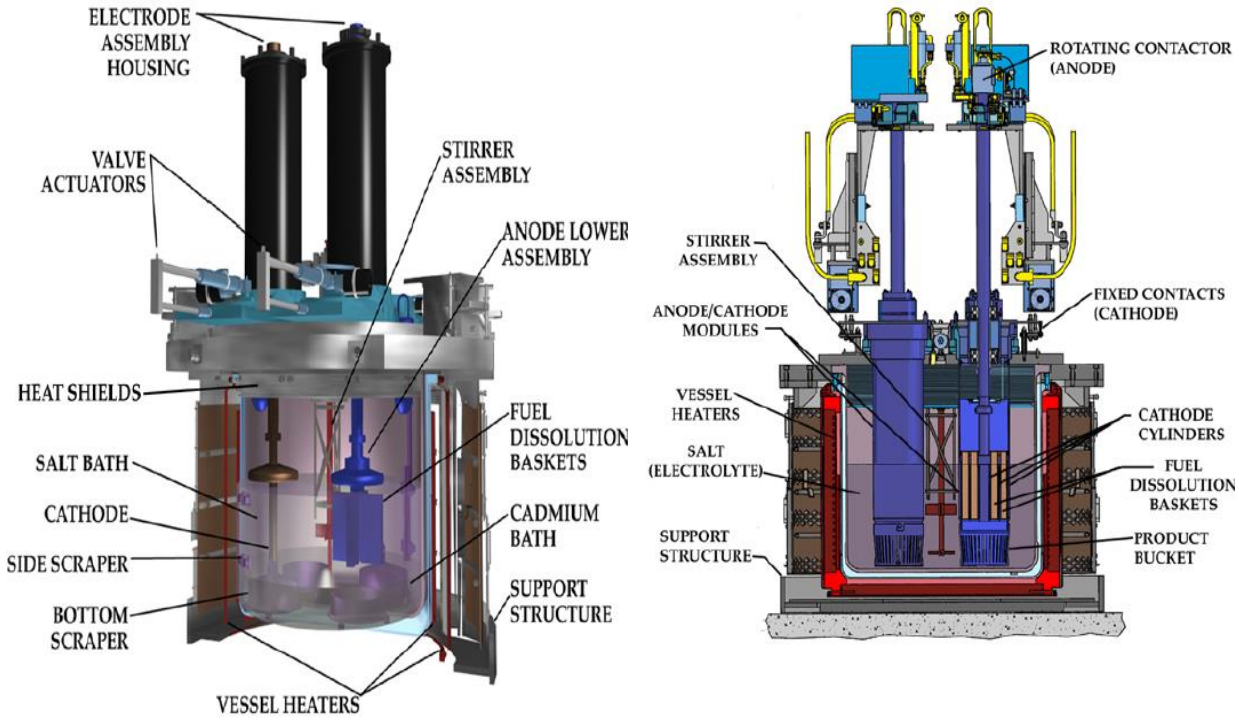

Figure 1.125 Engineering scale electrorefiner at INL Fuel Conditioning Facility, Mark IV (left) and Mark V (right) [19].

Table 1.22 Critical used driver fuel composition and equilibrium potential of the elements

Elements	Weight % in the used fuel [21]	E^0 (V vs. Ag/AgCl) at 723 K [22]	
Bromine (Br)	0.007	0.920 (723 K)	Noble species (remain in anode basket)
Tellurium (Te)	0.112	0.64 (723 K)	
Ruthenium (Ru)	0.407	0.615 (723 K)	
Rhodium (Rh)	0.111	0.526 (723 K)	
Palladium (Pd)	0.090	0.513 (723 K)	
Iodine (I)	0.048	0.473 (723 K)	
Arsenic (As)	0.005	0.283 (723 K)	
Molybdenum (Mo)	0.771	0.119 (723 K)	
Antimony (Sb)	0.004	0.087 (723 K)	
Silver (Ag)	0.004	0.000 (723 K)	
Copper (Cu)	0.003	0.295 (723 K)	
Tin (Sn)	0.015	-0.355 (723 K)	
Niobium (Nb)	0.002	-0.41 (723 K)	
Selenium (Se)	0.019	-0.459 (723 K)	
Cadmium (Cd)	0.007	-0.589 (723 K)	
Vanadium (V)	0.003	-0.806 (723 K)	
Titanium (Ti)	0.077	-1.010 (723 K)	
Zirconium (Zr)	10.81	-1.088 (723 K)	
Europium (Eu)	0.011	-1.471 (773 K)	
Uranium (U)	80.60	-1.496 (723 K)	Active species (dissolved into the salt)
Neptunium (Np)	0.041	-1.519 (723K) [23]	
Plutonium (Pu)	0.413	-1.570 (723 K)	
Gadolinium (Gd)	0.005	-2.066 (723 K)	
Neodymium (Nd)	0.930	-2.097 (723 K)	
Yttrium (Y)	0.126	-2.109 (723 K)	
Lanthanum (La)	0.284	-2.126 (723 K)	
Promethium (Pm)	0.011	-2.147 (773 K)	
Cerium (Ce)	0.542	-2.183 (723 K)	
Praseodymium (Pr)	0.269	-2.316 (773 K)	
Sodium (Na)	2.160	-2.5 (723 K)	
Samarium (Sm)	0.177	< -2.5 [24]	
Europium (Eu)	0.011	< -2.5 [25]	

Table 1.23 The fission product dissolution (wt%) from used EBR-II driver fuel into LiCl-KCl salt [19]

Fission products dissolved into the salt	Weight percent in average
Uranium (U)	99.72
Lanthanum (La)	99.74
Cerium (Ce)	99.67
Neodynium (Nd)	99.96
Zirconium (Zr)	87.85
Technetium (Tc)	23.42
Molybdenum (Mo)	27.32
Ruthenium (Ru)	17.92

1.3 Motivation

As shown in Table 1.1, the used fuel contain a variety of fission products and active fission products are dissolved into the salt, which makes the system more complicated and difficult to be understood. Since U is the most abundant element in the ER, it is important to understand the fundamental properties of U in the salt in terms of effective system operation, and material accountability for safeguarding purposes. In these aspects, many studies have been conducted by several researchers to determine the electrochemical and kinetic properties of U in the salt. However, discrepancies through the literature survey can be observed due to many different experimental conditions; therefore, the general trends for the data sets can be hardly found. In addition, several properties have not been reported and fully understood due to the difficulty of the measurement, such as the exchange current density of U, which is necessary to be understood for near real time material detection and development of the kinetic model for pyroprocessing. Furthermore, although the LCC in the ER plays an important role in the feasibility of pyroprocessing toward non-proliferation characteristic [29], only a few studies had been conducted to explore the properties of actinides on LCC in the salt [30-32]. Therefore, more reliable data sets of U in the salt system with a variety of experimental conditions are necessary to advance fundamental knowledge and gain new data library sets.

1.4 Goal/Outcome

The primary goal of this NEUP assigned task is to develop the experimental methods to evaluate electrochemical and kinetic properties of U in the LiCl-KCl salt based ER. Bench-scaled ER system have been developed in argon environment glovebox system. The main focus of this project is to perform electrochemical experiments including cyclic voltammetry (CV), open circuit potential (OCP), Tafel plot, linear polarization (LP), and electrochemical impedance spectroscopy (EIS) techniques for determining the parameters needed for modeling and developing a

methodology for safeguards. Specially, the exchange current density (i_0) of U/U^{3+} reaction will be intensively explored in LiCl-KCl eutectic salt. While i_0 values are necessary for the kinetic models, these have not been fully understood in the system. In addition, the electrochemical and kinetic behaviors of U will be further examined in multi-component systems, which may occur in the ER. The approach in this NEUP study will integrate the measurement of electrochemical data and the outcome will identify the various electrochemical and kinetic operating parameters. The resulting data base will provide an insight into fundamental understanding and signatures for material accountability for the ER process in pyroprocessing technology.

1.5 Approach

Three phases have been established in this research study. In phase I, pure argon environment (O_2/H_2O levels < 5 ppm) was established in glovebox systems (RAM I and RAM II) for the treatment of the LiCl-KCl salt due to the fact that the salt is extremely hygroscopic and corrosive. Experimental setups including furnace, ceramic crucibles, and electrode assemblies were prepared in RAM I glovebox. Simultaneously, extensive literature review on fundamental properties of U in LiCl-KCl was conducted for understanding trends of the properties from the previously established data bases. In addition, the electrochemical techniques were studied for better understanding and reliable electrochemical measurements. The main purpose of phase II was to develop the experimental methods to determine the fundamental properties by using Ce as a surrogate material for U. All methods—CV, EIS, Tafel plot, LP, and OCP—were performed to determine the apparent standard potential, diffusion coefficient, exchange current density, and Gibbs free energy. The experiments were done at different concentrations (0.5 wt% to 4 wt% in LiCl-KCl) and temperatures (698 K to 823 K) in order to establish the data library and to understand the physical trends of Ce in LiCl-KCl. The studies focused on assessing the feasibility of EIS technique to measure the exchange current density in the salt system. Furthermore, the same experiments were carried out on the LCC in order to understand the Ce properties on a liquid cathode. A liquid cadmium surface was constructed with a design of an electrode vessel; therefore, electrochemical measurements could be performed on the surface. In Phase III, electrochemical studies of U were performed in LiCl-KCl salt at various concentrations (ranging from 0.5 wt% to 4 wt% UCl_3) and temperatures (from 723 K to 798 K). Based on the methodologies developed in Phase II, the electrochemical and thermodynamic properties of U were evaluated. Additionally, the measurement of i_0 for U/U^{3+} reaction was done via EIS, Tafel, LP, and CV methods for building reliable data base. Plus, the same measurement procedures were followed to explore the U properties in LiCl-KCl-UCl_3-$GdCl_3$ salt mixtures. These phases were planned, explored and accomplished at Virginia Commonwealth University (VCU) for the 3-year period. Specific timeframe is described in Table 1.3. Other extra studies in support of this project for the extension of this project is given in the appendix.

Table 1.3 Estimated schedule and timeframe for the present project

Phase	Year 1 (2014)				Year 2 (2015)				Year 3 (2016)			
	1	2	3	4	1	2	3	4	1	2	3	4
I												
II												
III												

1.6 Organization of the Final Report from the Virginia Commonwealth University

This final report is composed of six sections. In Section 2, thermodynamic and kinetic properties of uranium reported in the literature are reviewed and discussed. The significance of the properties with respect to pyroprocessing applications is pointed out, and methods of the electrochemical techniques used in the NEUP study are described in detail. Section 3 contains basic information of equipment, experimental setups, and reagents. In addition, procedures for electrochemical preparations, sample collections, and sample analysis by inductively coupled plasma-mass spectrometry (ICP-MS) are being discussed with step-by-step illustrations. Section 4 presents the preliminary studies with Ce as a surrogate material for U in LiCl-KCl eutectic salt. Two studies are being described in this section: (1) measurements of Ce properties with solid cathode and (2) with liquid cadmium cathode. Since each study has different motivations and experimental procedures, an additional introductory information and experimental programs are briefly highlighted at the beginning of both studies for clarity. The main goal of this section is to develop experimental methods to measure the desired properties; therefore, specific methodologies are explained with corresponding equations associating with experimental results of Ce properties. Section 5 provides a detailed explanation and experimental procedures including discussion of the properties of U in LiCl-KCl eutectic salt under different effects—concentration, temperature, and additional species (that is, Gd). Here, the same experimental methods developed in Section 4 have been utilized; hence, discussions of resulting data are more focused in this section. The final section (Section 6) summarizes the resulting data sets in the present research and discusses necessary future steps. In the Appendix sections, there are extra work and assignments during the extension period of this NEUP project.

2 Literature Review

2.1 Molten salt in electrorefining and general electrochemistry

The advantages of molten salt electrochemistry include high radiation resistance, low criticality concern, low vapor pressure, low secondary wastes and high stability [33]. Thus, physical, chemical and electrochemical properties of the salts and their interactions with actinides and fission products should be considered. Currently, two chloride salt mixtures (LiCl–KCl and NaCl–KCl) and two fluoride salt mixtures (BeF_2–LiF and CaF_2–LiF) have been recognized as good candidates for pyroprocessing [34-36]. The compositions of these salts and their melting temperatures are given in Table 2-1. LiCl-KCl molten salt is widely selected as a candidate for electrorefining system because of its lower melting eutectic temperature. Typically, electrorefining system is operated at a temperature ranging between 723 K and 773 K.

Table 2.1 Physical properties of the salt mixtures [34-36]

Properties	**LiCl-KCl**	**NaCl-KCl**	**BeF_2-LiF**	**CaF_2-LiF**
Composition (A-B, Mol % B)	40	50	67	77
Eutectic melting temperature (K)	623	931	733	1042
Molar mass (g mol^{-1})	55.25	66.50	32.89	37.93
Density at melting point (kg m^{-3})	1644.6	1604.1	2055.7	2066.8
Viscosity at melting point (Pa s)	0.2798	0.2128	0.1947	-
Electrical conductance (S m^{-1})	63.72	220.07	128.37	624.68

2.2 Uranium Studies

Several researchers previously focused on understanding its electrochemical and kinetic behavior of uranium (U) in the molten LiCl-KCl system. The most important parameters are

- Apparent standard potential (E^{0*}),
- Activity coefficient (γ),
- Diffusion coefficient (D), and
- Exchange current density (i_0).

The values of E^{0*} and D for U have been reported widely by using different electrochemical techniques, such as cyclic voltammetry (CV), chronopotentiometry (CP), and open circuit potential (OCP) [37-47]. Yet, these data values are scattered due to the fact that these experiments have been done under different concentrations, temperatures, and experimental setups and environments. Based on the E^{0*} values, several thermodynamic properties can be calculated including the Gibbs free energies of UCl_3 formations and γ. Specially, only a few researchers reported the values of γ, which, however, show wide discrepancy [37, 39, 41]. These issues will be further discussed in Section 2.2.1. In addition, the properties have been poorly understood by

using LCC electrode, which plays an important role in the electrorefining process. Also, very few i_0 values are available [48-51], which started to be explored and reported since 2009. Choi et al., Ghosh et al., and Rose et al. [48-50] reported the values of i_0 at different concentrations (ranging from 3 wt % to 5 wt %) at 773 K. Lim et al. in 2016 [51] reported i_0 for U at different concentrations and temperatures. Yet, there is a lack of understanding in the trend of i_0 and a meaningful comparison is difficult among the literature studies due to the fact that the data were measured in different experimental conditions and scales. Also, none of the authors has mentioned the challenge of the electrode area growth during the measurements by using the Tafel or LP methods (this concern will be discussed in Section 2.2.3).

2.2.1 Redox process and Apparent Standard Potential (E^{0*})

The electrochemical process of U/U^{3+} reduction-oxidation (which is called "redox") reaction is governed by the Nernst equation exhibiting the equilibrium potential for the reaction with respect to temperature and concentrations of oxidant/reductant [52]:

$$E^{eq}_{U^{3+}/U} = E^{0}_{U^{3+}/U} + \frac{RT}{nF}\ln\left(\frac{a_{U^{n+}}}{a_U}\right) \quad (2\text{-}1)$$

where $E^{eq}_{U^{3+}/U}$ is the equilibrium potential between U metal and U^{3+} ions, $E^{0}_{U^{3+}/U}$ is the standard reduction potential which is the theoretical potential when the cell is ideally reversible at equilibrium states with a solution concentration of 1 mol L^{-1} at 1 atm and 298 K, R is the universal gas constant (8.314 J $mol^{-1}K^{-1}$), F is the Faraday's constant (96485 C mol^{-1}), and T is the absolute temperature (K). The $a_{U^{3+}}$ is the activity of UCl_3 which can be expressed by $a_{U^{3+}} = \gamma_{U^{3+}} \times \chi_{U^{3+}}$ where $\gamma_{U^{3+}}$ is the activity coefficient and $\chi_{U^{3+}}$ is the mole fraction of U. Thus, the equation can be expressed using the mole fraction [52]

$$E^{eq}_{U^{3+}/U} = E^{0*}_{U^{3+}/U} + \frac{RT}{nF}\ln\left(\frac{\chi_{U^{3+}}}{\chi_U}\right) \quad (2\text{-}2)$$

where $E^{0*}_{U^{3+}/U}$ is the apparent standard potential (this is often referred as a 'formal potential'). The apparent standard potentials is the function of temperature and activity coefficient; therefore, it can be determined by plotting $E^{eq}_{U^{3+}/U}$ against $\ln(\chi_{U^{3+}})$. This property gives an insight into the reduction potential that the operator will be able to apply for the U recovery in the ER. Therefore, several researchers have reported the values of $E^{0*}_{U^{3+}/U}$, in which they used different temperatures, concentrations, reference electrodes, and experimental methods [37-45], as shown in Figure 2.1. The reported data values show good agreement within 50 mV deviation from the average values, which are linearly dependent with temperature in general. The result reported by Hoover et al. [42] stands at more negative potential compared to the trend; this discrepancy may be due to the fact that they measured the E^{0*} at a high concentration range between 1 and 10 wt% of UCl_3 in LiCl-KCl. Typically, the property of E^{0*} is considered as independent of concentration; however, this must be experimentally evaluated.

Once the $E^{0*}_{U^{3+}/U}$ values were determined, the thermodynamic properties of UCl_3 can be further investigated by combining Eq. (2-1) and (2-2); therefore, $E^{0*}_{U^{3+}/U}$ can be defined as

$$E^{0*}_{U^{3+}/U} = E^{0}_{U^{3+}/U} + \frac{RT}{nF}\ln(\gamma_{U^{3+}}) \quad (2\text{-}3)$$

where $\gamma_{U^{3+}}$ is the activity coefficient of UCl_3 in LiCl-KCl. Since $E^{0}_{U^{3+}/U}$ is a theoretical value at the aforementioned ideal state, the value does not exist in reality. Therefore, super cooled liquid state was commonly considered as ideal as possible in the real system [37, 39, 41], and the Eq. (2-3) can be re-written by using the basic thermodynamic equation as following,

$$\Delta G^{SC}_{UCl_3} - \Delta G^{0*}_{UCl_3} = RT\ln(\gamma_{U^{3+}}) \quad (2\text{-}4)$$

where $\Delta G^{SC}_{UCl_3}$ is the Gibbs free energy at super cooled liquid state. The data for the pure substance can be found in several references [37, 53]. If $\Delta G^{SC}_{UCl_3}$ is known, $\gamma_{U^{3+}}$ can be calculated. Figure 2.2 plots the reported values of $\gamma_{U^{3+}}$, showing wide discrepancy up to 10^1 order of magnitude [37, 39, 41, 54]. This may be due to the challenges of obtaining $\Delta G^{SC}_{UCl_3}$ from literatures, and calculating exponential term ($\exp\left(\frac{\Delta G^{SC}_{UCl_3} - \Delta G^{0*}_{UCl_3}}{RT}\right)$). Therefore, sufficient data sets need to be collected in order to understand thermodynamic properties of U in the salt system.

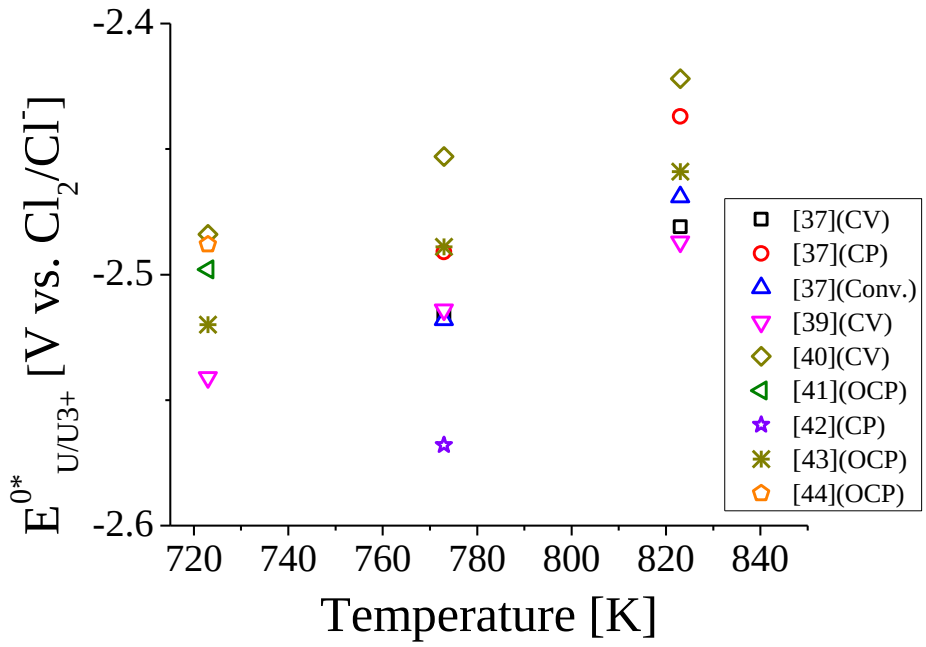

Figure 2.1 Comparison of the apparent standard potential in LiCl-KCl salt reported by various researchers (Note: CV = cyclic voltammetry, CP = chronopotentiometry, and OCP = open circuit potential).

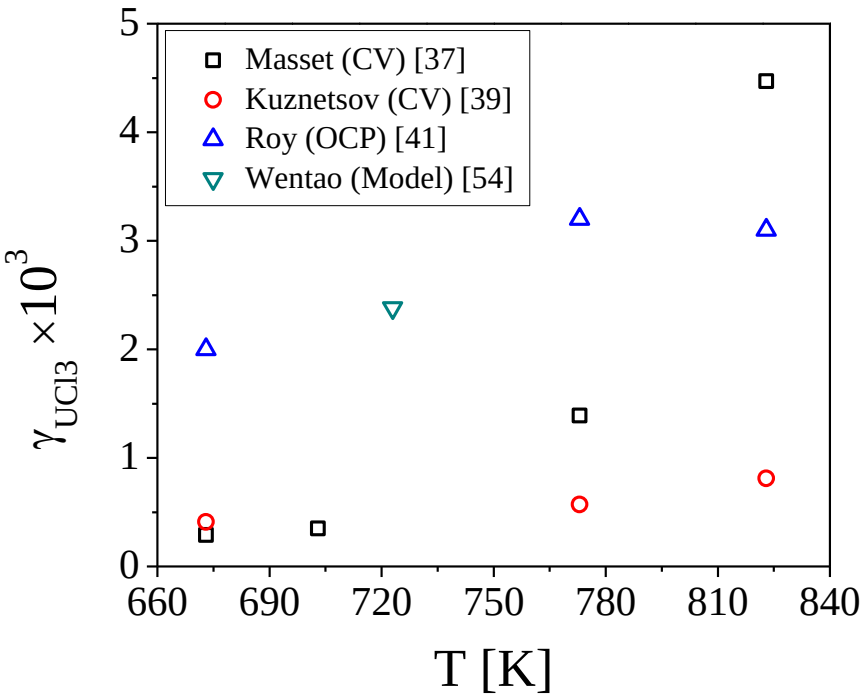

Figure 2.2 Activity coefficients of UCl_3 in LiCl-KCl reported by previous studies.

2.2.2 Diffusion coefficient

Mass transfer from and to the electrodes in an electrochemical cell can be expressed by diffusivity or diffusion coefficient which is constant between molar flux and concentration gradient [22]. Its knowledge on UCl_3 in LiCl-KCl eutectic melt provides essential data for optimization of U electrorefining. The diffusion coefficients of U^{3+} have been electrochemically measured in the salt via CV and CP techniques. Several studies [37, 39, 42, 45-47] have reported the values in LiCl-KCl which are plotted in Figure 2.3. The diffusion coefficient is linearly dependent to temperature; however, data are scattered, especially at high temperature. It should be noted that the values reported by Masset and co-workers [37] are relatively higher than data from other studies. The CP method generally provides higher values than those from CV method. Therefore, the values of D_{U3+} are necessary to be measured and collected in various experimental conditions for further comparison and understanding.

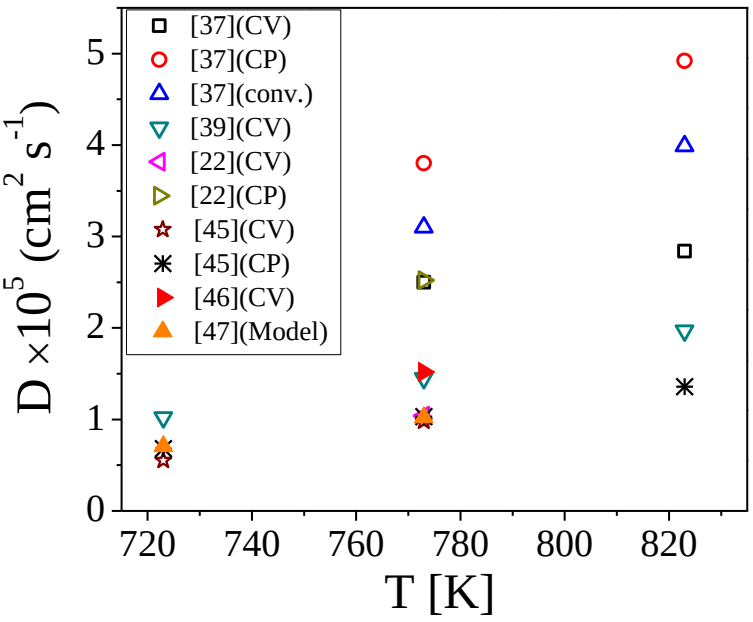

Figure 2.126 Plot of the diffusion coefficients of UCl_3 in LiCl-KCl salt reported by various researchers.

2.2.3 Exchange current density

Exchange current density (i_0) is an important parameter to understand the kinetics of electrochemical reactions (U^{3+}/U) on the electrode surface. Additionally, the values are essential to the physics-based model used in Butler-Volmer equation which shows fundamental relationship between current and overpotential applied on the electrode. The equation can be expressed as

$$i = i_0 \cdot \left\{ \exp\left[\frac{\alpha_a n F \eta}{RT}\right] - \exp\left[-\frac{\alpha_c n F \eta}{RT}\right] \right\} \quad (2\text{-}5)$$

where i_0 is the exchange current density, i is the current, α_a is the anodic charge transfer coefficient, α_c is the cathodic charge transfer coefficient, and η is the activation overpotential. There are several methods to measure the value of i_0: Tafel plot, linear polarization (LP), and electrochemical impedance spectroscopy (EIS). However, the i_0 of U^{3+}/U couple has not been well measured and understood due to challenges of the measurement. Choi et al. in 2009 [48] performed LP experiments in 3.3 wt% UCl_3-LiCl-KCl salt where Cd coexisted at the bottom of the vessel. The authors conducted the experiments by using different materials for the electrode and concluded that the different materials of electrodes result in different values of i_0, ranging from 0.0202 to 0.0584 A cm^{-2}. Ghosh and co-workers [49] showed that it is $8 \pm 2 \times 10^{-3}$ A cm^{-2}, by Tafel plot technique, which stands far from the trend of other literature studies. Rose et al. in 2015 [50] measured the i_0 of U/U^{3+} in 5 wt% UCl_3-LiCl-KCl salt by using Tafel plot method. Tafel plots were analyzed by using the Oldham-Mansfeld model in a very small overpotential region, which is theoretically not a Tafel region. The i_0 value from that study was from 0.0695 to 0.220 A cm^{-2}.

Recently, Lim et al. [51] reported the i_0 values of U via the Tafel and LP methods; this published study is the only source with reported i_0 data at the different temperatures and concentrations. The values of i_0 for U^{3+}/U are plotted and compared in Figure 2.4. From these literature results, there are still missing data sets for i_0 of U in order to fully understand the general trend. Also, a meaningful comparison among the reported data is not possible due to the data discrepancy resulting from differences in the experimental conditions, the size of the system, and the data acquisition methods. Furthermore, the authors never mentioned the challenges and uncertainties in measuring the electrode surface area during the Tafel and LP measurements. The measurements at different concentrations and temperatures under the same experimental environments would be necessary in order to build up a meaningful data base for i_0 of U/U^{3+} in LiCl-KCl salt.

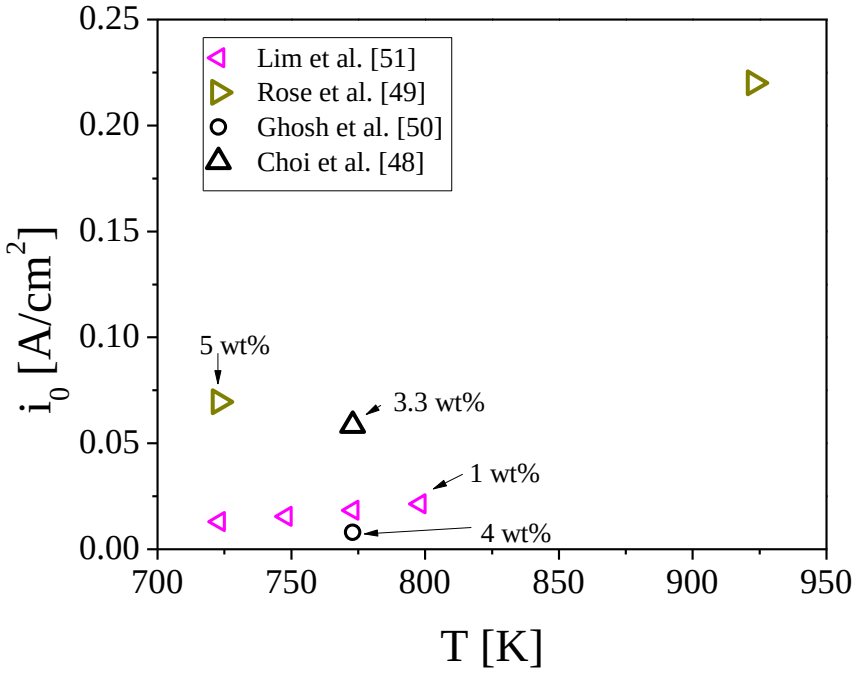

Figure 2.4 Plot of i_0 from literature studies (measuring with a tungsten electrode).

2.3 Review of the electrochemical techniques

Five electrochemical techniques have been considered for the measurement of parameters: CV, OCP, EIS, Tafel plot, and LP methods. CV is widely used to understand the redox process of the elements and determine diffusion coefficient and the apparent reduction potential. The equilibrium potential and the apparent reduction potential also can be easily extracted via OCP. In addition, kinetic parameters including the exchange current density and the rate constant can be calculated by conducting EIS, Tafel, and LP methods. These five techniques and their associated equations to measure the electrochemical and thermodynamic properties will be discussed in the following subsections.

2.3.1 Cyclic voltammetry (CV)

CV may be a most widely used technique among all methods available for studying electrode processes [52]. In this technique, linear scan voltammetry is carried out by switching the direction of the potential scan at a certain time, as shown in Figure 2.5 (a). This applied potential results in the reduction and oxidation of the species on the electrode surface. A current increase can be observed due to the electrode reaction, and peak current can be found because of the depletion of species on the electrode surface, as shown in Figure 2.5 (b).

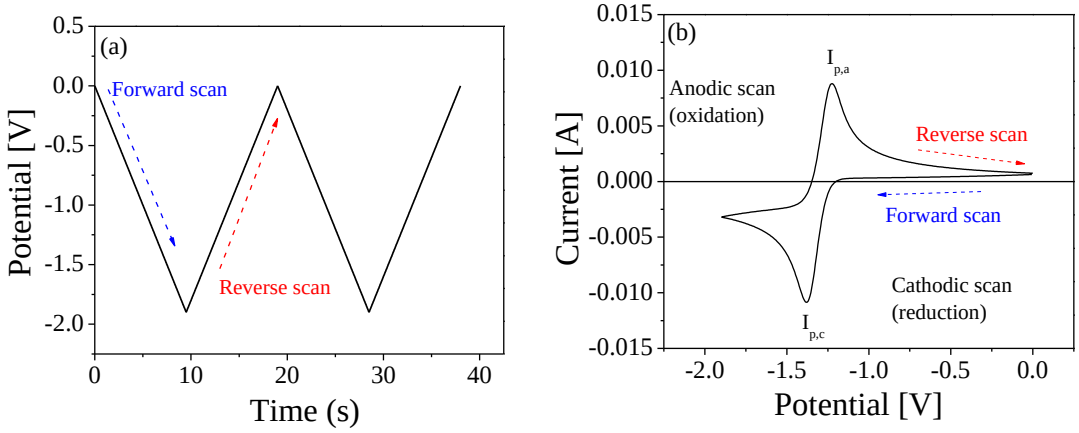

Figure 2.5 (a) A typical potential waveform in CV, and (b) a typical reversible CV response with reduction and oxidation reactions.

From the results of the CV data, a reversibility of the redox reaction can be verified, which is a relationship between the redox reaction rate and the mass transfer rate. The reversible system is characterized by faster kinetic reaction than mass transfer of the species. In this case, the peak potential (E_p) will remain at the same potential under different sweeping scan rates [52]. If the electrode reaction rate is slowly moving than the mass transfer, the system is irreversible; that is,

the peak potential will shift toward a negative direction with an increasing scan rate [52]. The quasi-reversible system is intermediate between reversible and irreversible systems [55]. The condition for the reversibility is established at stationary planar electrode as [52, 55]:

$$\text{reversible system: } k_1^0 \geq 0.3\, \upsilon^{1/2} \text{ cm s}^{-1} \quad (2\text{-}6)$$

$$\text{quasi} - \text{reversible system: } 0.3\, \upsilon^{\frac{1}{2}} \geq k^0 \geq 2 \times 10^{-5} \upsilon^{1/2} \text{ cm s}^{-1} \quad (2\text{-}7)$$

$$\text{irreversible system: } k^0 \leq 2 \times 10^{-5} \upsilon^{1/2} \text{ cm s}^{-1} \quad (2\text{-}8)$$

where k^0 is the rate constant for the electrode reaction (cm s^{-1}) and υ is the scan rate. The number of electrons transferred in the electrode reaction can be determined by the measurement of cathodic and anodic peak currents, which can be exhibited [37, 55] by

For reversible system:
$$\left|E_{pc} - E_{pc/2}\right| = 0.77\, \frac{RT}{nF} \quad (2\text{-}9)$$

For irreversible system:
$$\left|E_{pc} - E_{p/2}\right| = 1.857\, \frac{RT}{n\alpha F} \quad (2\text{-}10)$$

where $E_{p/2}$ is the half peak potential, and E_{pc} and E_{pa} are the cathodic and anodic peak potentials, respectively. Dalahay solved the boundary value problem for soluble/soluble diffusional system, the peak current can be expressed [56] as

For reversible system:
$$i_p = 0.446 nFSC_0 \sqrt{\frac{nFD\upsilon}{RT}} \quad (2\text{-}11)$$

For irreversible system:
$$i_p = 0.499 nFSC_0 \sqrt{\frac{\alpha nFD\upsilon}{RT}} \quad (2\text{-}12)$$

where S is the electrode surface area (cm^2), C_0 is the bulk concentration of species (mol cm^{-3}), υ is the scan rate (V s^{-1}), and D is the diffusion coefficient (cm^2 s^{-1}). Model for the reversible soluble/insoluble diffusion system (electrodeposition on the electrode) was developed by Berzins and Delahay [57]. The model used the assumption that the deposited species (in metal form) has a constant activity at unity. The equation can be expressed as

$$i_p = 0.611\, nFSC_0 \left(\frac{nF\upsilon D}{RT}\right)^{1/2}. \quad (2\text{-}13)$$

Therefore, Eq. 2-11 – Eq. 2-13 allow to calculate diffusion coefficient by plotting i_p over the square root of the scan rate. In Eq. (2-12), αn can be estimated by using Eq. (2-10) from CV measurements. The diffusivity generally follows Arrhenius temperature relationship, which can be expressed as

$$D = D_0 \exp\left(\frac{-E_a}{RT}\right) \quad (2\text{-}14)$$

where D_0 is the pre-exponential factor, and E_a is then an activation energy (kJ mol^{-1}) for the diffusion. Therefore, the activation energy for the diffusion can be calculated from the slope when ln(D) is plotted versus 1/T.

The measured peak potentials from the cyclic voltammogram can be used to calculate the apparent standard potential. For a reversible soluble/insoluble system, the cathodic peak potential can be expressed as [55, 56]

For reversible system:
$$E_p = E^{0*} + \frac{RT}{nF}\ln(X) - 0.854\frac{RT}{nF} \quad (2\text{-}15)$$

For irreversible system: (soluble/soluble)
$$E_p = E^{0*} - \frac{RT}{n\alpha F}\left[0.78 - \ln k_i + \ln\left(\sqrt{\frac{n\alpha F\upsilon D}{RT}}\right)\right] \quad (2\text{-}16)$$

where E_p is the peak potential (V) obtained from the cathodic side, X is the mole fraction, and E^{0*} is the apparent standard potential (V), and k is the rate constant (cm s^{-1}). Using Eqs. (2-14) and (2-15), the apparent standard potential of species for the reversible and irreversible systems can be experimentally calculated via the CV measurements.

2.3.2 Open circuit potential (OCP)

The thermodynamic properties in terms of redox reaction can be readily measured by using the OCP method. During this measurement, a potential is measured with no appreciable current flowing through the cell; therefore, OCP is also known as 'the zero-current potential' or 'the rest potential' [55]. When the redox couple is present at an equilibrium state on the electrode, the OCP provide a steady potential between oxidant and reductant, which is the equilibrium potential. An example potential response is described in Figure 2.6, in which the equilibrium potential of U was measured at the concentration of 0.5 wt% UCl_3-LiCl-KCl at 773K. By providing the equilibrium potential, the apparent standard potential (typically referred as a formal potential) of the redox reaction can be calculated by plotting the equilibrium potential versus concentration of species. Also, the values of the equilibrium potential can be directly substituted in Eq. (2-2) to determine the apparent standard potential. Furthermore, the OCP measurement is useful in monitoring whether electrochemical cell/electrode is in equilibrium state; therefore, OCP should be checked before or between electrochemical measurements to verify that the electrochemical cell is under the same condition at the equilibrium state.

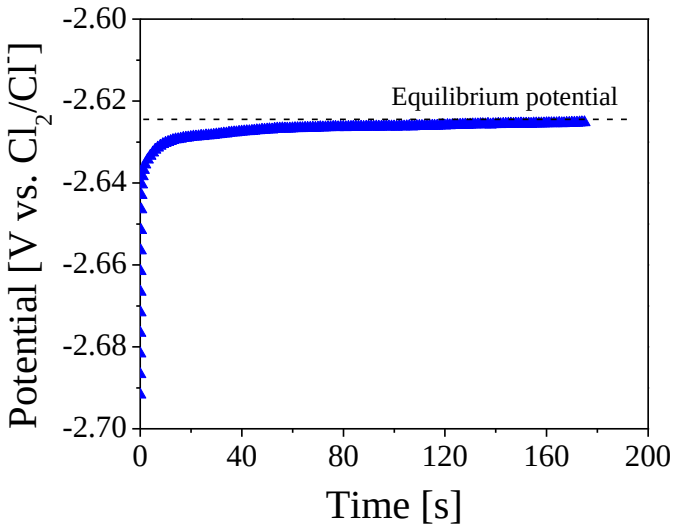

Figure 2.6 An example of OCP measurement in 0.5 wt %UCl_3-LiCl-KCl at 773 K.

2.3.3 Electrochemical impedance spectroscopy (EIS)

EIS is a technique to measure the cell/electrode impedance as a function of the frequency [55]. This technique is useful to understand the electrode process with respect to contributions from diffusion, kinetics, double layer, and reactions; therefore, there are many broad applications that EIS can be used to yield insightful information, such as corrosion, membranes, batteries, etc. [52]. The impedance can be measured by applying a perturbation signal which results in a corresponding response (i.e. solution resistance, double layer capacitance, and charge transfer resistance). The potential perturbation input can be expressed as a function of time: [55]

$$\mathrm{E(t)} = \mathrm{E(0)sin(\omega t)} \tag{2-17}$$

where E(t) is the potential at time t (V), E(0) is the amplitude of the potential signal (V), and ω is the angular frequency (rad s^{-1}) which is 2π times the conventional frequency in Hz. The current response can be expressed as [55, 58]

$$\mathrm{i(t)} = \mathrm{i(0)\ sin(\omega t + \phi)} \tag{2-18}$$

where i(t) is the current at time t (A), i(0) is the amplitude of the current signal (A), and ϕ is the phase angle which is illustrated in Figure 2.7. This current-voltage relation is analogs to Ohm's law; therefore, the impedance, Z, can be expressed as

$$Z(\mathrm{t}) = \frac{\mathrm{E(t)}}{\mathrm{i(t)}} = \frac{\mathrm{E(0)sin(\omega t)}}{\mathrm{i(0)sin(\omega t + \phi)}} = \mathrm{Z(0)}\frac{\mathrm{sin(\omega t)}}{\mathrm{sin(\omega t + \phi)}} \tag{2-19}$$

where Z(t) is the impedance (Ω) and Z(0) is the amplitude of the impedance. When the E(t) and i(t) are considered in complex plane, the equations can be described as

$$E(t) = E(0)\exp(j\omega t) \tag{2-20}$$

$$i(t) = i(0)\exp(j(\omega t - \phi)) \tag{2-21}$$

where j is the imaginary number, $\sqrt{-1}$. By applying complex function, $\exp(j\phi) = \cos\phi + j\sin\phi$, the impedance, Z, can be expressed in complex plane as

$$Z(t) = Z(0)(\cos\phi + j\sin\phi) = Z(Re) + Z(im) \tag{2-22}$$

where Z(Re) and Z(Im) are the real and imaginary part of the impedance. The Z(Re) and Z(Im) can be plotted on x-axis and y-axis, respectively, which is called the 'Nyquist plot.'

The EIS can be interpreted with an equivalent circuit consisting of resistances, capacitances, diffusion related impedances (Warburg impedance), and so on. The simplest model for the electrode process is called Voigt model containing solution resistance (R_s), charge transfer resistance (R_{ct}), and double layer capacitance (C_{dl}), as shown in Figure 2.8. The impedance of the Voigt model can be expressed by using following equation [55]:

$$Z(t) = R_s + \frac{1}{\frac{1}{R_{ct}} + j\omega C_{dl}} = R_s + \frac{R_{ct}}{1 + j\tau\omega} \tag{2-23}$$

where τ is the time constant relating with RC circuit. The second term in Eq. (2-20) can be considered with two different scenarios. First, it becomes very small and is negligible at high frequency. Second, it approaches R_{ct} at very low frequency. Figure 2.9 shows the ideal Nyquist plot for the Voigt model where R_s and R_s+R_{ct} can be easily found on the x-axis. The R_{ct} is formed when an electrochemical reaction occurs on the electrode at the equilibrium state, $R \leftrightarrow O + ne^-$, and the exchange current density (i_0, A cm^{-2}) and rate constant (k^0, cm s^{-1}) for the charge transfer can be calculated by using [55]:

$$R_{ct} = \frac{RT}{nFSi_0} = \frac{RT}{n^2F^2Sk^0C_0^{1-\alpha}} \tag{2-24}$$

Since the polarization of the electrochemical system in reality can be non-ideal and more complex according to the interfacial formations, the constant phase element (CPE) is typically being utilized to fit the experimental EIS spectra through the following expression: [59]

$$Z_{CPE} = \frac{1}{T(j\omega)^{\phi}} \tag{2-25}$$

where T is a constant in F cm^{-2} $s^{\phi-1}$ is the constant, ϕ is the number constant between -1 and 1, and ω is the frequency. Here, CPE can easily become double-layer capacitance, Warburg resistance, or pure resistance by changing the number of ϕ in Eq. (2-25).

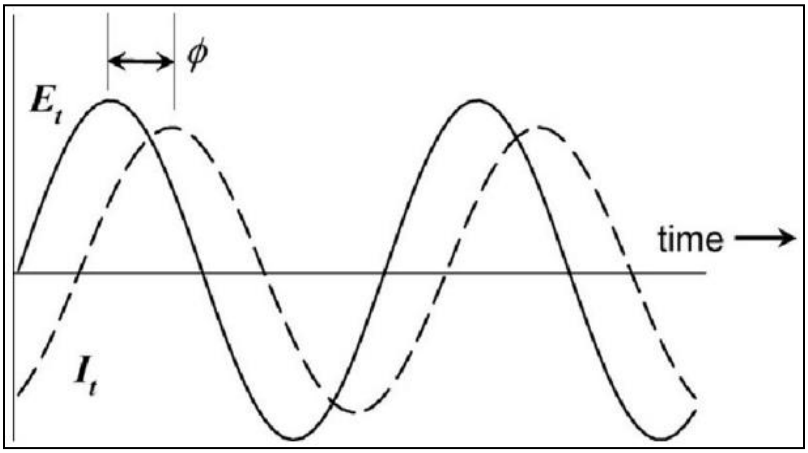

Figure 2.7 Sinusoidal potential input and sinusoidal current response in typical EIS measurements [58].

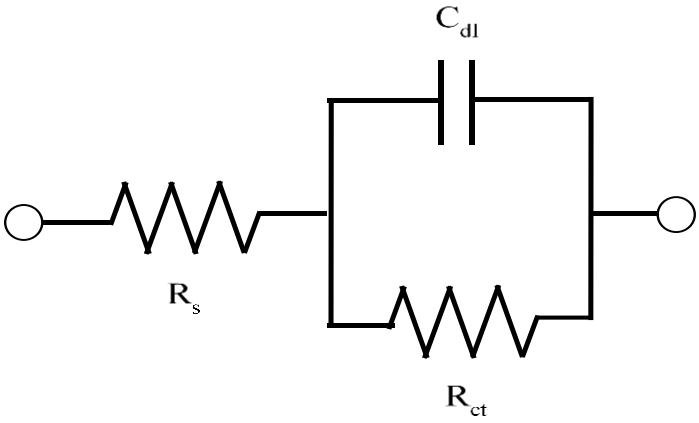

Figure 2.8 An equivalent circuit for Voigt model which is composed with resistance and capacitance.

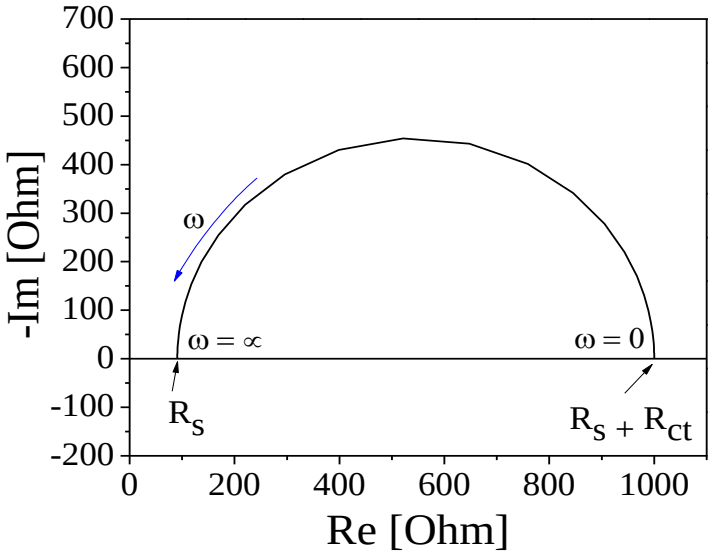

Figure 2.9 An ideal Nyquist curve for the Voigt model. Rs is bulk solution resistance and Rct is the charge transfer resistance on electrode surface.

2.3.4 Tafel and linear polarization (LP) methods

Considering a single step electrode reaction, $R \leftrightarrow O + e^-$, the rate of reaction controlled by the electron transfer can be examined via Tafel and linear polarization (LP) methods. The electrode reaction can be derived using current and overpotential relation under the assumption of fast mass transfer of the species, which can be expressed in another form of Eq. (2-5) as

$$i = i_0 \left[\exp\left(\frac{-\alpha n F}{RT}\eta\right) - \exp\left(\frac{(1-\alpha) n F}{RT}\eta\right) \right]. \quad (2\text{-}26)$$

When η is large, the second term on the RHS will be negligible and Eq. (2-25) becomes [55]

$$\log(i) = \log(i_0) + \frac{\alpha n F}{2.303\ RT}\eta\ , (\eta < 0). \quad (2\text{-}27)$$

The plot of log(i) versus η, known as the 'Tafel plot,' is useful in determining the value of i_0 by extrapolating to an intercept of log (i). Figure 2.10 shows an example the Tafel plot [55] in which linear Tafel region can be obtained at large overpotential region. Here, the value of i_0 can be determined at y-intercept. In the case that small η is applied to the cell, the Butler-Volmer equation can be further simplified to [55]

$$i = i_0 \left(\frac{nF}{RT}\right) \eta. \tag{2-28}$$

By plotting current-overpotential in very small overpotential region (Figure 2.11 shows an example of current-overpotential curve and the overpotential is typically less than 10 mV), R_{ct} can be obtained from the slope. Then, the value of i_0 can be calculated by using the Eq. (2-28).

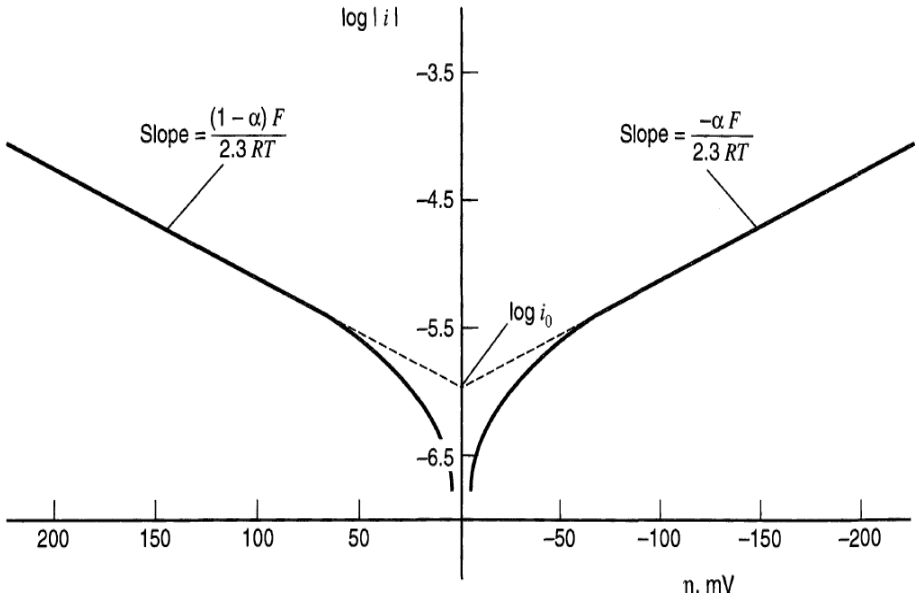

Figure 2.10 An example of Tafel plot for anodic and cathodic branches [55].

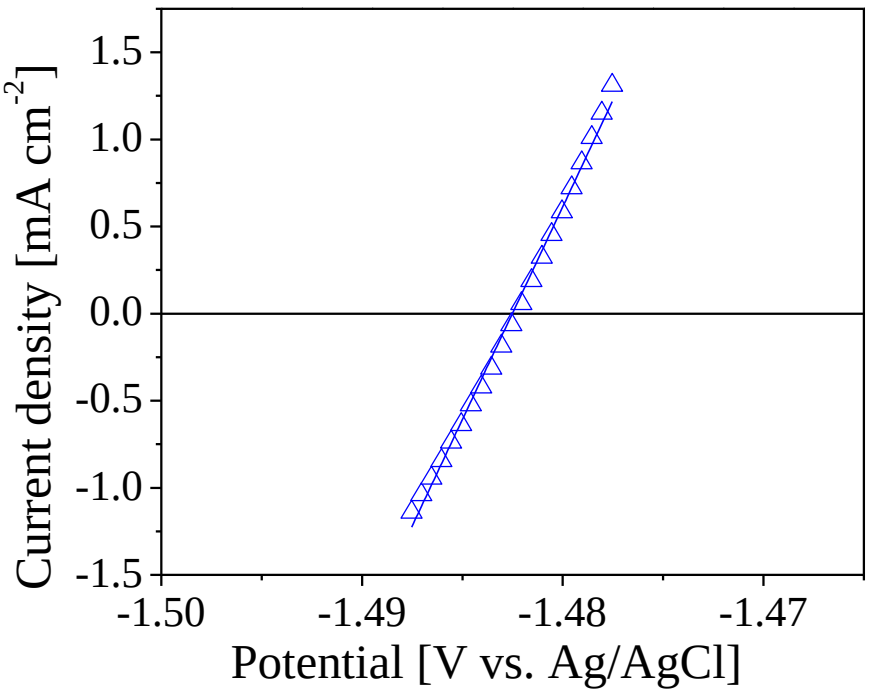

Figure 2.11 An example of current-potential curve at small overpotential region.

Table 2.2 Summary of electrochemical techniques used in each section and measured properties

Experiments	Elements	Electrode	Electrochemical methods				
			CV	OCP	EIS	Tafel/LP	OCC
Section 4.1	Ce	W	O		O		
Section 4.2	Ce	LCC	O			O	O
Section 5.1	U	W	O	O	O	O	
Section 5.2	U-Gd	W	O	O	O		
Measured Properties			D E0* ΔG γ	E E0* ΔG γ	R_{ct} i_0 k^0	i_0 k^0	ΔG ΔH ΔS

2.4 Summary

Literature surveys were performed to understand the available properties of nuclear elements previously reported. It was discussed that some data sets are scattered and not fully understood due to challenges in experimental measurements. In addition, electrochemical techniques and methods used in this project were investigated based on the literatures and textbooks. For the proper evaluation of uranium properties including diffusion coefficient, apparent standard potential, Gibbs free energy, activity coefficient, and exchange current density, specific techniques and equations must be applied to obtain accurate data sets. Table 2.2 summarizes the selected techniques and specific design to be used for each experiment in Sections 4 and 5.

3 Experimental setup and procedures

To elucidate the fundamental characteristics of UNF, it is important to carefully prepare and design the experiments in a controlled environment. As an example, the salt chemicals including LiCl and KCl have a hygroscopic characteristic; hence, the chemicals need to be prepared in free oxygen and water environment, or need to be purified. Therefore, the main purpose of this section is to provide detailed description of the experimental program used in the present research—installments of the equipment, reagents, materials, and sample preparation methods for performing all experimental runs. These steps are extremely critical in order to obtain reliable and repeatable results from the electrochemical measurements. It should be noted that this section will only provide general experimental setups and materials conducted in the laboratory. More detailed setups, designs, and experimental procedures specific to each experiment will be provided and discussed in Sections 4 and 5.

3.1 Equipment

Two glovebox systems (Innovative Technology) were established in the Radiochemistry laboratory (E4262 School of Engineering at VCU) as shown in Figure 3.1. The O_2 and H_2O levels are being monitored by oxygen and water sensors preinstalled on the glovebox system as shown in Figure 3.2(a). Occasionally, O_2 level was analyzed with a portable O_2 sensor (Advanced Instruments Inc. (see Figure 3.2(b))) to confirm the accuracy of the O_2 sensor on glovebox. All the electrochemical experiments were prepared and conducted when the O_2 level is less than 5 ppm. RAM II glovebox was designed to utilize radioactive materials; therefore, all researchers working in RAM II must take radiation safety training through VCU radiation safety section (RSS) and pass a test. When working in RAM II glovebox, researchers monitor hands, arms, and any materials moving in and out the glovebox by using hand-held monitors or Friskers as seen in Figure 3.3. Within the glovebox systems, commercial furnaces were installed to heat and maintain the salt samples at desired temperature. During preliminary studies, Kerrlab melting furnace was mainly utilized (see Figure 3.4(a)); however, this furnace had an issue in failing to control the temperature

after a continuous intensive use (e.g., 1-2 weeks duration). This may be due to failure of heating coil or temperature controller. After experiencing this issue several times during the preliminary studies, another commercial furnace (Muffle furnace) was purchased from Thermo Scientific and redesigned for the electrochemical experiments, as shown in Figure 3.4(b). Therefore, all the uranium studies (Section 5) were performed using Muffle furnace, which has been working remarkably well until now.

All the salt samples were handled, and precisely prepared by using the Mettler Toledo balance (< 1 μg tolerance, see Figure 3.5) installed in the glovebox systems. Here, it should be noted that further errors can be introduced by build-up of static charges on the weighting plates or pressure difference in the glovebox system. When the sample preparations and electrodes setup were completed, VSP-300 potentiostat/galvanostat (purchased from Biologic Science Instrument as shown in Figure 3.6) were connected through the isolated feed through ports on the glovebox wall. For collecting and processing the measured data, EC-Lab software released from Biologic-Science Instruments was utilized for all electrochemical experiments in the present research. During the data measurements, the salt samples were taken using a tungsten rod and analyzed by an Agilent 7900 inductively coupled plasma-mass spectrometry (ICP-MS), as shown in Figure 3.7.

Figure 3.1 Glovebox systems (RAMI (Left) and RAMII (Right)) for electrochemical experiments.

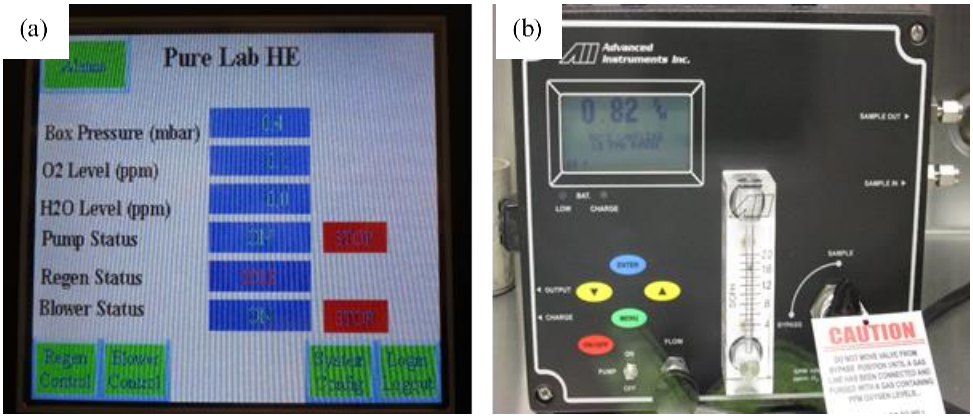

Figure 3.2 (a) Digital control panel on the glovebox systems reading oxygen and water levels and (b) a portable oxygen analyzer from Advanced Instruments Inc.

Figure 3.3 Pancake detector frisking meter (left) and hand survey meter (right) from Atlantic Nuclear Corporation.

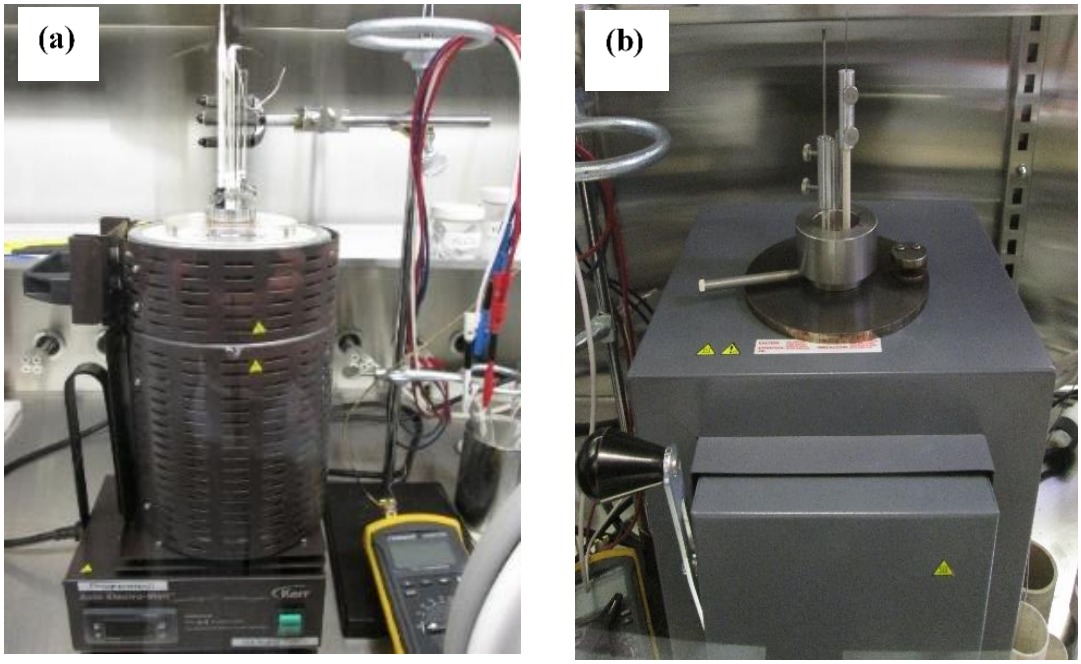

Figure 3.4 (a) Kerrlab melting furnace, and (b) Muffle furnace from Thermo Scientific.

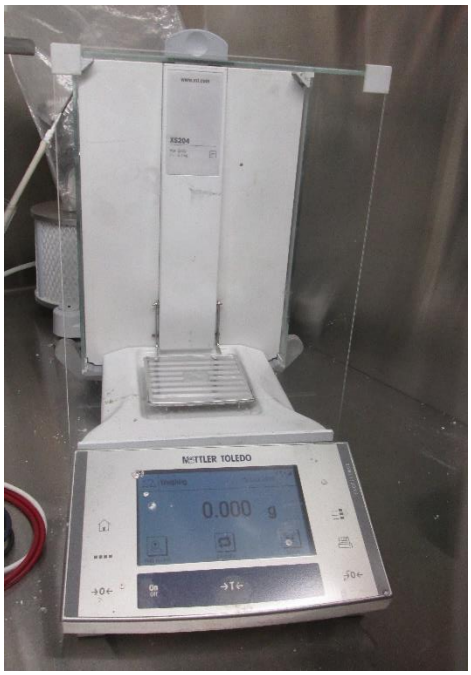

Figure 3.5 Mettler Toledo balance placed in the glovebox systems.

Figure 3.6 VSP-300 potentiostat/galvanostat, Biologic Science Instrument.

Figure 3.7 Agilent 7900 ICP-MS instrument installed in the Radiochemistry laboratory.

3.2 Experimental preparation

3.2.1 Reagents and crucibles

Anhydrous lithium chloride (LiCl, 99.995%, bead type) and potassium chloride (KCl, 99.95%) were purchased from Alfa Aesar. The beads of LiCl and KCl were well mixed in quartz crucible to prepare a LiCl-KCl (58.2:41.8 in mol%) eutectic salt. The prepared mixtures were loaded in a vessel and heated in furnace (melting temperature of LiCl-KCl eutectic salt is 623 K). Once LiCl-KCl eutectic salt was prepared, target elements including cerium chloride ($CeCl_3$), uranium chloride (UCl_3), and gadolinium chloride ($GdCl_3$) were added in the vessel. The depleted UCl_3 powders (73 wt% UCl_3 in LiCl-KCl) provided by INL (see Figure 3.8(a)) were used for the uranium studies in Section 5. It should be noted that all the salt samples were dried at 523 K for 5 hours to remove possible moisture contents despite having the salt in sealed glass ampoules under argon prior the melting processes. Prior to the electrochemical measurements, few more hours (3 to 5 hours) were given for the salt system to reach the equilibrium state at the desired temperature.

In preliminary studies, alumina (Al_2O_3) crucible was generally used as the vessel, which was washed/sonicated with ultra-pure water and dried in an oven at 473 K for 2 hours. All the uranium studies were performed with Inconel® crucible (Inconel 601 alloy, nickel-chromium-iron alloy from Alfa Aesar) owing to the reactions happening between uranium chloride and oxygen/adhesives from the alumina crucibles. These main vessels were placed in a secondary crucible to contain any molten salt upon possible failure of the primary crucible as can be seen in Figure 3.9. The specific information of the reagents and crucibles can be found in Table 3.1.

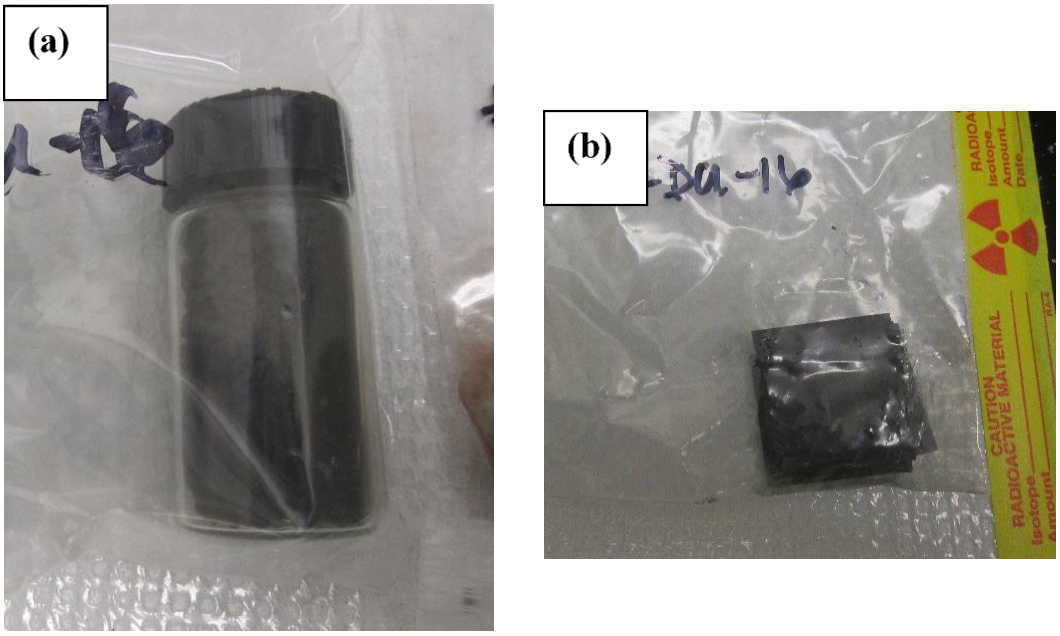

Figure 3.8 Depleted uranium samples: (a) LiCl-KCl - 73 wt% UCl_3 eutectic, and (b) uranium plates provided by INL.

Figure 3.9 Alumina crucible (left) and Inconel crucible (right) placed in safety crucible for preliminary and uranium studies, respectively.

Table 3.1 Material summaries for reagents and crucibles used in the present study

Materials	Detailed data	Manufacturers	Applications
LiCl	99.995%, bead type	Alfa Aesar	Prepare LiCl-KCl electrolyte
KCl	99.95%, bead type	Alfa Aesar	Prepare LiCl-KCl electrolyte
AgCl	99.998%, bead type	Alfa Aesar	Reference electrode
$CeCl_3$	99.9%, bead type	Alfa Aesar	Preliminary study
$CdCl_2$	99.999%, powder	Alfa Aesar	Preliminary study
Ce metal	99.9%, metal chips	Sigma-Aldrich	Preliminary study
Cd	99.999%, shots	Alfa Aesar	Preliminary study
UCl_3	73% in LiCl-KCl, powder	INL	Uranium study
$GdCl_3$	99.99%, powder	Alfa Aesar	Uranium study
U metal	Depleted U metal plate	INL	Uranium study
Al_2O_3 crucible	99.8%, OD: 48, H: 47 mm	Coorstek	Vessel in Preliminary study
	OD: 28, H: 40 mm		Vessel in Preliminary study
	OD: 40, H: 165 mm		Safety crucible in Preliminary study
	OD: 54, H: 91 mm		Safety crucible in Uranium study
Inconel® crucible	OD: 47 mm, H: 41 mm	Alfa Aesar	Vessel in Uranium study

3.2.2 Electrodes: Working, Counter, and Reference Electrode

All electrode rods were preinstalled in alumina sheath for the prevention of a shortage in the electrical circuit as indicated in Figure 3.10(a). Tungsten rods (99.95%, 1.5 mm – 2.0 mm in diameter, Alfa Aesar) were typically used as a working electrode. The geometric surface area was determined by measuring the immersed length of the working electrode into the molten salt as shown in Figure 3.10(b). A glassy carbon rod (HTW, 3mm in diameter), Ce metal chips (Sigma-Aldrich 99.9%), and U metals (see Figure 3.8(b) provided by INL) were used for a counter electrode according to the experimental runs. Since designs and configurations of the working/counter electrodes vary with the different tasks, specific information can be found in the experimental section of each Section (see Sections 4 and 5). In contrast, all the experiments utilized the Ag/AgCl reference electrode, so that the preparation of reference will be discussed in this section. Specific procedure of the preparation is as follows:

- Prepare the LiCl-KCl eutectic salt in a closed-end Quartz tubing (22 mm in OD, Research Glass),
- Add a certain amount of AgCl in the Quartz crucible and melt the salt at 773 K,
- Stir the LiCl-KCl-AgCl salt and leave it for 3 hours for homogeneity of the salt,
- Insert a Pyrex tube (4 mm in OD, Research Glass) into the salt solution, and draw the salt into the tube by using a syringe,

- Leave the drawn salt under a room temperature to solidify the salt, and
- Obtain the solid rod of LiCl-KCl-AgCl salt as shown in Figure 3.11.

The prepared AgCl salt rod was loaded in a 7 mm diameter Pyrex tube (Research Glass), which is closed at one end. At the tip of the tube, the thickness of the wall was made thin enough (less than 0.5 mm in thickness, see Figure 3.12(a)) allowing ionic conduction between the solution and electrolyte. As shown in Figure 3.12(b), the prepared AgCl salt rod is loaded in the Pyrex tube, which is melted at high temperature and contacted with Ag wire (99.99%, 1 mm in diameter, Alfa Aesar). Therefore, the equilibrium potential between Ag metal and AgCl solution was established and used as a standard potential for all electrochemical measurements in the present researches.

In the preliminary study (Section 4), 5 mol% AgCl reference was prepared and used as a reference electrode, while Ag/AgCl (1 mol%) reference was utilized for the uranium studies in Section 5. Since various concentrations of AgCl solution were utilized for electrochemical research in literature, the results data should be converted into Cl_2/Cl^- scale for meaningful comparison. Therefore, the conversions from Ag/AgCl (1 mol% and 5 mol %) to Cl_2/Cl^- reference electrode were being performed by the interpolation/extrapolation of the data reported by Yang and Hudson [60]. The potential differences between Ag/AgCl and Cl_2/Cl^- used in the present study are summarized in Table 3.2.

Figure 3.10 (a) Tungsten rod sheathed with alumina tube, (b) measurement of submerged electrode area in the salt by using digital caliper.

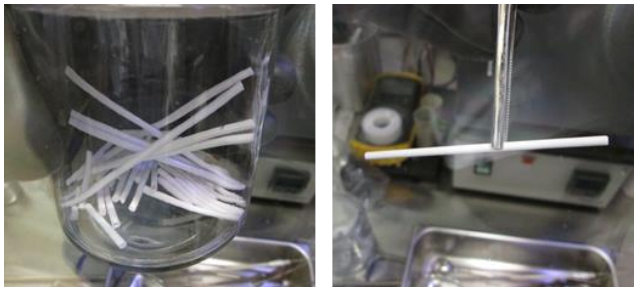

Figure 3.11 Prepared AgCl salt rods.

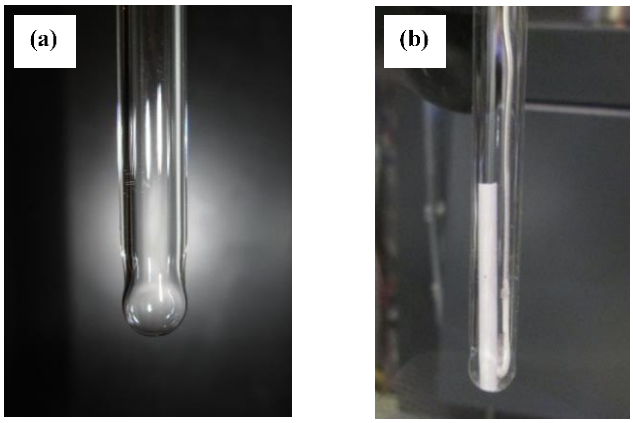

Figure 3.12 (a) Pyrex tube with thin end for ionic conductivity, (b) Ag/AgCl reference built in Pyrex tube.

Table 3.2 Potential differences between Ag/AgCl reference electrodes and Cl_2/Cl reference at different temperatures [60]

T [K]	ΔE between Ag/AgCl and Cl_2/Cl references [V]	
	1 mol% Ag/AgCl	5 mol% Ag/AgCl
698	1.155	1.069
723	1.157	1.068
748	1.159	1.067
773	1.161	1.067
798	1.161	1.066
823	1.163	1.065

3.2.3 Electrode assembly

For securely placing the electrodes and thermocouple under the molten salt at high temperature, an electrode assembly was designed and manufactured in VCU School of Engineering machine shop, which is indicated in Figure 3.13. Main purpose of the design was to 1) assemble the electrode as a single body for easy access into the furnace from the top lid, 2) place the electrodes at demanding vertical position, and 3) take the salt sample during experiments. Figure 3.14 shows the parts of the electrode assembly and its specific diagram. There are three main bodies made with stainless steel where four holes (two holes are designed for 5 mm OD cylinder and the other holes are for 7 mm OD cylinder). On top of the Part (c) in Figure 3.14, high temperature rubber O-rings were placed which the electrodes were slid in. When Parts (a) and (c) are tighten by using the threads, the O-rings are squeezed and therefore tightly holding the electrodes without breaking the alumina sheath. In this manner, the electrodes are securely assembled in a single body; hence, an access of the assembly can be easily made into the furnace at high temperatures. In addition, electrode rods inside the alumina sheath can be separately removed from the assembly body. Thus, electrode cleaning and salt sampling can be readily conducted during the electrochemical measurements.

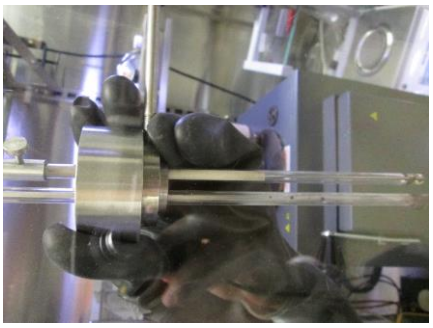

Figure 3.13 Electrode assembly for electrochemical applications.

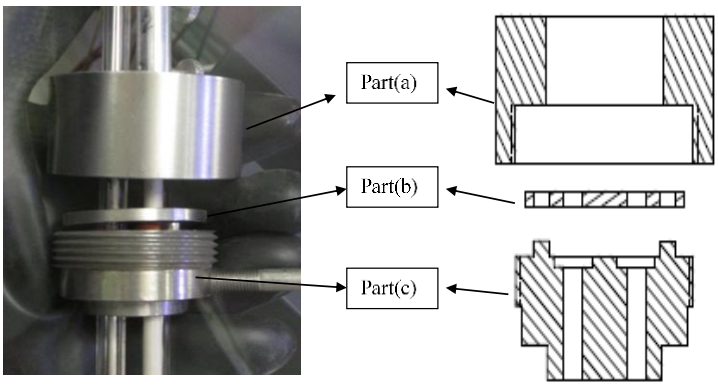

Figure 3.14 Electrode assembly parts and its diagram.

3.2.4 Sample preparations for ICP-MS Analysis

In particular, all uranium salt samples provided by INL may be non-homogenous and contain oxide formations, which will have an influence on the chemical compositions. Therefore, the concentration of the prepared UCl_3 salts were demonstrated by using an ICP-MS analysis. Due to the hygroscopic feature of the salt sample, the following sample preparation procedures were used:

- Prepare the nitric acid (2% HNO_3) with the ultrapure (Type 1) water,
- Prepare 6 – 9 standard samples using multi-element blends: CCS1 and CCS4 (Inorganic Ventures),
- Prepare different internal standards at ~5000 µg/L,
- Take 15 mL centrifuge tubes into the glovebox,
- Measure the weight of salt sample (be careful of static and pressure effects),
- Load salt samples in the centrifuge tubes and close the lid,
- Take out the centrifuge tubes from the glovebox,
- Open the lid and quickly fill out the tubes with 10 mL HNO_3 in order to minimize water absorption from an environment,
- Wait for the solid salts to be fully dissolved into the HNO_3 solution,
- Dilute the stock samples with 500 - 5000 times for running uranium samples lower than EPA regulation (U.S. EPA regulation for drinking water is less than 30 µg/L), and
- Run the ICP-MS with the diluted samples and calculate concentrations with the used dilution factors.

3.3 Summary

In this section, general experimental preparations generally were described. Apparatus including the glovebox systems, the furnaces, and the potentiostat were first presented. Then, the reagents and crucibles used in the present study were introduced and their specifications and preparation methods were discussed. It was followed by the explanation of electrodes. While the working and counter electrodes are particularly designed for achieving goals of each experiment, the Ag/AgCl reference electrode was commonly used for all electrochemical measurements; therefore, Ag/AgCl reference construction and the potential difference from Cl_2/Cl^- reference electrode were mainly focused. In addition, the electrode assembly were designed and built based on the concept for easy access into the molten salt at high temperature. Lastly, all sample preparations and procedures for the ICP-MS quantitative analysis were provided. This given information will be useful to understand other experimental setups and conditions in following sections discussing the electrochemical measurements and results.

4 Preliminary Studies: Experimental Development with Ce as a Surrogate Material for U

The main purpose of this section is to provide the information on a development of experimental methodologies, and electrochemical techniques with a non-radioactive material, which can be applied toward uranium. Cerium chloride ($CeCl_3$) was selected as a surrogate material for UCl_3 because the Ce^{3+} has similar electrochemical characteristic and ionic size of U^{3+} [61]. The ionic sizes are about 115 pm and 117 pm, for Ce^{3+} and U^{3+}, respectively [62], and diffusion coefficients of both elements are in order of 10^{-5} cm s^{-1} [37, 45, 61, 63, 64]. Therefore, electrochemical measurements were performed to evaluate Ce properties such as diffusion coefficient, apparent standard potential, thermodynamic properties, and exchange current density in LiCl-KCl eutectic salt. Section 4.1 will discuss the measurements of Ce properties using solid working electrode while Section 4.2 discuss the Ce behaviors on LCC electrode, which will elucidate the fundamental properties of actinide (An) and lanthanide (Ln) in ER process with LCC operations.

4.1 Electrochemical properties and analyses of $CeCl_3$ in LiCl-KCl eutectic salt[1]

4.1.1 Introduction

Several studies on the electrochemical behaviors of cerium in the molten salt at high temperatures have been previously conducted. In 1998, Iizuka [7] conducted CP to determine

[1] Contents in Section 4.1 are cited from the author's publication:
D. Yoon and S. Phongikaroon, "Electrochemical properties and analyses of $CeCl_3$ in LiCl-KCl eutectic salt," *Journal of The Electrochemical Society*, **162** (10), E237-E243 (2015).

diffusion coefficient of $CeCl_3$ at different temperatures. Marsden and Pesic in 2011 [61] measured apparent standard potentials and diffusion coefficients of $CeCl_3$ by CV technique. They also determined the exchange current densities of $CeCl_3$ using the LP method. While the diffusion coefficients and apparent standard potentials of Ce elements were well evaluated from many researchers with various techniques, only LP method was used for the measurement of i_0. Due to the difficulties in measuring the i_0 with LP method, Marsden and Pesic [61] provided wide ranges of i_0 values for Ce^{3+}/Ce.

The main goal of this section is to provide measurement and analyses of electrochemical and kinetic properties of $CeCl_3$ in LiCl-KCl eutectic salt at different concentrations and temperatures using two methods: (1) CV for measuring the D and E and (2) EIS for determining the i_0 values. The outcomes will provide useful insight into these properties with a unique feature of EIS technique by reducing uncertainty of electrode area measurement because very small current is applied at around an open circuit potential.

4.1.2 Particular experimental setup and routine

For the preparation of chemicals, crucibles, and reference electrode, general procedures as discussed in Section 3.2 were followed. Figure 4.1 indicates the schematic design of the electrochemical cell placed in the Kerrlab furnace. Tungsten rods (1.5 mm and 2 mm in diameter) were used as the working electrode. The length of the working electrode submerged into the salt was measured, and the surface areas were ranging from 0.32 cm^2 to 0.63 cm^2 depending on experimental runs. The cerium chips were loaded in a molybdenum basket and lowered into the prepared salt, which works as the counter electrode. Prior to using the counter electrode, an oxide layer on the cerium chips was eliminated using sand paper under argon environment. Ag/AgCl (5 mol%) was used as a reference electrode. Table 4.1 summarizes the experimental program developed in this study. Prior to each experiment, the working electrode was anodically cleaned by stripping at a potential of -0.1 V versus the reference electrode for 3 minutes. Then, OCP was checked to ensure the equilibrium condition has reached in the system. This was repeated for each electrochemical measurement, and anodic stripping and OCP were carried out longer in case of higher concentrations.

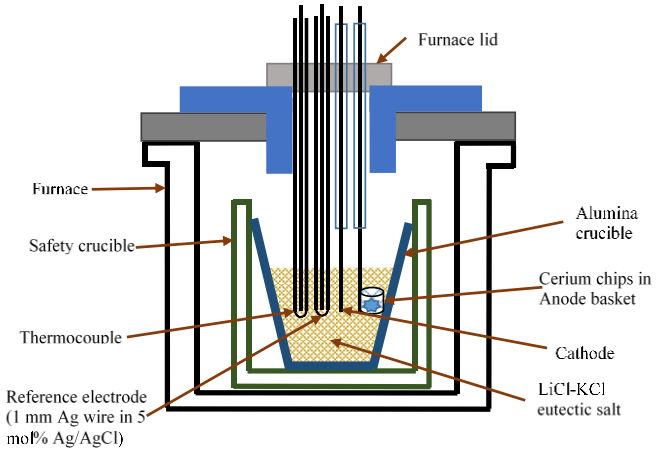

Figure 4.1 Schematic sketch of the experimental setup of all electrochemical experiments.

Table 4.1 Detailed experimental program for electrochemical measurements of $CeCl_3$

Experimental runs	Temperature [K]	Electrode area [cm^2]	$CeCl_3$ concentration		
			[wt%]	[mol%]	[mole/cm^3] × 10^5
Ce_S_1	698 – 798	0.559	0.507	0.115	3.33 – 3.44
Ce_S_2		0.685	0.498	0.113	3.27 – 3.37
Ce_S_3		0.597	2.06	0.473	13.7 – 14.1
Ce_S_4		0.324	4.03	0.944	27.4 – 28.3

4.1.3 Results and Discussion

4.1.3.1 Cyclic voltammetry (CV) of the LiCl-KCl-$CeCl_3$ system

The CV technique was first applied to the pure LiCl-KCl system to identify that no other reactions occurring in the range between 0 V and -2.5 V versus Ag/AgCl reference. The voltammogram of pure LiCl-KCl (in Figure 4.2) shows that Li reduction starts at -2.55 V (vs. Ag/AgCl). No redox reaction between 0 to -2.4 V was observed and residual current in that region was less than 2 mA. Therefore, it was safe to perform the CV experiments over that potential range without interference from other reactions. Figure 4.3 shows the cyclic voltammograms of $CeCl_3$ (0.5 wt%, 2 wt%, and 4 wt%) in LiCl-KCl at 773 K. It was extremely important to obtain repeatable and reproducible CV data. Table 4.2 provides the summary of the methods for the CV measurements and data acquisition in detail.

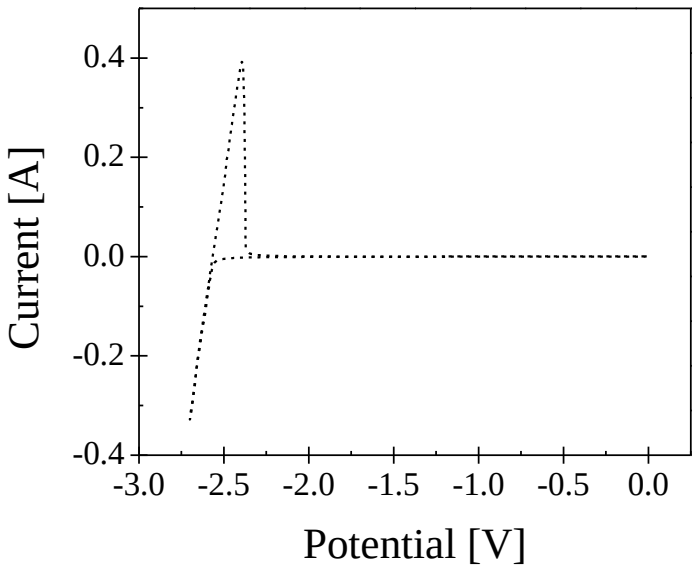

Figure 4.2 Cyclic-voltammogram of pure LiCl-KCl eutectic salt at 773 K at the scan rate of 0.1 V s^{-1}. Tungsten rod (2 mm in diameter) was used as cathode electrode, and the surface area was 0.471 cm^2.

Here, Ce reduction and oxidation peaks were observed at around -2.2 and -2.09 V versus the Ag/AgCl reference electrode, respectively. For 0.5 wt% $CeCl_3$, the peak potentials stay at the same potential under different scan rates representing the reversibility of the reaction in the range of the scan rate. However, the peak potentials move slightly in the negative direction according to the scan rate when the concentration of $CeCl_3$ was being increased to 4 wt%. This may be considered as a quasi-reversible reaction.

Table 4.2 Steps of CV measurements and data acquisition

Step	Description
1	Clean the working electrode by applying an oxidative potential (-0.1 V vs. Ag/AgCl) for 3 minutes,
2	Wait for 1 ~ 3 minutes until the OCP becomes stable,
3	Perform CV measurements at least 5 cycles,
4	Obtain the data if the CV curves are repeatable,
5	Repeat Steps 1 – 4 for next CV measurement,
6	Measure peak current, peak potential, and half peak current using the EC-LAB software, and
7	Calculate the values of D and E^{0*} using Eq. (2-13) and Eq. (2.15), respectively.

The difference between peak potential and half peak potential can be used to calculate the number of electron transferred by using Eq. (2-9). The calculated number of electron transferred, n, was ranging from 2.5 to 3.1 agreeing with the expected value for the reduction process of Ce^{3+}/Ce. The cathodic peak currents were plotted with respect to the square root of the scan rate to calculate diffusion coefficient of $CeCl_3$ in LiCl-KCl using Eq. (2-13). The diffusion coefficient of $CeCl_3$ was determined at different concentrations, as indicated in Figure 4.4. Small decrease of the values could be observed by increasing concentration from 0.5 wt% to 2 wt%; however, the diffusion coefficients of $CeCl_3$ in LiCl-KCl salt were approximately the same between the concentrations of 2 and 4 wt%. Present study shows smaller values for the diffusion coefficients comparing with those from Marsden and Pesic [61] and Iizuka [7] with a similar trend.

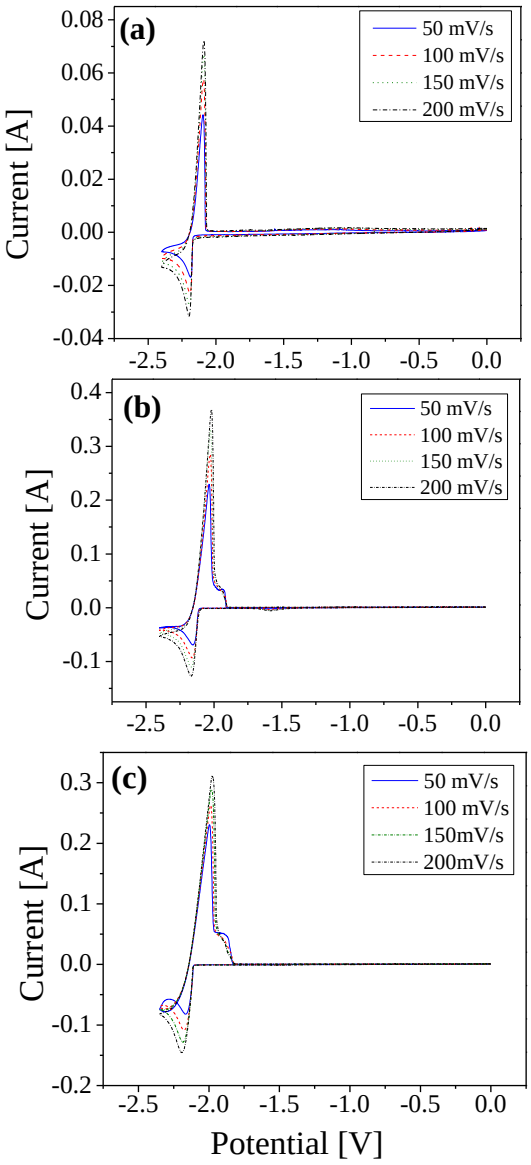

Figure 4.3 Cyclic-voltammogram of $CeCl_3$ in LiCl-KCl at 773 K at scan rates of 0.05, 0.1, 0.15, and 0.2V s^{-1}: (a) 0.5 wt % $CeCl_3$, (b) 2 wt % $CeCl_3$ (c) 4 wt % $CeCl_3$.

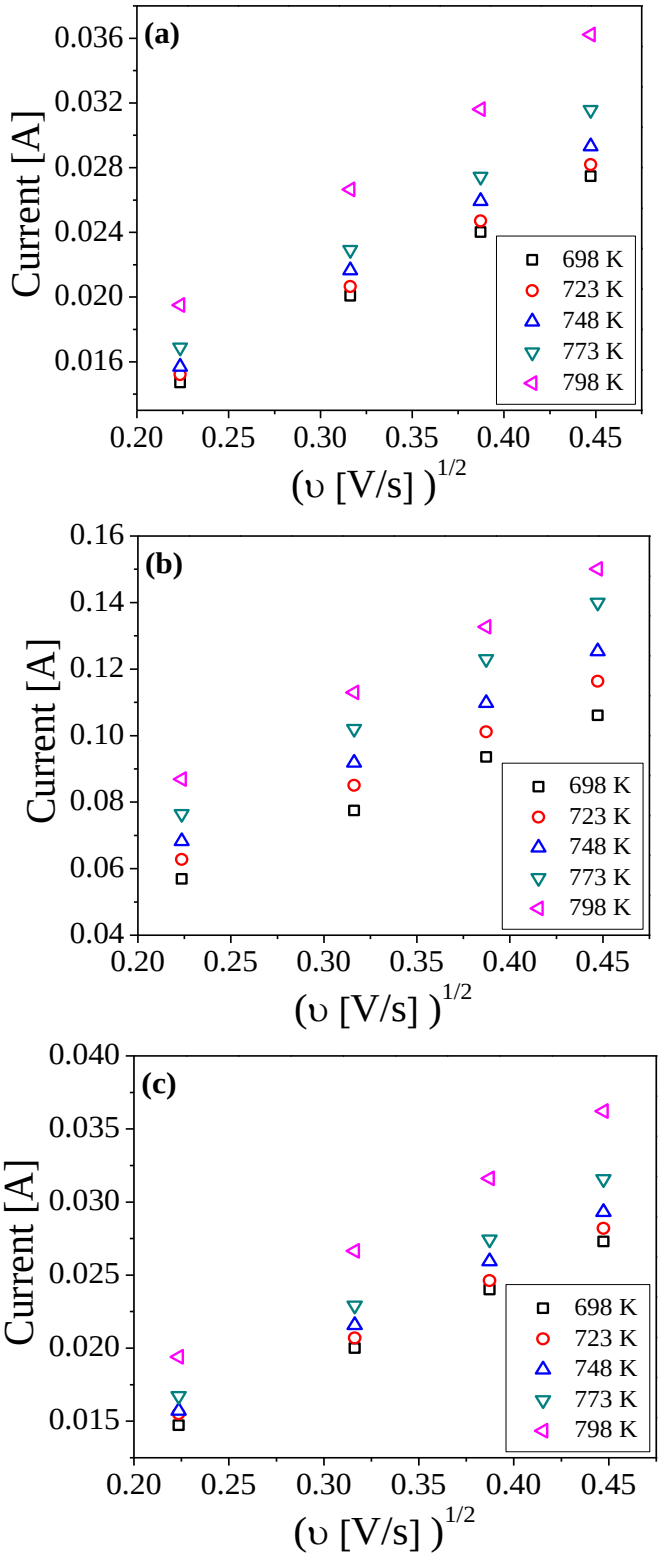

Figure 4.4 Plots of the peak currents versus the square roots of the scan rates at (a) 0.5 wt%, (b) 2 wt%, (c) 4 wt% $CeCl_3$.

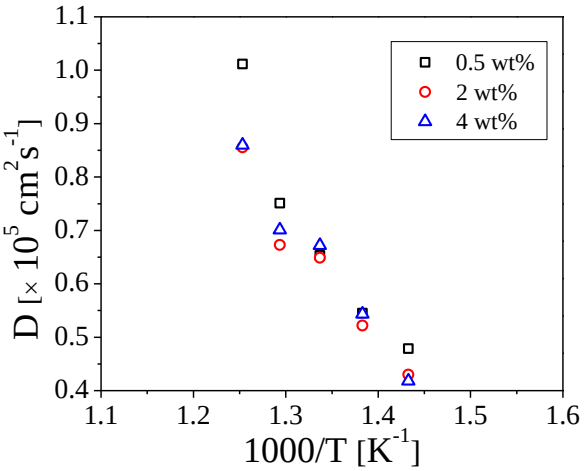

Figure 4.5 Plots of diffusion coefficient of Ce^{3+} versus inverse temperature at different $CeCl_3$ concentrations (0.5, 2, and 4 wt %).

The square root of D was plotted against inverse temperature, allowing calculation of the activation energy for $CeCl_3$ diffusion by using the Arrhenius relationship in Eq. (2-14). The R^2 values between the fitted regression lines and experimental points were all greater than 0.96 indicating a good fit to the data sets. Table 4.3 lists the D of $CeCl_3$ and the average E_a with different temperatures and concentrations.

Table 4.3 Diffusion coefficients (D) measured from CV experiments and activation energy (E_a) at different concentrations and temperatures

$CeCl_3$	0.5 wt %		2 wt %		4 wt %	
T [K]	D [$\times 10^5$ cm^2 s^{-1}]	E_a [kJ mol^{-1}]	D [$\times 10^5$ cm^2 s^{-1}]	E_a [kJ mol^{-1}]	D [$\times 10^5$ cm^2 s^{-1}]	E_a [kJ mol^{-1}]
698	0.479		0.430		0.418	
723	0.545		0.547		0.544	
748	0.653	30.7	0.675	31.6	0.672	33.4
773	0.751		0.690		0.700	
798	1.012		0.875		0.860	

From the cathodic peak potentials in the cyclic voltammogram, the apparent standard potential of $CeCl_3$ was calculated by using Eq. (2-15). The calculated apparent standard potentials are plotted in Figure 4.6 showing a proportional relationship with respect to an increase in temperature. The apparent standard potentials for the concentration of 0.5 wt% and 2 wt% agree

with each other (staying within similar ranges of values), but the apparent standard potential for 4 wt% of $CeCl_3$ was slightly more negative. Once the apparent standard potentials were determined, thermodynamic properties can be further investigated using Eq. (2-4). Although the melting temperature (T_m) of $CeCl_3$ salt is 1080 K in nature, $CeCl_3$ is dissolved in LiCl-KCl eutectic salt

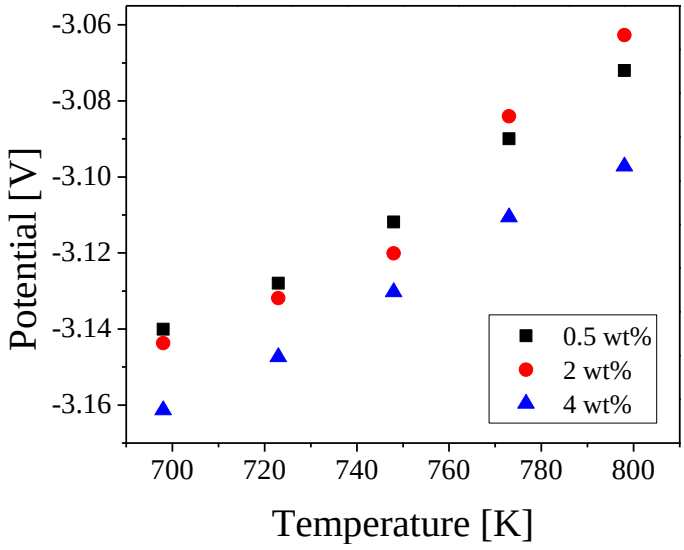

Figure 4.6 Plot of apparent standard potentials versus temperature.

under a liquid phase; therefore, the fusion energy between solid and liquid phases need to be considered as well. Several literature studies mistakenly use the Gibbs energy for the formation at super cooled state ($\Delta G^{Formation}$) as an ideal Gibbs free energy without considering the fusion energy [61, 65]. Thus, ΔG^{SC} can be re-written with considering the fusion energy between liquid and solid state through the following relationship:

$$\Delta G^{SC} = \Delta G^{Formation} + \Delta G^{Fusion} \quad (4\text{-}1)$$

where $\Delta G^{Formation}$ is the Gibbs free energy for the formation (kJ mol^{-1}) and ΔG^{Fusion} is the Gibbs energy for the fusion between liquid and solid phases. This second term can be expressed as

$$\Delta G^{Fusion} = \Delta H^{Fusion} - T\Delta S^{Fusion} + \int_{T_m}^{T} \Delta C_p \, dT - T\int_{T_m}^{T} \frac{\Delta C_p}{T} dT \quad (4\text{-}2)$$

where ΔH^{Fusion} is the enthalpy of fusion (kJ mol^{-1}), ΔS^{Fusion} is the entropy of the fusion at T_m (kJ mol^{-1} K^{-1}), and ΔC_p is the heat capacity between T_m and T (kJ mol^{-1} K^{-1}). These thermodynamic values for $CeCl_3$ at desired temperatures were obtained from the literature published by Barin [53], which are listed in Table 4.4 with the calculated thermodynamic data values (ΔG^{Fusion}, ΔG^{SC}). The values of $\Delta G^{0*}_{CeCl_3}$ were calculated from the apparent standard potentials using the thermodynamic equation ($\Delta G = -nF\Delta E$); therefore, the values of γ_{CeCl_3} could be calculated using Eq. (2-4). Results

from Figure 4.7 show that values increase as temperature rises. However, these values need to be further evaluated to provide an overall trend with temperature. Compared with literature values [61, 65], the activity coefficients in the present study are smaller with an order from 10^1 to 10^2. This deviation may be because previous researcher used only the Gibbs free energy for the formation to represent ΔG^{SC} as mentioned above. Detailed calculated values are summarized in Table 4.4.

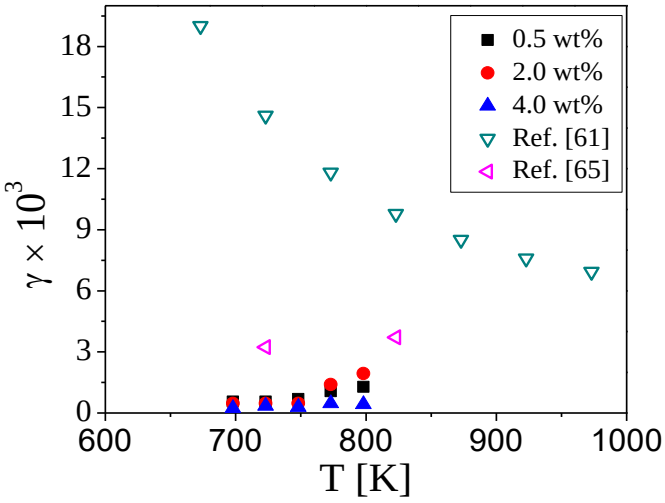

Figure 4.7 Activity coefficients of $CeCl_3$ in LiCl-KCl, compared with literature values.

Table 4.4 Thermodynamic information from the literature [53]and calculated values

		698 K	723 K	748 K	773 K	798 K	T_m (1080 K)
$\Delta G^{Formation}_{CeCl_3}$ (kJ mol^{-1})		-880.90	-875.1	-869.31	-863.53	-857.28	
$\Delta H^{Fusion}_{CeCl_3}$ (kJ mol^{-1})							53.14
$\Delta S^{Fusion}_{CeCl_3}$ (J mol^{-1} K^{-1})							49.20
C_p (J mol^{-1} K^{-1})		115.93	116.6	117.20	117.84	118.47	
$\Delta G^{Fusion}_{CeCl_3}$ (kJ mol^{-1})		15.40	14.67	13.90	13.07	12.20	
$\Delta G^{SC}_{CeCl_3}$(kJ mol^{-1})		-865.5	-860.4	-855.4	-850.5	-845.1	
$\Delta G^{0*}_{CeCl_3}$ (kJ mol^{-1})	0.5 wt%	-908.9	-905.4	-900.7	-894.4	-899.2	
	2.0 wt%	-910.0	-906.5	-903.1	-892.7	-886.5	
	4.0 wt%	-914.1	-908.4	-906.1	-899.6	-896.5	
$\gamma_{CeCl_3} \times 10^3$	0.5 wt%	0.56	0.56	0.68	1.07	1.29	
	2.0 wt%	0.47	0.47	0.47	1.40	1.94	
	4.0 wt%	0.23	0.34	0.29	0.48	0.43	

4.1.3.2 Electrochemical impedance spectroscopy (EIS)

The EIS technique was selected and performed to calculate exchange current density (i_0) of Ce^{3+}/Ce couple in LiCl-KCl salt. Compared to the LP and Tafel techniques, EIS has an advantage that the electrode surface area is almost maintained the same due to an extremely small current that is being applied at OCP or in that proximity. Therefore, uncertainty of electrode area can be reduced significantly in determining i_0. For analyzing impedance spectra, a simple equivalent circuit was proposed as shown in Figure 4.8 where CPE was used instead of double layer capacitance and Warburg impedance. It is important to point out that R_s is the solution resistance, R_{ct} is the charge transfer resistance on the electrode surface, C_{dl} is the double-layer capacitance and W is the diffusion related resistance (Warburg). A frequency ranging from 50 kHz to 50 mHz was used, and the applied potential amplitude was set at 10 mV. Figure 4.9 shows impedance spectra for 0.5 wt% of $CeCl_3$ in which the potential was gradually increased from the equilibrium potential (-2.169 V). In general, an impedance should be measured at an equilibrium potential to properly calculate i_0. However, at the equilibrium potential, the impedance swiftly increases at the high frequency and downward distortion was observed at low frequency as shown in Figure 4.9 because no ion transfer can occur between the tungsten electrode and cerium ions. Therefore, minimum overpotentials (η = 1 - 5 mV) was applied to the cell for the cerium reduction to occur at the electrode surface. For an example, in Figure 4.9, by increasing η from equilibrium potential, a transition point can be observed at -2.172 V (open circles in Figure 4.9) with a noticeable behavior that, a diffusion related impedance (Warburg impedance) starting to occur at low frequency region. This occurrence implies that electrons transfer and diffusion from the bulk salt to the electrode surface starts to occur at that potential. In this case, current density flows through the EIS experiment was only less than 1.5 mA cm^{-2}. The electron exchange was confirmed by OCP measured right after the EIS experiments. After performing EIS at the potential of -2.172 V, OCP was maintained at the equilibrium potential for 500 s while OCP was released from the equilibrium potential when the applied potential was lower than -2.172 V. Therefore, minimum η for Ce^{3+}/Ce reduction to occur could be found and R_{ct} values were measured at those voltages by fitting the Nyquist plot to an equivalent circuit.

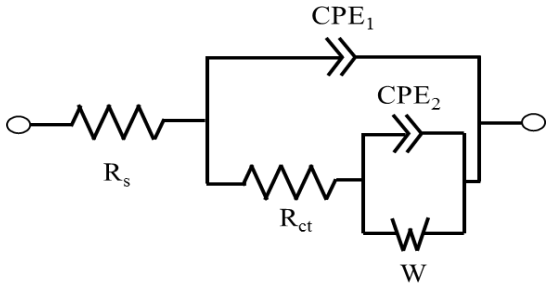

Figure 4.8 Equivalent circuit for the electrochemical cell showing bulk solution resistance, charge transfer resistance, CPEs and Warburg impedance.

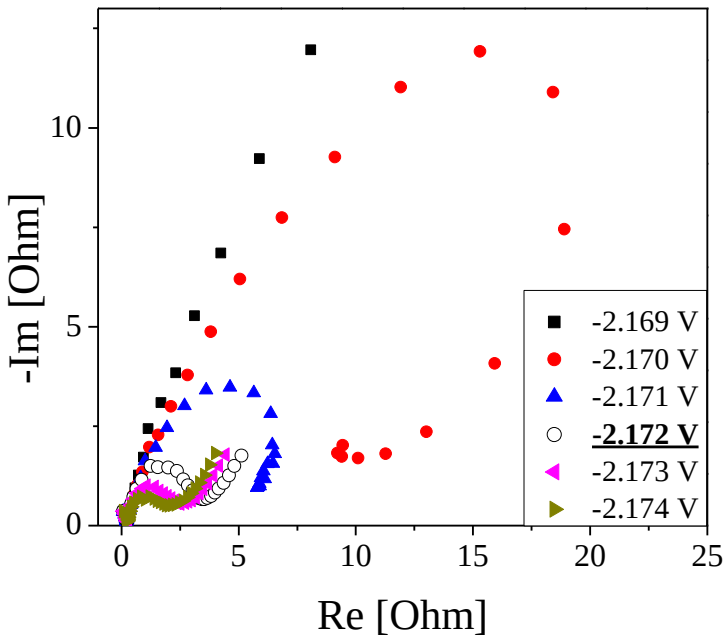

Figure 4.9 Nyquist plot for 0.5 wt % of $CeCl_3$ in LiCl-KCl at 723 K on a tungsten electrode. The frequency was from 50 kHz to 50 mHz, and the amplitude of applied sinus potential was 10 mV. Applied potentials were ranging from -2.169 to -2.174 V with an equilibrium potential of -2.169 V.

The measured and fitted impedance spectra of Ce^{3+}/Ce for the three different concentrations of $CeCl_3$ at various temperatures are shown in Figure 4.10. First, the measured spectra were automatically fitted by using randomize and simplex method in Z-fit software (Bio-Logic), then a manual adjustment was done by changing the values of the equivalent circuit components. As the manual curve fitting was performed, the relative error could be minimized below a fraction of 10^{-1}. Table 4.5 describes the methods to obtain EIS spectra and curve fittings as aforementioned. As a result of the curve fittings, the product of electrode surface area (S) and R_{ct} and η were being measured; these values are summarized in Table 4.6. From the measured R_{ct}, i_0 can be readily computed by using Eq. (2-24). In addition, k^0 can be calculated by assuming α is 0.5 based on the observation from CV experiments that Ce^{3+}/Ce reaction follows reversible behaviors with a weak diffusion effect (at slow scan rates). Table 4.7 provides a list of i_0 and k^0 calculated from R_{ct}. Figure 4.11 plots the exchange current densities of Ce^{3+}/Ce reaction which can be characterized with concentrations and temperatures. The results indicate that i_0 values with 0.5 wt% of $CeCl_3$ are in between 0.0076 A cm^{-2} and 0.016 A cm^{-2}, agreeing well with repeated experimental runs. By increasing the concentration of $CeCl_3$ to 4 wt%, the exchange current density appears to increase up to 0.18 A cm^{-2}. Marsden and Pesic [61] reported the exchange current density of $CeCl_3$ at 4 wt% concentration using the linear polarization method, ranging from

0.01 A $cm^{-2}$to 0.2 A cm^{-2}. The values of i_0 from this study are slightly higher, but both studies show similar range of values for the i_0 of $CeCl_3$ in LiCl-KCl salt.

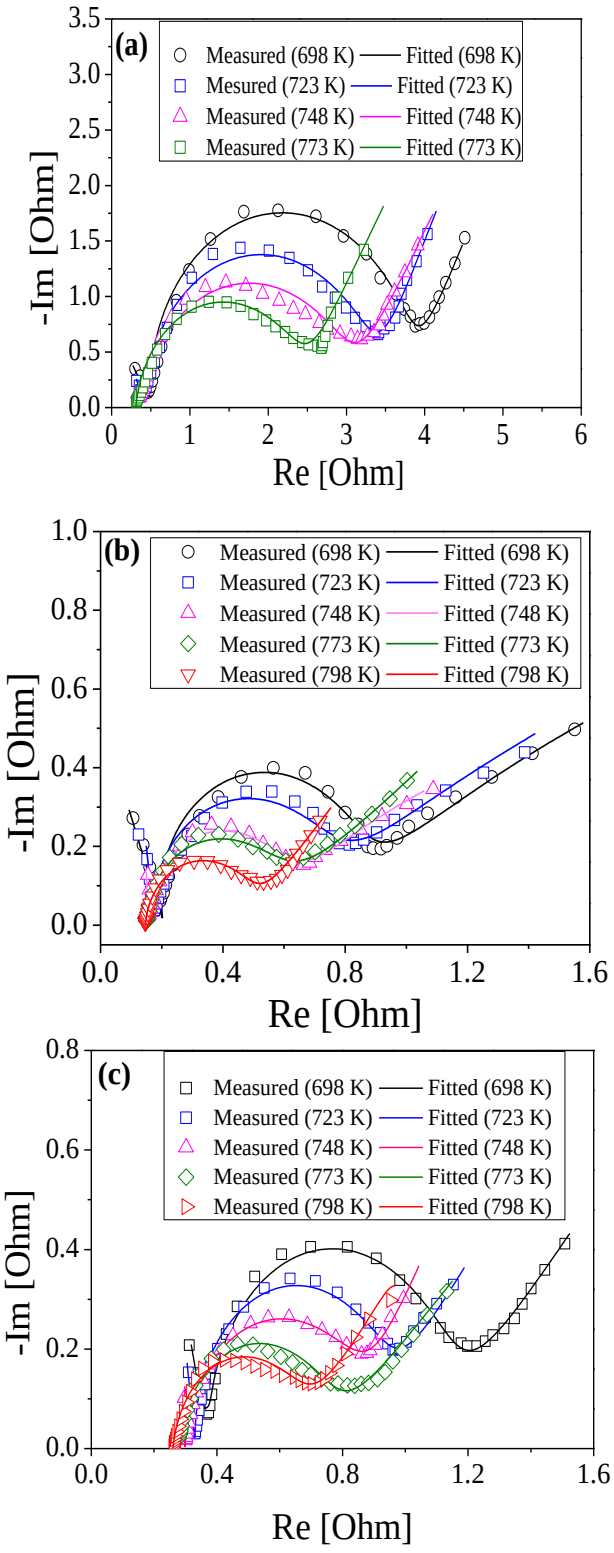

Figure 4.10 Measured and fitted Nyquist plots at temperatures of 698, 723, 748, 773, and 798 K: (a) 0.5 wt % $CeCl_3$; (b) 2 wt % $CeCl_3$; and (c) 4 wt % $CeCl_3$.

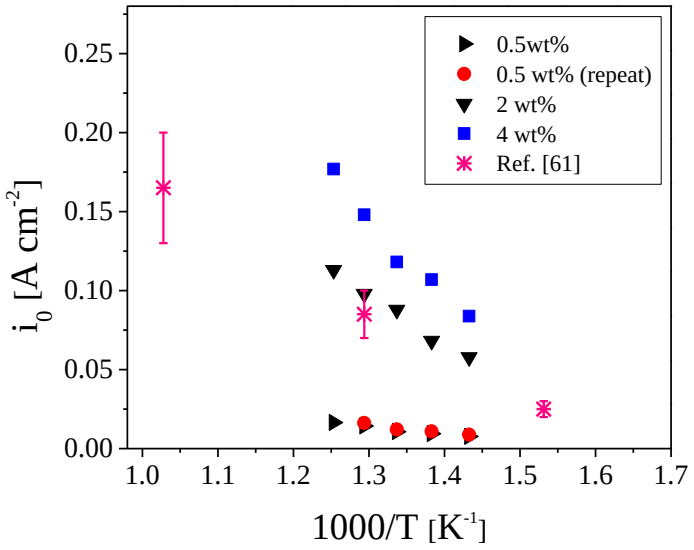

Figure 4.11 Plots of exchange current densities versus inverse temperature from various experiment sets at $CeCl_3$ concentrations of 0.5 wt%, 2wt%, and 4 wt%, compared with values measured by Marsden and Pesic [61].

Table 4.5 Steps for the measurements of EIS spectra and curve fitting

Step	Description
1	Clean the working electrode by applying an oxidative potential (-0.1 V vs. Ag/AgCl) for 3 minutes and wait until OCP becomes stable,
2	Measure EIS at equilibrium potential,
3	If spectra start showing the double layer capacitance and Warburg impedance, move next step. If not, move to Step 1 and increase the applied overpotential,
4	Find the minimum overpotential and repeat the measurements 3 times at the same overpotential,
5	Fit the measured curve by Randomize and Simplex method in Z-fit software (Bio-Logic),
6	Adjust values in the equivalent parameters for the best fit and obtain $R_{ct,}$ and
7	Calculate i_0 and k_0 by using Eq. (2-24).

Table 4.6 The applied overpotential (η) and measured charge transfers (R_{ct}) times electrode surface area (S) values at different concentrations and temperatures

$CeCl_3$	0.5 wt %		2 wt %		4 wt %	
T [K]	η [V]	R_{ct} S [Ω cm^2]	η [V]	R_{ct} S [Ω cm^2]	η [V]	R_{ct} S [Ω cm^2]
698	0.006	2.63	0.004	0.34	0.003	0.24
723	0.006	2.29	0.004	0.30	0.003	0.19
748	0.006	2.09	0.004	0.24	0.002	0.18
773	0.006	1.62	0.004	0.22	0.002	0.15
798	0.005	1.45	0.004	0.20	0.001	0.13

Table 4.7 Calculated exchange current density (i_0) and rate constant (k^0) for the charge transfer at different concentrations and temperatures

$CeCl_3$	0.5 wt %		2 wt %		4 wt %	
T [K]	i_0 [A cm^{-2}]	k^0 [× 10^5 cm s^{-1}]	i_0 [A cm^{-2}]	k^0 [× 10^5 cm s^{-1}]	i_0 [A cm^{-2}]	k^0 [× 10^5 cm s^{-1}]
698	0.0076	0.450	0.058	1.71	0.086	1.69
723	0.0091	0.536	0.068	1.99	0.107	2.20
748	0.0103	0.610	0.088	2.57	0.112	2.44
773	0.0137	0.817	0.098	2.88	0.146	3.03
798	0.0158	0.944	0.113	3.33	0.177	3.69

Based on the given data sets, Arrhenius temperature dependence form can be applied to further looking into temperature effects on the exchange current density using the expressing $i_0 = I_0 \exp(-E_a/RT)$ where I_0 is the pre-exponential factors (often referred to as an exchange current density at an infinite temperature). Figure 4.12 shows a plot of the natural logarithm of i_0 against the inverse temperature. Here, a straight line can be seen for all three different $CeCl_3$ concentrations. E_a and I_0 were calculated from the slope of the straight lines and the intercept of ln i_0, respectively. E_a values for Ce^{3+}/Ce were 34.5, 30.9, and 32.4 kJ mol^{-1} ($R^2 > 0.98$) for 0.5 wt%, 2 wt% and 4 wt%, respectively. These values are similar to the activation energy for U^{3+}/U measured by Rose et al. [50], which is 34.5 kJ mol^{-1}. As expected, higher activation energy is required for the charge transfer at lower concentration of $CeCl_3$. Interestingly, the activation energy values from the diffusion coefficients shown in Table 4.2 are within similar range in comparing to those for the charge transfer, but behave in an opposite trend. That is, the activation energy for the diffusion increases with increasing $CeCl_3$ concentration, suggesting that it would be due to interaction between particles at high concentration. Dimensionless quantities of i_0/I_0 are plotted versus $\exp(-E_a/RT)$ in Figure 4.13. Marsden and Pesic [61] reported the values of i_0 in a broad range, so that values were averaged, calculated, and superimposed onto Figure 4.13 for comparison. All exchange current density values from three different concentrations are laid on a single straight line. Although the data point at 773 K in the study by Marsden and Pesic [61] is

slightly off from the trend line, it is shown here that the exchange current densities from both studies exhibit a similar trend on temperature effect.

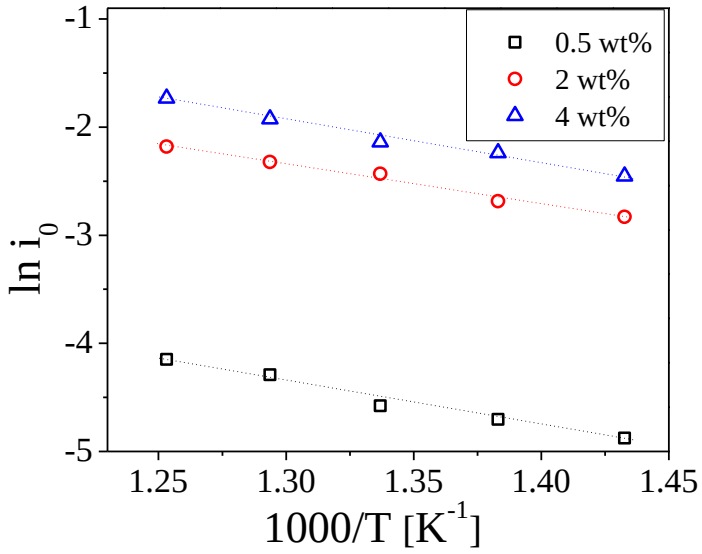

Figure 4.12 Plot of ln (i_0) versus inverse temperature showing Arrhenius dependency.

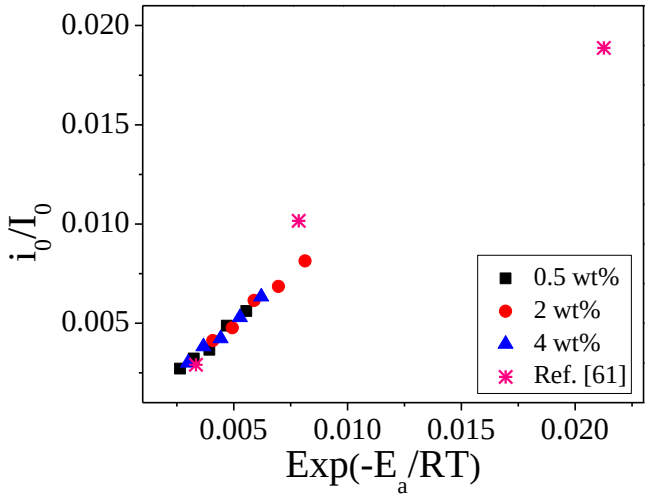

Figure 4.13 Plot of i_0/I_0 versus exp($-E_a/RT$).

4.1.3.3 Analysis on practical application

The results of this work provide the fact that cerium is a good surrogate material for uranium since they show similar electrochemical and thermodynamic behaviors in LiCl-KCl eutectic salt. By comparing the properties of cerium with those of uranium reported in the literatures, both are very stable in the trivalent form in LiCl-KCl salt and are reduced to metal form by gaining three electrons at certain potentials. However, the standard reduction potential of UCl_3 is ranging from -2.4 to -2.6 V versus Cl_2/Cl^- reference electrode [37-39, 42], which is about 0.7 V more positive than the standard reduction potential for $CeCl_3$. The diffusion coefficients for UCl_3 in LiCl-KCl molten salt have been reported by many researchers [30, 37-39, 42, 48, 66], which are shown in the Figure 4.14. Although the values for UCl_3 are generally higher than those for $CeCl_3$, the diffusion coefficients for both UCl_3 and $CeCl_3$ are in the same order of magnitude and can be correlated with the temperature. The activation energies for the diffusion of UCl_3 have been reported, ranging from 24.2 to 34.4 kJ mol^{-1} [37, 39], which is in a good agreement with the activation energy for $CeCl_3$. The similarity between both the activation energies for the diffusion may be owing to the similar ionic size of uranium and cerium.

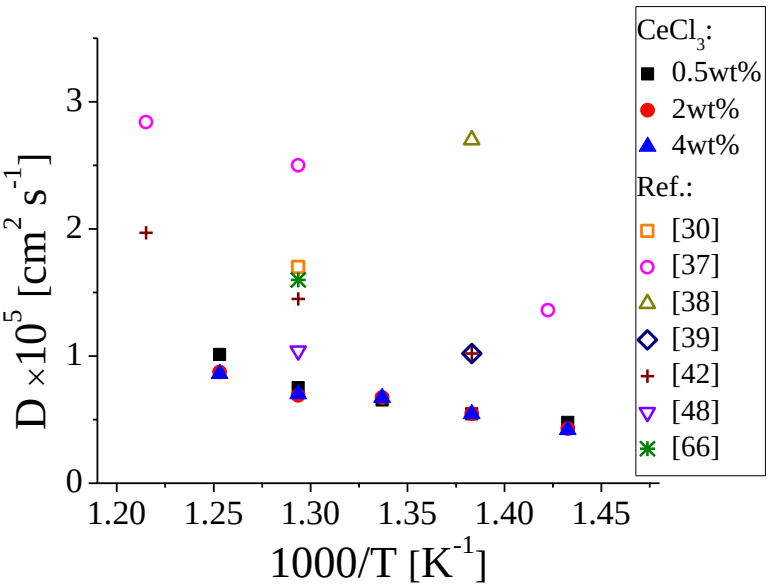

Figure 4.14 Plot of diffusion coefficients for UCl_3 from other studies, comparing with the diffusion coefficients of $CeCl_3$ in this study.

The exchange current densities of uranium in the molten salt have been reported with few different methods [48-50]. As shown in Figure 4.15, the reported i_0 values for U^{3+}/U reaction are scattered in the order from 10^{-2} to 10^{-1}; thus, it is difficult to compare each data or observe its trend. The main reason of the deviation could be that the authors performed the different methods to measure i_0 at different temperatures and concentrations (including other aforementioned challenges). Therefore, further study is necessary to determine the exchange density for U^{3+}/U reaction, and observe its trend regarding the concentration and temperature. EIS technique in this study shows an alternative method in determining i_0 of $CeCl_3$ and can also be an important tool to investigate the exchange current density of UCl_3 in LiCl-KCl eutectic salt.

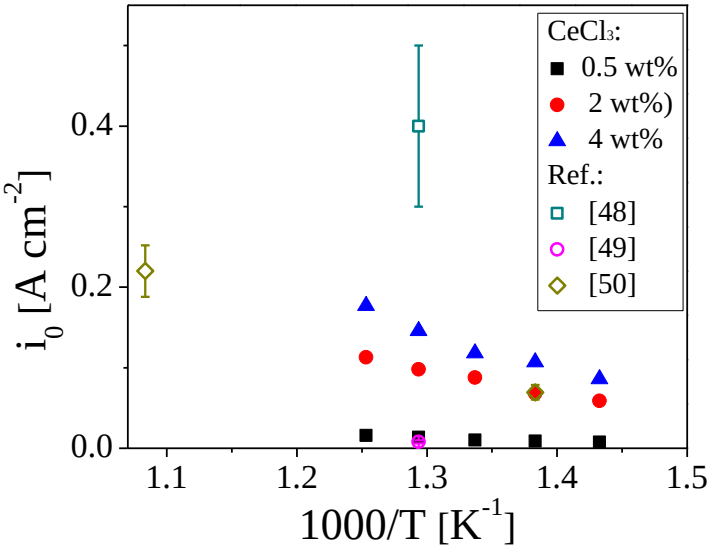

Figure 4.15 Plot of the exchange current densities for U^{3+}/U reaction from other research studies comparing with those of Ce^{3+}/Ce measured in this study.

4.1.4 Conclusions

Electrochemical properties of $CeCl_3$ in LiCl-KCl eutectic salt at different concentrations and temperatures have been studied by using CV and EIS techniques. From the CV experiments, three-electron exchange was observed for the Ce^{3+}/Ce reaction. The diffusion coefficients of $CeCl_3$ in LiCl-KCl were measured and calculated to be from 0.48×10^{-5} to 1.01×10^{-5} $cm^2\ s^{-1}$, which can be correlated with temperature using Arrhenius expression. The results reveal that the concentration of $CeCl_3$ has a weak effect on the diffusion coefficients. Comparing with the resulting values for UCl_3, the diffusion coefficients of $CeCl_3$ are slightly smaller than those of UCl_3. Apparent standard potentials were also computed by using peak potentials from the CV experiments, which were linearly dependent on temperature. EIS experiments were performed to determine exchange current density of Ce^{3+}/Ce couple in LiCl-KCl molten salt system. Minimum

η was applied for Ce reduction to happen and the charge transfer resistance was measured to calculate the exchange current density. The exchange current densities range from 0.0076 A cm^{-2} and 0.18 A cm^{-2}, which can be related to temperature and concentration. From Arrhenius temperature dependence, the activation energy for Ce^{3+}/Ce exchange was determined though EIS data, which is in the same range obtaining through CV data sets and in similar range with the activation energy for U^{3+}/U [50]. By plotting dimensionless quantities of the exchange current density, the exchange current densities of Ce^{3+}/Ce reaction in this work are in good agreement with those measured by linear polarization method [61]. In comparison with the exchange current densities of U^{3+}/U measured by other researchers, the values for Ce^{3+}/Ce are in a similar order, but a meaningful comparison is hard to be made due to the dispersed data for uranium.

4.2 Electrochemical and Thermodynamic Properties of $CeCl_3$ on Liquid Cadmium Cathode (LCC) in LiCl-KCl Eutectic Salt[2]

4.2.1 Introduction

The biggest advantage of pyroprocessing is to provide a strong resistance for nuclear proliferation, which is because of the production of mixed fuel including U, Pu, and MA. This mixed fuel is produced in the ER system by using LCC electrode because the activity of the fission products become very small in LCC. Therefore, the operation of the LCC plays an important role in the feasibility of electrochemical processes toward material accountability and safeguarding of ER [29]. Several studies have been done to understand electrochemical and thermodynamic features of U, Pu, and MAs on the LCC. Shirai and co-workers [32, 67] investigated the reaction of U^{3+}/U and Pu^{3+}/Pu couples on the LCC. The redox reaction for both couples were almost reversible, and the reduction potential on the LCC showed more positive values than that at the molybdenum electrode. Murakami and co-workers [31] measured diffusion coefficients of actinides and rare earth elements with LCC by performing chronopotentiometry (CP) in LiCl-KCl at temperature ranging from 723 K to 823 K. Castrillejo et al. [29, 68, 69] investigated the activities and Gibbs energy of rare earth materials in both Cd and Bi liquid electrodes.

However, only few elements in the electrorefiner have been examined with LCC, and there are still many actinides and lanthanides need to be explored in terms of electrochemical and thermodynamic properties on the interface between the LiCl-KCl molten salt and the LCC. In addition, the i_0 of the elements, which is necessary for the kinetic model, has not been reported. Therefore, Ce was selected as a surrogate material in this study for a purpose of accumulating electrochemical and thermodynamic data sets which can be meaningfully compared with those

[2] Contents in Section 4.2 are cited from the author's publication:
D. Yoon and S. Phongikaroon, and Jinsuo Zhang, "Electrochemical and Thermodynamic Properties of $CeCl_3$ on Liquid Cadmium Cathode (LCC) in LiCl-KCl Eutectic Salt," *Journal of The Electrochemical Society*, **163**(3), E97-E103 (2016).

from other researchers and developing an experimental method to measure the i_0 of actinides on the LCC. Few electrochemical and thermodynamic properties of Ce have been reported on the LCC in the LiCl-KCl eutectic salt. Kim et al. [64] explored Ce reduction process and large potential difference were observed between tungsten electrode and LCC due to the Ce activity change with intermetallic compound formations in LCC. Shibata and co-workers [70] measured the Gibbs free energies and other thermodynamic properties of the Ce-Cd intermetallic compounds using an open circuit chronopotentiometry. These values will provide useful insight into features of Cd distillation from Cd-MA alloys. However, electrochemical behaviors of $CeCl_3$ on the LCC have not been well explored and understood. In addition, there is not enough data on the thermodynamic properties of the intermetallic compounds to be compared.

The characteristic of i_0 were studied on the solid cathode in LiCl-KCl salt by Marsden and Pesic [61] as mentioned in Section 4.1. However, significant differences would be expected using LCC since the properties of actinides are dramatically changed in the LCC (for an example, an activity of Ce and formation of intermetallic compounds in Cd). In this section, Tafel plot and LP methods were selected to estimate the value of i_0 on the LCC. For soluble-insoluble reactions, the main disadvantage of those techniques is the measurement of apparent electrode surface area when the metal elements are deposited on the solid cathode. However, identical surface condition of liquid cadmium was observed with the naked eye after Ce metal was deposited on the LCC due to the fact that deposited metal was readily diffused into the LCC. Therefore, the steady surface area can be expected on the LCC during the Tafel and LP measurements.

The main goal of this section is to explore the electrochemical methods to estimate the electrochemical and thermodynamic properties of $CeCl_3$ on the LCC in LiCl-KCl molten salt. CV experiments were performed to investigate the electrode reaction of the Ce^{3+}/Ce couple, and determine diffusion coefficient of Ce^{3+} on the LCC. The cyclic voltammogram of LiCl-KCl-$CeCl_3$-$CdCl_2$ was obtained to confirm the intermetallic compound formations of Ce with Cd. Then, the open circuit chronopotentiometry was performed to measure the Gibbs free energy and other thermodynamic properties of the Ce-Cd intermetallic compounds. Finally, Tafel and LP plots were obtained with increasing Ce concentration in Cd to determine i_0 of Ce on the LCC regarding to Ce-Cd phase formation.

4.2.2 Detailed Experimental Setup and Preparation

The amount of cerium chloride (0.26 g ± 0.1 mg) was weighed and added into 25 g ± 0.18 mg of the LiCl-KCl salt, which is equivalent to 1 wt% of $CeCl_3$ in the LiCl-KCl salt. For the experiment of Ce-Cd intermetallic compounds, 0.022 g ± 0.1 mg of cadmium chloride was added to the LiCl-KCl-1wt% $CeCl_3$ yielding $CeCl_3$ and $CdCl_2$ mole fractions of 2.36×10^{-3} and 2.68×10^{-4}, respectively. The prepared sample was loaded in the high purity alumina crucible (25 mm ID × 40 mm H). Figure 4.16 shows a schematic design of the electrode assembly in the cell. The glassy carbon rod was immersed as the counter electrode. Ag/AgCl (1 mol%) reference was used as the reference electrode. As the working electrode, liquid Cd was used. The Cd metal shots were

delivered in a regular polyethylene bottle; thus, the surface of Cd shots were partially oxidized. For purification of the oxidized Cd prior to the experiments, Cd shots were melted in a closed-end Pyrex tube to separate the pure Cd from the oxidized layer. When Cd was melted, the oxide form of Cd (yellow color) floated on the surface of liquid Cd. A Pyrex tube (4 mm in OD) was inserted into the Cd below the oxide layer and a syringe was used to draw the pure liquid Cd up into the tube. The Cd in the tube was cooled to room temperature. As a result, a pure Cd rod was obtained from the tube indicated by observing clean silver color of the Cd rod as shown in Figure 4.17.

For utilizing the liquid Cd in the electrochemical experiments, the pure Cd rods were contained in a Pyrex tube (8 mm ID × 18 mm H, see the inserted photo in Figure 4.16), which was contacted with molybdenum wire (Alfa Aesar, 0.5 mm in diameter). When the Cd was melted in the furnace, the surface of the LCC was observed in the shape of a dome owing to high surface tension of liquid cadmium (600 dynes cm^{-1} at 773 K [71]) in the Pyrex tube crucible. As shown in Figure 4.18(a), the surface shape was conserved when liquid cadmium was cooled quickly to room temperature. The diameter and the height of the half elliptical shape were measured as 8 mm and 2.25 mm, respectively (see Figure 4.18(b)). By assuming that the surface of the LCC is an ideal oblate spheroid, the surface area can be computed by the following formula [72],

$$S = \pi a^2 \left(1 + \frac{\left(\frac{c}{a}\right)^2}{2\sqrt{1-\frac{c^2}{a^2}}} \ln\left(\frac{1+\sqrt{1-\frac{c^2}{a^2}}}{1-\sqrt{1-\frac{c^2}{a^2}}} \right) \right) \quad (4\text{-}3)$$

where S is the surface area of the LCC, a is the radius of spheroid, and c is the height of the half spheroid. The surface areas of Cd were calculated ranging from 0.729 cm^2 to 0.733 cm^2 depending on experimental runs.

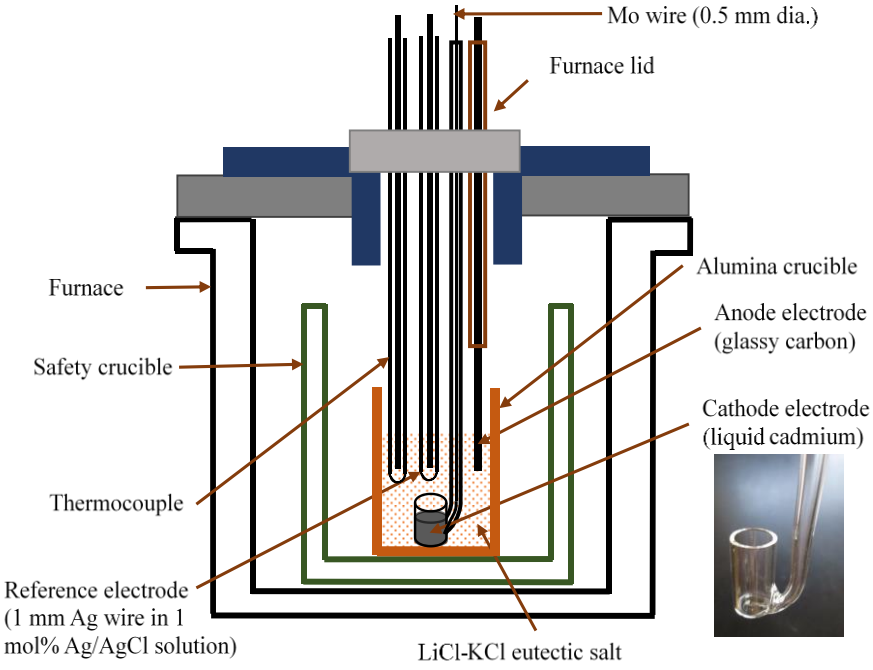

Figure 4.16 A schematic design of the experimental setup for electrochemical experiments.

Figure 4.17 Purified Cd rods under argon environment.

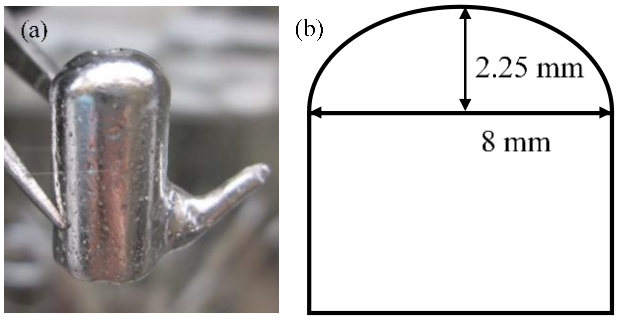

Figure 4.18 Solid cadmium cooled fast to room temperature in a Pyrex crucible and (b) a sketch showing measured dimensions of half elliptical dome.

4.2.3 Results and Discussion

4.2.3.1 Cyclic voltammetry (CV) of the LiCl-KCl-$CeCl_3$ on the LCC

CV experiments were conducted in a LiCl-KCl-1 wt% $CeCl_3$ system at temperatures from 723 ± 1K to 798 ± 1 K. Figure 4.19 shows representative CV curves of $CeCl_3$ with a 100 mV s^{-1} scan rate at 748 K. Curve (1) was obtained in a pure LiCl-KCl salt, in which Li reduction starts approximately from -1.3 V versus 1 mol% Ag/AgCl reference electrode. This is mainly due to very small activity coefficient of metals in Cd. Lewis and Johnson [73] reported activity coefficients of Li in Cd, ranging from 1.8×10^{-3} to 2.6×10^{-3} over a concentration range of 0.06 – 7.0 atom% in Cd. Therefore, Li co-deposition can be expected in reduction process with the LCC. Curve (2) is cyclic voltammogram for $CeCl_3$, but Li was deposited simultaneously. Therefore, curve (1) (background current) needs to be subtracted from curve (2), so that Li deposition effect can be removed from the curve (2). This is shown by curve (3) attributing only to Ce reduction and oxidation on the LCC. This background subtraction method has been widely used by several researchers [29, 64, 68], and can be utilized based on the assumption that the interaction between Li and Ce is week and can be neglected. Table 4.8 briefly summarizes the procedure of the CV experiments on LCC electrode in LiCl-KCl eutectic salt.

Figure 4.20(a) combines the cyclic voltammograms of $CeCl_3$ on the LCC with increasing scan rate from 0.08 V s^{-1} to 0.2 V s^{-1}. The cathodic peak potential stays at near the same potential below the scan rate of 0.2 V s^{-1} while the peak potential starts shifting toward negative potential when the scan rate was faster than 0.2 V s^{-1}, representing the reversibility of Ce^{3+}/Ce reaction below the 0.2 V s^{-1} scan rate. Figure 4.20(b) shows linear dependence between the cathodic peak current and the square root of the scan rate. The diffusion coefficient of $CeCl_3$ in LiCl-KCl salt can be calculated from the slope by using the Berzins-Delahay relationship, Eq. (2-13), which is applicable for a diffusion controlled process with a soluble-insoluble reversible system.

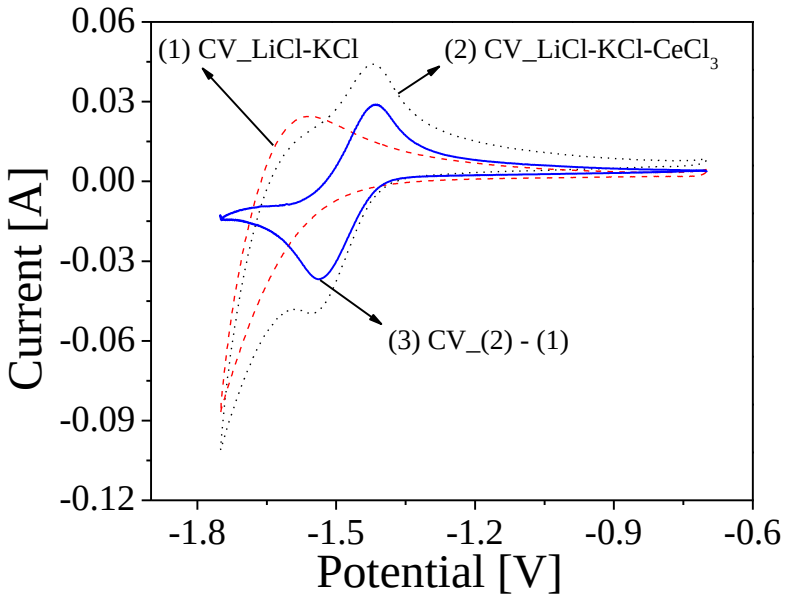

Figure 4.19 Cyclic voltammograms of a LiCl-KCl-1 wt% $CeCl_3$ solution on the LCC at 748 K with the surface area of 0.729 cm^2.

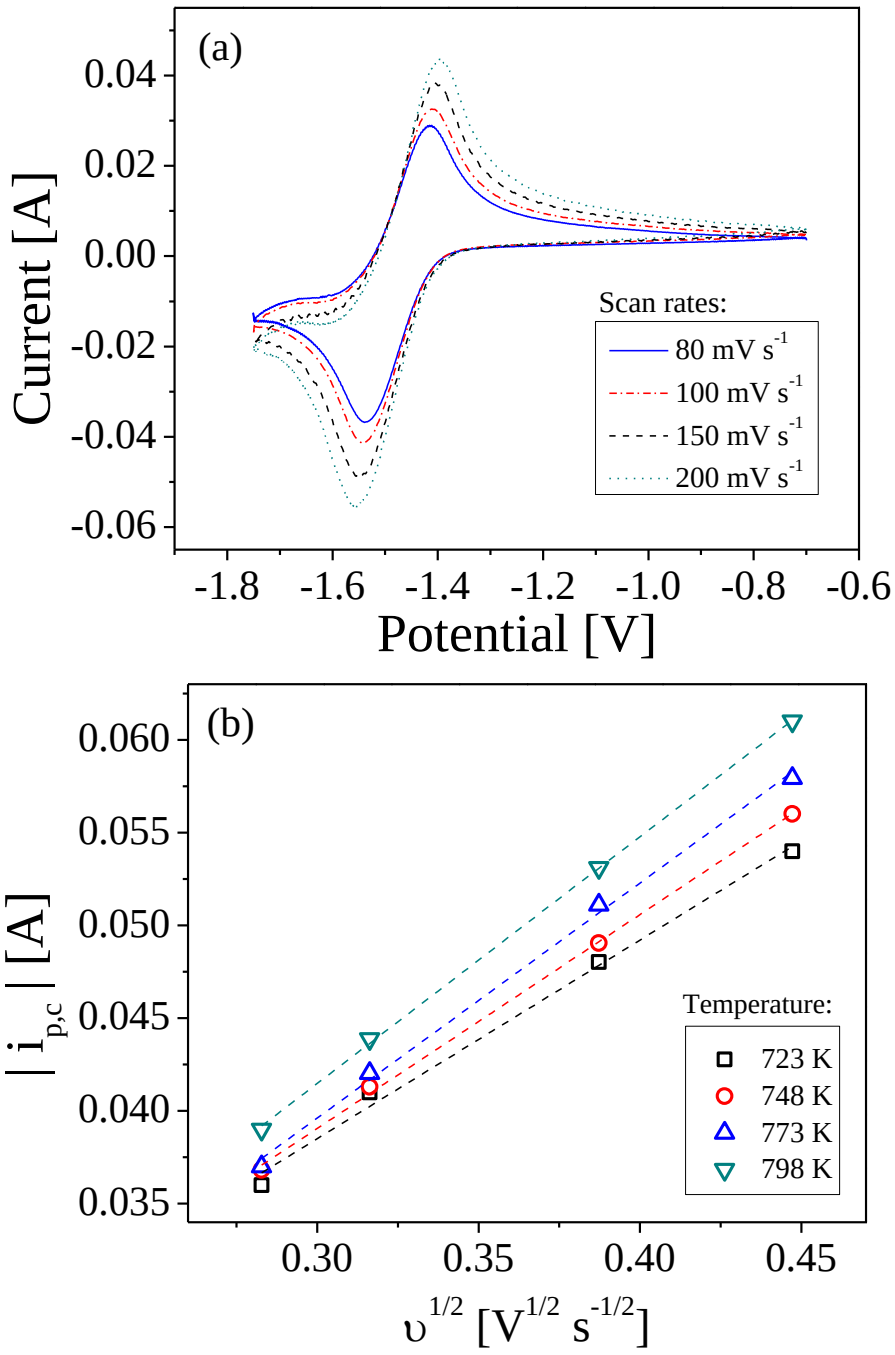

Figure 4.20 (a) The cyclic voltammogram of a LiCl-KCl-1 wt% $CeCl_3$ after subtraction of background current of LiCl-KCl, and (b) peak cathodic currents as a function of the square root of the scan rate. The surface area was 0.729 cm^2.

Table 4.8 Steps for the measurements of CV data using LCC

Step	Description
1	Load the pure Cd rods into the Pyrex crucible,
2	Lower the electrode assembly into the salt and wait until Cd is melted,
3	Clean the LCC surface by applying an oxidative potential (-0.7 V vs. Ag/AgCl for avoiding Cd oxidation) for 3 minutes,
4	Wait for 1 ~ 3 minutes until the OCP becomes stable,
5	Perform CV measurements at least 5 cycles,
6	Obtain the data if the CV curves are repeatable,
7	Repeat Steps 1 – 6 for next CV measurement,
8	Subtract LiCl-KCl base line in order to eliminate Li reduction effect, and
9	Measure the peak currents and calculate the values of D using Eq. (2-13).

The diffusion coefficients of Ce^{3+} ranged from 2.9×10^{-6} cm^2 s^{-1} to 5.1×10^{-6} cm^2 s^{-1} at temperatures from 723 to 798 K. Figure 4.21 shows the diffusion coefficients of $CeCl_3$ on the LCC versus 1000/T, which are superimposed on the diffusion coefficients of Ce^{3+} on tungsten electrode measured in Section 4.1. The diffusion coefficients on the LCC were almost half of the values of the diffusion coefficients on the tungsten electrode. Gha-Young and co-workers [30] also had a similar trend with uranium chloride. That is, diffusion coefficient of uranium on LCC was about one tenth of the diffusion coefficient on solid cathode. This reduced values may be attributed from Li co-deposition and mass transfer limit from the LCC structure. It is assumed that as Li is reduced along with Ce on LCC, diffusion of Ce^{3+} is interfered by the interaction between Ce and Li ions. In addition, to utilize LCC, the liquid cadmium was loaded in a Pyrex crucible having an upward surface area exposure to the molten salt LiCl-KCl. Therefore, mass transfers caused by electric force and convection are being restricted only through that exposure liquid cadmium surface. These speculated observations may be the main reasons for the small diffusion coefficient values. To date, the value of diffusion coefficient on LCC has not been measured well by researchers. Thus, diffusion coefficient on LCC needs to be further explored and understood in various experimental conditions. Generally, diffusivity is dependent on temperature change, which can be examined by Arrhenius temperature relationship. By plotting logarithm of diffusion coefficient against inverse temperature, E_a can be readily calculated from the slope. The activation energy for diffusion process of $CeCl_3$ on the LCC was 36.12 kJ mol^{-1}, which is slightly higher than the activation energies for Ce diffusion on the tungsten electrode reported by several researchers [61, 74]. This result also supports the idea of the slower diffusion process on the LCC as mentioned previously. The results of the diffusion coefficient on LCC in the present study motivate further investigations on understanding the difficulty of mass transfer onto LCC. Theoretically, diffusion coefficient is only function of temperature and species.

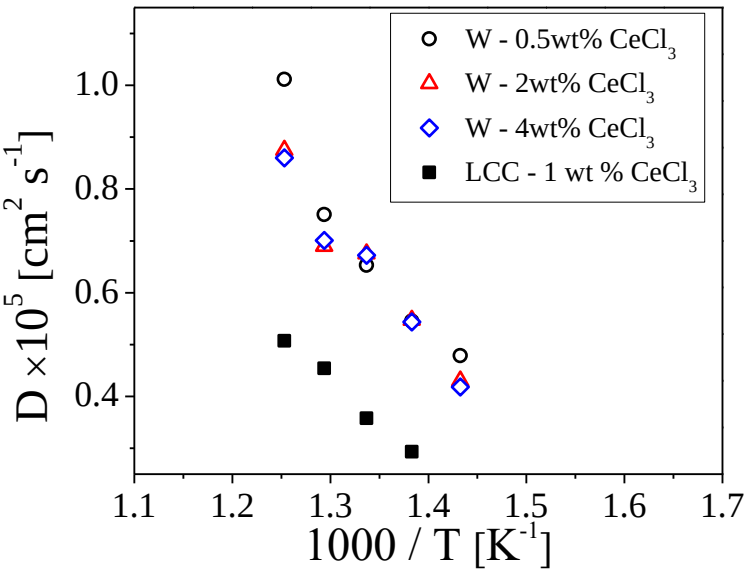

Figure 4.21 Plot of the diffusion coefficients of Ce^{3+} on the LCC versus inverse temperature, comparing with values on the tungsten cathode measured in Section 4.1.

4.2.3.2 Open circuit chronopotentiometry in LiCl-KCl-$CeCl_3$-$CdCl_2$

It has been known that Ce forms six different intermetallic compounds with Cd (CeCd, $CeCd_2$, $CeCd_3$, $Ce_{13}Cd_{58}$, $CeCd_6$, and $CeCd_{11}$) [75], which could be readily observed by performing CV experiments in LiCl-KCl-$CeCl_3$-$CdCl_2$ molten salt. Figure 4.22 shows a cyclic voltammogram of $CeCl_3$ deposited on a Cd film at a 50 mV s^{-1} scan rate at 773 K. During the reduction process from 0 V to -2.2 V versus Ag/AgCl reference electrode, the Cd film was formed first on the tungsten electrode and then Ce starts to be deposited on top of the Cd film. In this process, Ce-Cd intermetallic compounds have been gradually formed. When potential was swept in the oxidation direction, Ce metal in the intermetallic compounds was dissolved back into the salt. By decreasing the amount of Ce metal on the film, the formation of Ce-Cd intermetallic compound varies subsequently from CeCd to $CeCd_{11}$, which can be clearly observed as oxidation peaks from P_1 to P_6 in Figure 4.22. However, P_3 was combined with P_2 due to the relatively fast scan rate making it difficult be identified. Thus, it was considered that at slower scan rate than 50 mV s^{-1}, all six peaks corresponding to Ce-Cd intermetallic compounds would be separately shown in a cyclic voltammogram.

The thermodynamic properties of these Ce-Cd intermetallic compounds can be examined by performing the open circuit chronopotentiometry (OCC), which has been considered as a suitable technique to determine thermodynamic properties of intermetallic compound formations [29, 64, 68-70]. Figure 4.23 is an example of the chronopotentiogram, showing a transient potential curve with respect to the Ce-Cd binary phase. In advance, the tungsten electrode was coated with Cd and Ce metals by applying potential at -2.2 V for 25 second. Then, the chronopotentiometry

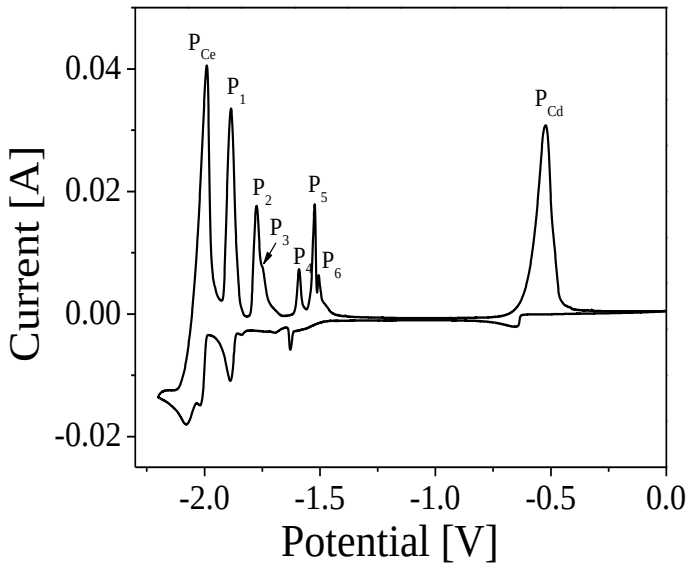

Figure 127.22 A cyclic voltammogram of LiCl-KCl-$CeCl_3$-$CdCl_2$ with the scan rate of 50 mV s^{-1}. Concentrations of $CeCl_3$ and $CdCl_2$ were 6.86×10^{-5} mol cm^{-3} and 7.81×10^{-6} mol cm^{-3}, respectively.

was conducted with positive current applied at 1 μA. By dissolving Ce metal from Cd film to the bulk salt, cathodic potential was shifted toward the positive direction. The routine methods for measuring the OCC are explained in Table 4.9. Regarding variation of the Ce-Cd phase formation, totally six potential plateaus were observed. These potential plateaus can correspond to two-phase coexisting state: CeCd-$CeCd_2$, $CeCd_2$-$CeCd_3$, $CeCd_3$-$Ce_{13}Cd_{58}$, $Ce_{13}Cd_{58}$-$CeCd_6$, $CeCd_6$-$CeCd_{11}$, and $CeCd_{11}$-Cd. When two phases are coexisting on the electrode surface, the activity of Ce is fixed by equilibrium [29]. Therefore, potential difference at each plateau was measured based on an OCP of a Ce electrode, then the relative partial molar Gibbs free energies and activities of Ce in binary phase state were calculated by using the following equations;

$$\Delta G_{Ce} = -3F\Delta E \tag{4-4}$$

$$\text{emf} = \Delta E = -\frac{RT}{3F}\ln\alpha_{Ce,Cd} \tag{4-5}$$

where ΔG_{Ce} is the relative partial molar Gibbs free energy of Ce (kJ mol^{-1}), ΔE is the potential difference between OCP and each plateau (V), and $\alpha_{Ce,Cd}$ is the activity of Ce in Cd. The chronopotentiometry was repeated several times with same experimental conditions for confirming the reproducibility of the data, and the uncertainty was verified by using standard deviation for each experiment. Table 4.10 provides a summary of ΔG_{Ce} and $\alpha_{Ce,Cd}$. The values of metal activity in Cd becomes smaller when Cd is more prevalent in LCC. For instance, activity of Ce in the phase of Ce-$CeCd_{11}$ has its value in the order of 10^{-11} while that in the CeCd-$CeCd_2$ coexisting phase is in the order of 10^{-2}. It should be mentioned that the reduction potentials of

actinide and lanthanide elements come together closely on the LCC at the beginning of the electrorefining process, and will be gradually detached by depositing more elements in the LCC. This result will give an insight into determining a proper rate and time of LCC electrorefining process considering non-proliferation feature of pyroprocessing technology.

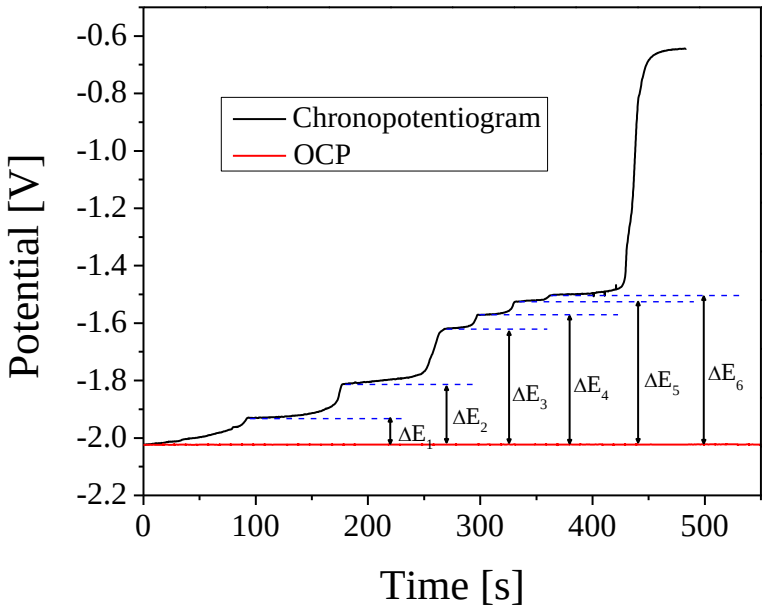

Figure 4.23 An example of the open circuit chronopotentiogram of Ce at Cd-coated tungsten electrode at 773 K. The applied current was 1 μA.

Table 4.9 Summary of the measurement step for OCC method

Step	Description
1	Prepare LiCl-KCl-1wt%$CeCl_3$-0.09wt% $CdCl_2$,
2	Lower the electrode assembly (working: tungsten, counter: glassy carbon),
3	Apply constant potential at -2.2 V vs. Ag/AgCl for 25 seconds,
4	Perform apply positive current a 1 μA (OCC),
5	Obtain plateaus corresponding to the Ce-Cd intermetallic compounds,
6	Measure the potential difference between the plateaus and OCP, and
7	Calculate thermodynamic data of the Ce-Cd intermetallic compounds

Table 4.10 The partial molar Gibbs free energies and activities of Ce in two-phase coexisting state at various temperatures

T [K]	$\Delta E_{Ce\text{-}Cd}$ [V vs Ce^{3+}/Ce]	ΔG_{Ce} [kJ mol^{-1}]	$\alpha_{Ce,\,Cd}$
In the region of the co-existing CeCd and $CeCd_2$ phases			
698	0.097 ± 0.0008	-28.2 ± 0.23	$7.73 \pm 0.03 \times 10^{-3}$
723	0.092 ± 0.002	-26.2 ± 0.45	$1.19 \pm 0.008 \times 10^{-2}$
748	0.090 ± 0.002	-26.0 ± 0.42	$1.53 \pm 0.009 \times 10^{-2}$
773	0.092 ± 0.003	-26.7 ± 0.84	$1.57 \pm 0.02 \times 10^{-2}$
798	0.088 ± 0.001	-25.4 ± 0.36	$2.17 \pm 0.01 \times 10^{-2}$
823	0.081 ± 0.002	-23.3 ± 0.43	$3.30 \pm 0.02 \times 10^{-2}$
In the region of the co-existing $CeCd_2$ and $CeCd_3$ phases			
698	0.218 ± 0.0007	-63.1 ± 0.21	$1.91 \pm 0.03 \times 10^{-5}$
723	0.210 ± 0.001	-60.9 ± 0.49	$4.06 \pm 0.07 \times 10^{-5}$
748	0.209 ± 0.002	-60.7 ± 0.55	$5.73 \pm 0.1 \times 10^{-5}$
773	0.211 ± 0.003	-61.0 ± 0.83	$7.53 \pm 0.2 \times 10^{-5}$
798	0.207 ± 0.006	-59.9 ± 0.16	$1.20 \pm 0.06 \times 10^{-4}$
823	0.203 ± 0.002	-58.3 ± 0.51	$1.98 \pm 0.03 \times 10^{-4}$
In the region of the co-existing $CeCd_3$ and $CeCd_{58/13}$ phases			
698	0.413 ± 0.001	-119.6 ± 0.36	$1.11 \pm 0.03 \times 10^{-9}$
723	0.414 ± 0.002	-119.8 ± 0.83	$2.19 \pm 0.04 \times 10^{-9}$
748	0.407 ± 0.003	-117.8 ± 0.87	$5.97 \pm 0.4 \times 10^{-9}$
773	0.405 ± 0.003	-117.2 ± 0.76	$1.19 \pm 0.06 \times 10^{-8}$
798	0.398 ± 0.006	-115.2 ± 0.16	$2.89 \pm 0.3 \times 10^{-8}$
823	0.391 ± 0.004	-112.9 ± 0.54	$6.83 \pm 0.2 \times 10^{-8}$
In the region of the co-existing $CeCd_{58/13}$ and $CeCd_6$ phases			
698	0.471 ± 0.0007	-136.3 ± 0.21	$6.30 \pm 0.1 \times 10^{-11}$
723	0.458 ± 0.0006	-132.4 ± 0.19	$2.67 \pm 0.04 \times 10^{-10}$
748	0.453 ± 0.002	-131.0 ± 0.67	$7.08 \pm 0.3 \times 10^{-10}$
773	0.451 ± 0.003	-130.6 ± 0.89	$1.47 \pm 0.09 \times 10^{-9}$
798	0.448 ± 0.009	-129.6 ± 0.25	$3.30 \pm 0.06 \times 10^{-9}$
823	0.439 ± 0.002	-126.8 ± 0.48	$8.98 \pm 0.3 \times 10^{-9}$
In the region of the co-existing $CeCd_6$ and $CeCd_{11}$ phases			
698	0.544 ± 0.001	-157.4 ± 0.30	$1.65 \pm 0.05 \times 10^{-12}$
723	0.529 ± 0.00	-153.2 ± 0.31	$8.54 \pm 0.2 \times 10^{-12}$
748	0.515 ± 0.002	-149.1 ± 0.45	$3.86 \pm 0.1 \times 10^{-11}$
773	0.499 ± 0.003	-144.5 ± 0.91	$1.72 \pm 0.1 \times 10^{-10}$
798	0.483 ± 0.002	-139.7 ± 0.47	$7.12 \pm 0.3 \times 10^{-10}$
823	0.469 ± 0.001	-135.4 ± 0.41	$2.52 \pm 0.07 \times 10^{-9}$
In the region of the co-existing $CeCd_{11}$ and Cd phases			
698	0.573 ± 0.0007	-165.7 ± 0.21	$3.95 \pm 0.08 \times 10^{-13}$

723	0.555 ± 0.001	-160.5 ± 0.29	$2.53 \pm 0.07 \times 10^{-12}$
748	0.540 ± 0.001	-156.4 ± 0.16	$1.20 \pm 0.03 \times 10^{-11}$
773	0.521 ± 0.003	-150.7 ± 0.76	$6.52 \pm 0.1 \times 10^{-11}$
798	0.502 ± 0.001	-145.4 ± 0.42	$3.02 \pm 0.03 \times 10^{-10}$
823	$0.487 \pm 1.4 \times 10^{-3}$	-140.7 ± 0.41	1.18×10^{-9}

The standard Gibbs free energy of Ce-Cd intermetallic compound formation can be calculated by the given relation [29, 68]:

$$\Delta G_f^0(Ce_{x_2}Cd) = \int_{x_1}^{x_2} \Delta E(x)dx + \Delta G_f^0(Ce_{x1}Cd) \quad (4\text{-}6)$$

where ΔG^0_f is the standard Gibbs free energy of formation of Ce-Cd intermetallic compounds. The x_1 and x_2 are stoichiometric coefficients of Ce (x_1, x_2 = 1, 1/2, 1/3, 13/58, 1/6, 1/11, $x_1 > x_2$). Based on the calculations, Figure 4.24 displays the variation of the Gibbs free energy for the formation of six different intermetallic compounds with the temperature changing from 698 K to 823 K. The molar enthalpy and entropy for the formation can be calculated from the linear dependence of Gibbs free energy, which is expressed as

$$\Delta G^0_{Ce} = \Delta H^0_{Ce} - T\Delta S^0_{Ce} \quad (4\text{-}7)$$

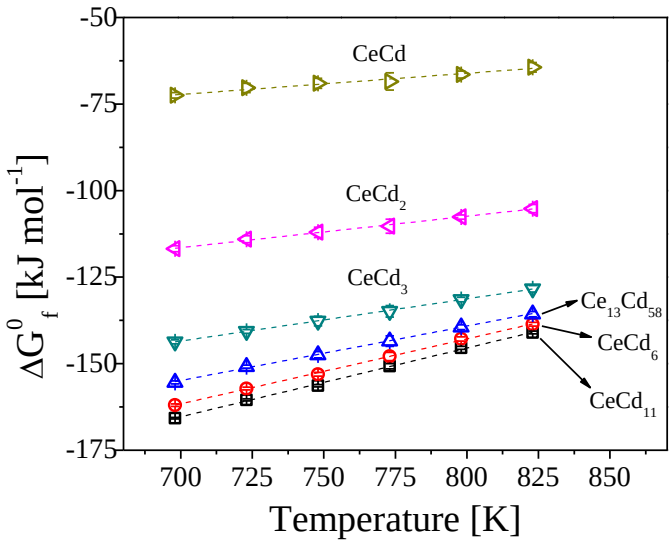

Figure 4.24 Variation of the Gibbs free energies of Ce-Cd intermetallic compound formations as a function of temperature.

where ΔH^0_{Ce} and ΔS^0_{Ce} are the enthalpy (kJ mol^{-1})and entropy (J mol^{-1} K^{-1}) for the formation, respectively. The R^2 values were all greater than 0.986 indicating that the fitted regression lines agree well with points of Gibbs free energies. Summary of the enthalpy and entropy of Ce-Cd intermetallic compound formations with equations used for the calculations is listed in Table 4.11.

The results obtained for the Ce-Cd intermetallic compounds in the present study show slightly smaller values compared with those reported by Kim et al. [64] and Shibata et al. [70], but follow similar linear trends for each intermetallic compound.

Table 4.11 The enthalpies and entropies of Ce-Cd intermetallic compound formations

Formation reaction of intermetallic compounds	Equation for ΔG^0_f	ΔH^0_f [kJ mol^{-1}]	ΔS^0_f [J mol^{-1} K^{-1}]
Ce + 11Cd → $CeCd_{11}$	$-3F\Delta E_6$	-304.3 ± 2.7	-198.6 ± 3.6
Ce + 6 Cd → $CeCd_6$	$\frac{5}{11}\left[\frac{6}{5}\Delta G^0_{f,CeCd_{11}} - 3F\Delta E_5\right]$	-293.1 ± 1.9	-187.8 ± 2.5
Ce + $\frac{58}{13}$ Cd → $CeCd_{58/13}$	$\frac{20}{78}\left[\frac{58}{20}\Delta G^0_{f,CeCd_6} - 3F\Delta E_4\right]$	-264.7 ± 2.1	-157.0 ± 2.9
Ce+3Cd → $CeCd_3$	$\frac{19}{58}\left[\frac{39}{19}\Delta G^0_{f,CeCd_{\frac{58}{13}}} - 3F\Delta E_3\right]$	-228.9 ± 0.6	-122.1 ± 0.8
Ce + 2Cd → $CeCd_2$	$\frac{1}{3}\left[2\Delta G^0_{f,CeCd_3} - 3F\Delta E_2\right]$	-179.8 ± 1.5	-90.5 ± 1.9
Ce + Cd → CeCd	$\frac{1}{2}\left[\Delta G^0_{f,CeCd_2} - 3F\Delta E_1\right]$	-115.3 ± 2.5	-61.4 ± 3.3

4.2.3.3 Linear polarization (LP) and Tafel methods on LCC in LiCl-KCl-$CeCl_3$

Tafel plot and LP methods were conducted for the measurement of the i_0 of Ce^{3+}/Ce couple on LCC in LiCl-KCl molten salt. All experiments were done with an incremental increase in mole fraction of Ce by adding pure Ce metal in liquid Cd. The mole fraction was varied from 0.0013 to 0.0303 (from 0.0016 to 0.0375 in weight fraction). For both techniques, a very slow scan rate (0.5 mV s^{-1}) was used for the purpose of obtaining the pure charge transfer kinetic which is directly related to the nature of i_0. The measurement methods for both LP and Tafel are described in Table 4.12.

Eqs. (2-27) and (2-28) can be used to estimate the i_0 of Ce on the LCC from the Tafel and LP methods, respectively. Figure 4.25 shows Tafel plots for the reduction and oxidation of Ce^{3+}/Ce couple on LCC in LiCl-KCl salt at 773 K. Significant asymmetry was observed between reduction and oxidation regions. In reduction region, Tafel curves are approaching the mass-transfer-limited current by an extreme reduction of Ce metal on the LCC while curves in oxidation region follow Tafel behavior. Thus, only oxidation regions of Tafel results were used for i_0 measurements. Once the desired amount of Ce metal was dissolved into the liquid cadmium, Tafel measurements were started from oxidation region. In the oxidation part of the Tafel plots, linear dependences of current-overpotential were observed at overpotential ranging from 50 mV to 110 mV. Therefore, linear fits were done at the overpotential range, and the intercepts of log (i) were determined for the calculation of i_0. Figure 4.26 plots current-potential curves in very small overpotential regions (< 10 mV). The Ce^{3+}/Ce redox potential was shifted toward negative direction with increasing Ce concentration in Cd, but maintained at similar potential when Ce was saturated. The current shows

linear dependence to the potential representing charge transfer resistance; therefore, Eq. (2-28) was used to calculate the i_0 of Ce. Figure 4.27 compares the results of i_0 with respect to increasing mole fraction of Ce in Cd from both Tafel and LP methods, and the values are listed in Table 4.13. The results from both methods show the relative difference less than 20%, but their trends of i_0 against mole fraction of Ce in Cd are in good agreement. Interestingly, when Ce concentration is lower than its solubility in Cd, i_0 of Ce is linearly dependent on Ce concentration (Ce solubility limit in Cd is 0.006 in mole fraction [76]). That is, i_0 linearly increases with increasing concentration of Ce in Cd until Ce mole fraction is less than 0.006. However, as Ce fraction exceeds its solubility limit in Cd, a nearly steady i_0 of Ce was observed. This may be attributed to the equilibrium state in the phase (Cd-$CeCd_{11}$), which can be explained along with the flat plateaus obtained in the Gibbs free energy study in the present study. The activity of Ce is fixed in the two phases co-existing state; therefore, this results in the constant values of i_0 beyond the Ce solubility limit in Cd (two phases co-existing between Cd-$CeCd_{11}$). It could be considered that the value of i_0 will increase with phase change to $CeCd_6$, $Ce_{13}Cd_{58}$, $CeCd_3$, and so on, due to the increase in the activity of Ce in Cd. However, the amount of each element deposited into the LCC is not expected to be more than 10 wt% in the electrorefining process. Therefore, the value of i_0 should follow the general trend after the concentration exceeds the solubility limit in liquid Cd. In the case of Ce, the i_0 of Ce stays at around 0.012 A cm^{-2} after its solubility in Cd. Unfortunately, there is no reported data of i_0 on the LCC for any meaningful comparison.

Table 4.12 Description for data acquisition from LP and Tafel methods

Step	Description
1	Load the pure Cd rods into the Pyrex crucible,
2	Lower the electrode assembly into the salt and wait until Cd is melted,
3	Lift the electrode assembly and add Ce metal chip into the LCC,
4	Lower the assembly and wait until OCP become stable,
5	Sweep potential from 0.2 V to -0.2 V based on OCP with 0.5 mV s^{-1} scan rate,
6	Obtain linear LP and Tafel regions,
7	Calculate i_0 of Ce^{3+}/Ce on LCC by using Eq. (2-27) and Eq. (2-28), and
8	Repeat Steps 3 – 7 for next LP and Tafel measurements.

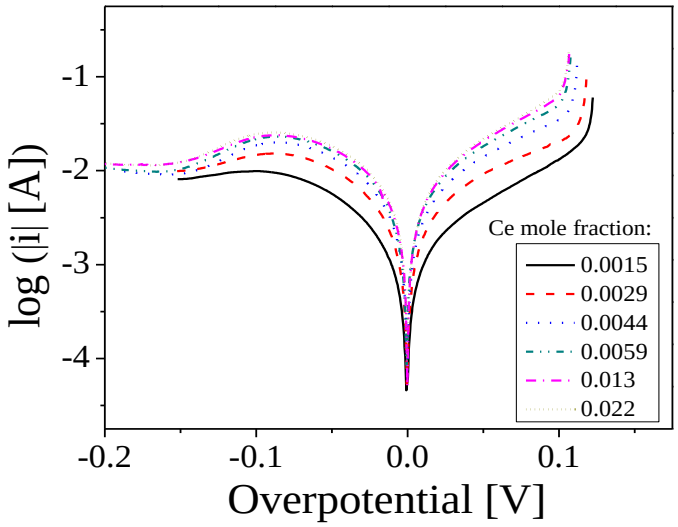

Figure 4.25 Tafel plots for Ce^{3+}/Ce on the LCC with respect to incremental change of Ce mole fraction in Cd. The scan rate was 0.5 mV s^{-1}, and the surface area was 0.731 cm^2.

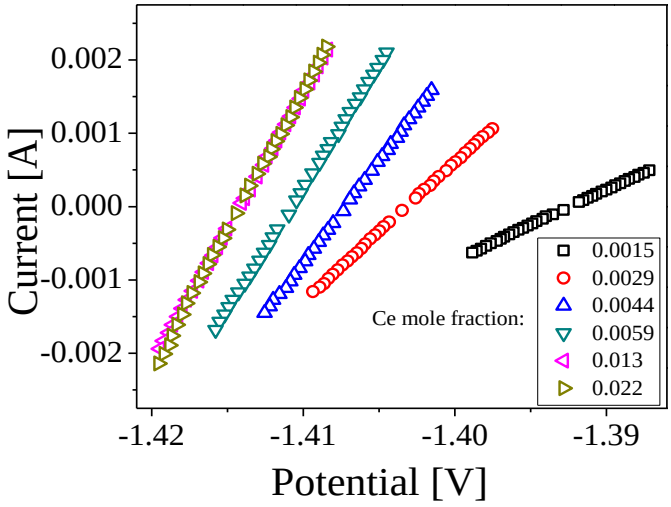

Figure 4.26 Plots of current versus potential in the region of small overpotential for Ce^{3+}/Ce redox in the LiCl-KCl at 773 K at different mole fractions of Ce in Cd. The scan rate of 0.5 mV s^{-1} and the surface area of 0.731 cm^2 were used for all measurements.

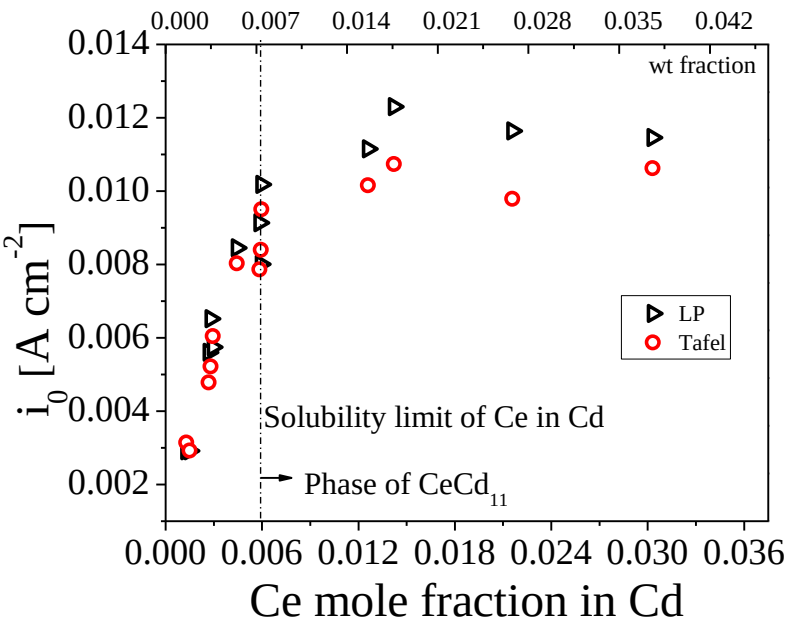

Figure 4.27 Plots of i_0 for the Ce^{3+}/Ce couple from both Tafel and LP methods regarding to Ce mole fraction in the LCC. The Ce solubility limit in Cd is 0.006 in mole fraction.

Table 4.13 The values of i_0 of Ce on Cd measured by both Tafel and LP methods

Mole fraction of Ce in liquid Cd	i_0 [A cm^{-2}]		
	Tafel method	LP method	Relative % difference
0.0013	0.00292	0.00315	7.8 %
0.0015	0.00291	0.00293	0.4 %
0.0027	0.0056	0.0048	14.7 %
0.0028	0.0065	0.0052	18.4 %
0.0029	0.0057	0.0060	5.2 %
0.0044	0.0084	0.0080	4.9 %
0.0058	0.0091	0.0079	13.9 %
0.0059	0.008	0.0084	4.9 %
0.006	0.01	0.0095	6.6 %
0.0126	0.011	0.010	8.9 %
0.0142	0.012	0.011	12.7 %
0.0216	0.012	0.0098	15.9 %
0.0303	0.0115	0.011	7.3 %

4.2.4 Conclusions

Electrochemical properties of Ce on LCC were investigated in LiCl-KCl eutectic salt via CV, OCC, Tafel, and LP techniques. The effect of Li co-deposition could be removed by subtracting CV curve of pure LiCl-KCl from the curve of LiCl-KCl-$CeCl_3$. Therefore cyclic voltammograms only attributed to Ce^{3+}/Ce redox reaction were obtained. The cathodic peak potential stays at almost the same potential within 0.2 V s^{-1} of scan rate, which reveals the redox reaction on the LCC is nearly reversible in the range of scan rates used. The diffusion coefficient of Ce on the LCC was measured by using the Berzins-Delahay equation. The values of the diffusion coefficient of Ce on the LCC were found to be in the range from 2.9×10^{-6} cm^2 s^{-1} to 5.1×10^{-6} cm^2 s^{-1}; these values are almost half compared with those on the tungsten solid electrode. The slow diffusion rate of Ce on the LCC may result from the special structure of the LCC. In the cyclic voltammogram of LiCl-KCl-$CeCl_3$-$CdCl_2$, the Ce-Cd intermetallic compound formations were verified by obtaining the different anodic peaks. The OCC was performed to determine the thermodynamic properties of Ce for Ce-Cd intermetallic compounds, including the Gibbs free energy, enthalpy, and entropy of the formation. Furthermore, activity of Ce showed the smallest value in phase of Cd-$CeCd_{11}$, and become larger when Ce fraction increases in Cd. The Tafel and LP techniques were conducted to determine i_0 of Ce on the LCC. The results from Tafel and LP methods agree well each other and show an interesting trend regarding to the Ce mole fraction in Cd. Within the solubility limit of Ce in Cd, the i_0 of Ce increases with increasing mole fraction of Ce in Cd. However, the i_0 of Ce was almost unchanged with increasing mole fraction of Ce beyond the solubility limit of Ce in Cd. Thus, it can be concluded that the i_0 of Ce is also dependent on the state of Ce-Cd intermetallic compound phase, and identical i_0 could be expected in the same phase formation.

4.3 Summary

Sections 4.1 and 4.2 illustrated the developments of the suitable setups and measurement methods to understand the behaviors of SNM. Ce was chosen as a surrogate element for the U. Its electrochemical, thermodynamic, and kinetic properties were explored in LiCl-KCl eutectic salts. In Section 4.1, CV and EIS techniques were being performed with solid cathode in LiCl-KCl-$CeCl_3$ salts. Peak currents and potentials from CV measurements were employed to calculate the diffusion coefficients of $CeCl_3$ and the apparent standard potentials of Ce^{3+}/Ce in the salt. Compared to previous literature, EIS technique was applied to determine the exchange current density. Minimum overpotentials for Ce^{3+}/Ce reaction to occur on the electrode surface were applied and EIS spectra were measured at that potential. By fitting the EIS spectra to the proposed equivalent circuit, the charge transfer impedances for Ce^{3+}/Ce could be measured, which were used to calculate the i_0 values. Therefore, the values of i_0 for Ce^{3+}/Ce reaction were examined at different temperatures and concentrations, indicating that the EIS method is feasible to determine the i_0 kinetics in LiCl-KCl eutectic salt.

Section 4.2 further explored the Ce behaviors on LCC electrode to understand behaviors of MA and Ln materials on liquid cathodes in ER system. When CV is performed with the LCC, Li metal is simultaneously deposited along with Ce; therefore, the CV baselines of pure LiCl-KCl were subtracted to obtain CV curves only attributed to the Ce redox reactions. From the processed CV curves, the diffusion coefficients of $CeCl_3$ were calculated revealing that the diffusivity was relatively weak by using LCC compared to usage of a solid electrode. For elucidation in thermodynamic behaviors of MA in LCC, the OCC method was performed by building Ce-Cd thin layer on tungsten electrode in LiCl-KCl-$CeCl_3$-$CdCl_2$. It was verified that the Ce forms the intermetallic compounds in liquid Cd, and thermodynamic characters were evaluated including the Gibbs free energies, enthalpies, entropies for the Ce-Cd intermetallic compound formations. The LP and Tafel methods were utilized to estimate the exchange current densities of Ce^{3+}/Ce on LCC.

5 Uranium Electrochemical Studies in Molten LiCl-KCl Eutectic[3]

We are exploring the electrochemical, thermodynamic, and kinetic properties of U in LiCl-KCl salt system via CV, OCP, LP, Tafel, and EIS techniques. The resulting data sets are provided in Sections 5.3.1 to 5.3.4. Here, the i_0 of U^{3+}/U were intensively investigated via EIS, LP, Tafel, and CV techniques and being delivered in Sections 5.3.4.1 to 5.3.4.3. The discussion and further analyses on these results are given in the following subsections. In addition, LiCl-KCl-UCl_3-$GdCl_3$ salt systems were investigated and the same electrochemical measurements were carried out to gain insight on the effect of other elements on U properties which could be happening in ER system.

5.1 Introduction

For the advancement of the safeguard technologies in pyroprocessing, it is necessary to build fundamental database for SNM, which will enhance the developments of kinetic models and the real-time monitoring technologies. Particularly, uranium is the most abundant element in reprocessing paths (UNF contains ~96 % of U [6]); thus, the assessment of fundamental features must be accurately done. For the pyroprocessing applications, kinetic, thermodynamic, and electrochemical properties of uranium should be known and documented under different conditions. Despite numerous studies on kinetic, thermodynamic, and electrochemical features in LiCl-KCl eutectic salt, the i_0 values of uranium have not been fully explored and understood as discussed in Section 2. The i_0 is a criterion of the reaction rate on the electrode, which plays a significant role in electrochemical equations and expressions; hence, the measurement and

[3] Contents in Section 5 are cited from the author's publications:
- D. Yoon and S. Phongikaroon, "Measurement and Analysis of Exchange Current Density for U/U^{3+} Reaction in LiCl-KCl Eutectic Salt via Various Electrochemical Techniques," *Electrochimica Acta* **227**, 170-179 (2017).
- D. Yoon and S. Phongikaroon, "Electrochemical and Thermodynamic Properties of UCl_3 in LiCl-KCl Eutectic Salt System and LiCl-KCl-$GdCl_3$ System," Journal of The Electrochemical Society, **164**(9), E217-E225 (2017).

collection of i_0 for U^{3+}/U reaction in LiCl-KCl are extremely crucial for developing the kinetic models and near-real time monitoring system for pyroprocessing technology. In addition, ER salt system contains a number of fission products including actinide An and Ln components [21]; therefore, effects of multi-elements on the U behavior should be explored in LiCl-KCl eutectic salt system. Here, electrochemical, thermodynamic, and kinetic properties of U were investigated by using CV, OCP, LP, Tafel and EIS methods. The properties were determined at different concentrations ranging from 0.5 wt% to 4 wt% and temperatures from 723 K to 798 K to understand the concentration and temperature effects on U behaviors. For the confidence of the i_0 evaluation, four different electrochemical methods including LP, Tafel plot, EIS, and CV were performed. In addition, $GdCl_3$ under different concentrations was added into LiCl-KCl-UCl_3 eutectic salt at 773 K, and the effects of $GdCl_3$ co-existence were explored on the properties of U such as diffusion coefficient, equilibrium potential, and exchange current density. The resulting data in this work will help elucidating the U behaviors in multi-components salt system.

5.2 Detailed Experimental Setup and Program

Figure 5.1 illustrates the schematic design of the electrochemical cell in the Muffle furnace. The salt samples were prepared in the Inconel® crucible, which is located in the furnace with the alumina secondary safety crucible. The tungsten rod (2 mm in diameter) was used as the working electrode. The U metal plates were chopped and loaded in a molybdenum basket, which were used as a counter electrode; therefore, the salt concentration could be maintained the same during the electrochemical measurements. The Ag/AgCl (1 mol%) reference was used for all experiments here. The specifications can be found in Table 3.1 and same methods for salt preparations and electrode preparations were followed as mentioned in Section 3.2. For exploring the U characteristics and the effect of $GdCl_3$ on U properties, the experimental program was developed as being summarized in Table 5.1. Concentration information based on the ICP-MS quantitative analyses and the electrode surface area for each run were obtained for verification and analysis.

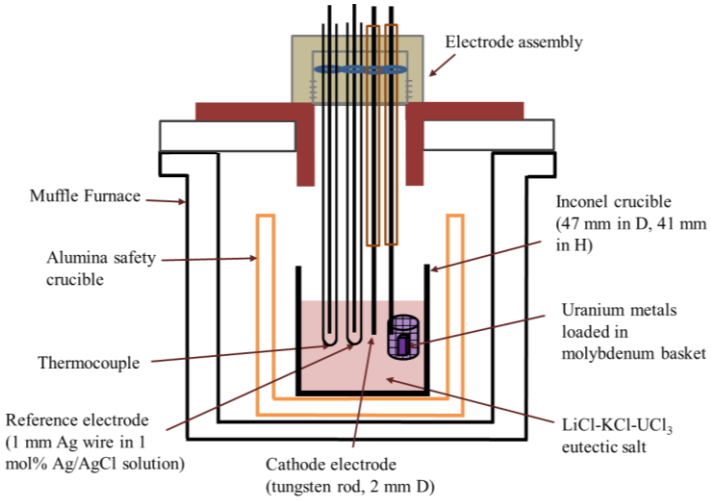

Figure 5.1 Schematic design of electrode assembly and electrochemical cell in Muffle furnace.

Table 5.1 Electrolyte concentration and the working electrode surface area for each experimental run

No.	Samples	UCl_3 (wt%)	$GdCl_3$ (wt%)	Electrode surface area (cm^2)
1	UCl_3-0.5	0.559		0.621
2	UCl_3-1.0	1.06		0.723
3	UCl_3-2.0	2.04		0.471
4	UCl_3-4.0	4.04		0.396
5	U0.5_Gd0.5	0.59	0.49	0.565
6	U1.0_Gd0.25	1.04	0.29	0.584
7	U1.0_Gd0.5	1.45	0.47	0.503
8	U1.0_Gd1.0	1.09	0.95	0.522
9	U2.0_Gd1.0	1.71	0.96	0.471
10	U2.0_Gd2.0	1.94	2.09	0.452

5.3 Results and discussion

5.3.1 Diffusion coefficient of UCl_3 in LiCl-KCl

CV curves were obtained by sweeping the potential from 0 V to -2.35 V with different scan rates to determine the diffusion coefficient of UCl_3 in LiCl-KCl eutectic salt. The same procedure for the measurement was used as developed in Table 4.2; however, the cleaning process was done by applying potential at -0.45 V (vs. Ag/AgCl) for avoiding oxidation of U^{3+} to U^{4+}. Figure 5.2 is

an example of CV curves in LiCl-KCl-0.5 wt% UCl_3 salt at 773 K. Reduction and oxidation peaks for U^{4+}/U^{3+} and U^{3+}/U were observed at I_a/I_c and III_a/III_c, respectively; no other reaction was found beyond the U^{3+}/U reduction potential. In addition, small pre-peaks were observed on the reduction and oxidation processes at II_a and II_c respectively. These pre-peaks were also observed at different concentrations up to 4 wt% UCl_3 as shown in Figure 5.3, which has been reported by many researchers [40-41, 45-46, 77]. Reddy et al. [45] and Serrano and Taxil [77] further studied the pre-peaks by observing the peak current at different scan rates and concentrations, concluding that the peaks were being attributed by an adsorption and desorption of uranium monolayer on the working electrode.

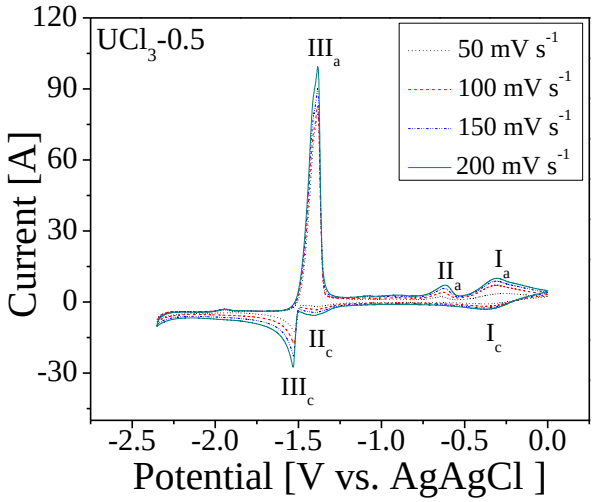

Figure 5.2 CV graphs in LiCl-KCl-0.5 wt% UCl_3 at 773 K. The potential was swept at the scan rate from 50 mV s^{-1} to 200 mV s^{-1}.

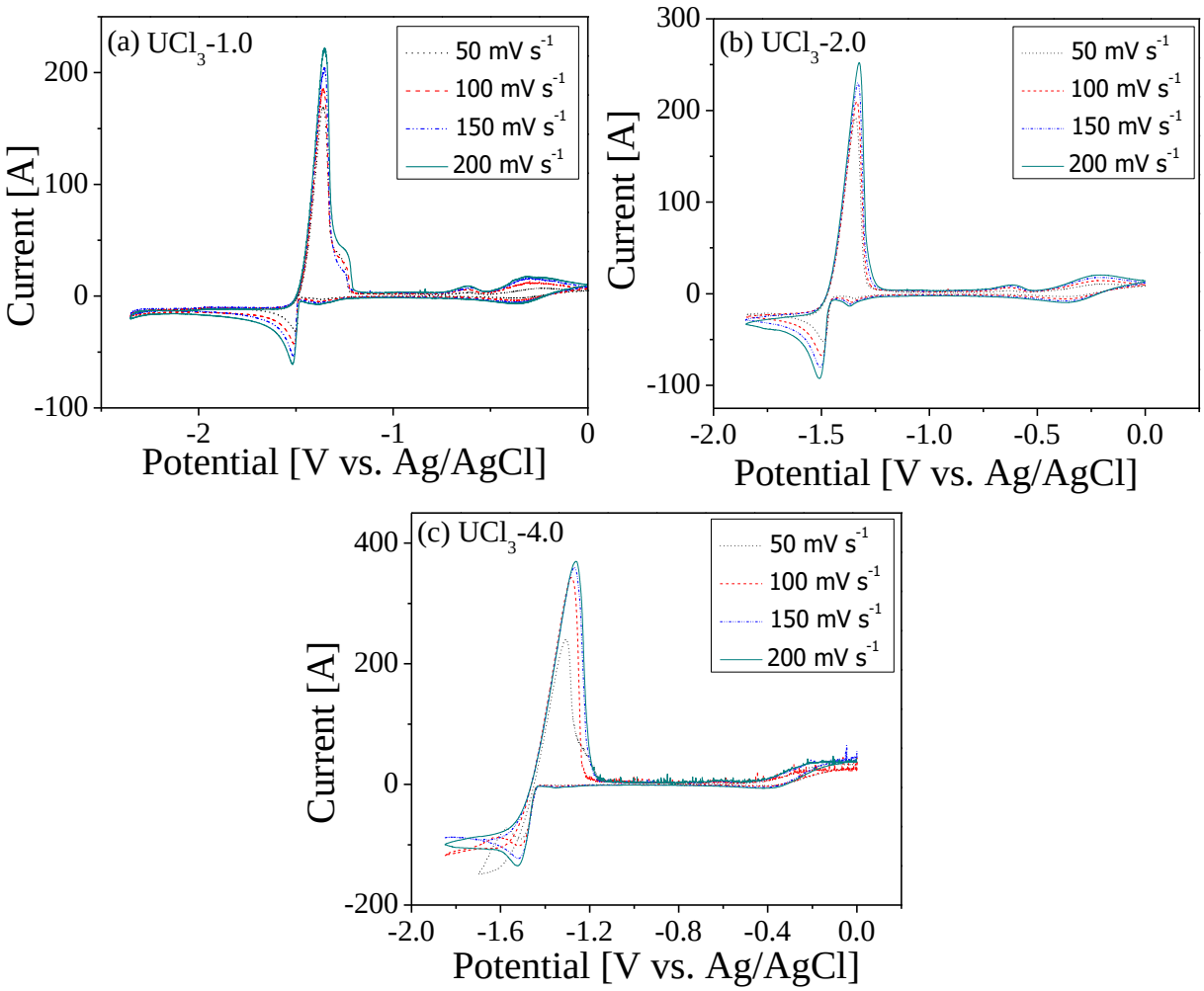

Figure 5.3 Cyclic voltammograms at concentrations of (a) 1.0 wt% UCl_3, (b) 2.0 wt% UCl_3, and (c) 4.0 wt% UCl_3 in LiCl-KCl eutectic salt at 773 K. The potential was swept at the scan rate from 50 mV s^{-1} to 200 mV s^{-1}.

The reduction peaks for U^{3+}/U (III_c) stay at the same potential with the scan rate change between 50 mV s^{-1} and 200 mV s^{-1}; thus, the redox reactions were considered as a reversible system under the experimental conditions. The height of peak currents were measured from the base line, which were linearly proportional to the square root of the scan rate. The linear slopes were employed through the use of Berzin-Delahay equation (Eq. (2-13)) for the UCl_3 diffusion calculation in LiCl-KCl. Figure 5.4 plots the calculated diffusion coefficients of UCl_3, showing the linear trend over temperature. The values are weakly affected by the concentration change up to 2 wt% of UCl_3; however, the diffusion coefficient begins decreasing at 4 wt% of UCl_3 (see red circles in Figure 5.4) due to a challenge of the CV measurement at high concentration with the lower scan rate as shown in Figure 5.3(c). Here, the reduction peaks can be hardly obtained because of the massive U reduction on the working electrode. When the CV were measured in LiCl-KCL-4wt% UCl_3 at scan rate ranging from 700 mV s^{-1} to 1500 mV s^{-1}, distinct peaks were obtained and massive U

reduction was diminished as shown in Figure 5.5. However, the relationship between the peak current and the diffusion coefficient need to be derived for irreversible soluble-insoluble system to determine the diffusion coefficient. Despite of incompatibility, Eq. (2-12) was used to estimate the diffusion coefficients of UCl_3 at 4 wt% by using the peak currents at faster scan rate (in Figure 5.5). The values of nα were calculated by using Eq. (2-10). The resulting data are illustrated in Figure 5.6 indicating that the diffusion coefficients (4 wt% UCl_3) measured by the irreversible relationship (Eq. (2-12)) were moved in the same trend line observed at lower concentrations (0.5 wt%, 1 wt%, and 2 wt% UCl_3). This phenomenon (decrease of diffusion coefficient at higher concentration) were also observed in a previous literature [46]; however,
further studies are necessary to explain this issue. The effect could be due to the attractive interaction among the particles or that the reversible equation (Berzin-Delahay, Eq. (2-13)) is not likely applicable at a high concentration.

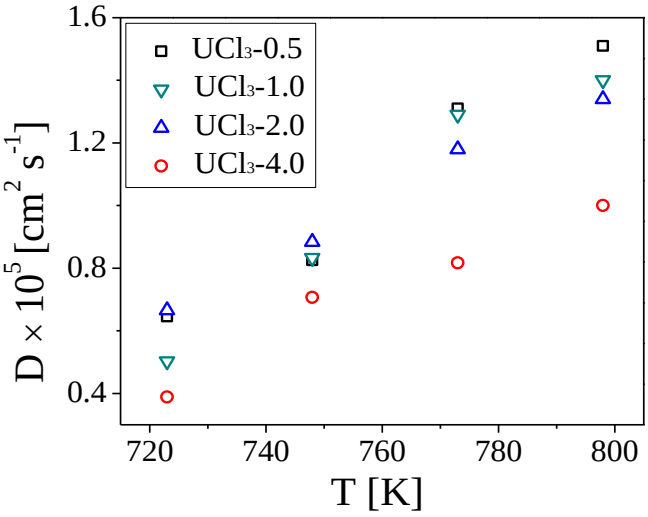

Figure 5.4 Diffusion coefficients of UCl_3 in LiCl-KCl as a function of temperature.

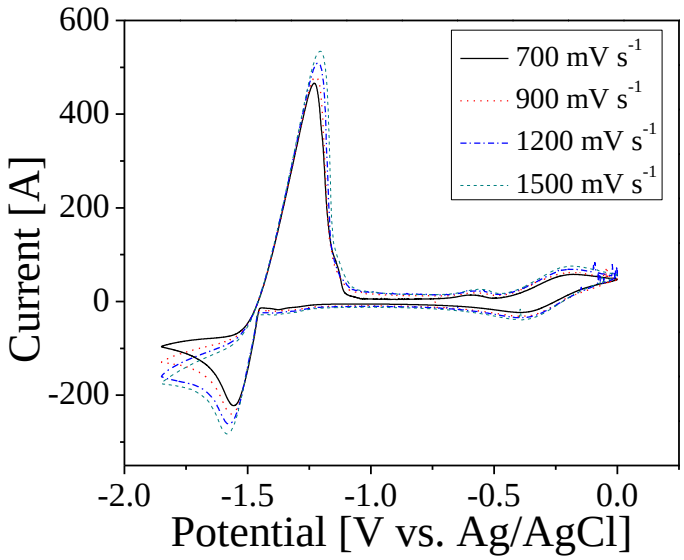

Figure 5.5 Cyclic voltammograms in LiCl-KCl-4wt% UCl_3 at 773 K with faster scan rates ranging from 700 mV s^{-1} to 1500 mV s^{-1}.

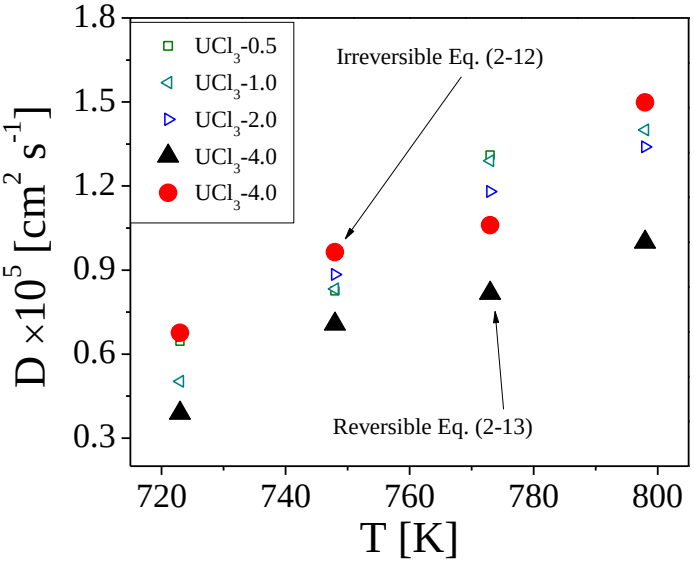

Figure 5.6 Diffusion coefficients of UCl_3 in LiCl-KCl. The values for 4wt% were measured by using Eq. (2-13) (black triangle) and Eq. (2-12) (red circle).

5.3.2 Apparent standard potentials of U^{3+}/U via CV and OCP

The cathodic peak potentials were obtained from the CV results in Section 5.3.1 to calculate the values of $E^{0*}_{U^{3+}/U}$ using Eq. (2-15). The resulting values are plotted in Figure 5.7 and showing proportional increase with rising temperature. The values of $E^{0*}_{U^{3+}/U}$ seem to be independent on concentration change up to 2 wt% UCl_3, but start shifting toward negative direction at 4 wt% UCl_3.

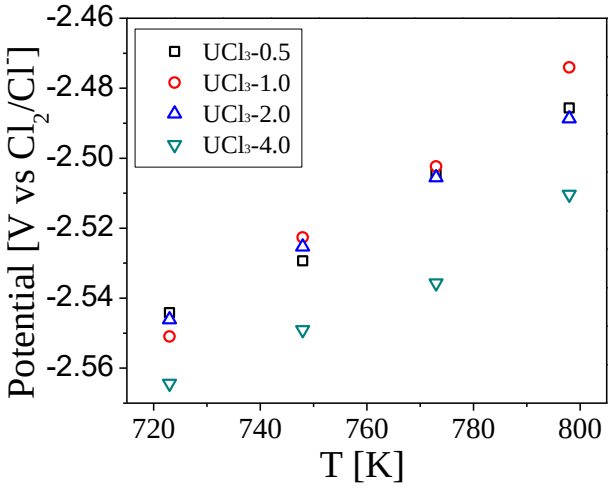

Figure 5.7 Apparent standard potentials for U^{3+}/U couple versus Cl_2/Cl^- measured via CV techniques with Eq. (2-15).

In addition, OCPs were measured between U metal and U^{3+} ions in LiCl-KCl, which can be employed to calculate $E_{U^{3+}/U}$ and $E^{0*}_{U^{3+}/U}$. Prior to the OCP measurements, U was deposited on the tungsten electrode by applying potential at -1.6 V (vs. Ag/AgCl reference) for 30 seconds, which was repeated at least three times. Figure 5.8 shows the representative OCP data which were obtained in LiCl-KCl-0.5 wt% UCl_3 at temperature range (723 K to 798 K). Flat plateaus were observed within 30 seconds, which is due to the fact that the charge transfer between U metal on the electrode and U^{3+} ions in bulk salt reached the equilibrium state. The deviations of the measured equilibrium potentials were less than 1 mV, and the average values are plotted in Figure 5.9(a). The equilibrium potential of U^{3+}/U proportionally increases with increasing UCl_3 concentration up to 3.3×10^{-3} mole fraction (2 wt % of UCl_3 in LiCl-KCl); however, the rate of increase starts decreasing at 6.6×10^{-3} mole fraction. It seems that the equilibrium potential is more correlated at higher concentration (> 4 wt% UCl_3); however, this should be experimentally demonstrated in future works. The apparent standard potentials of U/U^{3+} can be determined using Nernst equation (Eq. (2-2)) with the assumption that the U metal activity is unity. Here, the measured $E_{U^{3+}/U}$ in Figure 5.9(a) can be directly substituted in Eq. (2-3) to calculate

$E^{0*}_{U^{3+}/U}$ according to the UCl_3 mole fractions. In addition, $E^{0*}_{U^{3+}/U}$ can be evaluated by plotting $E_{U^{3+}/U}$ versus $\ln(X_{U^{3+}})$. Within the concentration range in the present work, values of $E_{U^{3+}/U}$ show linear correlations with $\ln(X_{U^{3+}})$, as can be seen in Figure 5.9(b). The linear regressions show good R^2 values greater than 0.991, and $E^{0*}_{U^{3+}/U}$ can be determined at y-intercept. The slopes of the linear lines equal to RT/nF; therefore, the number of charge transferred can be experimentally evaluated (which is referred as $n_{exp.}$). The calculated values of $n_{exp.}$ varried from 2.46 to 2.55, which are slightly smaller than the ideal number of the charge transferred for the U^{3+}/U reaction (n_{ideal} = 3). This may be due to lower probability of the charge transfer in reality, and the number becomes smaller with increasing concentration. Figure 5.10 plots the results from both the direct substitution and linear regression methods with Nernst equation. If the n_{ideal} is used in Eq. (2-3) for the direct substitution methods, the result values are approximately 30 mV more negative. However, the data sets would fall on top of the values determined by the linear regression method when n_{exp} values were being used through the direct substitution method. Comparing to values from literatures, Figure 5.11 plotted the resulting data from CV and OCP measurement

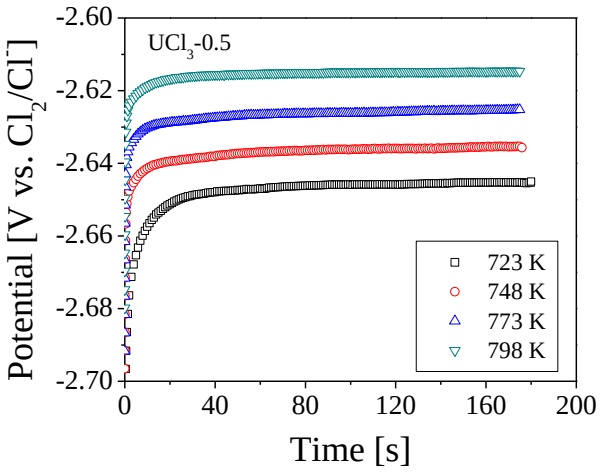

Figure 5.8 Potential plateaus results from OCP experiments in LiCl-KCl-0.5 wt% UCl_3 at temperature ranging 723 K to 798 K.

along with the literature values, revealing that the values are close and follow a similar trend to temperature. However, it can be noticed that $E^{0*}_{U^{3+}/U}$ values measured by CV and CP are generally more negative than the values measured by OCP. This may be because of the characteristics of CV and CP methods by applying overpotential to the working electrode for U^{3+}/U reaction to occur. The applied overpotential depends on the used scan rates and currents used in CV and CP, respectively.

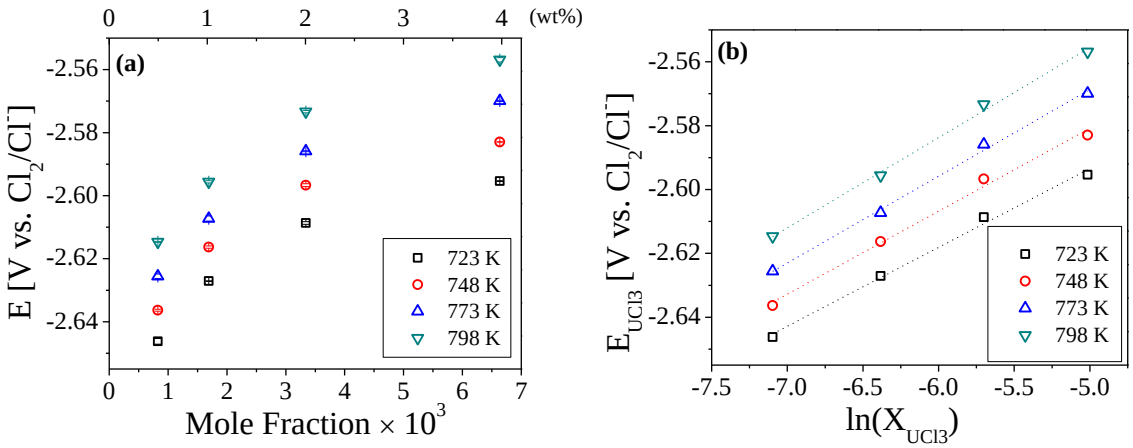

Figure 5.9 Plots of the equilibrium potentials of U^{3+}/U in LiCl-KCl versus (a) mole fraction and (b) logarithm of mole fraction.

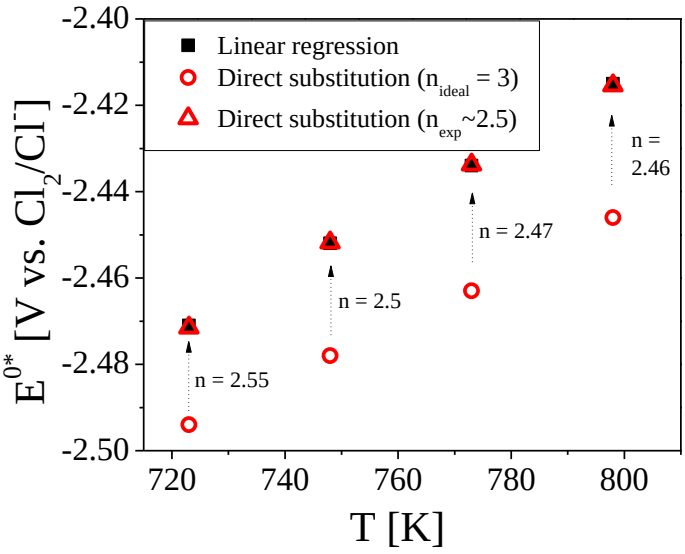

Figure 5.10 The apparent standard potentials of U^{3+}/U in LiCl-KCl salt measured via OCP and calculated in different methods.

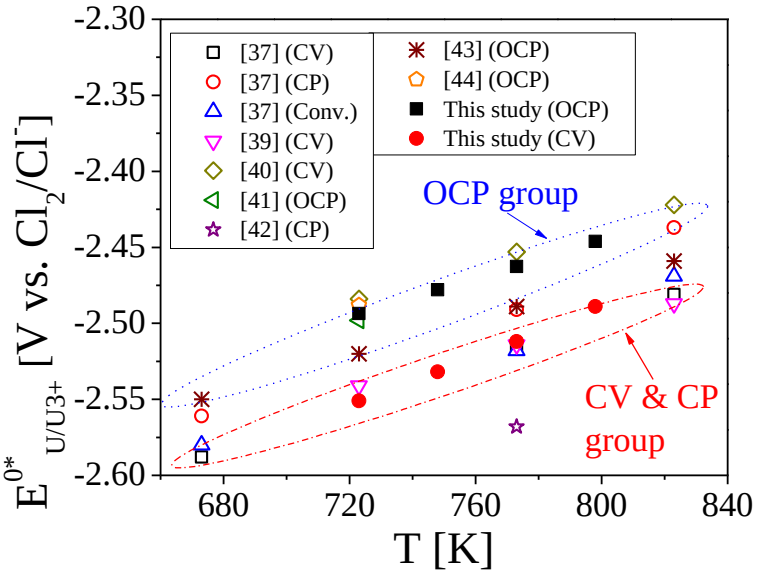

Figure 5.11 The averaged values of $E^{0*}_{U^{3+}/U}$ via CV and OCP technologies, compared with literature values.

5.3.3 Activity coefficient of UCl_3

The previously determined values of $E^{0*}_{U^{3+}/U}$ were utilized to calculate thermodynamic properties of UCl_3 in LiCl-KCl eutectic salt. The partial molar Gibbs free and activity coefficient of UCl_3 were calculated with the same calculation methods developed in Section 4.1.3.1. In addition, the pure thermodynamic data for UCl_3 were found at the super cooled liquid state [53]. Using Eq. (4-1) and Eq. (4-2), $\Delta G^{Fusion}_{UCl_3}$ and $\Delta G^{SC}_{UCl_3}$ were calculated. The super cooled thermodynamic information and calculated values are summarized in Table 5.2. The values of $\Delta G^{0*}_{UCl_3}$ were calculated using the thermodynamic equation ($\Delta G = -nF\Delta E$), and therefore, the $\gamma_{U^{3+}}$ was readily calculated using Eq. (2-4). The resulting values are listed in Table 5.3 and $\gamma_{U^{3+}}$ data sets are compared with the reported values from literatures as shown in Figure 5.12. Here, the similar trend can be observed as seen in the results of the apparent standard potentials (Figure 5.11). The values of $\gamma_{U^{3+}}$ measured by CV and OCP are being divided into two different trends according to temperature. Between CV and OCP methods, significant discrepancies were found up to 10^2 order of magnitude, and OCP method generally provides higher values and show a steep increase rate when temperature rises.

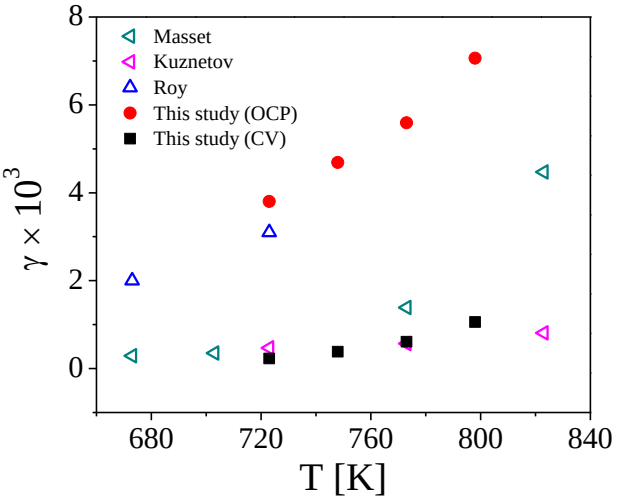

Figure 5.12 The values of $\gamma_{U^{3+}}$measured via OCP and CV methods compared with literature data.

Table 5.2 Thermodynamic information from the literature [53] and calculated values

	723 K	748 K	773 K	798 K	T_m (1100 K)
$\Delta G_{UCl_3}^{Formation}$ (kJ mol^{-1})	-703.03	-697.83	-692.64	-687.45	
$\Delta H_{UCl_3}^{Fusion}$ (kJ mol^{-1})					46.44
$\Delta S_{UCl_3}^{Fusion}$ (J mol^{-1} K^{-1})					41.84
C_p (J mol^{-1} K^{-1})	111.22	111.94	112.66	113.38	129.70
$\Delta G_{UCl_3}^{Fusion}$ (kJ mol^{-1})	14.76	13.96	13.12	12.26	
$\Delta G_{UCl_3}^{SC}$ (kJ mol^{-1})	-688.26	-683.87	-679.52	-675.19	

Table 5.3 Thermodynamic data evaluated by OCP and CV methods

	T (K)	Masset [37] (CV)	Kuznetsov [39] (CV)	Roy [41] (OCP)	This study (OCP)	This study (CV)
$\Delta G_{UCl_3}^{0*}$ (kJ mol^{-1})	673	-745.1		-731.7		
	723			-723.1	-721.8	-738.5
	748				-717.2	-732.8
	773	-726.2			-712.9	-727.1
	798				-708.1	-720.7
	823	-712.9				
$\gamma_{U^{3+}} \times 10^3$	673	0.29		2.0		
	723		0.47	3.1	3.80	0.23
	748				4.69	0.38
	773	1.39	0.57		5.59	0.61
	798				7.06	1.06
	823	4.47	0.81			

5.3.4 Exchange current density of U^{3+}/U

The EIS, LP, Tafel, and CV methods were conducted to investigate the i_0 kinetics of U^{3+}/U couple at UCl_3 concentrations ranging from 0.5 wt% to 4 wt% and temperature from 723 K to 798 K. Further dimensionless analyses will be also provided as well.

5.3.4.1 EIS

The same EIS measurement procedures and minimum over potential method developed in Section 4.1.3.2 were used in this section. Figure 5.13(a) illustrates the example procedure for finding minimum overpotential for U/U^{3+} reaction for UCl_3-0.5 salt at 748 K. At about -1.499 V, the minimum overpotential was obtained and the EIS measurements were repeated with the

different potential amplitudes ranging from 5 mV to 10 mV. As shown in Figure 5.13(b), the impedance spectra display a good agreement with the potential amplitudes, which indicate the stable charge transfer kinetic at the minimum overpotential. The obtained impedance spectra were fitted to the same equivalent circuit as shown in Figure 4.8. Figure 5.14 illustrates the measured and fitted impedance spectra in the complex plane for all four samples under the different temperature conditions. Small current values were applied during the EIS measurement (< 3 mA cm^{-2}), so that the surface area change by uranium deposition is expected to be negligible. After the manual curve fitting, the goodness of fittings (χ^2) was further checked by using an equation expressed as

$$\chi^2 = \frac{1}{N-m}\sum_{i=1}^{N}\frac{(\overline{V_r}-V_r)^2+\left(\overline{V_j}-V_j\right)^2}{(V_r^2+V_j^2)} \quad (5\text{-}1)$$

where N is the number of data points, m is the number of equivalent circuit parameters, $\overline{V_r}$ is the fitted real values, $\overline{V_j}$ is the fitted imaginary values, V_r is the measured real values, and V_j is the measured imaginary values. The values of χ^2 were lower than 0.003, indicating a good fit to the measured data sets. From the results of curve fitting, charge transfer resistances were measured, which were being employed to calculate the value of i_0 and k^0 for U^{3+}/U reaction in LiCl-KCl molten salt. Figures 5.15(a) and 5.15(b) show plots of the calculated i_0 values versus temperature (K) and concentration (UCl_3 mole fraction), respectively. The EIS experiments were repeated three to four times with the same experimental conditions to confirm the reproducibility of the results; the variations of the value are represented as the standard deviations (error bars). The values of i_0 for U/U^{3+} reaction are ranging from 0.0054 A cm^{-2} to 0.102 A cm^{-2} under different concentration and temperature conditions. The values were almost linearly proportional to an increase in the concentration and temperature, slight deviations were observed when the UCl_3 concentration is over 4 wt% in LiCl-KCl. The k^0 values were calculated from the slopes of the i_0 linear trends at different concentrations with the equation $i_0 = nFk^0C_{UCl3}$. The resulting values of k_0 and i_0 are listed in Table 5.4.

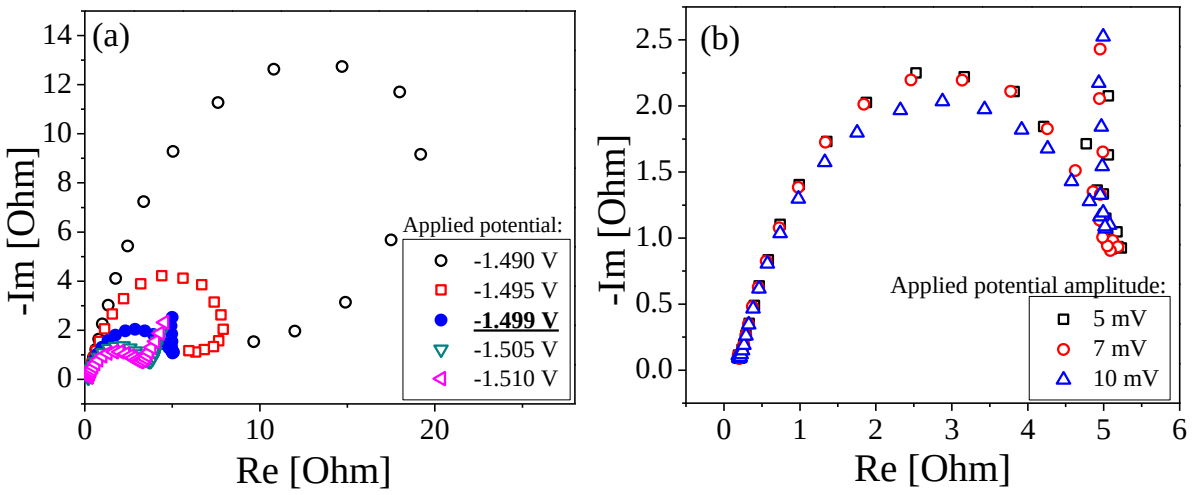

Figure 5.13 (a) Nyquist plots measured in UCl_3-0.5 salt at 748 K. The applied potential was changed from -1.490 V to -1.510V to find the minimum overpotential. (b) Repetition with the applied potential amplitude ranging from 5 mV to 10 mV at -1.499 V.

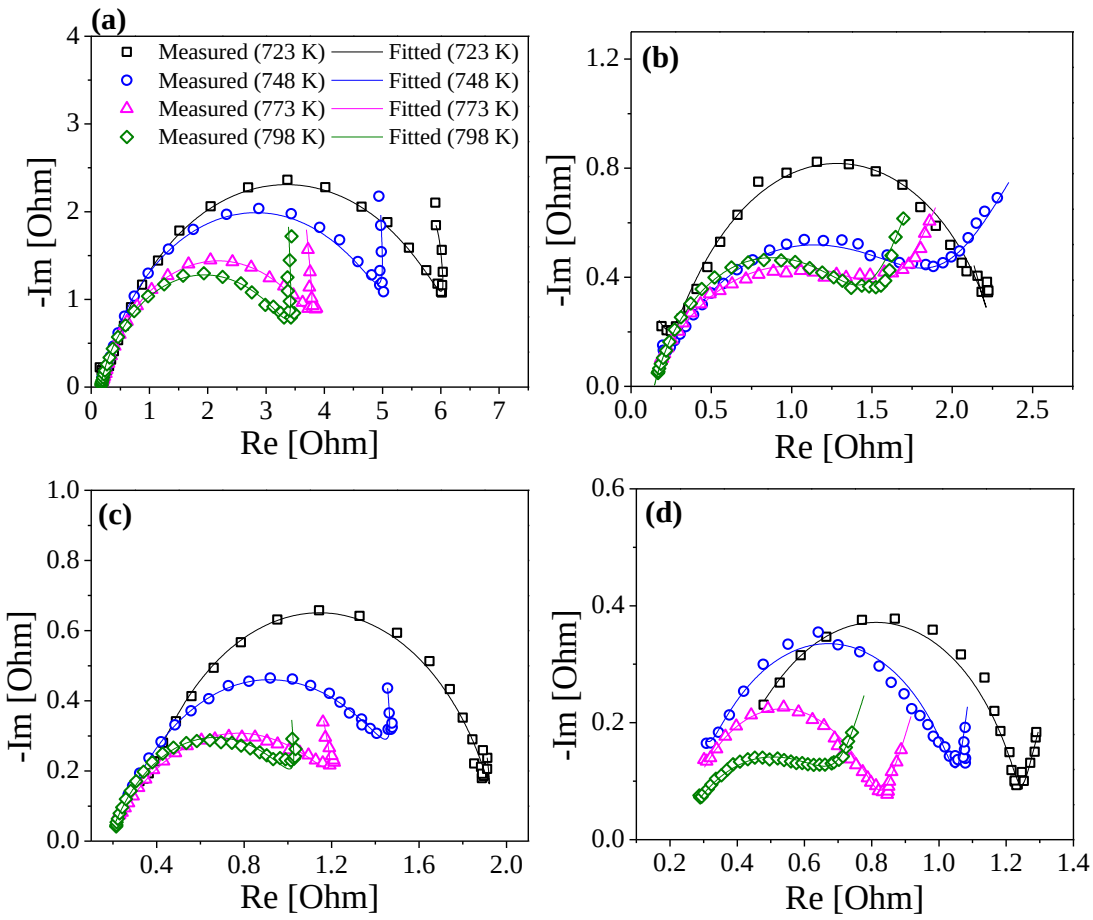

Figure 5.14 The measured and fitted impedance spectra in the salt of (a) UCl_3-0.5, (b) UCl_3-1.0, (c) UCl_3-2.0, and (d) UCl_3-4.0 at temperature ranging from 723 K to 798 K. Applied potential amplitude was 7 mV, and the chi-square goodness of fit (χ^2) was less than 0.003.

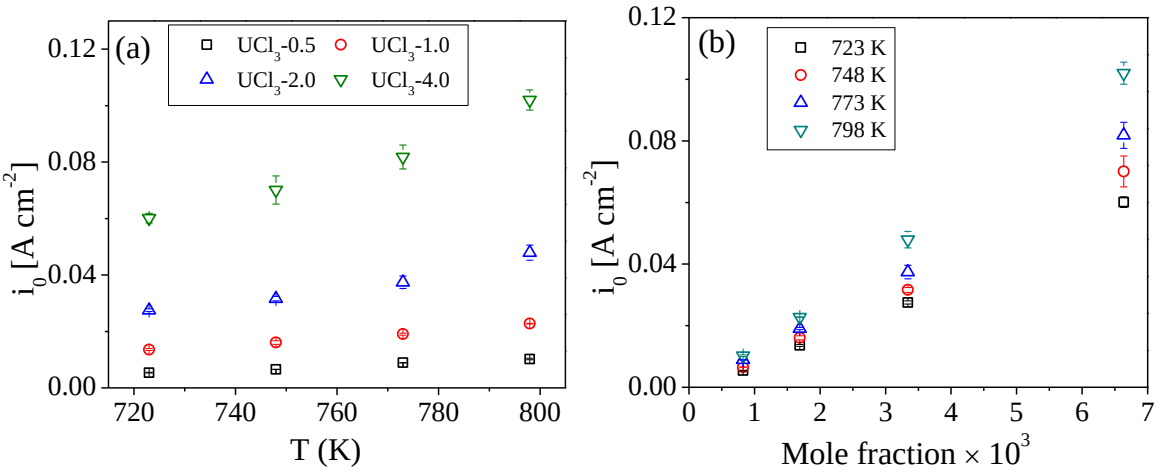

Figure 5.15 (a) plots the i_0 of U/U^{3+} against temperature for different concentrations, and (b) plots the i_0 of U/U^{3+} versus mole fraction of the UCl_3 under different temperatures.

Table 5.4 Summary of i_0 and k^0 for U/U^{3+} reaction measured by the EIS method

		Temperature, T (K)			
		723	748	773	798
	$k^0 \times 10^3$ [cm s^{-1}]	1.048 (R^2= 0.993)	1.230 (R^2= 0.993)	1.454 (R^2= 0.995)	1.827 (R^2= 0.996)
UCl3-0.5	$i_0 \times 10^3$ [A cm^{-2}]	5.4 ± 0.09	6.55 ± 0.03	8.91 ± 0.06	10.2 ± 0.25
UCl3-1.0		13.6 ± 0.32	16.1 ± 0.64	19.0 ± 0.35	22.8 ± 0.09
UCl3-2.0		27.5 ± 0.5	31.6 ± 0.77	37.4 ± 2.2	47.9 ± 2.7
UCl3-4.0		60.1 ± 1.7	70.1 ± 5.0	81.8 ± 4.2	102 ± 3.6

5.4.3.2 LP and Tafel methods

For both LP and Tafel measurements, the potential was swept from -350 mV to 250 mV based on the equilibrium potentials. Figure 5.16(a) shows an example of current-potential curve in UCl_3-0.5 salt. The slopes were obtained in the overpotential ranging from -5 mV to 5mV at the different temperatures, which were employed to calculate i_0 of U/U^{3+}. As Eq. (2-26) is valid with no diffusion effect; thus, very slow scan rate should be applied for the proper exploration of the charge transfer kinetics. However, at extremely slow scan rates (< 3 mV s^{-1}), the electrode surface area continuously increases due to the deposition of U metals on the electrode. Therefore, LP method was examined with the different scan rates ranging 3 mV s^{-1} to 100 mV s^{-1}. Figure 5.16(b)

illustrates Tafel curves in UCl_3-0.5 salt at the same temperature range. Here, the linear Tafel regions can be observed at the overpotential from -100 mV to -230 mV, which were fitted to measure the value of i_0. Unfortunately, the linear Tafel region cannot be acquired at the concentration higher than 1 wt% UCl_3 as shown in Figure 5.16(c). This issue is mainly owing to the vigorous U deposition with the high bulk concentrations. Therefore, Tafel plot method was only applied with the scan rates of 3 mV s^{-1}, 5 mV s^{-1}, and 7 mV s^{-1} in UCl_3-0.5 salt for determining the i_0 of U/U^{3+} pair.

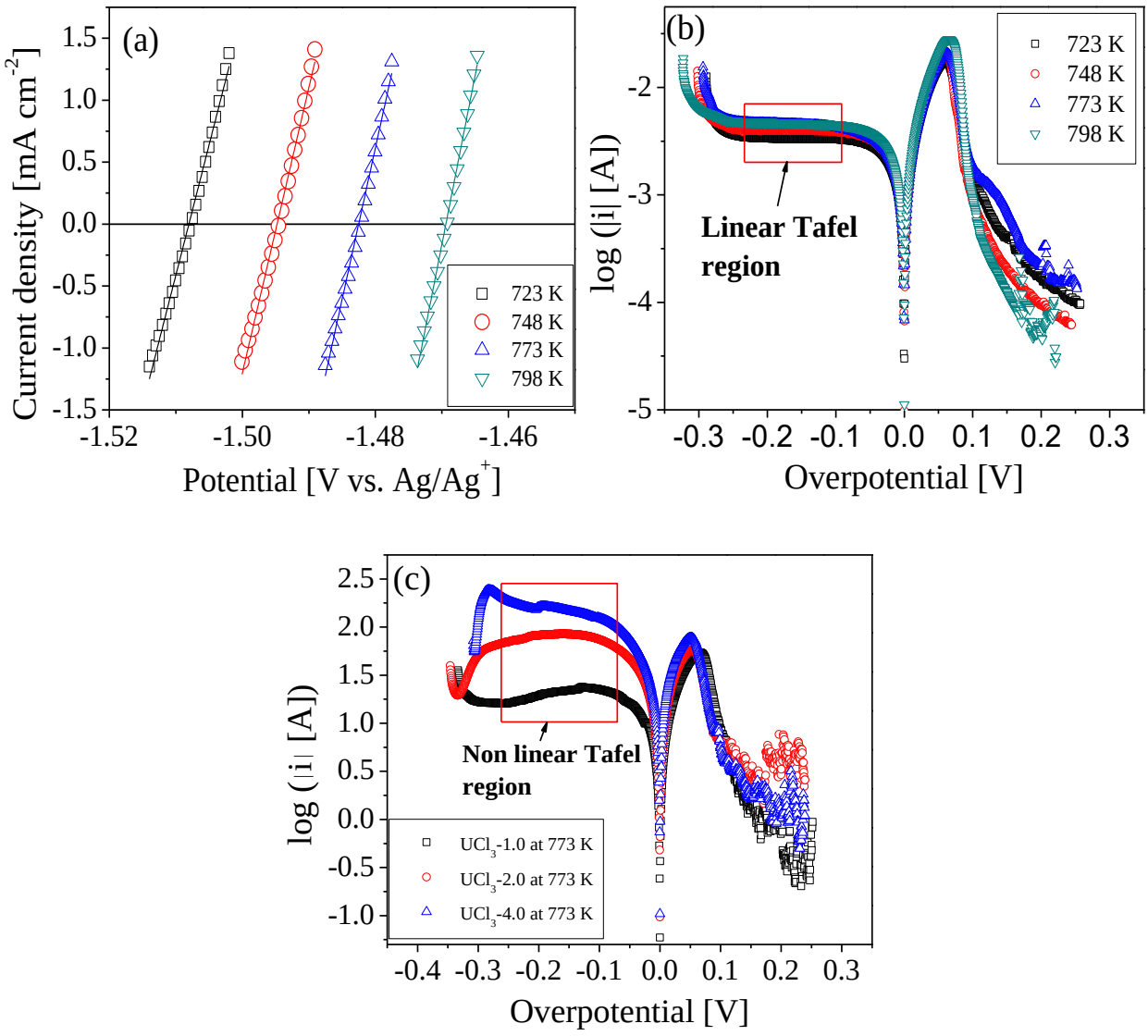

Figure 5.16 (a) Current density versus potential at small overpotential region (< 5 mV) in UCl_3-0.5 salt; (b) Plot of log (i_0) versus overpotential in UCl_3-0.5 salt; and (c) Plot of log (i_0) versus overpotential in UCl_3-1.0, UCl_3-2.0, and UCl_3-4.0 at 748 K. The scan rate was used at 5 mV s^{-1}.

Figure 5.17 shows the measured values of i_0 by LP method with different scan rates. For UCl_3-0.5 and UCl_3-1.0 (Figures 5.17(a) and 5.17(b), respectively), the i_0 values rapidly decrease when the scan rates increase from 3 mV s^{-1} to 15 mV s^{-1} while they increase sharply at the scan rate faster than 20 mV s^{-1}. This result signifies that the diffusion limits caused by an increase in the scan rate can dominantly affect the kinetic measurements. In contrary, steady decreases can be observed with increasing the scan rate in UCl_3-2.0 and UCl_3-4.0 salts as shown in Figures 5.17(c) and 5.17(d), respectively. The latter results indicate that the variation of the electrode surface area may contribute an effect on the resulting i_0 due to the U deposition. Therefore, having these challenges,

the measured i_0 values appear dispersed with varying scan rates. Figure 5.18(a) shows all measured i_0 values from LP and Tafel methods. The i_0 values of U/U^{3+} follow the linear relationship with temperature. While the relative errors from the averaged i_0 were less than 10% in both UCl_3-0.5 and UCl_3-1.0, these errors rose up to 24% in UCl_3-4.0 salt due to the above challenges. The effect of the change on surface area becomes problematic on the LP and Tafel measurements. Tafel curves were measured in UCl_3-0.5 salt, and the i_0 calculated from y-intercept was varying for the scan rates of 3 mV s^{-1} to 7 mV s^{-1} (see Figure 5.18(b)). Tafel results also show a linear trend with the temperature and agree with the LP result within 20% of relative error range.

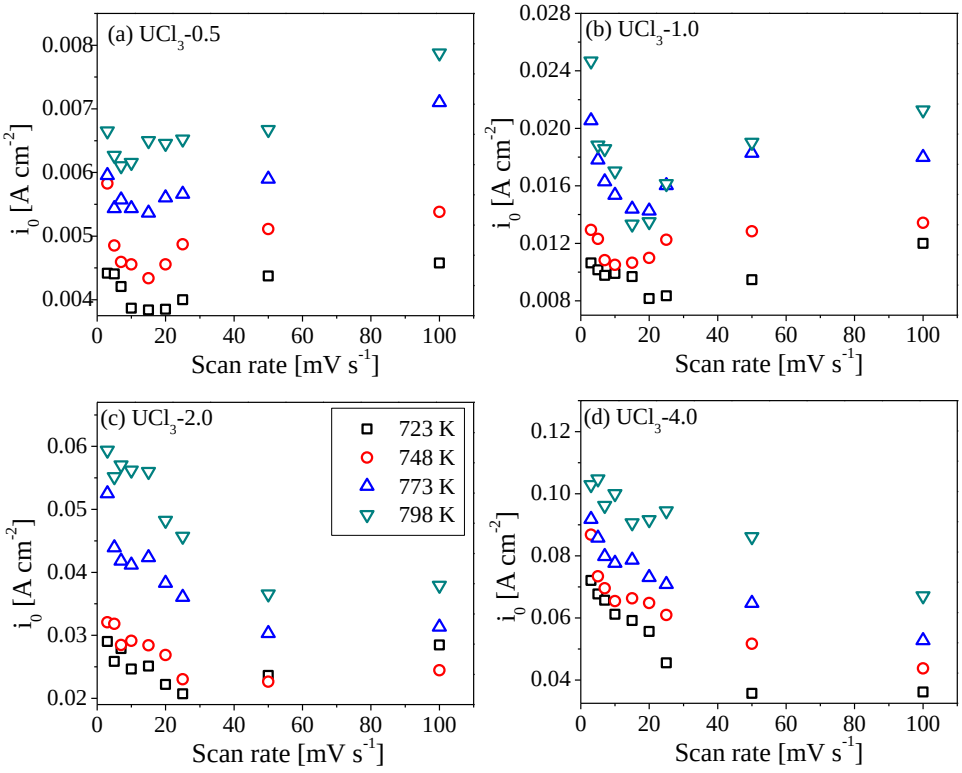

Figure 5.17 Plots of i_0 results measured by LP methods under different scan rates for (a) UCl_3-0.5, (b) UCl_3-1.0, (c) UCl_3-2.0, and (d) UCl_3-4.0.

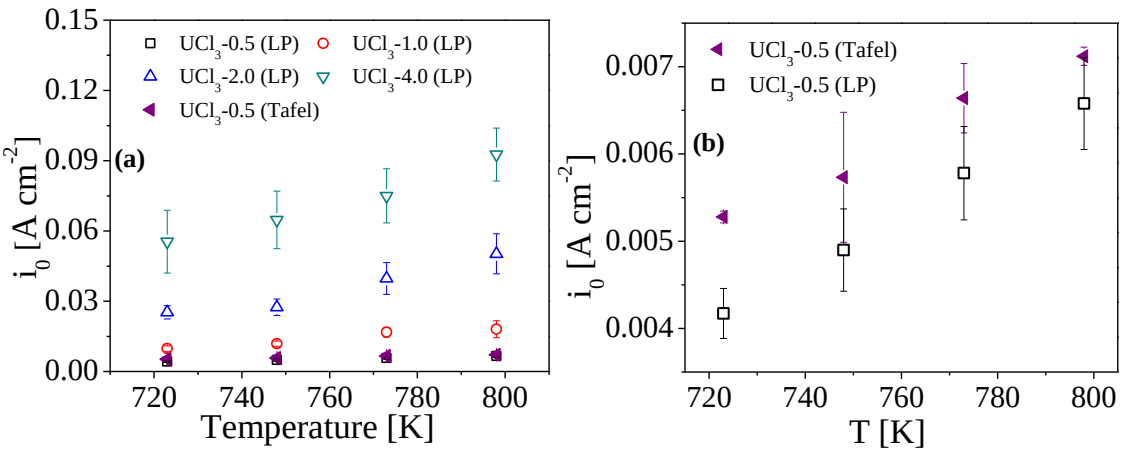

Figure 5.18 (a) Plots of i_0 values measured by LP and Tafel methods for concentrations of 0.5 wt%, 1.0 wt%, 2.0 wt%, and 4.0 wt% and (b) magnifying scale for the comparison of i_0 values between LP and Tafel methods at 0.5 wt% UCl_3.

5.4.3.3 Cyclic voltammetry (CV)

CV is powerful and the most widely practiced among the electrochemical methods [52]. The CV method is analogous to the LP measurement because CV observes current based on the potential change. Only difference from the LP method is that CV is a reversal method executed by higher scan rates. As mentioned in Section 5.4.3.2, the results from LP method show the agreement within 24% relative error range under the different scan rates (from 3 mV s^{-1} to 100 mV s^{-1}. Therefore, CV curves at the scan rate of 50 mV s^{-1} and 100 mV s^{-1} was used, and the charge transfer resistance in very small overpotential region was obtained to estimate the values of i_0 for U/U^{3+}. It should be mentioned that this selected scan rate is not considered fast in the CV application; however, this method was explored in order to compare with LP method and assess the applicability for the estimation of i_0. Figure 5.19 shows an example procedure on a CV curve in UCl_3-0.5 salt at 748 K. The potential where the deposited U starts to be oxidized (indicated by red circle in Figure 5.19 (a)) can be found, and the slope from current-potential curve within 10 mV overpotential can be measured as described in Figure 5.19(b), which is the charge transfer resistance. Then, the value of i_0 for U/U^{3+} reaction would be calculated by using Eq. (2-28). Figure 5.20 reveals that the value increases when both the concentration and temperature increase; however, it was difficult to observe the linearity from these results. The advantage of the CV method is the rapid data acquisition through an instant scan rate; hence, this technique would be useful in development of the near-real time technique for the material detection and accountability in the ER system.

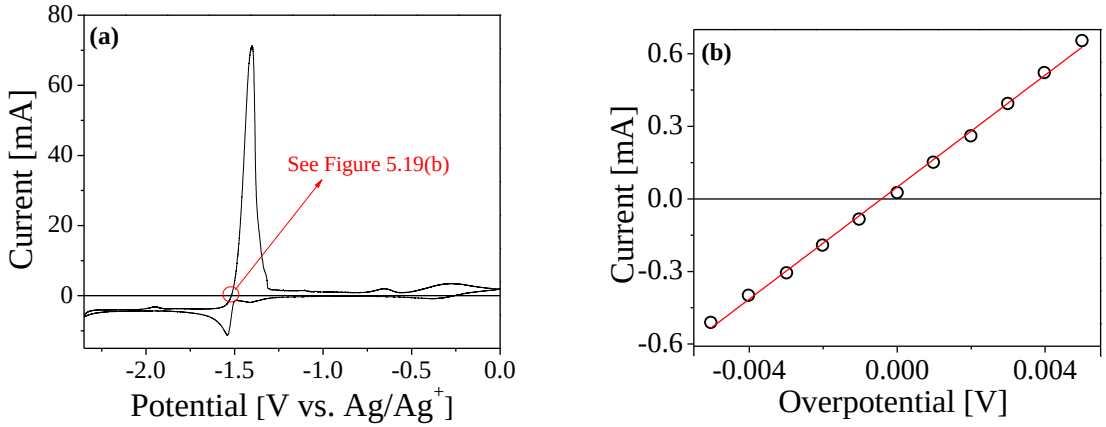

Figure 5.19 (a) Cyclic voltammogram at the scan rate of 50 mV s^{-1} in UCl_3-0.5 salt at 748 K, and (b) the magnifying scale of the small overpotential region (from (a)) for measuring the charge transfer resistance from the slope.

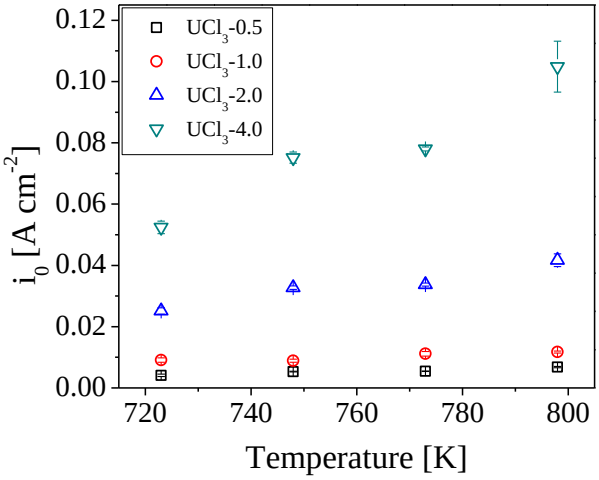

Figure 5.20 Plots of i_0 by using CV method for U/U^{3+} in UCl_3-0.5, UCl_3-1.0, UCl_3-2.0, and UCl_3-4.0 salt at the different temperatures with the standard deviations.

5.4.3.4 Data comparison and practical analysis

Figure 5.21(a) shows the results from the four techniques being explored. The i_0 values from EIS measurements show the most linear trends regarding to the concentration and temperature whereas the values measured by CV method are much scattered and do not have a strong linear correlation with the concentration and temperature. Overall, the results from the four methods are in a moderate agreement within 33% relative difference from their average values. Figure 5.21(b) shows i_0 results from this work in comparison to the reported i_0 values. Lim et al. [51] provided the equations of the i_0 as a function of the concentration and temperature. By plotting the equations from the literature, the results reside within the range of i_0 from this study. Particularly, EIS measurements for 1 wt% UCl_3 in the present study agree moderately well with those from Lim and co-workers [51]. However, LP results in this study are significantly influenced by the scan rate, which reputes the conclusion from the study of Lim et al. [51] that the scan rate (5 mV s^{-1} - 100 mV s^{-1}) has no significant effect on the i_0 value. Choi et al. [48] measured i_0 of U/U^{3+} at ~3.3 wt% concentration at 773 K and reported that the i_0 value measured with a tungsten electrode was 0.0584 A cm^{-2} which located in the vicinity of i_0 measured in this study.

Because the EIS method provides the most linear trends and agreements with other literature data, the results from EIS measurements have been selected for further analysis without considering the deviations (error bars) of the data. The linear relationships of i_0 in Figures 5.15(a) and 5.15(b) were modeled by using a linear equation, $y = ax + b$ (these fitted values are summarized in Table 5.5). Here, the equations in Table 5.5 can be used to determine any desired i_0. These equations were being extrapolated to estimate the i_0 of U/U^{3+} at the 5 wt% concentration under 723 K and 923 K reported by Rose and co-workers [50]. The resulting calculations reveal that the values of the i_0 are 0.0739 A cm^{-2} (C= 5 wt% (0.00848 mole fraction) and T = 723 K) and 0.214 A cm^{-2} (C = 5 wt% (0.00848 mole fraction) and T = 923 K) agreeing well with the values of i_0 reported by Rose et al. [50]. The projection for i_0 value at 5 wt% UCl_3 can be checked in Figure 5.21(b) (see a line of orange dot). Although literature i_0 values were being measured under different electrochemical scales and cell configurations, the results are in a good agreement (see Figure 5.21(b)). Thus, it can be postulated that the effect of system scale and configuration has a weak influence on the i_0 kinetics. In order to confirm this argument, a large number of data collections will be required in different electrochemical environments. Also, the i_0 value reported by Ghosh et al. [49] does not follow the general trends of this work. This discrepancy may be coming from their study on the anodic dissolution by using a uranium rod as an anode.

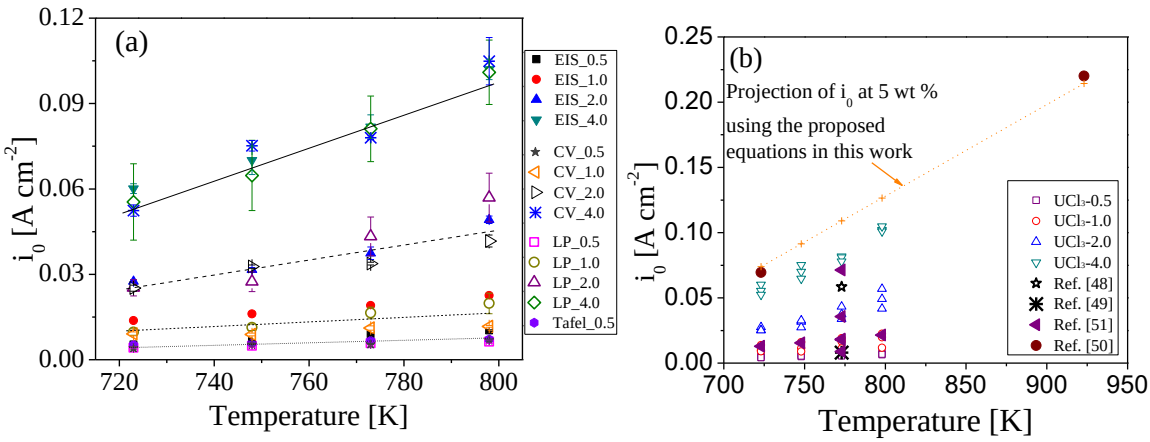

Figure 5.21 (a) The i_0 values measured by the four different methods in the present study, and (b) the reported values of i_0 for U/U^{3+} from different literature studies are being superimposed.

Based on the EIS data sets, additional temperature and concentration dependence were further investigated. Here, the temperature relationship of kinetic parameters can typically be expressed by Arrhenius equation (as discussed in Section 4.1.3.2) $i_0 = I_0 \exp(-E_a/RT)$. Figure 5.22 shows $\ln(i_0)$ versus 1/T for all concentrations where the slopes and y-intercepts can be used to tabulate I_0 and E_a, respectively; the calculated values are being summarized in Table 5.6. The dimensionless relationship between i_0/I_0 and $\exp(-E_a/RT)$ can be plotted (see Figure 5.23(a)); therefore, the i_0 can be easily estimated when I_0 and $-E_a$ are known. Furthermore, the concentration dependency of i_0 are being explored in Figure 5.23(b). The dimensionless quantity of $i_0/i_{0,\,max}$ were plotted against mole fraction. Here, $i_{0,max}$ is the i_0 value at 4 wt% UCl_3 which can be found in Table 5.6. Thus, i_0 quantity can be estimated by simply knowing $i_{0,max}$ at 4 wt% UCl_3 reported in the present study. The equations for the dimensionless relationships (i_0/I_0=1.0046 $\exp(-E_a/RT)$ and $i_0/i_{0,\,max}$=155.2 x) in Figures 5.23(a) and 5.23(b) are shown in each figure, respectively. The concentration is valid from 0.00083 to 0.00664 in mole fraction. The fitted equation of i_0/I_0=1.0046 $\exp(-E_a/RT) \approx \exp(-E_a/RT)$ with the R^2 of 0.997 confirms the Arrhenius behaviors within the system. Overall, these correlations can be used at the concentration less than 4 wt% of UCl_3 in LiCl-KCl eutectic salt.

Table 5.5 Linear models for concentration (mole fraction) and temperature (K) dependence

		Equations	R^2
Temperature (T) dependence of i_0	UCl_3-0.5:	6.752×10^{-5} T – 0.0436	0.973
	UCl_3-1.0:	1.221×10^{-4} T – 0.0750	0.987
	UCl_3-2.0:	2.682×10^{-4} T – 0.1678	0.932
	UCl_3-4.0:	5.494×10^{-4} T – 0.3393	0.956
Concentration (C)* relationship of i_0	723 K:	8.823 C	0.993
	748 K:	10.274 C	0.993
	773 K:	12.047 C	0.995
	798 K:	15.012 C	0.996

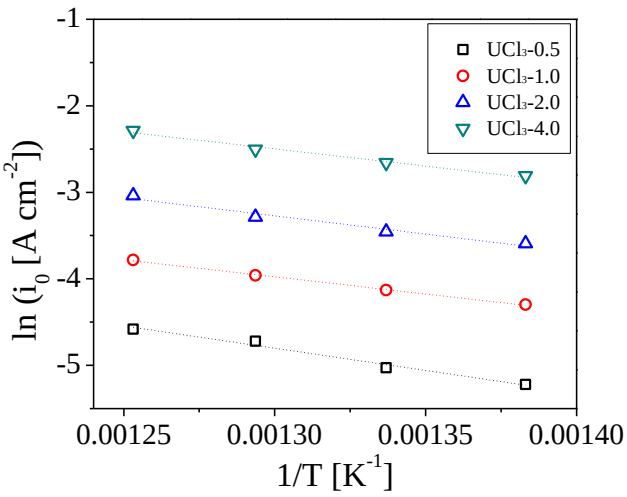

Figure 5.22 Natural logarithm of i_0 against the inverse temperature.

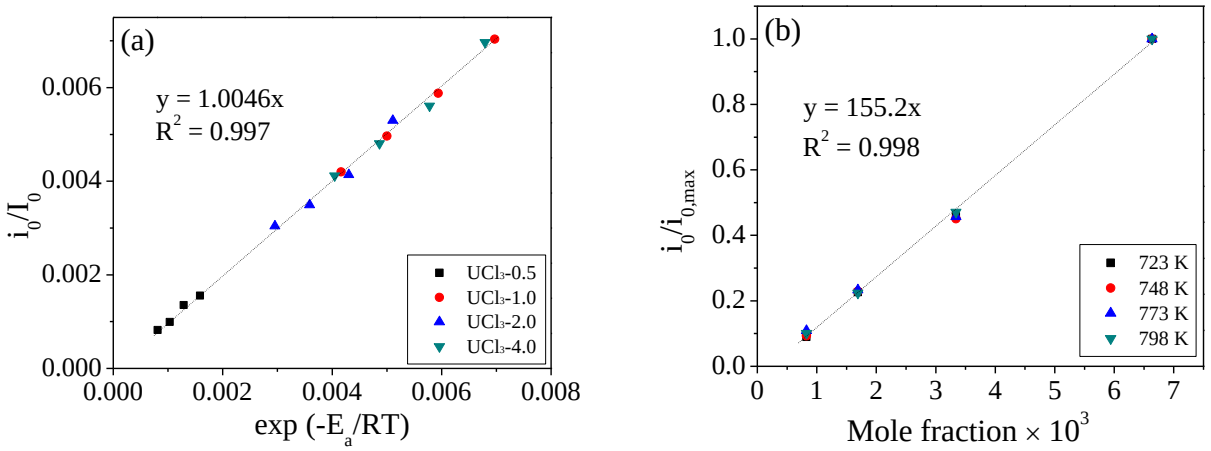

Figure 5.23 (a) i_0/I_0 versus exp(-Ea/RT), and (b) $i_0/i_{0,max}$ versus mole fraction.

Table 5.6 The pre-exponential factors and activation energies for U/U^{3+} based on the data from EIS measurements

UCl_3-0.5		UCl_3-1.0		UCl_3-2.0		UCl_3-4.0	
I_0 [A cm^{-2}]	E_a [kJ mol^{-1}]	I_0 [A cm^{-2}]	E_a [kJ mol^{-1}]	I_0 [A cm^{-2}]	E_a [kJ mol^{-1}]	I_0 [A cm^{-2}]	E_a [kJ mol^{-1}]
6.5883	-42.468	3.2368	-32.948	9.0449	-35.011	14.595	-33.119

5.3.5 Effects of $GdCl_3$ on U properties

The effects of $GdCl_3$ on UCl_3 behaviors were explored at 773 K by adding certain amounts of $GdCl_3$ into LiCl-KCl-UCl_3 salt (Sample No. 5 – 10 in Table 5.1). The concentration ratio of $UCl_3/GdCl_3$ varies from 1 to 4 through the samples. For measuring the diffusion coefficients, equilibrium potentials, and exchange current densities in the salt samples, the same procedures and data analyses were used. Figure 5.24 shows the measured CV data in LiCl-KCl-1wt% UCl_3 - 1 wt% $GdCl_3$ at scan rate ranging from 50 mV s^{-1} to 200 mV s^{-1}. Redox peaks for Gd^{3+}/Gd couple (IV_c and IV_a, respectively) were observed at potentials more negative than U^{3+}/U redox peaks; therefore, it can be considered that the U^{3+}/U reaction occurs independently whereas Gd^{3+}/Gd reaction is happening along with U deposition on the electrode. Since peaks of P_{3c} stays at the same potential even with addition of $GdCl_3$, Eq. (2-13) was utilized to determine the diffusion coefficient of UCl_3 in the salt mixtures. Figure 5.25 shows the diffusion coefficients of UCl_3 measured in Sample 5 – 10 along with the results reported in Section 5.3.1 at 773 K. By adding $GdCl_3$ to the LiCl-KCl-UCl_3 system, the diffusion coefficient of UCl_3 becomes smaller by $0.2 \times 10^{-5} \sim 0.3 \times 10^{-5}$ cm^2 s^{-1}. The values decreases slightly with increasing concentrations of UCl_3 and $GdCl_3$, but UCl_3-$GdCl_3$ mixtures need to be examined at concentrations higher than 4 wt%. At

lower concentration of UCl_3 (Sample No. 5), $GdCl_3$ co-existence significantly affects the diffusion behavior of UCl_3, which reveals that diffusivity of UCl_3 in ER system may be considerably affected by the concentration of other elements (e.g. actinide and lanthanide elements). However, further studies need to be done with different elements and multi-elements in order to understand the evidence of decreasing diffusivity. This may be affected by the physical and chemical interactions among the particles.

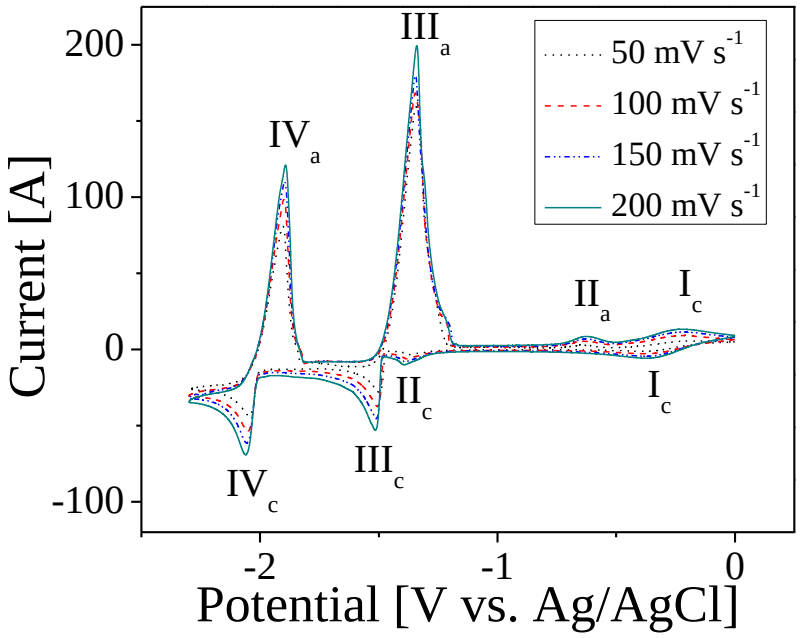

Figure 5.24 Cyclicvoltammogram in LiCl-KCl-1wt% UCl_3-1wt% $GdCl_3$ at 773 K, measured at scan rate from 50 mV s^{-1} to 200 mV s^{-1}.

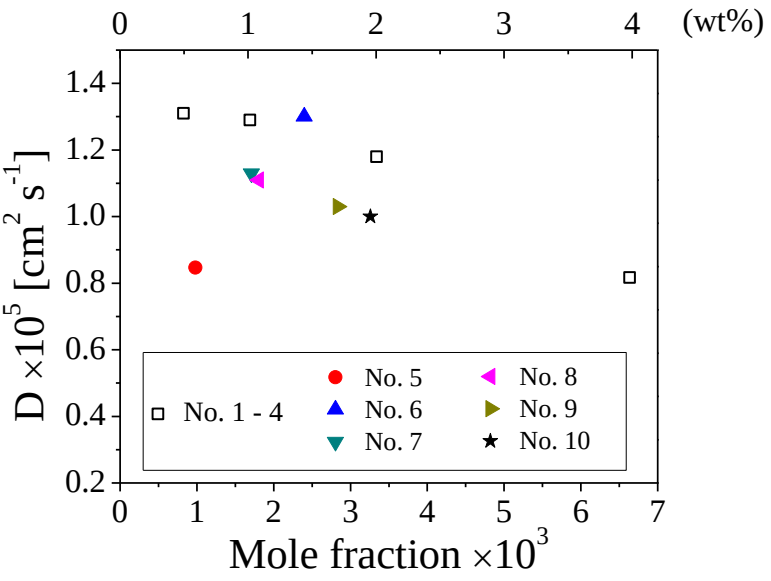

Figure 5.25 Plots of diffusion coefficients measured in LiCl-KCl-UCl_3-$GdCl_3$ mixtures (No. 5 – 10), which were compared with original data sets (Section 5.3.1) at 773 K.

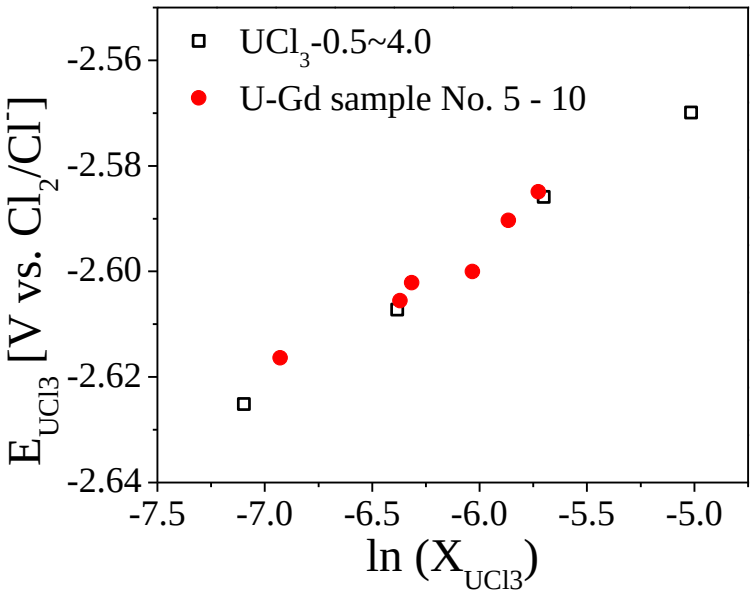

Figure 5.26 The equilibrium potentials of U^{3+}/U measured with presence of $GdCl_3$, which were superimposed in the original trend of the equilibrium potential at 773 K.

Figure 5.26 shows the equilibrium potentials as function of concentration in Sample No. 5 – 10 at 773 K which are superimposed on the pure UCl_3 data as seen in Section 3.1.2. The resulting values follow the linear dependence line within 0.2% relative difference. This indicates that the results of $E^{0*}_{U^{3+}/U}$ and $\gamma_{U^{3+}}$ also show good agreement with the original data with pure UCl_3; therefore, it could be believed that thermodynamic properties of UCl_3 is scarcely dependent on the presence of $GdCl_3$ in LiCl-KCl-UCl_3 salt system. The calculations of $E^{0*}_{U^{3+}/U}$ and $\gamma_{U^{3+}}$ are summarized in Table 5.7, and showing good consensus with the data sets measured with pure UCl_3 salts (reported in Table 5.3). Furthermore, the exchange current densities of U^{3+}/U were measured with the $GdCl_3$ additions and the resulting data are plotted in Figure 5.27. The values are laid along with the linear model, indicating that the kinetic parameters of U^{3+}/U are also independent on $GdCl_3$. The resulting data and trends from the experiments with the mixture salts provide a useful insight into behaviors of U such as electrochemical, thermodynamic, and kinetic behaviors with $GdCl_3$ existence in LiCl-KCl; however, further experimental database should be accumulated to understand U behavior among the various fission products which is occurring in real ER system. Unfortunately, the thermodynamic and kinetic properties of U in multi-components have not been explored in previous publications.

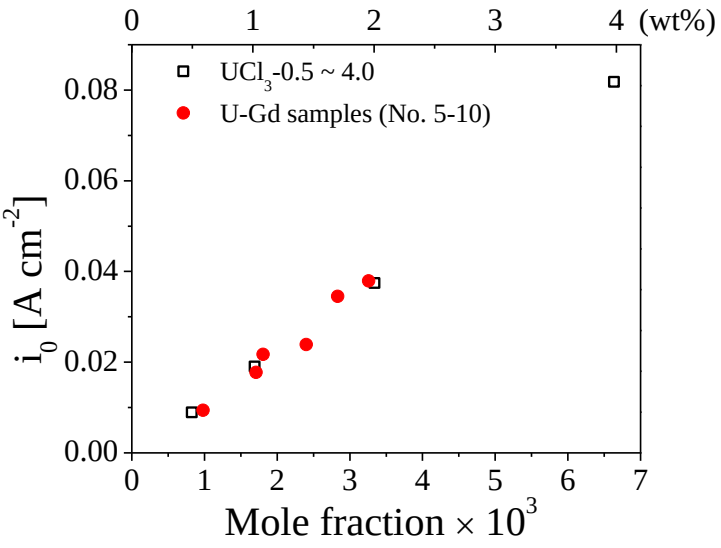

Figure 5.27 The exchange current densities measured in U-Gd samples, compared with the values measured with pure UCl_3 salts at 773 K.

5.4 Summary

The properties of U were investigated via various electrochemical techniques at different UCl_3 concentrations and temperatures. This section starts with evaluating the diffusion coefficients

of UCl_3, which were done by using CV technique. Although the reversible equation was used to calculate the values, the irreversible equation was also employed to develop a measurement method at high concentrations. However, the equation will need to be revised for the soluble-insoluble system. The equilibrium potentials of U^{3+}/U couple were measured using OCP, indicating that it shows a linear trend within 2 wt% UCl_3 concentration while the values reach to certain level at concentrations higher than 4 wt% UCl_3. From the measured equilibrium potential, the apparent standard potentials of U^{3+}/U were determined, which were used for further calculations of thermodynamic properties of UCl_3. The partial molar Gibbs free energies were calculated at the different temperatures, and activity coefficients of UCl_3 in LiCl-KCl were evaluated with the consideration of super cooled liquid state as an ideal salt state. Next, the exchange current densities of U^{3+}/U couple were focused by using four different techniques such as EIS, LP, Tafel, and CV methods. In general, the measured data sets via the four methods agree within 33% relative error range. The EIS method provided the most reproducible results which are linearly dependent on the concentration and temperature. LP and Tafel methods show large deviations with the different scan rates due to the change of electrode surface area. For the CV method, the results were similar to that from LP method, but the data sets did not show the linear relationship with either the concentration or temperature. This low to moderate discrepancies between data from CV and EIS measurements indicate that CV may be used as a rapid data acquisition and analysis providing advantage toward the real time material detection and accountability.

Table 5.7 Thermodynamic properties of UCl_3 in LiCl-KCl-UCl_3-$GdCl_3$ mixture salts

No	Sample	$E^{0*}_{U^{3+}/U}$ (V vs. Cl_2/Cl)	$\Delta G^{0*}_{UCl_3}$ (kJ mol^{-1})	$\gamma_{U^{3+}} \times 10^3$
5	U0.5_Gd0.5	-2.46 ± 6.0×10^{-3}	-712.8 ± 17.4	5.64 ± 1.53×10^{-1}
6	U1.0_Gd0.25	-2.46 ± 4.2×10^{-4}	-713.2 ± 1.2	5.26 ± 9.8×10^{-2}
7	U1.0_Gd0.5	-2.47 ± 4.5×10^{-5}	-713.8 ± 1.3	4.80 ± 9.7×10^{-3}
8	U1.0_Gd1.0	-2.46 ± 4.0×10^{-4}	-712.6 ± 11.6	5.80 ± 1.1×10^{-1}
9	U2.0_Gd1.0	-2.46 ± 2.7×10^{-4}	-712.1 ± 7.6	6.30 ± 7.5×10^{-2}
10	U2.0_Gd2.0	-2.46 ± 1.2×10^{-4}	-711.4 ± 3.5	6.98 ± 3.8×10^{-2}

Based on the i_0 data measured via EIS technique, further analyses were performed. The dependences with the concentration and temperature were linearly modeled and the equations were

provided. Arrhenius temperature relationship was used to fit these data sets, from which the maximum value of i_0 at infinite temperature and activation energy for U/U^{3+} reaction were obtained. Also, dimensionless equations were provided, which can be utilized to estimate the i_0 properties for U/U^{3+} reaction in various experimental conditions.

Lastly, the same experiments were performed with $GdCl_3$ addition to the salt. The diffusion coefficient was affected by the addition of $GdCl_3$: 12 ~ 35 % of declines in diffusion coefficient values were observed by adding $GdCl_3$ in LiCl-KCl-UCl_3 (ratio of UCl_3 was ranging from 1 to 4). The equilibrium potentials shows the similar values even when $GdCl_3$ was added in the salt which indicates that thermodynamics of UCl_3 in LiCl-KCl are hardly affected by co-existence of $GdCl_3$. In addition, having the additional $GdCl_3$ in the salts, the i_0 values follow the same trends with no $GdCl_3$; hence, this indicates that the kinetics for U^{3+}/U reaction on the electrode surface are not significantly being influenced by the presence of $GdCl_3$.

6 Summary and Suggested Future Work

6.1 Background

Pyroprocessing technology has been examined in several countries including the United State, Russia, France, Japan, South Korea, and India. The purpose of this technology is not only to treat the irradiated nuclear fuel, but also to reduce volume of the nuclear waste, recycle actinides, and close the fast reactor fuel cycle. The heart of this technology is the ER where pure U and An elements are being recovered in LiCl-KCl eutectic salt at 773 K. This recovery can be accomplished by using an electrolysis; therefore, many studies have been done to understand the electrochemical, thermodynamic, and kinetic behaviors of those products. However, several datasets reported in the past have been scattered and obscure due to challenges in the experimental measurements. Therefore, in this study, the main goal was to develop methods to provide reliable and repeatable data for U properties in LiC-KCl salt system, which will give fundamental understanding and signatures for material accountability in ER process.

6.2 Literature Data for U and Electrochemical Techniques

Literature survey was delivered in Section 2. The main focus was uranium properties in LiCl-KCl eutectic such as diffusion coefficients, apparent standard potential, activity coefficient, and exchange current density. Summarized information and discussion can be found below:

- Molten salts have several advantages over aqueous solvents: high radiation resistance, low criticality concern, low vapor pressure, low secondary wastes and high stability. Typically,

LiCl-KCl molten salt is selected as a candidate for electrorefining system with the benefit of low melting temperature (623 K).

- The apparent standard potential can be measured via CV and OCP methods, which gives an insight into the reduction potential that need to be applied for the U recovery in the ER. The reported data values show good agreement within 50 mV deviation, which are linearly dependent with temperature in general. It has been reported that the properties are independent on concentration variation; however, this needs to be experimentally evaluated at high concentrations.
- Several values of activity coefficient were reported, showing wide discrepancy up to 10^2 order of magnitude. This is because of the challenges of obtaining pure Gibbs free energy data.
- The diffusion coefficient data will provide an idea on the mass transport of U in the system; hence, the efficiency and the maximum current for the system can be optimized. The reported values are scattered depending on the techniques, ranging from 5.5×10^{-6} cm^2 s^{-1} to 4.9×10^{-5} cm^2 s^{-1}. Recent trend is that the resulting data sets from various research teams are agreeing well by the CV technique.
- Exchange current density (i_0) is an important parameter to understand kinetics of electrochemical reactions (U^{3+}/U) on the electrode surface, which will enhance the development of kinetic models and the real-time monitoring technologies. Only few data sets are available since 2009, from which meaningful comparison and trend are hardly understood. Most of the literature sources used linear polarization (LP) method, which seems to be limited to be used at high concentrations.
- In this NEUP study, five different electrochemical techniques including CV, OCP, EIS, Tafel, and LP were selected to obtain the significant datasets.

6.3 Experimental setup and procedure

All experimental preparations and measurement were carefully performed under argon environment due to the hygroscopic and corrosive characteristics of salt chemicals. Section 3 provide information on instrumental setups and materials generally used in the experiments. As each experiment require different setups and preparations, detailed descriptions were also provided and discussed in later main sections. Here are the summarizing points:

- Two glovebox systems for non-radioactive and radioactive materials (RAM I and RAM II, respectively) were installed in Radiochemistry laboratory at VCU. All experiments were done in these gloveboxes with O_2 and H_2O levels controlled less than 5 ppm.
- Commercial furnaces were used in the gloveboxes to heat and maintain the salt samples at desired temperature. Kerrlab melting furnace and Muffle furnace were utilized for the preliminary studies and uranium studies, respectively.
- LiCl-KCl eutectic salt was prepared by mixing LiCl (58.2 mol%) and KCl (41.8 mol%). Specifications of chemicals used in the present study are listed in Table 3.1.

- Prior to the melting the salts, the salt samples were dried at 523 K for 5 hours to remove possible water contents. In addition, when the salts were prepared at desired temperature, 3 – 5 hours were given for reaching the equilibrium state.
- Typically, alumina crucibles and Inconel crucibles were used as a main vessel. These are placed in a secondary alumina crucible for the safety purpose.
- All electrode rods were preinstalled in alumina sheaths for avoiding a shortage. Ag/AgCl (5 mol%) and Ag/AgCl(1 mol%) were used as a reference electrode. In the data analysis, the potentials were converted into Cl_2/Cl reference for providing comparable data.
- The electrodes are assembled into one body by designing electrode assembly, which provides security of electrodes at desired position, easy access into the molten salt, and salt sampling during the experiments.
- During uranium experiments, the salt samples were taken out from the vessel, and analyzed by ICP-MS. Detailed procedures for ICP-MS analysis are provided in Section 3.2.4.

6.4 Preliminary studies with Ce surrogate

The main objective of this preliminary study is to develop experimental methodologies and electrochemical techniques, which can be further applied to uranium studies. Cerium was selected as a surrogate material for uranium, and electrochemical measurements were performed to evaluate Ce properties in LiCl-KCl eutectic. The Ce behaviors were investigated with various electrochemical techniques on a solid and liquid cathodes.

6.4.1 Measurement of Ce properties by using a solid cathode in LiCl-KCl

The Ce properties were explored by using CV and EIS methods in LiCl-KCl-$CeCl_3$ salt at concentrations and temperatures ranging 0.5 wt% to 4 wt% and 698 K to 798 K, respectively. The following results were observed.

- The peak currents were obtained from CV measurements, and used into Berzin-Delahay relationship to calculate the diffusion coefficients of $CeCl_3$ in LiCl-KCl salt. The diffusion coefficient stays approximately the same over concentration change up to 4 wt%, while it shows a nearly proportional trend to temperature.
- The peak potentials from CV curves were used to calculate the apparent standard potentials of Ce^{3+}/Ce reaction. The resulting data sets are ranging from -3.16 V to -3.06 V versus Cl_2/Cl^- reference, which proportionally increase with rising temperature. Particularly, activity coefficients of $CeCl_3$ were calculated based on the pure Gibbs energy data at super cooled state. Here, the fusion energy was considered due to the nature of $CeCl_3$ (T_m=1080 K). The values of the diffusion coefficients and activity coefficients for $CeCl_3$ are summarized in Table 6.1.

- EIS spectra were measured at minimum overpotentials for Ce^{3+}/Ce reaction to be occurring, which were fitted to the equivalent circuit illustrated in Figure 4.8. The charge transfer resistances were obtained from the fitted curves, which were used to calculate the i_0 and k^0 for Ce^{3+}/Ce couple. The resulting data shows the linear correlation with temperature within concentration at 4 wt% $CeCl_3$, which was expressed as a linear equation in Table 6.2.
- The data measured by EIS in the present study show a good agreement with data reported by Marsden and Pesic [61]. The authors used the LP method to measure the i_0 of Ce^{3+}/Ce, however, they reported the broad range of data due to the electrode surface area change during the LP methods.

Table 6.1 Diffusion coefficients and activity coefficients of UCl_3 in LiCl-KCl salt

$CeCl_3$	0.5 wt %		2 wt %		4 wt %	
T [K]	D [$\times 10^5$ cm^2 s^{-1}]	$\gamma_{CeCl_3} \times 10^3$	D [$\times 10^5$ cm^2 s^{-1}]	$\gamma_{CeCl_3} \times 10^3$	D [$\times 10^5$ cm^2 s^{-1}]	$\gamma_{CeCl_3} \times 10^3$
698	0.479	0.56	0.430	0.47	0.418	0.23
723	0.545	0.56	0.547	0.47	0.544	0.34
748	0.653	0.68	0.675	0.47	0.672	0.29
773	0.751	1.07	0.690	1.40	0.700	0.48
798	1.012	1.29	0.875	1.94	0.860	0.43

Table 6.2 Linear relationships of the exchange current densities against the inverse temperature

$CeCl_3$	**i_0 [A cm^{-2}]**	**R^2**
0.5 wt%	$-46.284\frac{1}{T} + 0.0733$	0.954
2 wt%	$-306.4\frac{1}{T} + 0.4957$	0.987
4 wt%	$-488.93\frac{1}{T} + 0.7818$	0.960

based on the experimental data

- The practical analysis was performed to compare the measured properties cerium with those of uranium reported from previous literatures. The diffusion coefficients for both UCl_3 and $CeCl_3$ are in the same order of magnitude and showing the similar correlation with the temperature. The activation energies for the diffusion of UCl_3 have been reported,

ranging from 24.2 to 34.4 kJ mol^{-1} [37, 39], which is in a good agreement with the activation energy for $CeCl_3$.

- The similarity between both the activation energies for the diffusion may be owing to the similar ionic size of uranium and cerium. In contrast, the standard reduction potential of $CeCl_3$ was about 0.7 V more negative than the standard reduction potential for UCl_3. Due to the dispersion of the reported i_0 for U^{3+}/U reaction, it was difficult to compare the i_0 values between cerium and uranium.

6.4.2 Measurement of Ce properties on liquid cadmium cathode

In Section 4.2, further electrochemical measurements were performed to estimate the electrochemical and thermodynamic properties of $CeCl_3$ on liquid cathode. Liquid cadmium was loaded in a Pyrex crucible (see Figure 4.16), which was used as a working electrode. CV, OCC, LP, and Tafel methods were conducted to explore the diffusion coefficient, Gibbs energies for the intermetallic formations, and exchange current densities of $CeCl_3$ on the liquid cadmium cathode (LCC).

- CV curves measured in LiCl-KCl obtained at concentration of 1 wt% $CeCl_3$ and temperature ranging from 723 K to 798 K. The CV results show the Li co-deposition; therefore, background CV curves (for pure LiCl-KCl salt) were subtracted. Then, CV curves only attributed to the Ce redox on LCC were obtained. From the peak currents, the same calculation with Berzin-Delahay relationship was done to determine the diffusion coefficients of $CeCl_3$ on LCC.
- The diffusion coefficients of $CeCl_3$ ranged from 2.9×10^{-6} cm^2 s^{-1} to 5.1×10^{-6} cm^2 s^{-1} at temperatures from 723 to 798 K, which are almost half values of the diffusion coefficients on the tungsten electrode. The diffusion of Ce^{3+} may be interfered by deposition of Li^+ or LCC structure. To utilize LCC, the liquid cadmium was loaded in a Pyrex crucible having an upward surface area exposure to the molten salt LiCl-KCl. Therefore, mass transfers caused by electric force and convection are being restricted only through that exposure liquid cadmium surface.
- OCC experiments were performed to understand thermodynamic properties of Ce-Cd intermetallic compounds in LCC. In advance, Ce and Cd were deposited together on tungsten working electrode by applying reductive potential at -2.2 V (vs. Ag/AgCl) for 25 seconds. Then, the OCC were measured by applying the positive current at 1 μA. By changing Ce contents in liquid Cd film, Ce-Cd intermetallic formation also changes, which is indicated as a plateau on OCC curves. There were six different intermetallic compounds observed, and each potential of plateau was measured based on OCP. The potential differences were employed to calculate the partial molar Gibbs energy for the formations and activity of $CeCl_3$ in LiCl-KCl, which are summarized in Table 4.10.

- By observing the calculated values of activity, it can be implied that that the reduction potentials of An and Ln elements come together closely on the LCC at the beginning of the ER process, and will be gradually detached by depositing more elements in the LCC.
- Using Eq. (4-6), the standard Gibbs free energy for Ce-Cd intermetallic formations were calculated. The resulting data sets are listed in Table 4.11, which helps understanding thermodynamic energies of MA-Cd intermetallic formations in ER-LCC system and cathode processer where Cd separation is conducted by a distillation at high temperatures.
- Tafel plot and LP methods were conducted for the measurement of the i_0 of Ce^{3+}/Ce couple on LCC in LiCl-KCl molten salt by incrementally adding Cd metals in liquid Cd (mole fraction was varied from 0.0013 to 0.0303). The results from both methods (summarized in Table 4.13) show the relative difference less than 20%, but their trends of i_0 against mole fraction of Ce in Cd are in good agreement. When Ce concentration is lower than its solubility in Cd, i_0 of Ce is linearly dependent on Ce concentration (Ce solubility limit in Cd is 0.006 in mole fraction). However, as Ce fraction exceeds its solubility limit in Cd, a nearly steady i_0 of Ce is being observed. These phenomena are well illustrated in Figure 4.27, which may be attributed to the equilibrium state in the phase (Cd-$CeCd_{11}$) obtained in the Gibbs free energy study.

6.5 Measurements of uranium properties

The experimental designs and programs were established to explore the electrochemical, thermodynamic, and kinetic properties of U in LiCl-KCl salt system via CV, OCP, LP, Tafel, and EIS techniques. In addition, LiCl-KCl-UCl_3-$GdCl_3$ salt systems were being investigated and the same electrochemical measurements were carried out to give insight on an effect of other elements on U properties which could be happening in ER system. The results and discussion are summarized as follows:

- The diffusion coefficients of UCl_3 in LiCl-KCl eutectic were measured by plotting the peak currents versus the square roots of the scan rate with the Berzin-Delahay relationship. The result values are ranging from 3.9×10^{-6} cm^2 s^{-1} to 1.51×10^{-5} cm^2 s^{-1}, showing a good linearity with temperature, but weak influence by the concentration change up to 2 wt% UCl_3. The diffusion coefficients begin decreasing at 4 wt% of UCl_3, which may be due to the interaction among the particles or invalidity of the Berzin-Delahay equation at high temperatures. When the irreversible equation (Eq. (2-12)) was used with fast scan rates up to 1500 mV s^{-1}, the diffusion coefficients at 4 wt% matched with the results at lower concentrations (from 0.5 wt% to 2 wt%).
- The apparent standard potential of U^{3+}/U pair was evaluated by using CV and OCP methods. The peak potentials from CV curves were used along with the Eq. (2-15). The result values were ranging from -2.474 V to -2.564 V versus Cl_2/Cl^- reference depending on temperature, which were almost irrelevant to concentration changes up to 2 wt% UCl_3.

- In addition, OCPs were measured to calculate the apparent standard potentials. Both results show similar values of the apparent standard potentials, which also follow a similar trend to temperature. However, it can be noticed that values measured by CV are generally more negative than the values measured by OCP, which can be also observed from literatures. The results from both CV and OCP are summarized in Table 6.3
- Based on the results of the apparent standard potentials, the activity coefficients of UCl_3 in LiCl-KCl were calculated by considering the difference between ideal and actual Gibbs free energies. For understanding the ideal energies, thermodynamic data at super cooled state were utilized as listed in Table 5.2. Here, the resulting values of the activity coefficient from CV and OCP methods are being divided into two different trends according to temperature. The discrepancies were found up to 10^2 order of magnitude, and OCP method generally provides higher values and show a steep increase rate when temperature rises. Detailed data of the activity coefficients are listed in Table 6.3.

Table 6.3 Summary of apparent standard, Gibb free energy, and activity coefficient of UCl_3

	Apparent standard potential [V vs. Cl_2/Cl^-]		**Gibbs free energy of UCl_3 formation [kJ mol^{-1} K^{-1}]**		**Activity coefficient × 10^3**	
T (K)	**OCP**	**CV**	**OCP**	**CV**	**OCP**	**CV**
723	-2.494	-2.551	-721.8	-738.5	3.80	0.23
748	-2.478	-2.532	-717.2	-732.8	4.69	0.38
773	-2.463	-2.512	-712.9	-727.1	5.59	0.61
798	-2.446	-2.490	-708.1	-720.7	7.06	1.06

- The EIS, LP, Tafel, and CV methods were conducted to investigate the i_0 kinetics of U^{3+}/U couple at UCl_3 concentrations ranging from 0.5 wt% to 4 wt% and temperature from 723 K to 798 K.
- The values of i_0 for U/U^{3+} reaction are ranging from 0.0054 A cm^{-2} to 0.102 A cm^{-2} under different concentration and temperature conditions, showing the linear dependences on the concentration and temperature.
- For both LP and Tafel measurements, the potential was swept from -350 mV to 250 mV based on the equilibrium potentials.
- LP method was examined with the different scan rates ranging 3 mV s^{-1} to 100 mV s^{-1}. The result values were deviated up to 24 % depending on the applied scan rates, which is mainly due to the diffusion limits and electrode surface area changes.
- The linear Tafel region cannot be acquired at the concentration higher than 1 wt% of UCl_3 owing to the vigorous U deposition with the high bulk concentrations. Therefore, Tafel measurements were done only at concentration of 0.5 wt% UCl_3.
- The i_0 values from LP and Tafel methods follow the linear trends to concentration and temperature; however, repeatability was poor in obtaining values at 4 wt% UCl_3.

- CV data were processed in analogous methods to LP, The charge transfer resistance were measured at small overpotential region where the deposited U starts to be oxidized. Then the i_0 values were calculated. The calculated values increase when both the concentration and temperature increase; however, it is difficult to observe the linearity from these results.
- The advantage of the CV method is the rapid data acquisition through an instant scan rate; hence, this technique is useful in development of the near-real time technique for the material detection and accountability in the ER system.
- Figure 5.21(a) plots the results from the four techniques which show a moderate agreement within 33% relative difference from their average values. EIS measurements show the most linear trends regarding to the concentration and temperature whereas the values measured by CV method are much scattered and do not have a strong linear correlation with the concentration and temperature.
- As EIS measurements show the most linear trends regarding to the concentration and temperature, the linear relationships of i_0 with temperature and concentration can be modeled by using a linear equation ($y = ax + b$). The equations (listed in Table 5.5) are being extrapolated to estimate the i_0 at 5 wt% UCl_3, showing a good agreement with reported literature values.
- Dimensionless relationships ($i_0/I_0 \approx \exp(-E_a/RT)$ and $i_0/i_{0,max} = 155.2x$) were provided; therefore, estimation of the i_0 properties for U^{3+}/U could be easily tabulated.
- With addition of $GdCl_3$, the diffusion coefficients were declined by 12~35 % than the values from measurements with pure UCl_3. The apparent standard potentials and thermodynamic data remained around the same values with $GdCl_3$ being added into the salt. The i_0 values show the similar trends with the data sets measured with pure UCl_3 salts. The specific properties with co-existence of $GdCl_3$ are summarized in Table 6.4.

Table 6.4 Summary of the uranium properties with $GdCl_3$ additions

No	Sample	D $\times 10^5$ ($cm^2\ s^{-1}$)	$E^{0*}_{U^{3+}/U}$ (V vs. Cl_2/Cl)	$\Delta G^{0*}_{UCl_3}$ (kJ mol^{-1})	$\gamma_{U^{3+}} \times 10^3$	i_0 $\times 10^3$ (A cm^{-2})
5	U0.5_Gd0.5	0.847	-2.46 $\pm 6.0\times 10^{-3}$	-712.8 $\pm$ 17.4	5.64 $\pm 1.53 \times 10^{-1}$	9.39 $\pm$ 0.284
6	U1.0_Gd0.25	1.13	-2.46 $\pm 4.2 \times 10^{-4}$	-713.2 $\pm$ 1.2	5.26 $\pm 9.8 \times 10^{-2}$	17.7 $\pm$ 0.679
7	U1.0_Gd0.5	1.30	-2.47 $\pm 4.5 \times 10^{-5}$	-713.8 $\pm$ 1.3	4.80 $\pm 9.7 \times 10^{-3}$	23.9 $\pm$ 0.548
8	U1.0_Gd1.0	1.11	-2.46 $\pm 4.0 \times 10^{-4}$	-712.6 $\pm$ 11.6	5.80 $\pm 1.1 \times 10^{-1}$	21.7 $\pm$ 0.93
9	U2.0_Gd1.0	1.03	-2.46 $\pm 2.7 \times 10^{-4}$	-712.1 $\pm$ 7.6	6.30 $\pm 7.5 \times 10^{-2}$	34.5 $\pm$ 0.537

10	U2.0_Gd2.0	1.00	-2.46 ± 1.2 ×10^{-4}	-711.4 ± 3.5	6.98 ± 3.8 × 10^{-2}	37.9 ± 0.213

6.6 Future Works

Several suggestions of future work based on outcomes of the present study are as follows:

- Diffusion coefficients, the equilibrium potentials, and according thermodynamic properties need to be evaluated at concentrations higher than 5 wt% (UCl_3 concentration in Mark IV ER system is between 5 wt% and 10 wt%).
- The phenomenon of decreasing of diffusion coefficients with increasing concentration needs to be elucidated with proper methodologies. Equations for irreversible soluble-insoluble system need to be derived for using the fast scan rates in CV experiments, which may be applicable at high concentrations.
- The above properties need to be further investigated in multi components salt systems including An, Ln, and alkaline earth materials (which are likely in the ER system) for understanding the physical and chemical effects among the elements.

References

1. Nuclear Technology Review 2015, reported by the Director General, GC(59)/INF/2, July (2015).
2. Spent Fuel Reprocessing Options, IAEA-TECDOC-1587.
3. Nuclear Energy Data, NEA No. 7246, OECD 2015.
4. M. F. Simpson and Jack D. Law, Nuclear Fuel Reprocessing, INL/EXT-10-17753, February (2010).
5. T. Todd, Nuclear regulatory Commission Seminar, March 25 (2008).
6. S. Phongikaroon, EGMN 691 – Nuclear Fuel cycle, Lecture #1, Fall (2015).
7. M. Iizuka, "Diffusion Coefficients of Cerium and Gadolinium in Molten LiCl-KCl," *Journal of The Electrochemical Society*, **145**, 84-88 (1998).
8. Y.I. Chang, "The Integral Fast Reactor," *Nuclear Technology*, **88**, 129-138 (1989).
9. J.P. Ackerman, "Chemical Basis for Pyrochemical Reprocessing of Nuclear Fuel," *Industrial and Engineering Chemistry Research*, **30,** 141-145 (1991).
10. C.E. Till and Y.I. Chang, Plentiful Energy - The Story of the Integral Fast Reactor, ISBN: 978-1466384606 (2011).
11. Z. Wang, D. Rappleye, M. F. Simpson, "Voltammetric Analysis of Mixtures of Molten Eutectic LiCl-KCl Containing $LaCl_3$ and $ThCl_4$ for Concentration and Diffusion Coefficient Measurement," *Electrochimica Acta,* **191,** 29-43 (2016).
12. The Fukushima Daiichi Accident, Report by the Director General, GC(59)/14.
13. Pyrochemical Separations in Nuclear Applications, A Status Report, NEA No. 5427 (2004).
14. H.Lee, G. Park, J. Lee, K. Kang, J. Hur, J. Kim, S. Paek, I. Kim, and I. Cho, "Current Status of Pyroprocessing Development at KAERI," *Science and Technology of Nuclear Installations*, **2013,** Article ID 343492 (2013).
15. E. Choi, S. Jeong, "Electrochemical Processing of Spent Nuclear Fuels: An Overview of Oxide Reduction in Pyroprocessing Technology," *Progress in Natural Science Materials International (2015).*
16. S.D. Herrmann, S. X.Li, M.F. Simpson, "Electrolytic Reduction of Spent Light Water Reactor Fuel# Bench-Scale Experiment Results," *Journal of Nuclear Science and Technology,* **44**, 361–367 (2007).
17. K. Uozumi, M. Iizuka, T. Kato, T. Inoue, O. Shirai, T. Iwai, and Y. Arai, "Electrochemical Behaviors of Uranium and Plutonium at Simultaneous Recoveries into Liquid Cadmium Cathodes," *Journal of Nuclear Materials*, **325**, 34 - 43 (2004).
18. T. Koyama, M. Iizuka, Y. Shoji, R. Fujita, H. Tanaka, T. Konayashi, and M. Tokiwai, "An Experimental Study of Molten Salt Electrorefining of Uranium Using Solid Iron Cathode and Liquid Cadmium Cathode for Development of Pyrometallurgical Reprocessing," *Journal of Nuclear Science and Technology*, **34**, 384 (1997).
19. M. F. Simpson, "Developments of Spent Nuclear Fuel Pyroprocessing Technology at Idaho National Laboratory," DOI: 10.2172/1044209 (2012).

20. S.X. Li, T.A. Johnson, B.R. Westphal, K.M. Goff, and R.W. Benedict, "Electrorefining Experience for Pyrochemical Processing of Spent EBR-II Driver Fuel," *Proceedings of GLOBAL 2005*, Tsukuba, Japan, October 9-13 (2005).
21. S.X. Li and M.F. Simpson, "Anodic Process of Electrorefining Spent Driver Fuel in Molten LiCl-KCl-UCl_3/Cd System," *Minerals and Metallurgical Processing*, **22**, 192-198 (2005).
22. R.O. Hoover, "Uranium and Zirconium Electrochemical Studies in LiCl-KCl Eutectic for Fundamental Applications in Used Nuclear Fuel Reprocessing," Ph.D. Thesis, University of Idaho, Idaho Falls, ID (2014).
23. O. Shirai, M. Iizuka, T. Iwai, Y. Arai, "Electrode Reaction of the Np^{3+}/Np Couple in LiCl-KCl Eutectic Melts," *Journal of Applied Electrochemistry*, **31**, 1055-1060 (2001).
24. G. Cordoba, C. Caravaca, "An Electrochemical Study of Samarium Ions in the Molten Eutectic LiCl + KCl," *Journal of Electroanalytical Chemistry*, **572**, 145–151, (2004).
25. J.A. Plambeck, "Encyclopedia of Electrochemistry of the Elements," Fused salt systems. Vol. X., 1976.
26. S. Kim, D. Yoon, Y. You, S. Paek, J. Shim, S. Kwon, K. Kim, H. Chung, D. Ahn, H. Lee, "In-situ Observation of a Dendrite Growth in an Aqueous Condition and a Uranium Deposition into a Liquid Cadmium Cathode in an Electrowinning System," *Journal of Nuclear Materials*, **385**, 196–199 (2009).
27. D. Vaden, S. X. Li, B. R. Westphal, K. B. Davies, T. A. Johnson, D. M. Pace, "Engineering-Scale Liquid Cadmium Cathode Experiments," INL/CON-06-11544.
28. Robin Taylor, Reprocessing and Recycling of Spent Nuclear Fuel, ISBN-13: 978-1782422129.
29. Y. Castrillejo, M. R. Bermejo, P. D. Arocas, A. M.Martinez, and E. Barrado, "The Electrochemical Behaviour of the Pr(III)/Pr Redox System at Bi and Cd Liquid Electrodes in Molten Eutectic LiCl–KCl," *Journal of Electroanalytical Chemistry*, **579**, 343 (2005).
30. G. Kim, D. Yoon, S. Paek, S. Kim, T. Kim, D. Ahn, "A Study on the Electrochemical Deposition Behavior of Uranium Ion in LiCl-KCl Molten Salt on Solid and Liquid Electrode," *Journal of Electroanalytical Chemistry*, **682**, 128-135 (2012).
31. T. Murakamia, Y. Sakamura, N. Akiyama, S. Kitawakib, A. Nakayoshi, "Electrochemical Measurement of Diffusion Coefficient of Actinides and Rare Earths in Liquid Cd," *Procedia Chemistry*, **7**, 798 - 803 (2012).
32. O. Shirai, K Uozumi, T. Iwai, and Y. Arai, "Electrode Reaction of the U^{3+}/U Couple at Liquid Cd and Bi Electrodes in LiCl-KCl Eutectic Melts," *Analytical Sciences*, **17**, i959-i962 (2001).
33. J. Zhang, "Electrochemistry of Actinides and Fission Products in Molten Salts—Data," *Journal of Nuclear Materials*, **447**, 271-284 (2014).
34. G. Janz, Molten Salt Handbooks, New York and London: Academic Press (1967).
35. G. J. Janz, G. L. Gardner, U. Krebs, and R. P. T. Tomkins, Molten Salts: Volume 4, Part 1, Fluorides and Mixtures Electrical Conductance, Density, Viscosity, and Surface Tension Data, New York (1974).

36. G. J. Janz, R. P. T. Tomkins, C. B. Allen, J. R. Downey, Jr, G. L. Gardner, U. Krebs, and S. K. Singer, Molten Salts: Volume 4, Part 2, Chlorides and Mixtures—Electrical Conductance, Density, Viscosity, and Surface Tension Data, New York (1975).
37. P. Masset, D. Bottomley, R. Konings, R. Malmbeck ,A. Rodrigues, J. Serp, and J. Glatz, "Electrochemistry of Uranium in Molten LiCl-KCl Eutectic," *Journal of The Electrochemical Society*, **152**, A1109-A1115 (2005).
38. P. Masset, R. J.M. Konings, R. Malmbeck, J. Serp, J. Glatz, "Thermochemical Properties of Lanthanides (Ln = La, Nd) and Actinides (An = U, Np, Pu, Am) in the Molten LiCl–KCl Eutectic," *Journal of Nuclear Materials*, **344**, 173-179 (2005).
39. S.A. Kuznetsov, H. Hayashi, K. Minato, and M. Gaune-Escard, "Electrochemical Transient Techniques for Determination of Uranium and Rare-Earth Metal Separation Coefficients in Molten Salts," S. A. Kuznetsov, H. Hayashi, K. Minato, and M. Gaune-Escard, *Electrochimica Acta*, **51**, 2463-2470 (2006).
40. O. Shirai, H. Yamana, and Y. Arai, "Electrochemical Behavior of Actinides and Actinide Nitrides in LiCl–KCl Eutectic Melts," *Journal of Alloys and Compounds*, **408–412**, 1267–1273 (2006).
41. J.J. Roy, L.F. Grantham, D.L. Grimmett, S.P. Fusselman, C.L. Krueger, T.S. Storvick, T. Inoue, Y. Sakamura, and N. Takahashi, "Thermodynamic Properties of U, Np, Pu, and Am in Molten LiCl-KCl Eutectic and Liquid Cadmium," *Journal of the Electrochemical Society*, **143**, 2487-2492 (1996).
42. R. O. Hoover, M. R. Shaltry, S. Martin, K. Sridharan, S. Phongikaroon, "Electrochemical Studies and Analysis of 1–10 wt% UCl_3 Concentrations in Molten LiCl–KCl Eutectic," *Journal of Nuclear Materials*, **452**, 389–396 (2014).
43. L. Martinot, "Gmelin Handbuch der Anorganischen Chemie," Springer-Verlag, New York (1984).
44. Y. Sakamura, T. Hijikataa, K. Kinoshitaa, T. Inouea, T.S. Storvickb, C.L. Kruegerb, J.J. Royc, D.L. Grimmett, S.P. Fusselman, R.L. Gay, "Measurement of Standard Potentials of Actinides (U,Np,Pu,Am) in LiCl–KCl Eutectic Salt and Separation of Actinides from Rare Earths by Electrorefining," *Journal of Alloys and Compounds*, **271-273**, 592-596 (1998).
45. B.P. Reddy, S. Vandarkuzhali, T. Subramanian, P. Venkatesh, "Electrochemical Studies on the Redox Mechanism of Uranium Chloride in Molten LiCl–KCl Eutectic," *Electrochimica Acta*, **49**, 2471-2478 (2004).
46. M. M. Tylka, J. L. Willit, J. Prakash, and M. A. Williamson, "Application of Voltammetry for Quantitative Analysis of Actinides in Molten Salts," *Journal of The Electrochemical Society*, **162**, H852-H859 (2015).
47. W. Zhou, J. Zhang, "Chemical Diffusion Coefficient Calculation of U^{3+} in LiCl-KCl Molten Salt," *Progress in Nuclear Energy*, **91**, 170-174 (2016).
48. I. Choi, B. E. Serrano, S. X. Li, S. Hermann, S. Phongikaroon, "Determination of Exchange Current Density of U^{3+}/U Couple in LiCl-KCl Eutectic Mixture," *Proceedings of GLOBAL 2009*, Paris, France, Sept. 6-11 (2009).

49. S. Ghosh, S. Vandarkuzhali, N. Gogoi, P. Venkatesh, G. Seenivasan, "Anodic Dissolution of U, Zr and U–Zr alloy and Convolution Voltammetry of $Zr^{4+}|Zr^{2+}$ Couple in Molten LiCl–KCl Eutectic," *Electrochimica Acta,* **56**, 8204-8218 (2011).
50. M. A. Rose, M. A. Williamson, and J. Willit, "Determining the Exchange Current Density and Tafel Constant for Uranium in LiCl/KCl Eutectic," *ECS Electrochemistry Letters*, **4,** C5-C7 (2015).
51. K. H. Lim, S. Park, and J. Yun, "Study on Exchange Current Density and Transfer Coefficient of Uranium in LiCl-KCl Molten Salt," *Journal of The Electrochemical Society*, **162**, E334-E337 (2015).
52. Christopher M. A. Brett and Ana Maria Oliveira Brett, Electrochemistry Principles, Methods, and Applications, Oxford University Press Inc., New York.
53. Barin, Thermochemical Data of Pure Substances, Third Edition, Wiley-VCH Verlag GmbH, 1995.
54. W. Zhou and J. Zhang, "Direct Calculation of Concentration-Dependent Activity Coefficient of UCl_3 in Molten LiCl-KCl," *Journal of The Electrochemical Society*, **162**, E199-E204 (2015).
55. A. J. Bard, L. R. Faulkner, Electrochemical Methods, Fundamentals and Applications, New York: Wiley (2001).
56. P. Delahay, New Instrumental Methods in Electrochemistry: Theory, Instrumentation and Application to Analytical and Physical Chemistry, Interscience, New York (1954).
57. T. Berzins and P. Delahay, "Oscillographic Polarographic Waves for the Reversible Deposition of Metals on Solid Electrodes," *Journal of American Chemical Society*, **75**, 555-559 (1953).
58. H. D. ErtuğruL and Z. O. Uygun, "State of the Art in Biosensors - General Aspects," book edited by Toonika Rinken, ISBN 978-953-51-1004-0.
59. A. Lisa, Electrochemical Impedance Spectroscopy and Its Applications, New York: Springer (2014).
60. L. Yang and R.G. Hudson, "Some Investigations of the Ag/AgCl in LiCl-KCl Eutectic Reference Electrode," *Journal of the Electrochemical Society*, **106**, 986-990 (1959).
61. K. C. Marsden and B. Pesic, "Evaluation of the Electrochemical Behaviors of $CeCl_3$ in Molten LiCl-KCl Eutectic Utilizing Metallic Ce as an Anode," *Journal of Electrochemical Society*, **159**, F111-F120 (2011).
62. R. D. Shannon, "Revised Effective Ionic Radii and Systematic Studies of Interatomic Distances in Halides and Chalcogenides," *Acta Crystallographica,* **A32**, 751- 767 (1976).
63. D. K. Sahoo, A. K. Satpati, and Krishnamurthy, "Electrochemical Properties of Ce(III) in an Equimolar Mixture of LiCl–KCl and NaCl–KCl Molten Salts," *The Royal Society of Chemistry*, **5**, 33163-33170 (2015).
64. S. Kim, Seungwoo Paek, Tack-Jin Kim, Dae-Yeob Park, Do-Hee Ahn, "Electrode Reactions of Ce^{3+}/Ce Couple in LiCl–KCl Solutions Containing $CeCl_3$ at Solid W and Liquid Cd Electrodes," *Electrochimica Acta,* **850**, 332-335 (2012).

65. Y. Castrillejo, M. Bermejo, R. Pardo, and A. Martinez, "Use of Electrochemical Techniques for the Study of Solubilization Processes of Cerium–Oxide Compounds and Recovery of the Metal from Molten Chlorides," *Journal of Electroanalytical Chemistry*, **552**, 124-140 (2002).
66. S.A. Kuznetsov, H. Hayashi, K. Minato, and M. Gaune-Escard, "Electrochemical Behavior and Some Thermodynamic Properties of UCl_4 and UCl_3 Dissolved in a LiCl-KCl Eutectic Melt," *Journal of the Electrochemical Society*, **152**, C203-C212 (2005).
67. O. Shirai, M. Iizuka, T. Iwai, Y. Suzuki, Y. Arai, "Electrode reaction of plutonium at liquid cadmium in LiCl-KCl eutectic melts," *Journal of Electroanalytical Chemistry*, **490,** 31-36 (2000).
68. Y. Castrillejo, R. Bermejo, A. M. Martinez, E. Barrado, P. Diaz Arocas, "Application of Electrochemical Techniques in Pyrochemical Processes – Electrochemical Behavior of Rare Earths at W, Cd, Bi, and Al Electrodes," *Journal of Nuclear Materials*, **360,** 32-42 (2007).
69. Y. Castrillejo, P. Hernandez, R. Fernandez, E. Barrado, "Electrochemical Behavior of Terbium in the Eutectic LiCl-KCl in Cd Liquid Electrodes. – Evaluation of the Thermochemical Properties of the TbCdx Intermetallic Compounds," *Electrochimica Acta*, **147**, 743-751 (2014).
70. H. Shibata, H. Hayashi, M. Akabori, Y. Arai, M. Kurata, "Evaluation of Gibbs Free Energies of Formation of Ce–Cd Intermetallic Compounds Using Electrochemical Techniques," *Journal of Physics and Chemistry of Solids*, **75,** 972-976 (2014).
71. R. N. Lyon, Liquid-Metals Handbook, Oak Ridge National Laboratory (1952).
72. J. M. P. Q. Delgado and M. Vazquez da Silva, Analytical Solutions of Mass Transfer Around a Prolate or an Oblate Spheroid Immersed in a Packed Bed, Multiphase System and its Applications, ISBN: 978-953-307-215-9, InTech (2011).
73. M. A. Lewis and T. R. Johnson, "A Study of the Thermodynamic and Reducing Properties of Lithium in Cadmium at 773 K," *Journal of The Electrochemical Society*, **137**, 1414-1418 (1990).
74. F. Lantelme, T. Cartailler, Y. Berghoute, "Physicochemical Properties of Lanthanide and Yttrium Solutions in Fused Salts and Alloy Formation with Nickel," *Journal of The Electrochemical Society*, **148**, C604-C613 (2001).
75. K. A. Gschneidner Jr. and F. W. Calderwook, "The Cd-Ce (Cadmium-Cerium) System," *Bulletin of Alloy Phase Diagrams*, **9**, 21 (1988).
76. M. Kurata and Y. Sakamura, "Thermodynamic Assessment of Systems of Actinide or Rare earth with Cd," *Journal of Phase Equilibria*, **22**, 232-240 (2001).
77. K. Serrano, P. Taxil, "Electrochemical Reduction of Trivalent Uranium ions in Molten Chlorides," *Journal of Applied Electrochemistry*, **29**, 497 (1999).
78. D. Yoon and S. Phongikaroon, "Electrochemical Properties and Analysis of $CeCl_3$ in LiCl-KCl Eutectic Salt," *Journal of The Electrochemical Society*, **162**, E237-E243 (2015).
79. D. Yoon, S. Phongikaroon, and J. Zhang, "Electrochemical and Thermodynamic Properties of $CeCl_3$ on Liquid Cadmium Cathode (LCC) in LiCl-KCl Eutectic Salt," *Journal of The Electrochemical Society*, **163,** E97-E103 (2016).

80. D. Yoon and S. Phongikaroon, “Measurement and Analysis of Exchange Current Density for U/U^{3+} Reaction in LiCl-KCl Eutectic Salt via Various Electrochemical Techniques,” **Submitted** in *Electrochimica Acta* (2016).

Appendix A. Data from Literatures

Table A.1 Summary of literatures performed to understand U properties in application of pyroprocessing technology

Reference	Concentration & Temperature	Elements	Properties	Measurement methods used
Masset [37]	C: 9.87×10^{-5} mol cm^{-3} T: 673 K – 823 K	U	D, E^{0*}, ΔG^{*}, γ	CV, CP
Masset [38]	C: 9.87×10^{-5} mol cm^{-3} T: 673 K – 823 K	U, Pu, Np, Am, La, Nd	D, E^{0*}	CV, CP
Kuznetsov [39]	C: 6.26×10^{-5} mol cm^{-3} T: 723 K – 823K	U, Np, Pu, Am	D, E^{0*},γ, k_0	CV, LSV, CP, CA, EIS
Shirai [40]	C: 8.8×10^{-4} mol frac. T: 773 K	U, Np, Pu	E^{0*}	CV
Roy [41]	T: 673 - 723 K	U, Np, Pu, Am	E^{0*}, γ, ΔG^{*}	OCP
Hoover [42]	C: 1 – 10 wt% T: 773 K	U	E^{0*}, D, γ, ΔG^{*}	CV, CP, ASV
Martinot [43]		U	E^{0*}	
Sakamura [44]	C: 0.0016 mol frac. T: 723 K	U,Np,Pu,Am	E^{0*}	OCP
Reddy [45]	C: 0.474 mol % T: 755 K	U	E^{0*}, D	CV, CP, EIS
Tylka [46]	C: 0.5 – 4.3 wt% T: 773 K	U, Pu	D	CV
Gha-Young [30]	C: 1.0 wt% T: 773 K	U (LCC)	D, impedance	CV, EIS
Shirai [32]	C: 0.5 – 1.0 wt% T: 723 K - 823 K	U (LCC)	E^{0*}, ΔG^{*}	CV
Murakami [31]	C: 1.6 wt% T: 723 K - 773 K	U, Pu, La, Pr, Nd, Gd, Y, Sc (LCC)	D, ΔG^{*}	CV, CP
Choi [48]	C: 3.3 wt% T: 773 K	U	i_0	LP
Rose [50]	C: 5.0 wt% T: 723 K - 923 K	U	i_0	Tafel
Ghosh [49]	C: 4.0 wt% T: 773 K	U, Zr	D, i_0	CV, Tafel
Lim [51]	C: 1.0 wt% T: 738 K - 773 K	U	i_0	Tafel, LP

Table A.2 Summary of diffusion coefficients for U^{3+} in LiCl-KCl from literatures

Reference	Diffusion coefficient of U^{3+}, $D \times 10^5$ ($cm^2\ s^{-1}$)			
	698 K	**723 K**	**773 K**	**823 K**
Masset [37]	1.71 (CP)		3.8 (CP)	4.92 (CP)
			2.5 (CV)	2.84 (CV)
			3.1 (Conv.)	3.99 (Conv.)
Masset et al		2.7 (CV)		
Kuznetsov [39]		1.02 (CV)	1.45 (CV)	1.97 (CV)
Hoover [42]			1.04 (CP)	
Reddy [45]		0.552 (CV)	0.98 (CV)	1.36 (CP)
		0.68 (CP)	1.03 (CP)	
Tylka [46]			1.52 (CV)	
Martinot [43]		0.68 (CV)		

Table A.3 Summary of apparent standard potentials of U/U^{3+} from literatures

Reference	Apparent standard potential, E^{0*} (V vs Cl_2/Cl^-)			
	698 K	**723 K**	**773 K**	**823 K**
Masset [37]	-2.588 (CP)		-2.516 (CP)	-2.481 (CP)
	-2.561 (CV)		-2.491 (CV)	-2.437 (CV)
	-2.58 (Conv.)		-2.518 (Conv.)	-2.469 (Conv.)
Masset [38]	-2.60 (CV)		-2.484 (CV)	-2.462 (CV)
Kuznetsov [39]		-2.541 (CV)	-2.514 (CV)	-2.487 (CV)
Shirai et al. [40]		-2.484 (CV)	-2.453 (CV)	-2.422 (CV)
Roy [41]	-2.515 (OCP)	-2.498 (OCP)		
Hoover [42]			-2.568 (CP)	
Martinot [43]		-2.52 (OCP)	-2.489 (OCP)	-2.459 (OCP)
Sakamura [44]		-1.283 (OCP)		

Table A.4 Thermodynamic properties of UCl_3 in LiCL-KCl reported by literature

Literature	T (K)	Concentration	ΔG [kJ mol^{-3}]	γ × 10^3	Methods
Masset [38]	673	9.87×10^{-5}	-745.1	0.29	CV, CP
	703	(mol cm^{-3})	-741.8	0.35	
	773		-726.2	1.39	
	823		-712.9	4.47	
Kuznetsov [39]	723	6.26×10^{-5}		0.41	CV, LSV,
	773	(mol cm^{-3})		0.57	CP, CA, EIS
	823			0.81	
Roy [41]	673		-731.7	2.0	OCP
	694		-726.4	3.2	
	723		-723.1	3.1	
Shirai [40]	773	8.8×10^{-4}	-710.1		CV
		(mol fraction)			
Wentao [54]	723	4.98×10^{-3}		8.42	Computation
		9.90×10^{-3}		11.5	al modeling
		1.48×10^{-2}		15.4	
		1.96×10^{-2}		20.2	
		2.44×10^{-2}		26.8	
		2.91×10^{-2}		34.5	
		(mole fraction)			

Table A.5 Exchange current density of U/U^{3+} in LiCl-KCl from literature studies

Reference	Concentration	Exchange current density, i_0 (A cm^{-2})			
		723 K	773 K	798 K	923 K
Choi [48]	3.3 wt%		0.0584 (W)		
			0.0398 (C)		
			0.0204 (SS)		
			0.0202 (Zr)		
Rose [50]	5 wt%	0.0695			0.22
Ghosh [49]	4 wt%			0.008	
Lim [51]	1 wt%		0.01295	0.01833	0.02146

*W: tungsten, C: carbon based, SS: stainless steel, and Zr: zirconium.

Appendix B. Data from U-Gd mixture

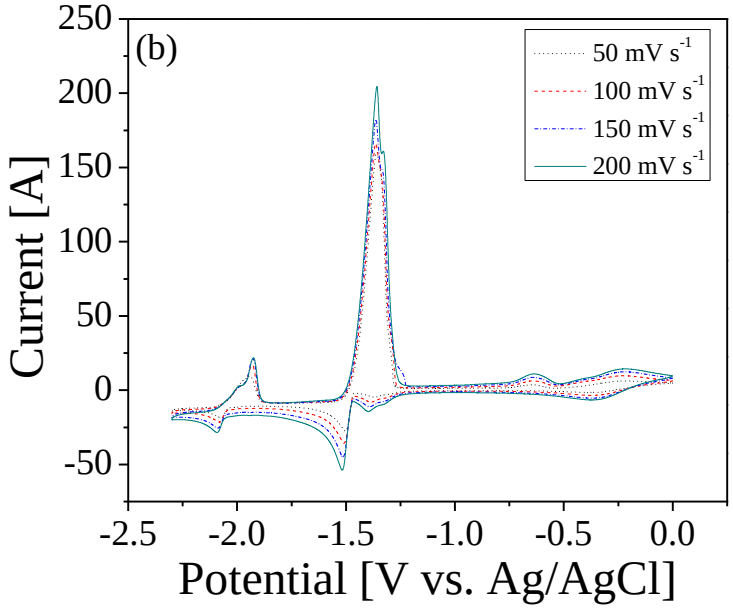

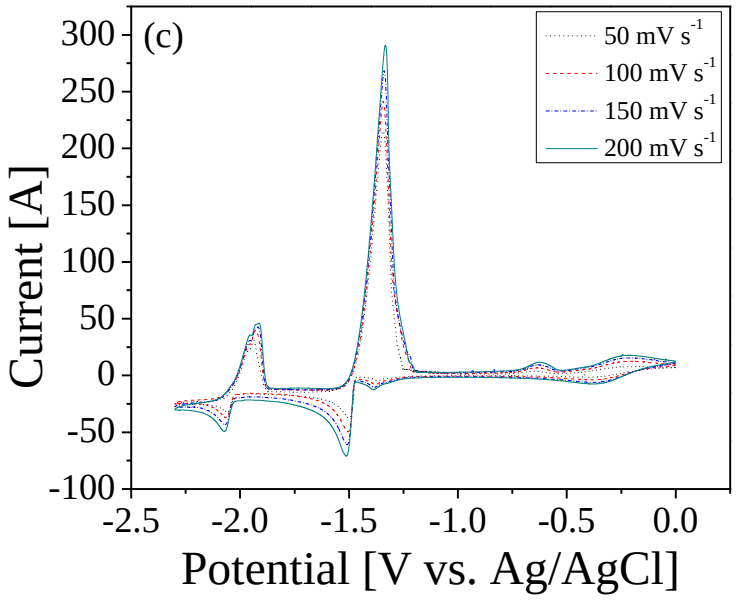

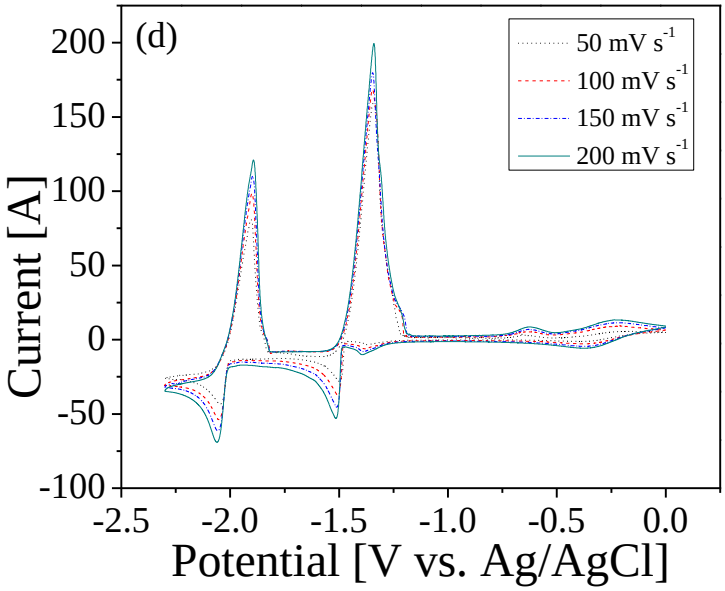
(d)
50 mV s-1
100 mV s-1
150 mV s-1
200 mV s-1
Current [A]
Potential [V vs. Ag/AgCl]
200
150
100
50
0
-50
-100
-2.5
-2.0
-1.5
-1.0
-0.5
0.0

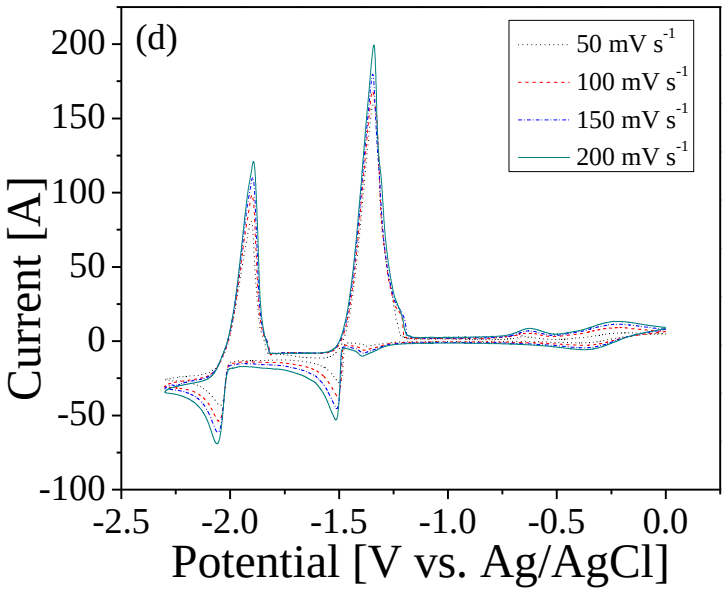
(d)
50 mV s-1
100 mV s-1
150 mV s-1
200 mV s-1
Current [A]
Potential [V vs. Ag/AgCl]
200
150
100
50
0
-50
-100
-2.5
-2.0
-1.5
-1.0
-0.5
0.0

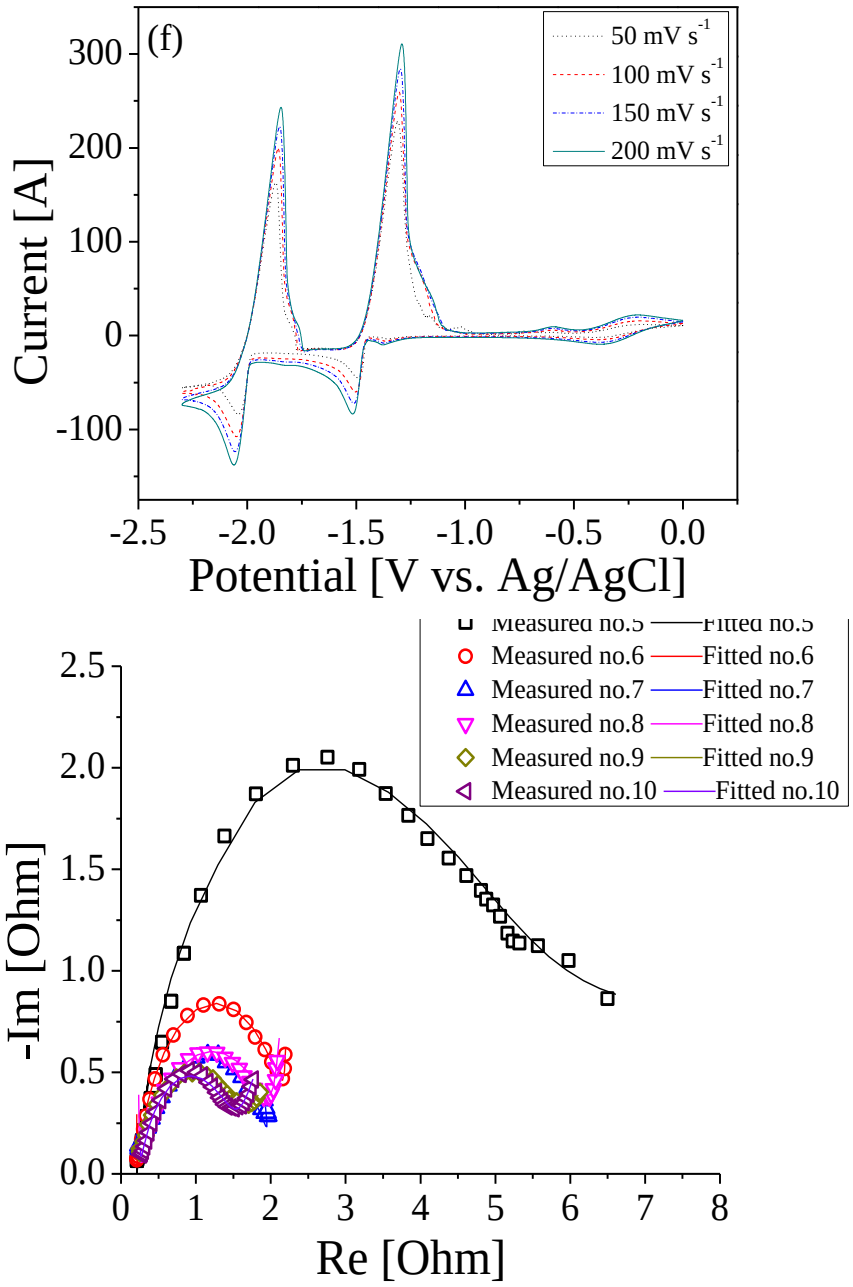

Figure B.1 Cyclic voltammogram in (a) sample no. 5, (b) sample no. 6, (c) sample no. 7, (d) sample no. 8, (e) sample no. 9, (f) sample no. 10 at temperature of 773 K. The scan rate was ranging from 50 mV s^{-1} to 200 mV s^{-1}.

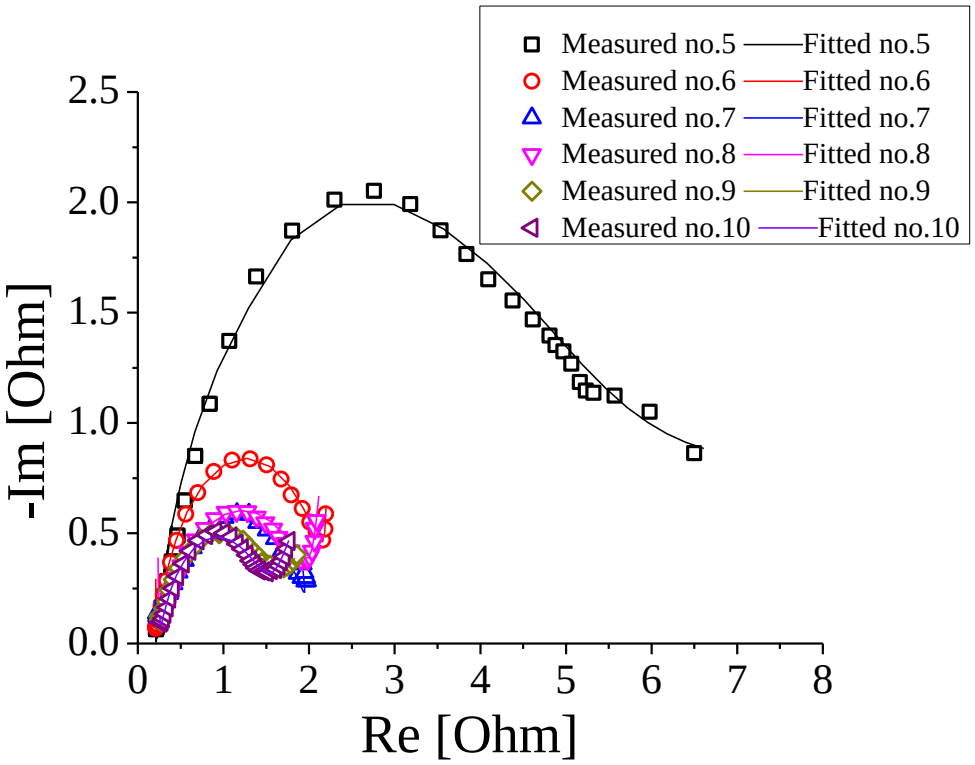

Figure B.2 The measured and fitted impedance spectra in the mixture salts (sample no. 5 – 10) at 773 K.

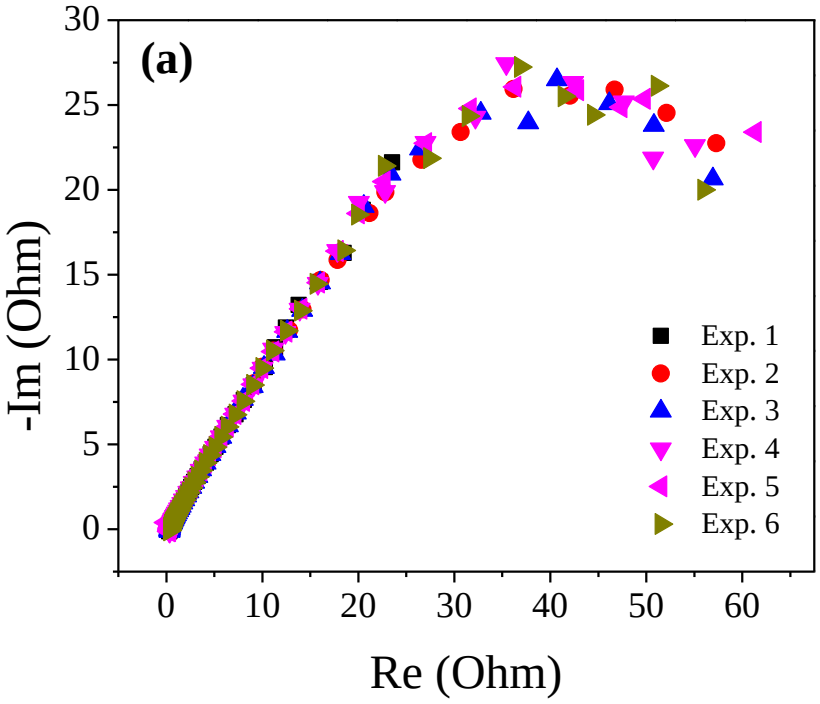

Figure B.3 Equilibrium potentials of U^{3+}/U in LiCl-KCl-UCl_3-$GdCl_3$ samples (no. 5 – 10), measured by OCP method. U metal was pre-deposited on the tungsten rod by applying potential at -1.6 V (vs. Ag/AgCl) for 30 seconds.

Appendix C. Extension Study of the NEUP Project: Exchange Current Density of Uranium with Magnesium in LiCl-KCl Eutectic Salt

Hunter Andrews and Supathorn Phongikaroon

Department of Mechanical and Nuclear Engineering

Virginia Commonwealth University, Richmond, VA 23284

RESEARCH DEVELOPMENT

Objectives and Goals

The main objective of this study is to conduct the electrochemical measurements of uranium in the presence of another species (magnesium) in the LiCl-KCl eutectic salt to provide safeguard signatures and improve the material detection analysis. Exchange current density (i_0) of uranium has been focused by using three methods: (1) Linear polarization (LP), (2) Tafel, and (3) Cyclic voltammetry (CV).

New Experimental Setup

The electrochemical experiments were contained within an argon atmosphere glove box with oxygen and water concentrations maintained at less than 5 ppm. The experiments were run using a Biologic VSP-300 potentiostat and a ThermoScientific FB1300 furnace, as shown in Figure C.1.

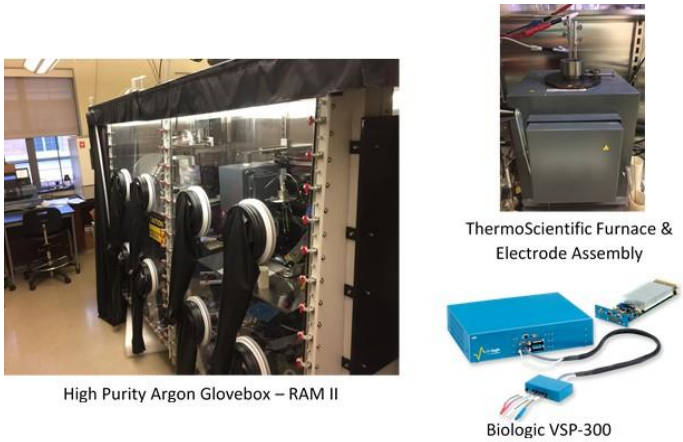

Figure C.1. Experimental apparatus and instruments at VCU.

Before preparing all samples, the primary alumina crucible was cleaned ultrasonically in acid for one hour and then baked for 24 hours at 773 K to remove any impurities that may contaminate samples. Samples were created by mixing proper ratios of lithium chloride (LiCl, 99.95%) and potassium chloride (KCl, 99.95%) from Alfa Aesar into an aluminum oxide crucible to form LiCl-KCl (58.2:41.8 mol%) eutectic salt. This crucible was then lowered into an aluminum oxide secondary crucible. The crucibles and salt mixture were placed into a furnace to be dried at approximately 523 K for a minimum of 5 hours to remove any moisture in the salt. After the drying period, the furnace temperature was raised to 773 K to allow the salt to melt and fully mix at an incremental rate of 5 K min^{-1} in order to prevent any thermal shock within the system. After the melting period had come to completion, the salt was allowed to cool to room temperature. Then, specific amounts of uranium chloride (UCl_3, 69.7%) and or magnesium chloride ($MgCl_2$, 99%) were added to the LiCl-KCl salt to form the various sample compositions. All salt samples underwent the same drying and melting process as mentioned previously after adding UCl_3/$MgCl_2$. For the electrochemical testing, the UCl_3-$MgCl_2$-LiCl-KCl sample remained in the alumina crucible located at the bottom of the furnace. A thermocouple, oriented so that it was centered in the crucible and the tip is submerged into the mixture, was used to monitor the salt temperature.

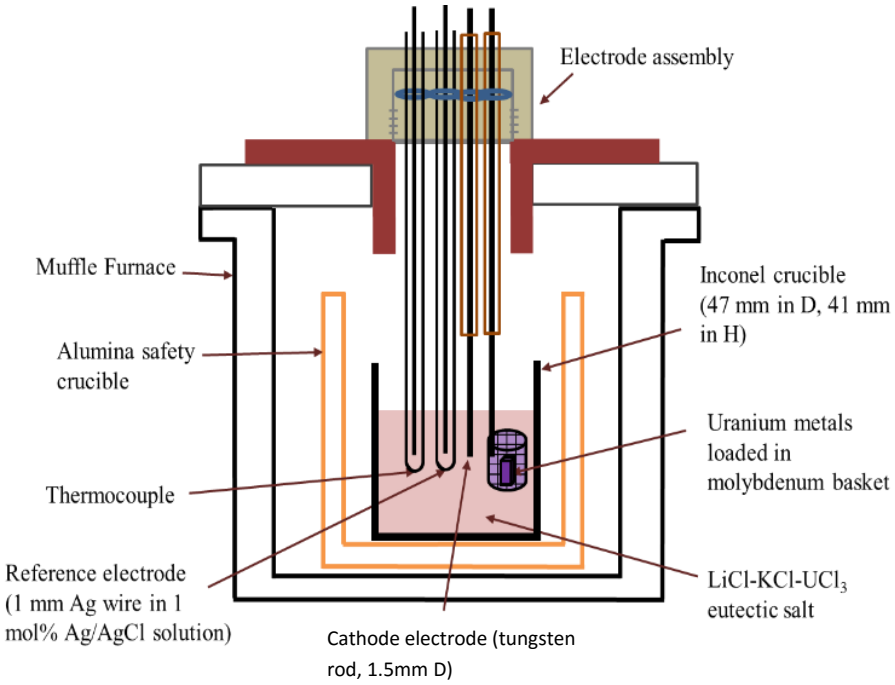

Figure C.2. Furnace schematic for electrochemical experiments.

Silver-silver chloride (1 mol% Ag/AgCl) was used as the reference electrode throughout the measurements. This reference electrode was prepared by contacting a 1 mm Ag wire to LiCl-KCl-5 mol% AgCl within a 7 mm diameter Pyrex tube. This custom made Pyrex tube was designed so that the thickness at the tip is thin enough to permit ionic conduction. Tungsten rod (1.5mm D) was used as the working electrode and uranium metal chips in a molybdenum basket submerged into the molten salt was used as the counter electrode. The submerged depth of the electrodes were

measured for each test in order to calculate the contact surface area. This experimental set up is depicted in Figure C.2.

Results and Discussion

Comparison of Exchange Current Density Acquisition Methods of UCl_3 in LiCl-KCl

The goal of this comparison was to find which method could be used as a near real-time approximation of the value. Exchange current density of uranium was found from cyclic voltammetry curves by applying linear regression to the small overpotential window. The slope of this line is equal to the current over the overpotential and can be used in a reduced form of the Butler-Volmer equation:

$$i_0 = \frac{RT}{nFS}\frac{i}{\eta} \quad (1)$$

where i_0 is the exchange current density (A cm^{-2}), i is the current density (A), η is the overpotential (V), R is the universal gas constant, T is the absolute temperature, and F is the Faraday constant. By using the slope of the small overpotential region, ±10 mV, as the value of the RHS term in Eq. (1), the exchange current density can be found. The same method can be used with LP data sets to find the exchange current density value. Detailed procedures can be found in Ref. [1].

Tafel plots were used as the third and final method for determining i_0. Tafel plots were created using LP data by modifying the vertical axis to a logarithmic scale. The Tafel method is done by utilizing a reduced form of the Butler-Volmer equation that is applicable to a large overpotential window:

$$\log(i) = \log(i_0) + \frac{\alpha n F}{2.303RT}\eta \quad (2)$$

where α is the dimensionless charge coefficient. By using linear regression in this large overpotential region, a line can be extrapolated along the plot. The point where this line and the zero overpotential line intersect is equal to $\log(i_0)$. For this technique, the selected Tafel region was ranging from -2.15 V to -2.30 V to properly compare all resulting values.

The three methods were used to compute the i_0 values of UCl_3 in LiCl-KCl at concentrations of 1.0 wt% and 2.0 wt% and temperatures ranging from 723K – 798K. The same experiments were repeated with 0.5 wt% $MgCl_2$ present in the system. The exchange current density values calculated using CV, LP, and Tafel methods are shown in Tables C.1 - C.3, respectively. Additionally the exchange current density values are graphically compared in Figure C.3. Here, Figure C.3 shows that the exchange current density increases with temperature as expected. As seen in Tables 2-3, the errors for LP and Tafel are greater due to deposition changing the working electrode surface area during testing. CV proves to be the most advantageous method due to its lack of error originating from deposition. Additionally, CV is capable of being run at greater scan rates which is more favorable for future near-real time applications. When both CV and LP exchange current densities are compared with those found by Yoon and Phongikaroon [1], CV is the most consistent following both the same trends and being comparable in values (see

Figures C.4 and C.5). Further analysis will be accomplished in the next report. Addition Figures can be found in the Additional Data Profiles section.

Table C.1. Exchange current density values acquired through cyclic voltammetry

	CV Exchange Current Density, i_0 (A/cm^2)			
T (K)	1.0wt% UCl_3-0.0wt% $MgCl_2$	2.0wt% UCl_3-0.0wt% $MgCl_2$	1.0wt% UCl_3-0.5wt% $MgCl_2$	2.0wt% UCl_3-0.5wt% $MgCl_2$
723	0.01241 ± 0.0020	0.02857 ± 0.0040	0.02429 ± 0.0039	0.07456 ± 0.0048
748	0.02233 ± 0.0007	0.03439 ± 0.0027	0.03065 ± 0.0066	0.09254 ± 0.0289
773	0.01384 ± 0.0026	0.03980 ± 0.0029	0.03875 ± 0.0072	0.12169 ± 0.0368
798	0.01409 ± 0.0009	0.04648 ± 0.0005	0.05126 ± 0.0076	0.14012 ± 0.0343

Table C.2. Exchange current density values acquired through linear polarization

	LP Exchange Current Density, i_0 (A/cm^2)			
T(K)	1.0wt% UCl_3-0.0wt% $MgCl_2$	2.0wt% UCl_3-0.0wt% $MgCl_2$	1.0wt% UCl_3-0.5wt% $MgCl_2$	2.0wt% UCl_3-0.5wt% $MgCl_2$
723	0.00970 ± 0.0013	0.02372 ± 0.0034	0.02235 ± 0.0009	0.13859 ± 0.0097
748	0.01218 ± 0.0031	0.04349 ± 0.0128	0.03848 ± 0.0020	0.14649 ± 0.0172
773	0.01493 ± 0.0027	0.05821 ± 0.0151	0.03881 ± 0.0005	0.20363 ± 0.0179
798	0.01347 ± 0.0021	0.05761 ± 0.0066	0.06147 ± 0.0130	0.32357 ± 0.0673

Table C.3. Exchange current density values acquired through the Tafel method

	Exchange Current Density, i_0 (A/cm^2)			
T(K)	1.0wt% UCl_3-0.0wt% $MgCl_2$	2.0wt% UCl_3-0.0wt% $MgCl_2$	1.0wt% UCl_3-0.5wt% $MgCl_2$	2.0wt% UCl_3-0.5wt% $MgCl_2$
723	0.00379 ± 0.0003	0.01148 ± 0.0012	0.00306 ± 0.0021	0.09667 ± 0.0086
748	0.00696 ± 0.0029	0.03024 ± 0.0136	0.01934 ± 0.0049	0.17036 ± 0.0527
773	0.00791 ± 0.0009	0.06517 ± 0.0345	0.01294 ± 0.0087	0.22984 ± 0.0288
798	0.00770 ± 0.0035	0.05632 ± 0.0159	0.04040 ± 0.0175	0.42768 ± 0.1689

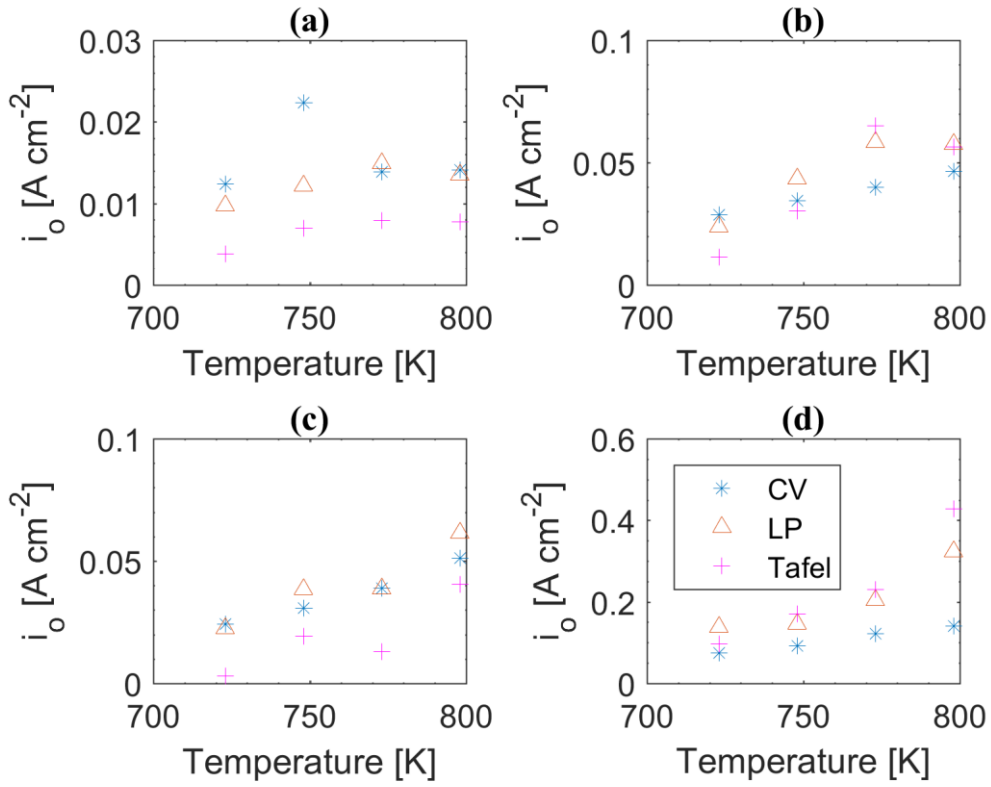

Figure C.3 Comparison of i_0 acquisition methods (a) 1.0wt% UCl_3-0.0wt% $MgCl_2$, (b) 2.0wt% UCl_3-0.0wt% $MgCl_2$, (c) 1.0wt% UCl_3-0.5wt% $MgCl_2$, and (d) 2.0wt% UCl_3-0.5wt% $MgCl_2$

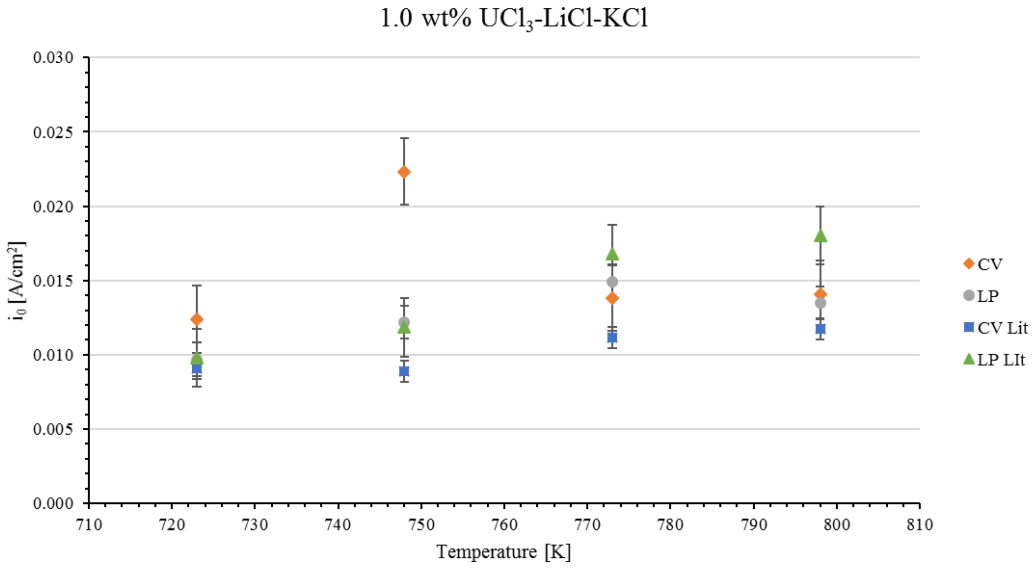

Figure C.4 Comparison of experimental and literature values for 1.0wt% UCl_3-LiCl-KCl [1].

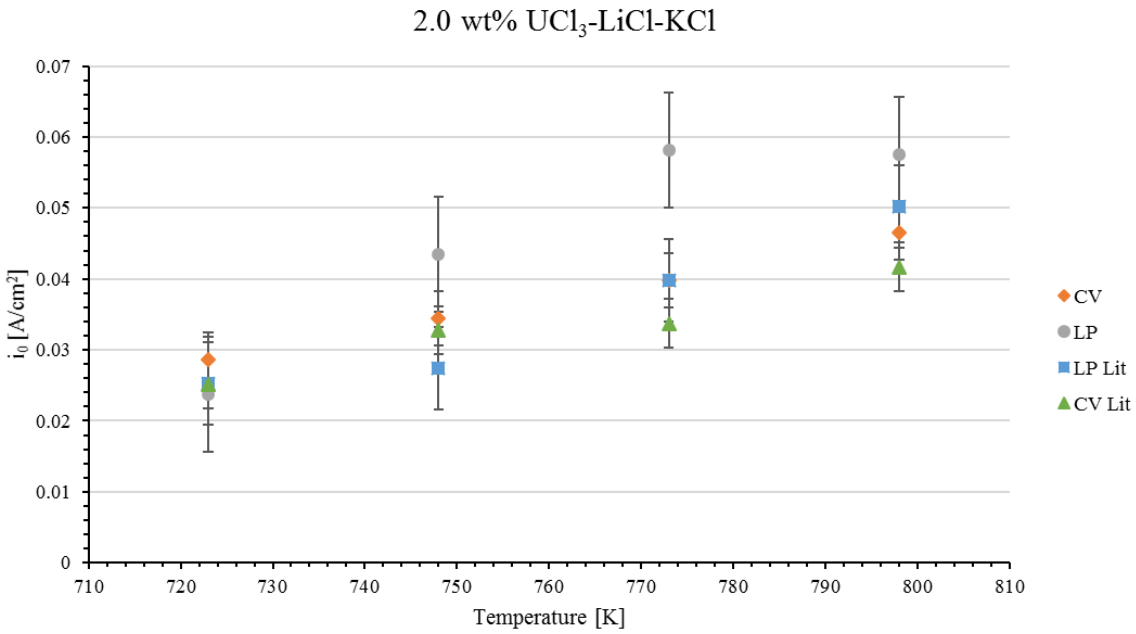

Figure C.5 Comparison of experimental and literature values for 2.0wt% UCl_3-LiCl-KCl [1].

Future works

- Complete the analysis of the fundamental properties in LiCl-KCl-UCl_3-$MgCl_2$ mixtures.

References

[1] Yoon, D., and Phongikaroon, S., *Electrochimica Acta*, 227 (2017) 170-179.

Additional Data Profiles:

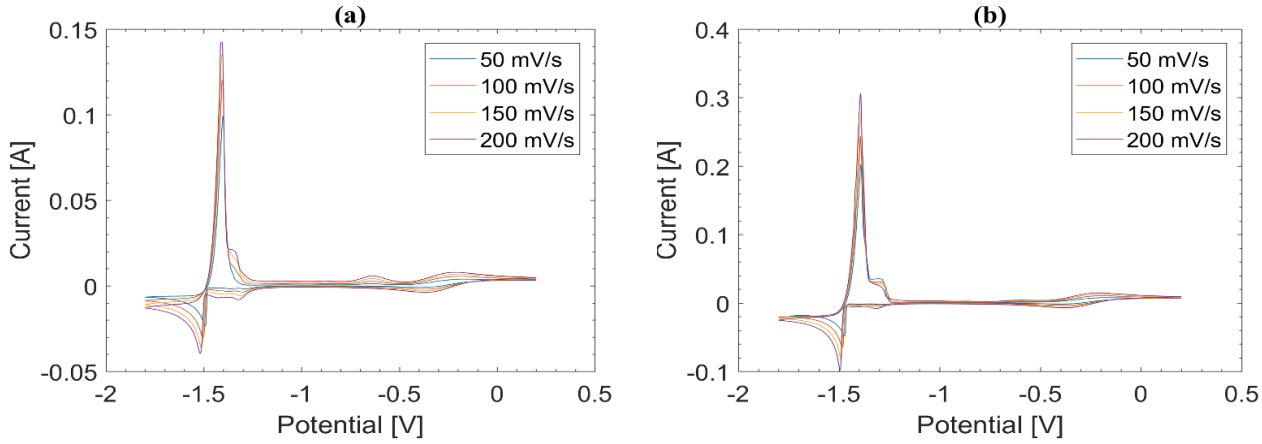

Figure A1. Cyclic voltammograms of (a) 1.0wt% UCl_3-LiCl-KCl and (b) 2.0wt% UCl_3-LiCl-KCl

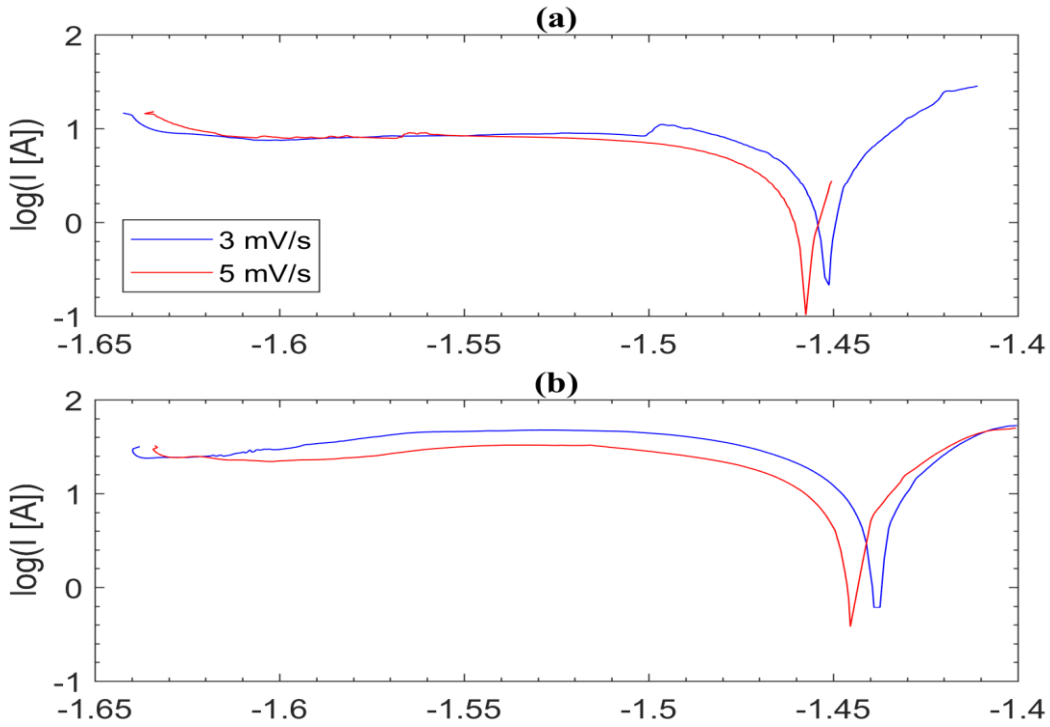

Figure A2. Linear polarization of (a) 1.0wt% UCl_3-LiCl-KCl and (b) 2.0wt% UCl_3-LiCl-KCl

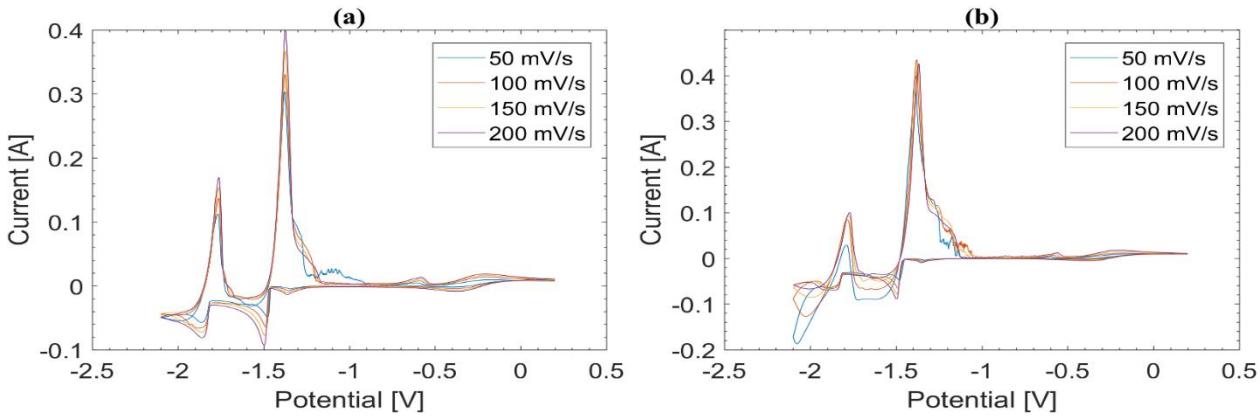

Figure A3. Cyclic voltammograms of (a) 1.0wt% UCl_3-0.5wt% $MgCl_2$-LiCl-KCl and (b) 2.0wt% UCl_3-0.5wt% $MgCl_2$-LiCl-KCl

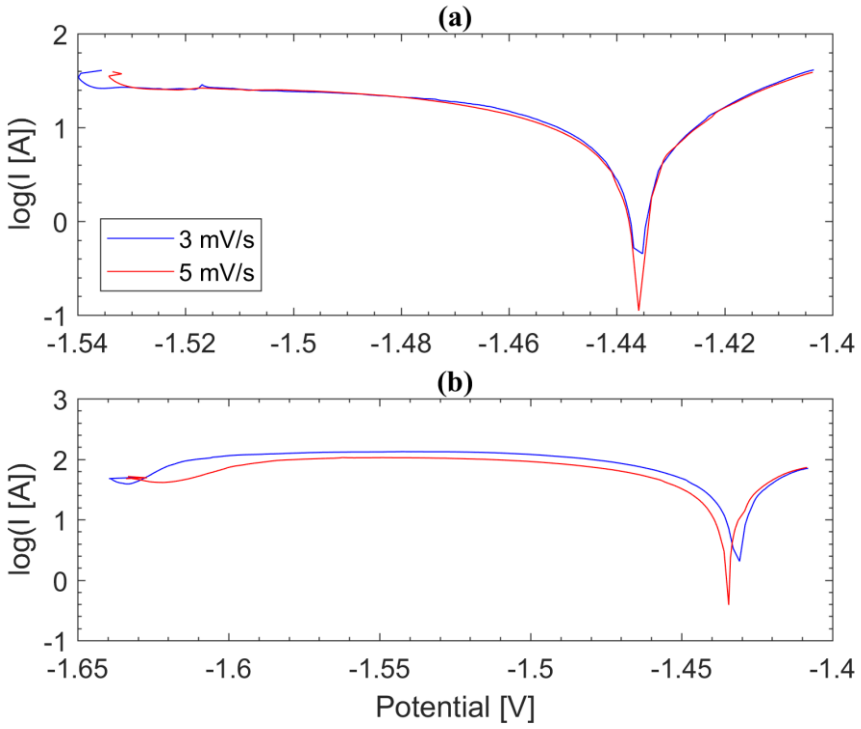

Figure A4. Linear polarization of (a) 1.0wt% UCl_3-0.5wt% $MgCl_2$-LiCl-KCl and (b) 2.0wt% UCl_3-0.5wt% $MgCl_2$-LiCl-KCl